Large scale modelling of the long-term performance of nuclear graphite cores of AGRs

A thesis submitted to the University of Manchester for the degree of Doctor of Philosophy in the Faculty of Science and Engineering

2021

Ahmadreza Farrokhnia

School of Engineering

Department of Mechanical, Aerospace and Civil Engineering

Table of Contents

Table of figures

Word count: 45435

Abstract

The UK Advanced Gas-Cooled reactors (AGRs) have cores made of graphite bricks with dual functions: as structural elements of the core, providing space for and separating fuel and control rods; and as moderator of the nuclear reaction. Nuclear graphite is a quasi-brittle material, where the dominant mechanism for failure is cracking. While cracking of isolated bricks is expected due to operation-induced changes in graphite microstructure and the gradual build-up of stresses due to irradiation, these could be tolerated as far as the overall structural function of the core is maintained. Assessment of the whole core behaviour has been previously done with full-scale models where bricks have been considered as rigid body elements connected by springs. This approach does not allow for the realistic assessment of the stresses in the bricks and associated brick cracking.

This thesis is dedicated to the development of the first physically realistic full-scale model of AGR reactor cores. The work explores the existing capabilities of the commercial software ABAQUS to represent the complexity of the core in terms of the geometries of various components, their interactions, and different formulations of graphite mechanical behaviour. The resulting model is shown to resolve the evolution of strains, stresses, and damage during reactor operation with higher fidelity than previous models.

The simulation results presented in the thesis illustrate how the developed model can be used in a fitness-for-service assessment. One set of results show the gradual build-up of damage in the graphite core over 30 years of reactor operation, as well as how damage evolves in different regions of the core. This information is useful for planning targeted inspections, which can then be used for model validation. A second set of results show the changes in the channels diameters and alignments, which is essential information for deciding on continuing safe operation of the reactor. Once the proposed model is validated or recalibrated with operational data on local damage, the proposed methodology will become a trusted predictive tool.

Declaration

No portion of the work referred to in the thesis has been submitted in support of an application for another degree or qualification of this or any other university or other institute of learning;

Copyright Statement

i.   The author of this thesis (including any appendices and/or schedules to this thesis) owns certain copyright or related rights in it (the "Copyright") and s/he has given The University of Manchester certain rights to use such Copyright, including for administrative purposes.

ii. Copies of this thesis, either in full or in extracts and whether in hard or electronic copy, may be made only in accordance with the Copyright, Designs and Patents Act 1988 (as amended) and regulations issued under it or, where appropriate, in accordance with licensing agreements which the University has from time to time. This page must form part of any such copies made. Presentation of Theses Policy You are required to submit your thesis electronically Page 11 of 25

iii. The ownership of certain Copyright, patents, designs, trademarks and other intellectual property (the "Intellectual Property") and any reproductions of copyright works in the thesis, for example graphs and tables ("Reproductions"), which may be described in this thesis, may not be owned by the author and may be owned by third parties. Such Intellectual Property and Reproductions cannot and must not be made available for use without the prior written permission of the owner(s) of the relevant Intellectual Property and/or Reproductions.

iv. Further information on the conditions under which disclosure, publication and commercialisation of this thesis, the Copyright and any Intellectual Property and/or Reproductions described in it may take place is available in the University IP Policy (see http://documents.manchester.ac.uk/DocuInfo.aspx?DocID=24420), in any relevant Thesis restriction declarations deposited in the University Library, The University Library's regulations (see http://www.library.manchester.ac.uk/about/regulations/) and in The University's policy on Presentation of Theses.

Acknowledgments

I would like express my sincere gratitude to my supervisor Professor Andrey Jivkov for his unwavering support and encouragement during this project. Throughout the course of this research project, I benefited from his advice, particularly at times where I believed myself to be at an impasse. His positive outlook and confidence in my research inspired me to continue and finish the research presented in this thesis. Furthermore, I would like to thank Dr Graham Hall and Professor Paul Mummery for their guidance through this project.

I would also like to acknowledge the support received from the Engineering and Physical Sciences Research Council UK (EPSRC) for their Doctoral Training Partnership (DTP) and the Department of Mechanical Aerospace and Civil Engineering at the University of Manchester.

Publications

At time of writing, the work presented here has been published in a conference journals and is currently being peer reviews in a separate paper in the Journal of Pressure Vessel Technology. All papers are included in part E of the Appendix.

1 Introduction

Nuclear power is currently been responsible for over 20% of power generation in the UK. 14 of the reactors that generate this power output are reaching the end of their life expectancies, and all are due to be shut down by 2035. New reactors are due to be built with the first planned to be operational by 2025. However, as power facilities close down, not enough new facilities are currently planned to cover the loss in power. Therefore, the current nuclear power plants may need to extend their operation time beyond their initial closure dates. EDF, which owns and operates the power plants, has been operating such plants already at the cost of 600 million a year. Nevertheless, EDF and the Office for nuclear regulations will close down any plant they deem unsafe (World Nuclear Association, 2017).

In Advanced Gas-Cooled reactors, Graphite plays a vital role in the safe operation of the reactors. The reactor is built up from a series of individual bricks connected by a series of keys and keyways, which when assembled, create a large body with hundreds of channels where fuel, control rods, and gas will pass through. Acting as a moderator, the Graphite converts fast neutrons into thermal neutrons, enabling the fission process required to generate heat to continue. Beyond this, the channels in the graphite act as a structural component in that they ensure control rods, which allow for the safe shutdown of the reactor, to enter and exit the core safely. Gaps in these channels also allow Carbon dioxide gas to pass the fuel and collect the heat being generated from the fuel. If any of the channels become blocked, fuel can become jammed, control rods may be locked out, or gas flow could be blocked, and the generated heat can potentially lead to a fire (Muncaster, 1993).

Graphite has quasi-brittle material properties, that change dimensions and properties under irradiation. As explained in section 2.3.2, due to graphite's microstructure, when exposed to irradiation, the graphite will undergo some dimensional changes. Graphite used in an AGR contains many pores and cracks, and when exposed to irradiation, the graphite will begin to expand due to the effects of irradiation, however, this expansion is

taken up by the pores. This creates an overall effect that results in the graphite bricks shrinking, and after a specific dosage, where the pores and cracks are no longer able to take up the microscale expansion, the material will undergo a process referred to as stress reversal, where the material will begin to expand (Savija, et al., 2018).

The dosage received by the graphite bricks is not uniform. The centre of the brick receives a higher dosage due to the placement of the fuel. Thus, the centre of the graphite brick shrinks at a faster rate than the outside and will reach stress reversal first. After a specific dosage, the centre will begin expanding while the outside of the brick continues to shrinks. Research on modelling the effects of radiation on a single fuel brick has shown that the brick can fracture and even split into two. This can affect the integrity of the entire lattice of bricks (Zou, et al., 2006).

Due to the large number of bricks, studies have been mostly taken place smaller arrays or single bricks, with large-scale analysis considering rigid-body bricks connected by spring elements representing the keys (Ahmed, et al., 1985). In such a case, all mechanical effects are assigned to the springs: stiffness, friction, damping, and damage/failure. While the approach allows for calculating load transmission or impacts between the bricks, it has a significant limitation – deformation, damage, and fracture of the bricks cannot be analysed. Consequently, the effect of bricks' damage and failure on the core behaviour cannot be studied. Other research has taken place estimating the number of fractures that can occur over 30-years; however, many questions about the integrity of the core have been left unanswered (Mummery, et al., 2020).

The aim of this thesis it to develop a physically realistic model for long-term performance of the graphite core behaviour.

To achieve this aim, several objectives must be completed. First, a model must be developed that is a geometrically realistic representation of the core. This model must include deformable bricks. In order to complete this objective, a continuum damage mechanics approach is necessary. Through this both deformable bricks and the bespoke interactions are modelled.

Subsequently, material properties that realistically change based on thermal and irradiation loads are to be applied to the model. This will allow for an investigation of how changes in the properties of graphite throughout a reactor's lifespan affect the whole core geometry and integrity. A damage mechanics approach is used that considers a damage variable dependent on changes that occur in the graphite over its lifespan. This includes variations in porosity due to dimensional changes caused by fast neutron damage, which result in stresses and microstructural disparities. Any deviations in these parameters are combined to create a damage parameter that can be utilised to calculate the material stiffness throughout the reactor's lifespan.

Finally, through analysis of a model, fracture patterns and the development of damage and the corresponding geometric changes to the whole core will be used to predict an improved assessment of the core's fitness-for-purpose. Through this a projection can be made of the end of life of a reactor that can be used to update life-extension decisions.

The analysis approach takes place using ABACUS/CAE, a software suite used for finite element analysis. It provides a simple, consistent interface for creating, submitting, monitoring, and evaluating simulations. ABAQUS completes its analysis in 3 stages, first by pre-processing or modelling, followed by a stage that includes the creation of a model via an input file. This input file will contain all the information regarding the model that includes geometries and properties. The next stage is where processing or finite element analysis takes place, which results in the development of an output file. The final stage is post-processing, where a visual rendering of the output file displays images and animations.

2 Literature Review

2.1 Nuclear Power and the role of Graphite

2.1.1 Nuclear Power Plants in the UK

The UK currently has 15 nuclear reactors generating 21% of the electricity (figure 2-1) (World Nuclear Association, 2017). According to the data provided by the Department of Energy and Climate Change, in 2015, the total amount of electricity produced in the UK was 338 terawatt-hours (TWh). This energy is comprised of 70 TWh from nuclear, 100 TWh from gas, 76 TWh from coal, and 2TWh from oil. The remaining power comes from renewable sources, such as wind and solar. However, almost half of the nuclear reactors are due to be retired by 2025 at a decommissioning cost of £30 billion (60% of which the government will be liable) (World Nuclear Association, 2017). An aim of the 2008 Energy act indicated that 30% of all electricity in the UK must be obtained from renewable sources by 2020. This resulted in a change in the UKs government policy. In 2015 the UK announced plans to phase out coal-fired generation by 2025, with plans to build gas-fired plants, while also having a much greater reliance on nuclear power and offshore wind.
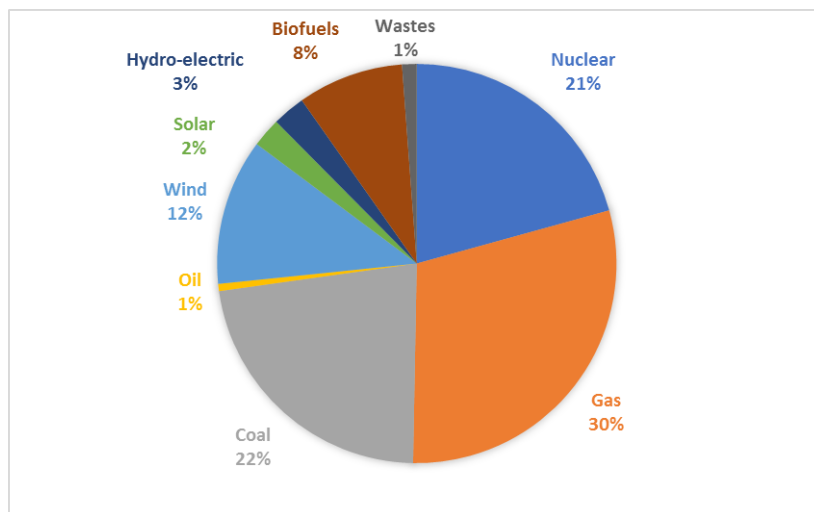
Figure 2-1: Distribution of power supply in the UK (2017) (World Nuclear Association, 2017).

Of the 15 operating nuclear reactors in the UK, seven are twin-unit advanced gas-cooled reactors (AGR), and one is a Pressurised Water Reactor (PWR). The last operating Magnox

reactor shut down in 2015. Table 2-1 (World Nuclear Association, 2017) shows each of the operating nuclear reactors in the UK, including the date each became operational and the date by which shut down of the reactors is planned. These power stations are owned and operated by a subsidiary of France's EDF called EDF Energy. The table shows that by 2030 all 15 AGR power plants are expected to shut down. Therefore, to abide by the aims set by the 2008 Energy act, new reactors must become operational over the next decade.

Plant Name	Type	First power	Expected shutdown
Dungeness B 1&2	AGR	1983 & 1985	2028
Hartlepool 1&2	AGR	1983 & 1984	2024
Heysham I 1&2	AGR	1983 & 1984	2024
Heysham II 1&2	AGR	1988	2030
Hinkley Point B 1&2	AGR	1976	2023
Hunterston B 1&2	AGR	1976 & 1977	2023
Torness 1&2	AGR	1988 & 1989	2030
Sizewell B	PWR	1995	2035

Table 2-1: Current Nuclear Power facilities in the UK, including the first date of operation and the current planned date of closure (World Nuclear Association, 2017)

2.1.2 Future power generation plans

Currently, the power output from nuclear power plants is approximately 9 Gigawatts of electrical output (GWe). Government plans will see this value rise to 25GWe. This will be reached through the production of 19 new-generation plants. The first of the new-generation plants is planned to be fully operational and producing electricity by 2025, with a further goal to have 16 new nuclear reactors operating by 2030. Although a fixed target has not been set for the power output from each of the new power facilities, government ministers have insisted that 16 GWe of new capacity should be built at five sites by 2030. The plans for future power facilities, and the planned output for the new plants is displayed in table 2-2 (World Nuclear Association, 2017). More power plants are to be built but have not passed the planning phase and are not included in the table.

Table 2-2 (World Nuclear Association, 2017) shows that the planned operation dates for new power plants are not final and are subject to change (indicated by a question mark (Data correct as of 2017)). As the landscape has changed substantially over time, the aim of opening 16 new reactors by 2030 is becoming a challenging goal to reach. This means to compensate for the loss of power, life extension for current operating reactors must be considered. Life extension for power plants is decided on commercial grounds by EDF Energy, who owns all operating nuclear power plants in the UK. EDF Energy is already planning life extensions for all the AGR units, starting with a seven-year life extension for Hinkley Point, Heysham II, Torness and Hunterson A ten-year life extension is planned for Dungeness, and a further 5-year extension has been confirmed for Heysham I. EDF have invested heavily to allow for these life extensions, and is currently spending £600 million per year on upgrades for all of its operating power plants to enable ongoing operation (World Nuclear Association, 2017).

However, the Office for Nuclear Regulation will shut down any plant it considers unsafe. Graphite plays a significant role in the operation of the power plant, as discussed in chapter 2.1.3. Hunterson and Hinkley point power stations have begun to exhibit age cracking in the graphite bricks, compromising the moderator. The damage has been carefully monitored, and while it has not yet reached a level of concern, it may become a factor in extending the life of the plant further in the future.

Proponent	Site	Type	Capacity (MWe gross)	Construction start date	Operation date
EDF Energyn	Hinkley Point C1	EPR	1670	2019	2026
	Hinkley Point C2	EPR	1670	2020	2027
	Sizewell C1	EPR	1670?	TBA	TBA
	Sizewell C2	EPR	1670?	TBA	TBA
Horizon	Wylfa Newydd 1	ABWR	1380	2019	2025
	Wylfa Newydd 2	ABWR	1380	2019	2025
	Oldbury B1	ABWR	1380	TBA	late 2020s
	Oldbury B2	ABWR	1380	TBA	late 2020s
NuGeneration	Moorside 1	AP1000	1135	2019?	late 2025
	Moorside 2	AP1000	1135	TBA	2026?
	Moorside 3	AP1000	1135	TBA	2027?
Total planned (11)			15,605 MWe		

Table 2-2: Planned Nuclear Power Facilities in the UK and the date of possible operation (World Nuclear Association, 2017)

2.1.3 Nuclear fission and the role of Graphite

Nuclear power stations in the UK generate electricity using the fission of uranium-235. Fission occurs when a neutron hits a uranium nucleus and causes it to split into two (Johnson, et al., 2000). Once a uranium nucleus absorbs a neutron, it will knock the nucleus out of shape. If this nucleus deforms enough, the electrostatic repulsion between the protons in each half becomes more significant than the forces holding the nucleus together, causing the nucleus to split. This process is called nuclear fission, where an average of 2.5 (typically 2 or 3) neutrons are released (depending on products of the fission) along with some energy in the form of heat. This energy is used to heat water into steam.

An example of the fission of a U-235 nucleus is displayed in Equation 2-1 (Johnson, et al., 2000). This is one of the many possible combinations that can take place when fission occurs. The fission of a uranium nucleus releases approximately 200MeV of energy (Johnson, et al., 2000).

$$^{235}_{92}U + {}^{1}_{0}n \ \rightarrow \ ^{236}_{92}U \rightarrow {}^{141}_{56}Ba + {}^{92}_{36}Kr + 3{}^{1}_{0}n + Energy \qquad (2.1)$$
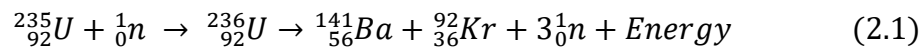
The heat released from the reaction transfers to pressurised carbon dioxide gas, which is pumped through the core by gas circulators. This carbon dioxide gas transfers the heat to boilers where feed water is contained, superheating the water into steam that subsequently drives turbines which power the generator (IAEA, 2012). These turbines contain rotating electromagnets, generating electricity. This system of generating electricity is preferred to the conventional coal-powered stations as it is a carbon-free method. It will require less mining as fission of 1Kg of U-235 provides more energy than 2 million kilograms of coal (Johnson, et al., 2000).

The principle of the thermal reaction is to cause the neutrons released to produce more fission reactions. More reactions occur when the neutrons collide and get absorbed by other uranium nuclei, causing a chain reaction to occur (Muncaster, 1993). The neutrons released from the fission of U-235 need to be slowed sufficiently to increase the capture

probability in the fission reactor. A fast neutron would not be captured and would result in chain reaction failing. To slow the neutrons a graphite moderator is utilised.

The fast neutrons collide elastically with the nuclei of the moderation, transferring energy to the moderator and slowing down the neutrons. After multiple collations with the moderator, the kinetic energy of the neutron falls to the point where it can initiate a fission reaction with U-235 Figure 2-2 (Johnson, et al., 2000). Graphite is used as a moderator as it has a small nucleus, which means the neutron is slowed efficiently and not absorbed. If too many of the neutrons are absorbed, the chain reaction would stop. In an AGR, the uranium fuel is sealed in tubes and arranged inside a large channel of Graphite. These channels are constructed from smaller blocks of Graphite.

For the chain reaction to be stable and controlled, ideally, one neutron per fission causes another fission reaction to occur. If a higher rate of neutron fission occurs, then too much energy is quickly released, causing the reaction to go out of control, creating what is referred to as a super-critical reaction. To stop this occurring, control rods are used to sustain the reaction (Muncaster, 1993).

Control rods play a vital role in the safe operation of nuclear power plants. Commonly made from boron or cadmium, control rods have a high neutron capture cross-section, which allows them to stop further fission reactions from occurring by capturing the neutrons before they can initiate a fission reaction (IAEA, 2000).

When the control rods are raised out of the heart of the reactor, the number of neutrons that cause fission to occur increases. When the control rods are lowered into the reactor, the neutrons are absorbed, reducing the number of neutrons available to cause a fission reaction. When the control rods are fully inserted into the core, the reactor will shut down (Muncaster, 1993). The channels in which the control rods pass through are integrated into the graphite moderator. These channels must remain open as in the event the graphite moderator fails, the safety of the reactor can become compromised by a blockage.
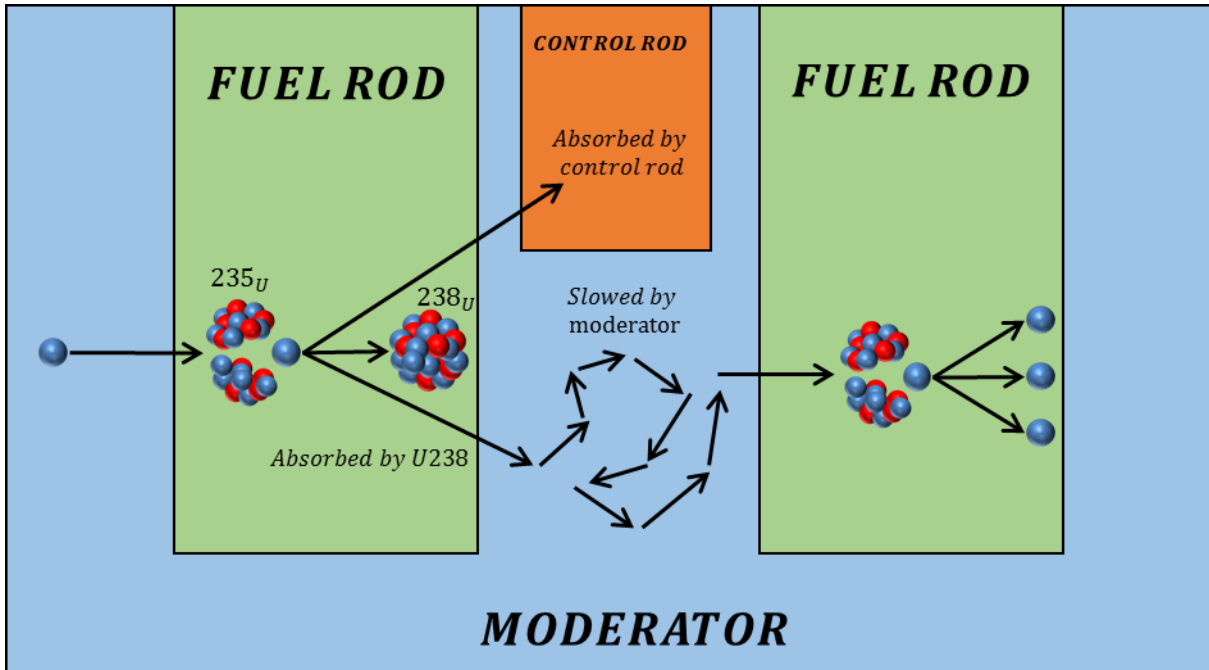
Figure 2-2: Fuel rod, Moderator and Control Rod in a Reactor

The heat produced by the fission reaction is absorbed by a coolant such as carbon dioxide (British Energy, 2006). This is shown in figure 2-3 (IAEA, 2017) . In Advanced Gas Reactors (AGR), a high pressurised CO_2 gas coolant is pumped through the graphite core up to the fuel channels, where it absorbs the heat from the fission reaction. The coolant, which now is at a high temperature, is routed through the boiler to the gas circulator. While it passes through, it transfers the heat to water in the boiler for steam, which then drives the turbines (British Energy, 2006).

The graphite moderator once again plays a vital role in the flow of the coolant. The coolant flows through the channels of Graphite, allowing it to interact with the fuel elements. If the channels become blocked, the flow of coolant can stop, leading to a build-up of Wigner energy in the channels, which can result in a fire. Something which previously occurred in the Windscale nuclear disaster of 1957, where a build-up of Wigner energy caused the graphite moderator to catch fire, and this was considered the most significant nuclear disaster in British history.

The reactor and coolant both are contained by a concrete pressure vessel that contains the high-pressure coolant. The coolant then passes through to a heat exchanger producing steam that drives the turbines (British Energy, 2006). Both the reactor and coolant become radioactive and are both placed inside a 5-meter-thick concrete wall, stopping neutrons and radiation escaping and reaching the operators (Johnson, et al., 2000) (Muncaster, 1993).
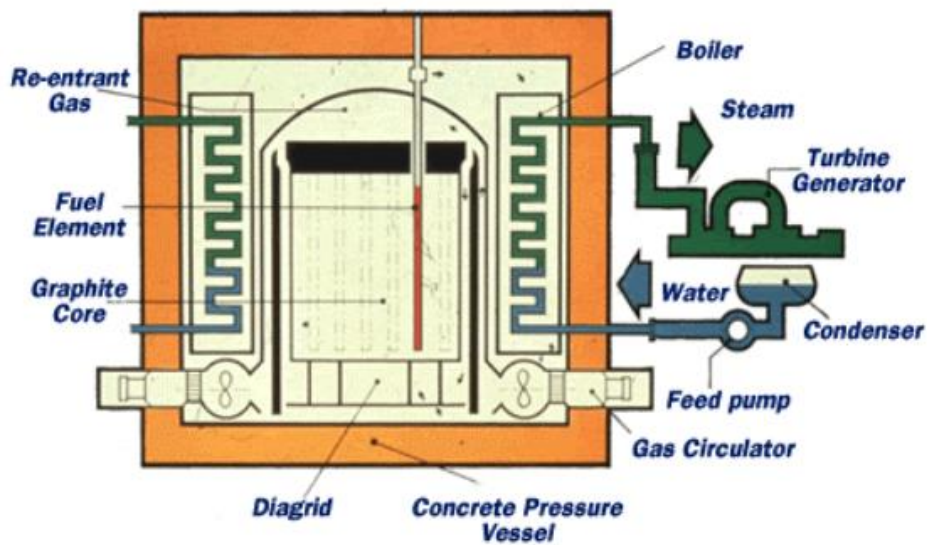
Figure 2-3: AGR Layout (IAEA, 2017)

2.1.4 Structure of the Graphite Moderator

As previously discussed, Advanced Gas-Cooled reactors in the UK have a Graphite moderator in them, which is build up from a series of graphite blocks. The model core used in this report will be based on that of Hinkley Point B. These moderators consist of three main components; fuel bricks, interstitial bricks and, filler interstitial bricks, all of which are connected through a series of keys and keyways. A visual representation of these components has been created and is shown in Figure 2-4**Error! Reference source not found.**. All four components are made from Gilsonite graphite (Nonbol, 1996).
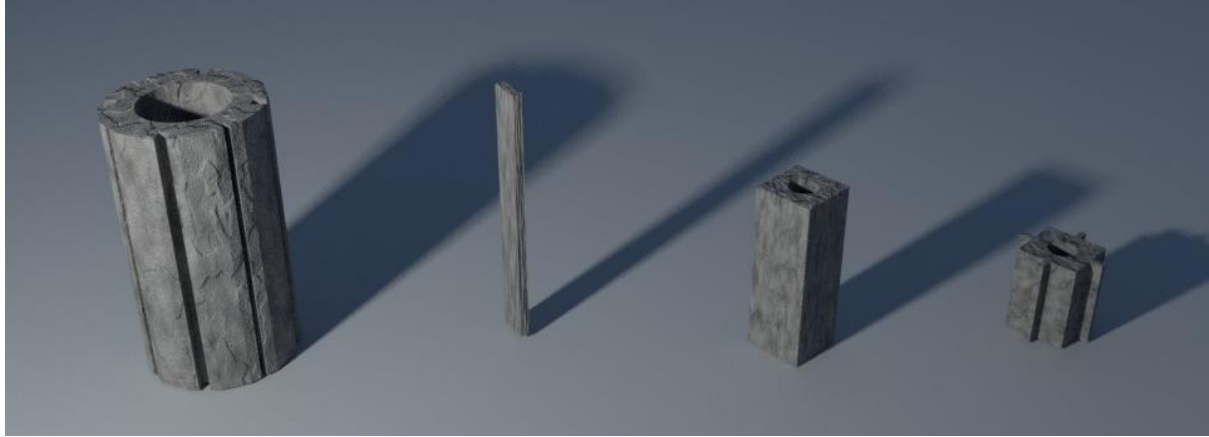
The Fuel bricks are 16-sided regular polygons. The edge of the brick contains eight keyways, where keys are located, blocking the shear movement of the bricks. Four of these keyways are used to connect to other fuel bricks, while the other four diagonal keyways connect to the interstitial bricks. When the bricks are stacked on top of each other, the gaps in the middle create channels for the fuel assemblies and coolant to flow.

Interstitial bricks are usually seen with built-in keys but can have keyways similar to the fuel brick where a separate key would sit. In this report as the models being generated are based loosely on that of Hinkley Point B, it will be assumed that the interstitial brick will contain built-in keys attached to the brick. The filler interstitial brick is similar to the interstitial brick; however, the brick contains no built-in keys or keyways.

When vertically stacked on top of each other, the graphite brick utilises built-in keys and keyways, which lock the bricks together. An offset exists between the keying system, which helps prevent any gross relative shear displacement. Figure 2-5 displays the keying layout of the core, however more detail is provided in sections 3.4.6 regarding the structure of the keying system in the lateral direction. (Duncan & Kralj, 2007).

The reactor consists of 20 fuel bricks in each row and column and consists of 12 vertical layers of bricks. The complete assembly will measure approximately 10 meters by 11 meters (Duncan & Kralj, 2007). A layer of Upper Neutron Shield (UNS) of graphite bricks

covers the top layer of bricks, and the entire assembly rests on Lower Neutron Shield (LNS) graphite bricks.
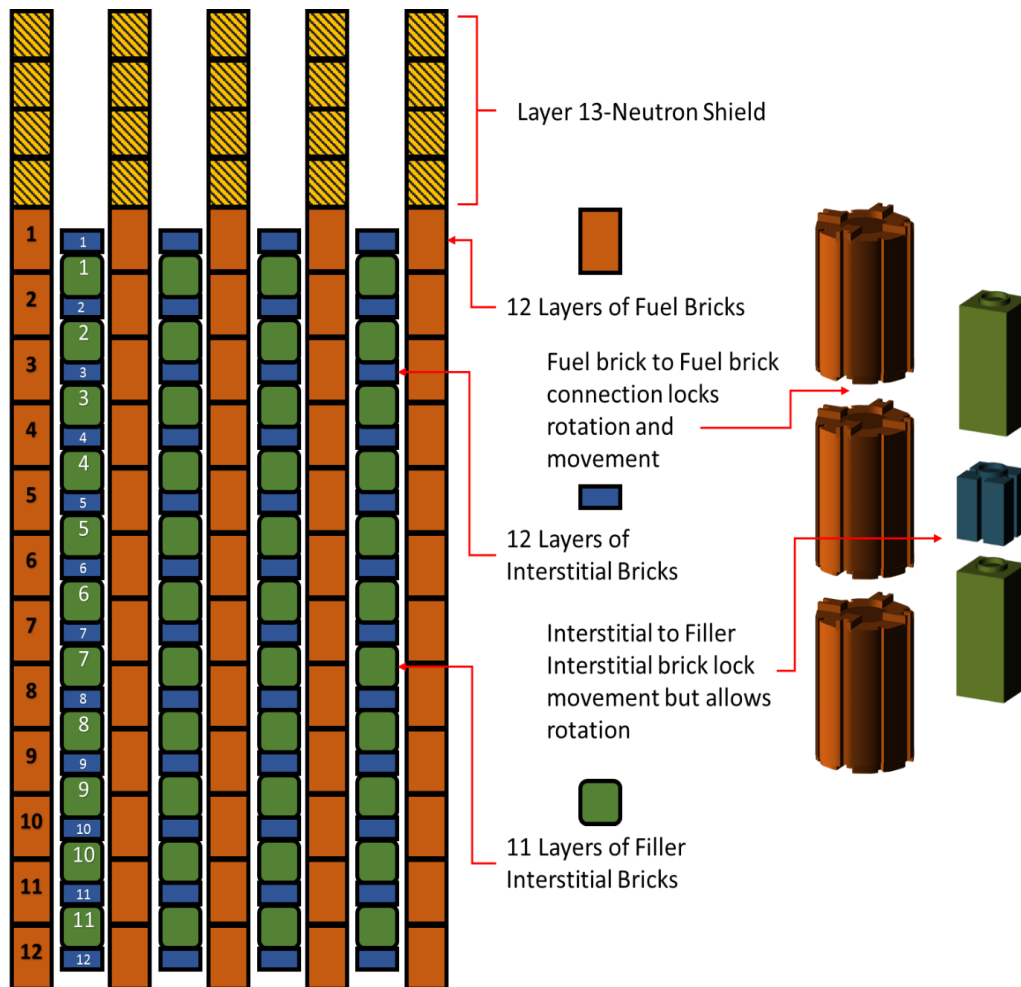
Figure 2-5: Layout of the core, Including arrangement of filler Interstitial brick and interstitial brick. (Duncan & Kralj, 2007)

The whole system is also kept laterally stable using a restraint structure consisting of restraint rods, restrains beam, centralising brackets, and Warwick links tied into the restrain rings. These are then attached to a surrounding boiler shield wall. The restraint systems around the core (shown in figure 2-6 (IAEA, 2019)) are designed to allow for expansion and contraction without failure. The restraint link is connected to the outer bricks using as spigot at a mid-layer plane. The opposite end of the restraint link is fixed into a restraint beam. There are 16 beams per horizontal mid-layer plane, with each beam supporting four restraint links. Each beam is connected to 2 Warwick links, creating a

trapezium on the plane. These Warwick links are connected at both ends. Also, the Warwick links are connected to the restrain ring beam, which is connected to the boiler shield wall. Each beam is also connected to a centralised bracket, designed to locate the restraint beam circumferentially in relation to the ring beam. This results in the free relative motion in the radial and vertical directions (Duncan & Kralj, 2007).
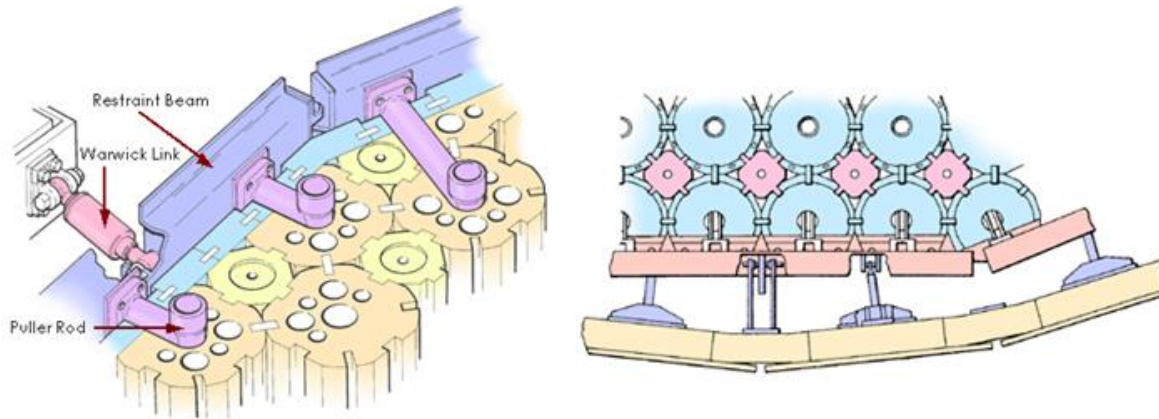
Figure 2-6: Support system for core

2.2 Structure and properties of Nuclear Graphite

Under service conditions, the irradiation of nuclear graphite causes it to undergo microstructural changes that lead to variations to its meso-scale mechanical properties. These changes in behaviour can compromise the functionality of the graphite as a structural component of the core. This section discusses the current understanding of structure and properties of graphite and their evolution during service.

2.2.1 Atomic scale structure

Graphite is constructed from carbon atoms. Each carbon atom has 4 electrons in their outer shell, three of which get shared with three other carbon atoms via a covalent bond. The final delocalised free electron in the bond becomes delocalised and is free to move. The structure of the bonds results in the creation of a single layer of carbon atoms in a hexagonal regular lattice arrangement, as shown in figure 2-7 (Marsden, et al., 2008). As these electrons move through each layer, they create very large temporary dipoles, which induce opposite dipoles in the layers above and below. This creates a weak force that holds the various layers together, referred to as Van der Waals forces. Once many layers connect, they form a graphite crystal. In general, the layers are connected in a
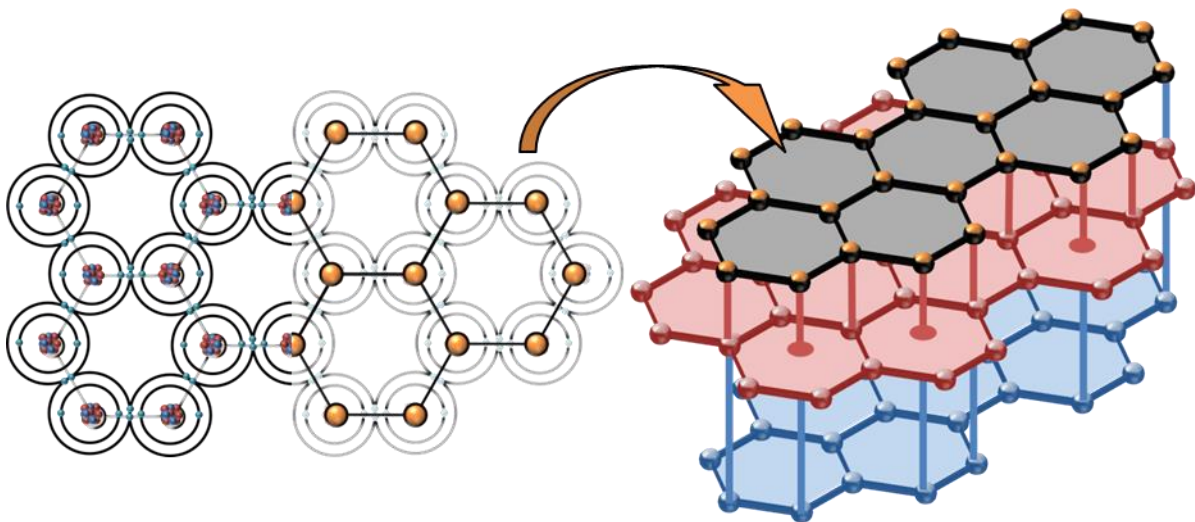
Figure 2-7: Atomic structure of Graphite (Blackman, 1970)

arrangement where every carbon atom is situated directly above the centre of a hexagonal ring of the layer below, with each successive layer being directly on top of each other (Blackman, 1970).

Due to its structure Graphite has many unique properties that make it ideal as a moderator and a structural component in a nuclear power plant. Although the Van der Waals forces holding each layer together is weak, the strength of the covalent bonds holding each layer together is significantly high, resulting in Graphite having a very high melting point, a high resistance to thermal shock, and a low coefficient of thermal expansion. Graphite increases in strength with temperature up to 2500°C. Making it an ideal material to use as a moderator in a reactor core as the temperatures of the core can also reach high temperatures (Morrison, 2015).

Graphite also has a high young's modulus and a high ultimate tensile strength, which means it can withhold large pressures without distorting or cracking, therefore it has been also utilised as a structural material in the power plant. It is also a good material for thermalizing and reflecting fast neutrons, which is why it is used as a moderator and a structural component of AGRs across the UK.

It is also worth noting that due to the delocalised electrons in each layer, graphite is a good conductor of electricity.

2.2.2 Meso-scale properties

Graphite has a very porous structure, which is affected by the irradiation of the graphite, altering its properties significantly. To understand how graphite got its porous structure and how changes to the porous structure due to irradiation affects its properties, the manufacturing of Graphite must first be understood. This includes every step from excavation through to implementation in the reactor core.

2.2.2.1 Manufacturing of graphite

Nuclear Graphite starts life as a Gilsonite ore. This black glassy rock is too brittle and can be easily fractured. Converting this into nuclear Graphite begins first by dehydrating the

ore and breaking it up into smaller spherical particles ranging from 0.5mm-4mm in diameter. The following step continues with the calcination of the particles (i.e., desiccation by exposing to intense heat). These particles are calcined to reduce the amount of volatile matter from approximately 15% to less than 0.5% (Morrison, 2015).

This calcination process is required to pre-shrink the particles before baking, which occurs later. This calcined Gilsonite coke is ground into even smaller particles, separating them into two categories, the larger intact spherical particles with diameters smaller than half a millimetre and the smaller micro-grain particles referred to as flour, ranging between 1 and 300 micro-meters. The flour particles allow for tighter packing and result in a higher density for the final product (Morrison, 2015).

Following this, the particles are mixed with a binding agent. This binder material is a distillation product from coal, such as coal-tar pitch, which soften once heated. The two particles are mixed with the coal-tar pitch binding agent at a temperature of 165°C before being cooled to 125°C; a temperature referred to as the softening point, which is the temperature where forming can take place. To avoid the anisotropic bias caused during forming, the mixture is compressed with plungers into a mould before cooling to ambient temperature. This easily breakable mixture is referred to as the "green article" (Bodel, 2012).

The next step is to bake the green article for up to 2 months, which ensured the binder material is fully integrated into the structure of the material. During this process, the organic material decomposes, resulting in a pure carbon product. As the pitch binder within the green article burns, 10 % of the mass is released as volatile gases. If all the gases are released simultaneously, it will disrupt the permeable structure of the baking process. Therefore, to avoid this from occurring, the baking takes place over 2 months to ensure the gases are steadily released and not all at once.

As the temperature is slowly increased up to 500°C, gases slowly get released. One of the gases removed during this process is hydrogen. This hydrogen, while being released, accelerates the bonding between the pre-shrunk coke filler and the binder. Once the

gasses have been withdrawn the temperature increases to 800-1000°C, which removes more impurities and causes the hardening of the material, resulting in a hard-brittle material (Bodel, 2012).

As the green article is baked and the gases released, the material becomes porous. In order to fill these pores, the materials are impregnated with more of the coal tar pitch agent. However, this agent has fewer heavier fractions than the pitch used for the binder. This is done by first heating the green article to 200°C and covering it in a molten pitch. A large amount of pressure is then applied for several hours to ensure the molten pitch fills all the gaps. Once the impregnation is complete, the material is re-baked. This process reduces the porosity from 25% to less than 20% ((Bodel, 2012; Morrison, 2015; Mantell, 1968)).

The next stage of manufacturing is graphitisation. During this process, additional impurities are removed. The process involves increasing the temperature of the material to a higher temperature than before and at a faster rate. When the temperature exceeds 1500°C, any remaining impurities that survived the baking process, such as hydrogen and sulphur compounds, are removed. This results in only carbon and metallic impurities remaining in the material.

As the temperature exceeds 1800°C, the structure of the materials becomes more graphitic, while at around 3000°C, less crystal growth occurs. This causes the structure of the filler particle to form mosaic regions of smaller graphitic crystallites. These crystals grow, change direction, and merge into longer-range order (Mantell, 1968). The most significant change is the removal of imperfections within the existing structure through annealing or diffusion. The entire graphitisation process will take up to 4 weeks to complete, however, most of this is due to the cooling of the material ((Bodel, 2012)).

The final stage of the production is to heat treat the Graphite in a halogen atmosphere. At this point, the introduction of halogens (Chlorine, bromine, and iodine) onto the surface of the material results in the thermal reduction of graphite oxide. This causes the

removal of the remaining metals, still residing in the material ((Bodel, 2012), (Poh, et al., 2013)).

The final microstructure of the Graphite is shown in figure 2-8 (Kane, et al., 2011). The Graphite created is high purity graphite, with a microstructure with three different zones. It contains areas with relatively large filler particles, which are the results of the graphitised coke particles. The Graphite also contains areas of graphitised binder, and finally, it contains large areas of porosity (Mantell, 1968).

The porosity in the Graphite accounts for approximately 20% of the virgin (un-irradiated) graphite volume. Due to the porosity of the Graphite, the density of the material is reduced from a theoretical density of 2.26g/cm^3 to approximately 1.6-1.8g/cm^3. The size of the holes created can range significantly from nanometres to millimetres in size. These gaps can merge and form micro-cracks within the structure of the graphite. These micro cracks merge with the pores forming interconnected networks through the structure, which are both open and closed to the external environment (Morrison, 2015).

Further cracks form during the calcination and graphitisation phases and form within the filler particles due to the thermal expansion and contraction as the temperature of the Graphite changes significantly. The various areas within the graphite will expand and
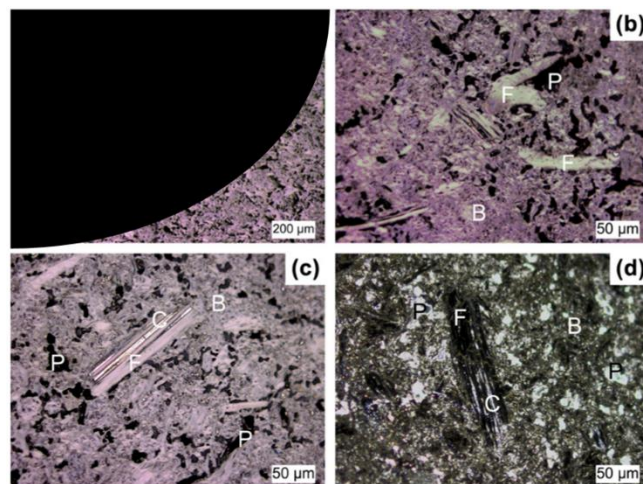
Figure 2-8:Optical Micrographs of IG-110 graphite, showing pitch
(P), Binder (B), Filler (F) and Micro-cracks (C) (Kane, et al., 2011)

shrink at different rates due to the different thermal expansion coefficient along the different axes within the graphite's atomic structure, with various crystals of Graphite in a different orientation form other crystal. The cracks resulting from the different cooling rates of the crystals in each direction (Morrison, 2015).

Depending on the process used, different grades of Graphite are created. Each grade contains its specific structures. Irradiation changes in the Graphite are strongly linked to the virgin Graphite (un-irradiated) microstructure. The various phases of the filler and binder and the pores and cracks, as well as quantities of these four components, will have a significant impact on the dimensional changes as well as the mechanical and thermal properties. These components will also affect the oxidation of the Graphite upon irradiation. This is discussed in section 2.4 of this report.

2.2.2.2 Grades of Graphite

There are many different types of grades of Graphite used throughout the world, with each type consisting of different grain sizes, ranging from coarse-grained Graphite to micro fine-grained Graphite. Reactors in the UK consist of two different grades of Graphite; Gilsocrabon graphite and Pile Grade A (PGA) graphite. While this report will look exclusively at Gilsocarbon, it is worth noting other grades of graphite exits which this section details, and is included for completeness.

The earliest generation of Magnox reactors in the UK used Pile Grade A (PGA) as a moderator. This is an anisotropic grade of Graphite that uses a carbonaceous filler phase, which is suspended in a coal tar pitch binder phase (Elcoate & Payne, 2001).

Advanced Gas-cooled reactors (AGR's) in the UK use Gilsocarbon (or IMI-24) as a moderator and reflector. Gilsocarbon contains spherical filler particles that are derived from Gilsonite pitch coke (which occurs naturally in Utah in the USA and range from 0.3 to 1.5 mm in size (Marrow, et al., 2008). Gilsocarbon has the same features as PGA, however, Gilsocrabon contains very different properties to PGA. During manufacturing, where PGA is extruded, Gilsonite is moulded, resulting in random distribution and orientation of coke particles. Due to being moulded the shape of the particles and crystals

within the material result in a small degree of anisotropy, however, this is much smaller than in other grades of Graphite; therefore, the Gilsocarbon is considered to be quasi-isotropic.

It is also worth noting that outside the UK, various other grades are also used. In Japan, the High-temperature test reactors (HTTR) use a grade of Graphite, which has an ultrafine grain size called IGI110, in contrast other grades of Graphite are being considered for future generation IV high-temperature reactor designs. In this report a model of an Advanced Gas-Cooled reactor is being investigated, where only one grade of Graphite is used in the UK, and this is Gilsocrabon.
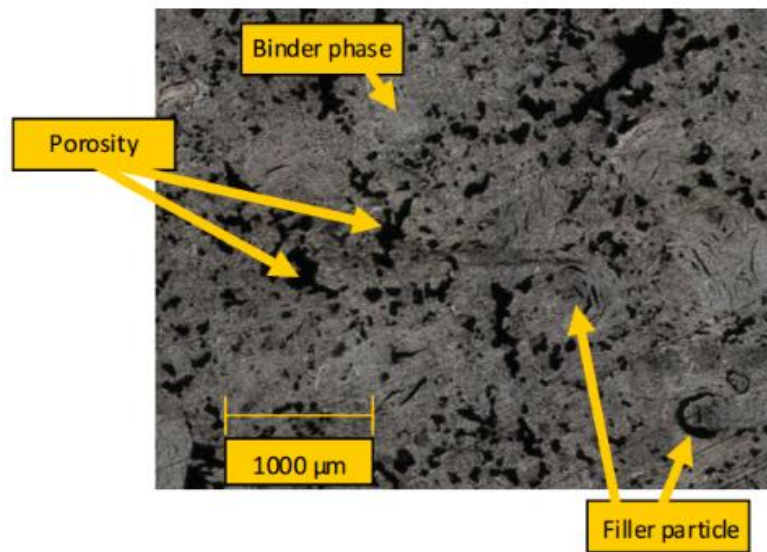
Figure 2-9:Microscopy image of Gilsonite (Kane, et al., 2011)

2.2.3 Mechanical properties

Materials have different behaviours when they are placed under a load. Some materials like glass and some ceramics are considered brittle materials, where the global response to an applied tensile or bending load follows a linear elasticity line (Figure 2-10 (Kumar & Barai, 2011)). This means as the load (pressure) on the material increases linearly, so does the extension (strain), right until the materials suddenly fail, and a fracture occurs.

Another behaviour a material can have is one of an elastic-plastic or a ductile material, for example, non-reinforced metals. These materials, similar to brittle materials, have a region of linear elasticity up to a point referred to as the yield point or elastic limit. From this point, the material will have a non-linear response where plastic deformation occurs, followed by crack localisation, where the material fails.

Graphite's material behaviour is unique in that Graphite possesses a quasi-brittle material behaviour (Marrow & Mostafavi, 2011). Quasi-brittle is a term used to describe many materials of heterogeneous microstructures. Non-irradiated Graphite has been shown to have non-linear behaviour. When a load is applied, the various pores and micro-cracks, produced by the manufacturing of Graphite, begin to join together, forming larger cracks. Crack propagation can become so extensive that it results in irreversible energy dissipation, where the yield limit of the material is reached (Becker & Marrow, 2013).

The difficulty with predicting the failure limit of Graphite comes down to the manufacturing process, where the micros-cracks and pores are randomly distributed. This is also seen in other quasi-brittle materials like concrete, toughened ceramics, grouted soils, bone, paper, wood, and even ice (Jimenez Pique, et al., 2003). All of these materials are normally considered as brittle; however, due to the joining together of micro-cracks, non-linear behaviour is observed.
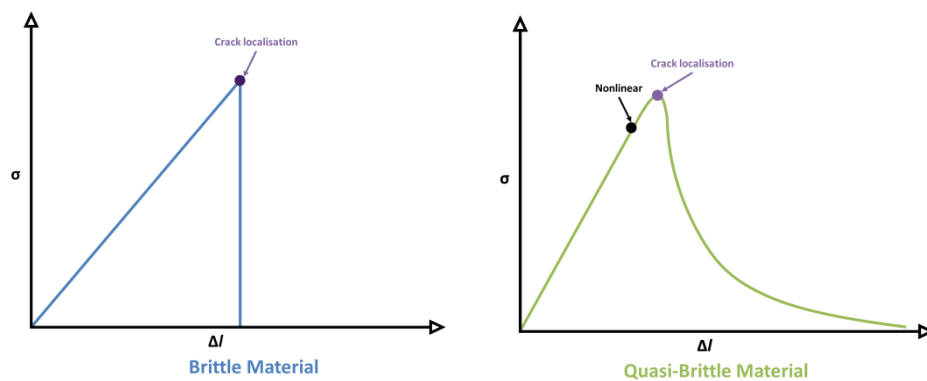
Figure 2-10:Stress strain graphs of various materials (Kumar & Barai, 2011)

2.2.4 Effects of irradiation on Gilsocarbon

Throughout the operation, the material properties and dimension of Graphite will change due to the neutron irradiation dose and temperature. The change in the temperature and dose will also result in significant changes in the stress and distortions of graphite components. Irradiation changes in the Graphite are linked to the microstructure of the virgin Graphite. The filler and binder phase, pores, and crack microstructures will significantly impact the dimensional changes and the mechanical and thermal properties (Kane, et al., 2011).
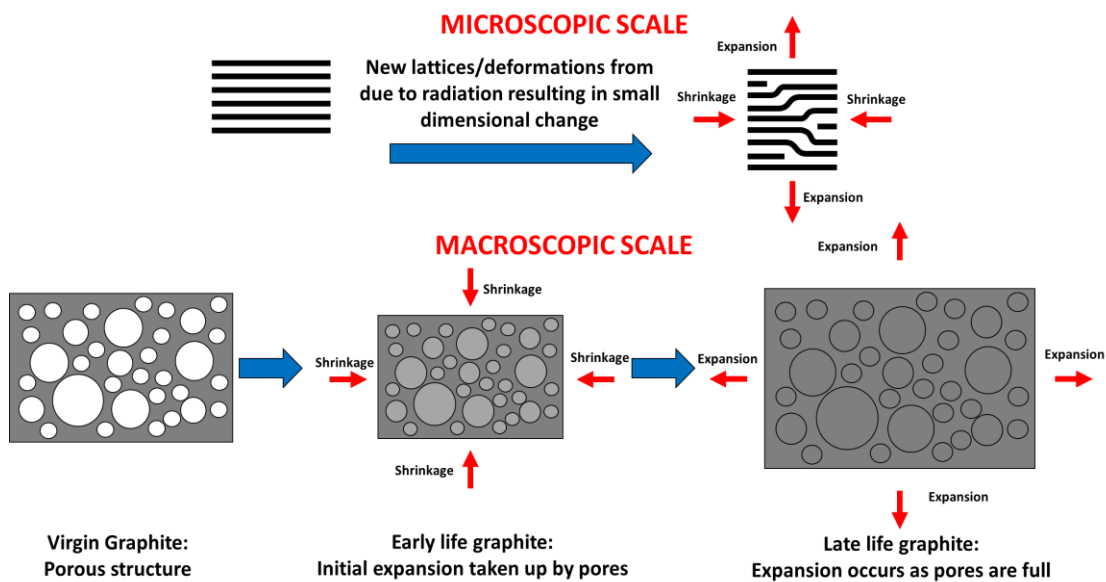
Figure 2-11: Microscopic and Macroscopic changes to graphite as a result of irradiation

At different scales, the irradiation of graphite results in different consequences. At atomic-scale, the fast neutrons produced during fission collide with the carbon atoms in the graphite lattice, as shown in Figure 2-11. The thermal energy of the fast neutrons is approximately 2 MeV, which is significantly higher than the energy required to knock a carbon atom from the lattice, which is approximately between 0.025-0.060 MeV. The difference is so high that many carbon atoms are also knocked out of the lattice due to secondary collisions between recoiling carbon atoms. During the operation time of a reactor, it is estimated that a single atom is displaced an average of 20 times, each time creating a vacancy in the graphite lattice.

In an AGR operating at high temperatures, the knocked-out carbon atoms can re-join or become trapped in the lattice, while the rest will form new graphite sheets. The new sheets will become interweaved between the original layers. Throughout the irradiation process, the carbon atoms are redistributed, which results in shrinkage in the basal plane and expansion in the perpendicular direction, as seen in figure 2-11. (Liang, 2012).

Price and Bokros propose the irradiation-induced crystal dimensional changes in the perpendicular and parallel direction to the basal planes can be referred to as $\frac{\Delta X_c}{X_c}$ and $\frac{\Delta X_a}{X_a}$ as a function of the fluence and temperature. This analysis can be used to produce an estimate for the dimensional changes of Gilsocarbon based on dosage. Using this data in conjunction with experimental data measured by Brooklehurst and B.T Kelly, figure 2-12 can be created, which shows the dimensional changes both parallel and perpendicular to the basal plane. The figure clearly shows that expansion occurs in the perpendicular plane, while shrinkage occurs parallel to the basal plane (Brocklehurst & Kelly, 1993).
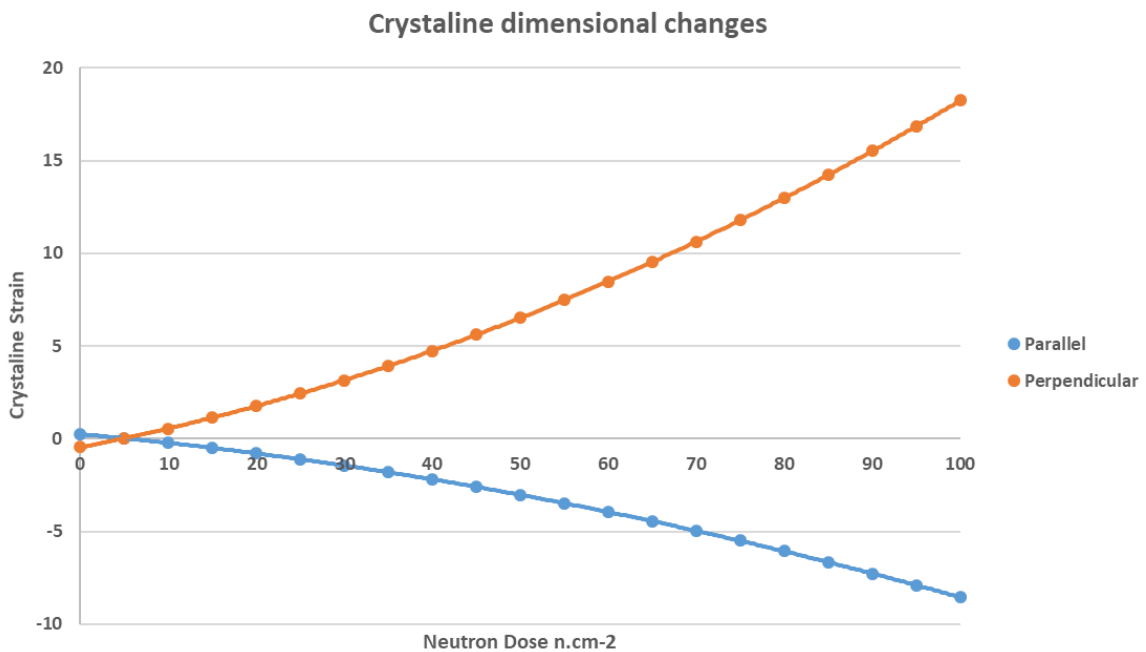
Figure 2-12: Crystalline Dimensional changes in parallel and perpendicular directions

The dimensional changes shown graphically in figure 2-12 for each direction can be defined by the following equations:

$$\frac{\Delta X_c}{X_c} = c_0 + \gamma c_1 + \gamma^2 c_2 \tag{2.2}$$

$$\frac{\Delta X_a}{X_a} = a_0 + \gamma a_1 + \gamma^2 a_2 \tag{2.3}$$

Where γ is the irradiation dosage, while c_i and a_i represent constants.

While on an atomic (crystalline) scale, shrinkage occurs in only the basal plane, on a meso-scale (polycrystalline) scale, initially, the Graphite will shrink in both directions while later expanding, in a phenomenon referred to as stress reversal. This occurs due to how the Graphite is manufactured. As discussed previously, on a meso-scale, the Graphite contains many pores. While the crystalline expansion takes place, this expansion takes place into the empty pores. After a specific limit, the pores are no longer able to take up the crystalline expansion. This results in stress reversal, where the continuing crystalline expansion results in expansion on a meso-scale (Oku & Ishihara, 2004) (Savija, et al., 2018).

The overall dimensional changes can be given as:

$$\frac{\Delta l}{L} = \frac{1}{3}\left[\frac{\Delta X_c}{X_c}F + 2\frac{\Delta X_a}{X_a}\right] \tag{2.4}$$

Where F is the influence function, a function of both temperature and fluence, which was obtained by using Gilsocarbon irradiation data, and experimental data considering irradiation of Highly Orientated Pyrolytic Graphite. This can be combined to produce the graph for irradiation of Gilsocarbon shown in figure 2-13 (Brocklehurst & Kelly, 1993).

This re-structuring of the lattice has an adverse effect on the material properties of the Graphite. The irradiation of the Graphite introduces pin dislocations within the graphite matrix, which blocks deformations forming in the lattices. The effect this has on the graphite results in an increase in strength and young's modulus, which only falls when stress reversal begins and the degradations of the Graphite occur (Ishihara, et al., 1991).
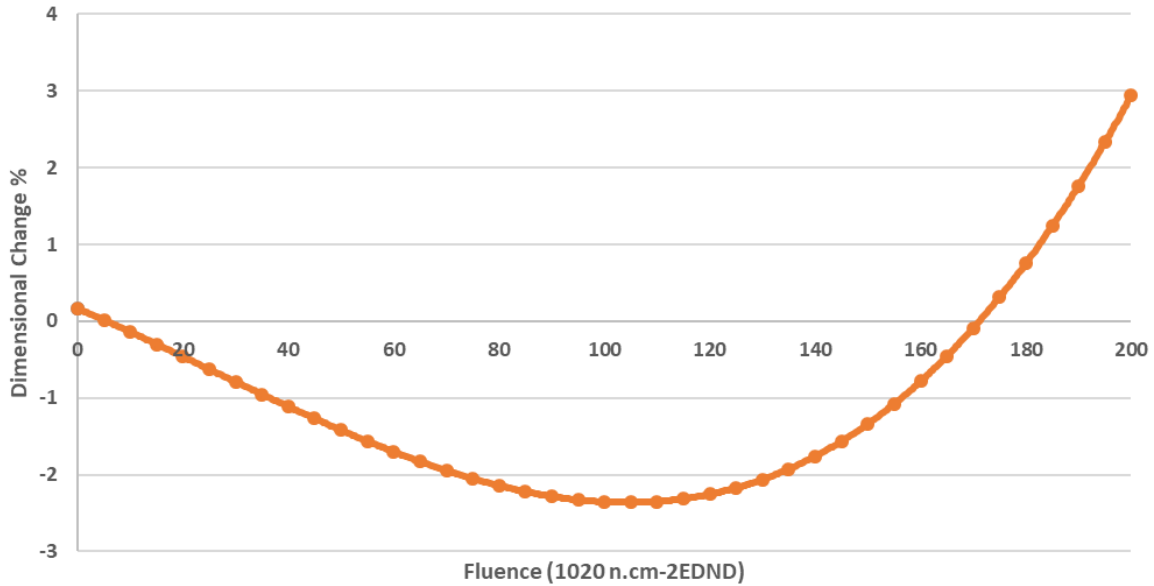
Figure 2-13: Graph showing Dimensional against irradiation dose

2.2.5 Effects of Oxidation on Gilsocarbon

Another aspect of the AGR that can affect the material properties of the Graphite is the coolant being used. As stated previously, Carbon dioxide is used due to its stability under irradiation. At the atomic-scale the Carbon dioxide breaks into Carbon monoxide and other oxidising ions. The carbon monoxide will have a high affinity for oxygen and will reform to create Carbon dioxide. However, these reactive oxides can also react with the Graphite in a process known as radiolytic corrosion. The build-up of gases in the graphite pores absorbs radiation energy (gamma radiation), which causes the break-down of the Carbon dioxide and results in the oxides to gasify the graphite, pulling Carbon atoms away to form Carbon monoxide (International Atomic Energy Agency, n.d.).

Under radiation, Carbon dioxide breaks down into Carbon monoxide and Oxides:

$$CO_2 \rightarrow CO + Ox \tag{2.5}$$

The products of the reaction can either recombine into Carbon dioxide or in the presence of Graphite create more Carbon monoxide through radiolytic corrosion.

$$Ox + CO \rightarrow CO_2 \tag{2.6}$$

$$Ox + C \ (graphite) \rightarrow CO \qquad\qquad (2.7)$$

Oxidation of the Graphite occurs quickly and uniformly throughout the Graphite regardless of the reactor's temperature and results in the enlargement on pores in the Graphite. As the carbon atoms leave the lattice, affecting the physical properties of the Graphite itself, most notably the density of the Graphite, resulting in the micro failures in the Graphite. This can however, be reduced by adding a methane inhibitor as sacrificial protection to the coolant, which protects the Graphite by producing a film on the surface of the pores, significantly reducing the corrosion of the Graphite. (Kyaw, et al., 2014)

$$Ox + CH_4 \rightarrow Hydrocarbons \qquad\qquad (2.8)$$

Radiolytic corrosion can lead to a reduction in the yield strength and Young's modulus of the Graphite. This happens as the expansion of the pores directly stops the closure of the pores required for the initiation of stress reversal. This prolongs the shrinking phase of the graphite and can eventually cause micro-cracks to form, resulting in the graphite's structure to fail.

The effects of radiolytic oxidation can be hidden, however. As the loss of carbon occurs within the graphite open porosity, visual inspection of graphite bricks will show no indication of the loss of mass. Weight loss significantly reduces Young's modulus, strength, and thermal conductivity, with Young's modulus dropping about 50% at 20% weight loss. To a lesser extent, weight loss influences thermal expansion and dimensional change. The effects of oxidation are not considered in the work presented and are only included for completeness (Marsden, et al., 2016).

2.3 Assessing Graphite's structural integrity

Assessment of core behaviour is of vital importance, both under normal and fault conditions. Through modelling and experimental analysis, the primary safety requirements of the core can be evaluated to ensure the core integrity is safe during the duration of the reactor's operational lifetime. The office of nuclear regulations ONR have provided regulations (Office for Nuclear Regulations, 2018) on how assessment of the core should take place. ONR states that a graphite reactor core should:

- Enable the removal of fuel and control rods from the reactor
- Ensure the flow of coolant gas is unimpeded as to ensure adequate cooling of the fuel and core.

The key drivers causing alterations in the cores integrity generally occur gradually and non-uniformly over time within the core. Here lies the difficulty in developing an experimental rig, as it would be difficult to replicate the driving forces which result in core failure. The primary causes of channel distortion have been investigated previously and it has been found to be due to (Mummery, et al., 2020):

- Internal forces between core components caused by dimensional changed that take place during the core operation.
- External forces caused by the changed to the cores either by tilting or due to gas differential pressure.
- Variations in stiffness in the bricks that can lead to channel distortions. The stiffness can change due to thermal, irradiation or oxidation.
- Interactions with the boundary conditions.

While periodic inspection of the core has been undertaken, this inspection can only give a measure of the damage present in a limited number of fuel channels, creating considerable uncertainty in information available on the cores structure at any time. To

assess the cores capacity to remain operational the alignment of the channels must be investigated.

During operation bricks shrink and expand until the shape of the core begins to shift. Dimensional changes due to irradiation can cause the bricks to shrink at higher rates in different layers. This results in core going through three different profiles. Phase one occurs while the middle layer shrinks at a faster rate than the upper and lower layers. The second phase occurs while the middle layers begin to expand while the upper and lower layers are still shrinking. The final phase occurs while the middle bricks begin to expand as the upper and lower layers are beginning to swell.

This creates three different profiles for the shape of the core, as shown in figure 2-14, with different rotational angles between the bricks of different layers at each phase. It is essential to investigate whether the angles between the bricks at different phases can result in blockages in the channels.

| Original | Phase 1 | Phase 2 | Phase 3 |
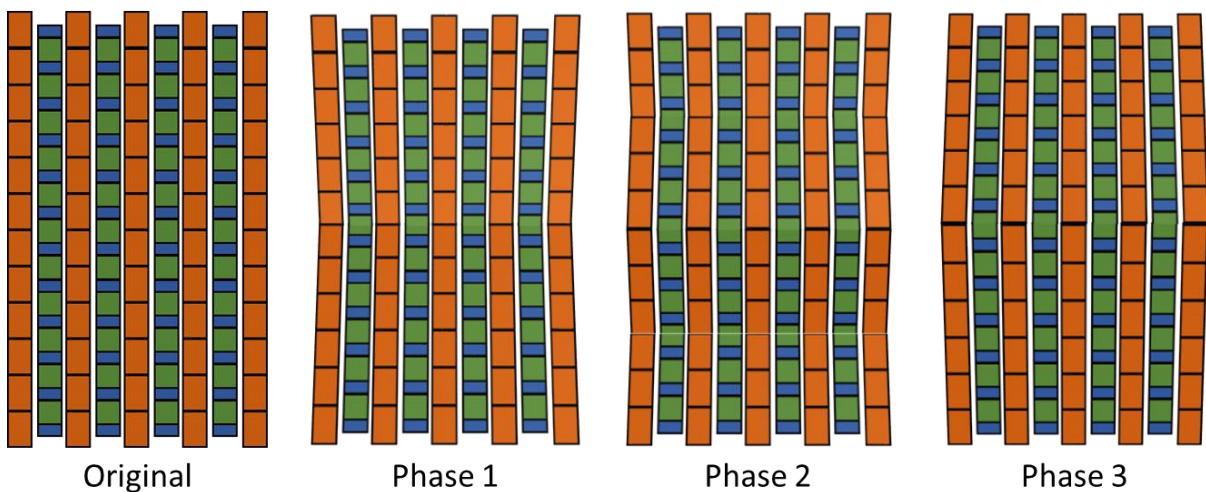
Figure 2-14: Different phases of the reactor's life cycle

This distortion becomes a concerned if it results in fuel assemblies becoming blocked from entering the core, or become jammed in the core. The fuel assemblies in an AGR are constructed from slightly enriched Uranium oxide in the form of cylindrical pellets, which are constrained within stainless steel cladding tubes. All of these components are surrounded by concentric graphite sleeves. Eight fuel elements are linked together with

a fuel stringer assembly within each for the 332 channels. The reactor has single-channel access to refuel when the reactor is on (Nonbel, 1996). Ensuring the fuel is free to move along the channel is paramount to the safe function of the reactor. As 2-15 shows, the fuel assemblies can become jammed in channels if the fuel bricks rotate too far. As the bricks are exposed to irradiation, the diameter of the fuel channels changes over time, which causes this angle to change over time as well.
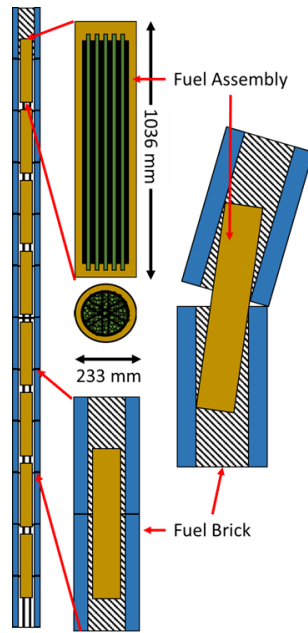
Figure 2-15: How channel distortion can result in fuel assemblies jamming

2.4 Past models of graphite and reactor core

ONR states that assessment of the core should consider the following (Office for Nuclear Regulations, 2018):

- Changes to the size, shape and position of graphite components
- Changes to the graphite bricks properties - including stored (Wigner) energy
- Development of internal stresses in the bricks
- The initiation and growth of cracks
- Development of forces, moments and interactions between components
- Formation of potentially mobile debris.

A number of studies of the effects of service conditions on nuclear graphite have been conducted and reported to date. These include effects at multiple length scales, from single brick to multi-brick models, each with varying levels of realism. Generally, as models increase in size, realistic mechanical behaviour is sacrificed. Here, previous methods of modelling of graphite's mechanical properties have been discussed. This is followed by analysis of models considering the effects of reactor conditions on both single bricks and multi-brick models, discussing the limitations of each approach used.

2.4.1 Models of Graphite mechanical behaviour

As discussed previously, Graphite is a quasi-brittle material and therefore has unique material properties. Creating a model which accurately shows damage has been previously completed. Becker-Marrow presented a paper by which non-local coupled plasticity and damage model for nuclear graphite was presented. This paper produced an accurate method of modelling Gilsocarbon damage and failure by adapting existing models for quasi-brittle materials that allow for the degradation of the material properties. A continuum modelling approach was used to model isotropic damaged elasticity.
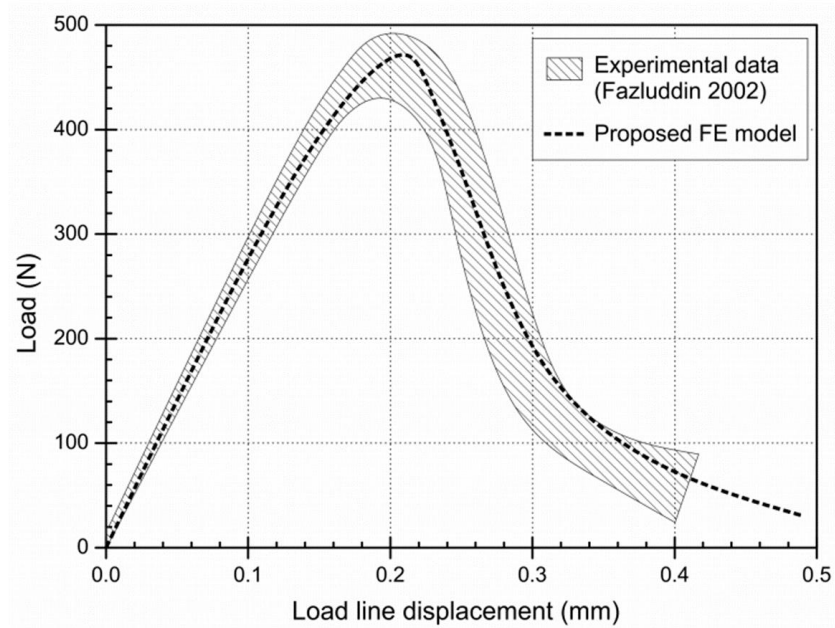
Figure 2-16: Indication of how accurate the Concrete plasticity model in comparison to experimental data

The analysis was completed using Concrete damage plasticity (CDP) model on ABAQUS. A CDP model in Abaqus can be used for modelling concrete and other quasi-brittle materials, in this case, Graphite. The method uses concepts of isotropic damaged elasticity in combination with isotropic tensile and compressive plasticity to represent the inelastic behaviour of a quasi-brittle material. The use of CDP to model graphite provided similar damage properties to that of experimental results, as shown in figure 2-16, proving it can be a very accurate method for developing a damage model.

Through defining yield surface and flow rule, with ABAQUS, a model can be created, which simulates failure implicitly in a finite element environment. This damage occurs during the fracture of the graphite bricks, and is described from non-associated multi hardening plasticity and isotropic elasticity variable. By using the fracture energy, the tensile cracking and compressive crushing can be defined (Lubliner, et al., 1989) (Lee & Fenves, 1998).

The material tension and compression properties are shown in figure 2-17 (Becker & Marrow, 2013). The non-elastic stress-strain compressive behaviour is defined using the Drucker-Prager hyperbolic function which is defined using the eccentricity ϵ_{cc}

(representing the rate at which where plastic potential function approaches asymptote), the hydrostatic and the Von Mises equivalent stress. While the tensile failure is described with reference to the fracture energy (G) and the failure stress (σ_{Tmax}). The model assumes a linear loss of strength after cracking (Hillerborg, et al., 1976), where the point of complete loss of strength being defined by:

$$u_{t0} = \frac{2G}{\sigma_{Tmax}} \quad (2.9)$$

Modelling softening behaviour in implicit analysis programs can lead to significant convergence complications. Demir et al and Ren et al performed experiments on ABAQUS using the viscosity parameter to allow for convergence to occur. Numerical results demonstrated that the lower the value given as the viscous parameter, the higher the accuracy of the results. However, this will come as a cost to computational run time. Demir et al states the optimal value for maximum accuracy to be 0.0005.
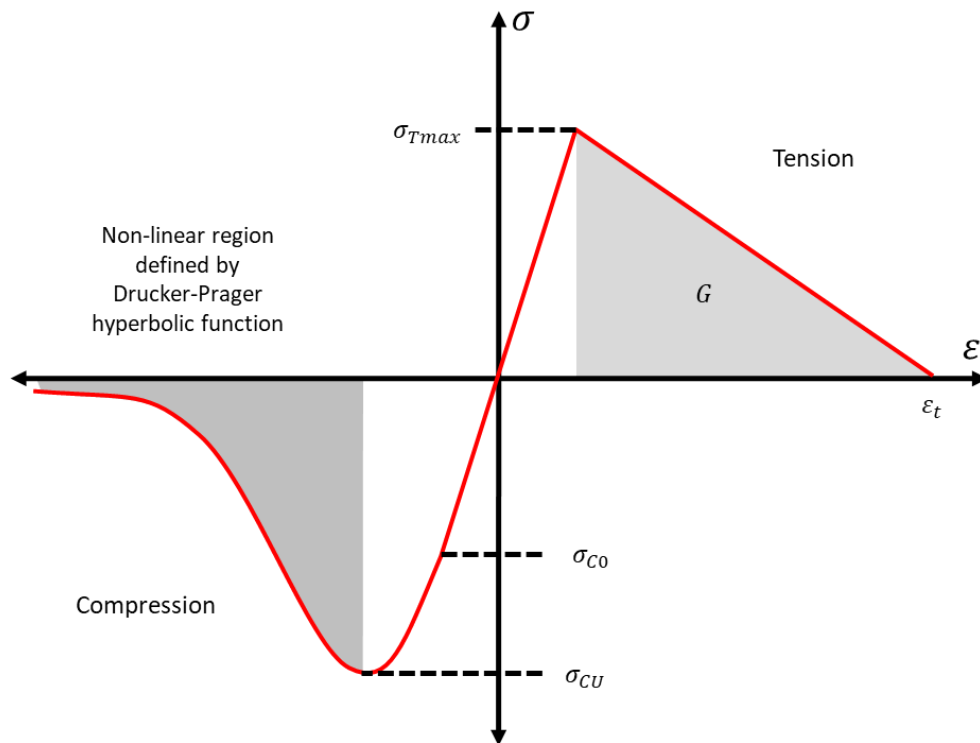
Figure 2-17: Material tension and compression properties with concrete damage plasticity (Becker & Marrow, 2013)

2.4.2 Single Brick modelling

Multiple experiments have investigated how a single graphite brick reacts to the environment within the core of a nuclear reactors. Previous findings show that Irradiation induced property changes to the Graphite bricks can significantly influence the stress distribution and geometric size of the bricks. As discussed previously, Graphite undergoes significant changes when exposed to irradiation, with significant deformations occurring. However, as the dose rates are not uniform through the brick, the rate of dimensional change is also not uniform. As the fuel assembly is placed in the centre of the brick, the centre of the brick will be exposed to a higher dosage than the outer surface of the brick. This results in the centre of the brick shrinking at a higher rate resulting in fracture and deformation of the bricks due to the internal and external stresses (International Atomic Energy Agency, 2000).
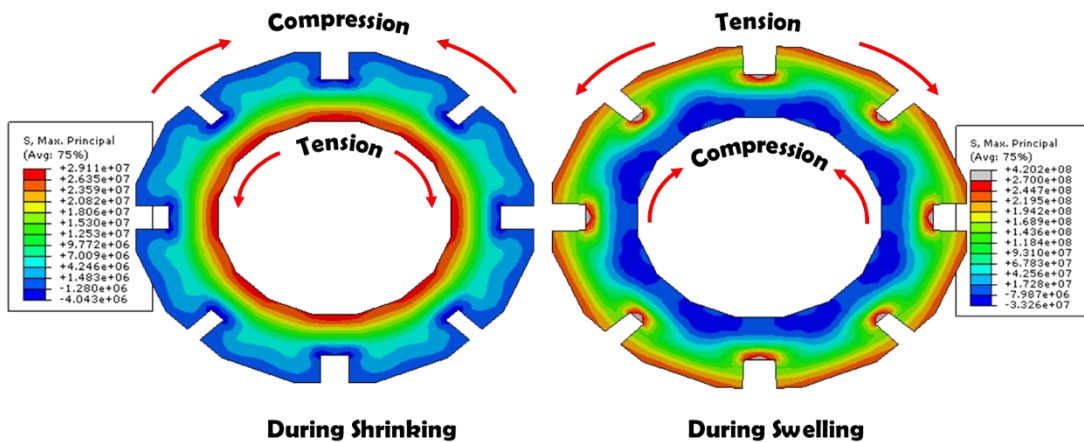
Figure 2-18: Difference in stresses between early life graphite and late life graphite (Zou, et al., 2006)

This creates a potential for bore cracking, where tensile stresses exist close to the centre of the brick, and compressive stresses exist outside. The effect is reversed later in the brick's life with the generation of compressive stresses at the inner surface and tensile stresses at the outer surface. These changes cause stress concentration in keyways and could lead to crack initiation. The cracks created due to bricks expansion can join up with cracks created during the initial shrinking resulting in brick failure (Treifi, et al., 2015).

Keyway cracking was of most significant concern to operators, as multiple brick failures can lead to compromising the whole keying system or multiple channels. Zou et al performed finite element modelling of a single brick which took a 3D slice of a brick and investigated the change in stresses as stress reversal takes place.

Similar models have been examined by a series of experiments with single un-irradiated graphite moderator bricks and corresponding finite element analyses replicating a real reactor (McLachlan, et al., 1996). The results showed good agreement between the predicted failure strength and available experimental data. Furthermore, fast cracking at one keyway is anticipated to trigger a secondary crack at another, potentially opposite keyway, leading to brick disintegration. This phenomenon, known as prompt secondary cracking, has been investigated in detail by dynamic fracture analysis, with results confirming the anticipation (Crump et al., 2017; Crump et al., 2019).

Fracture of the bricks may cause damage to the fuel assembly and controls rods, blocking their entry or removal from the reactor, while it can also affect the flow of coolant. This is why significant research has been conducted on the changes on individual bricks. Finite element analysis and Analytical analysis having taken place to investigate the internal stresses in the bricks. The finite element analysis has been replicated and is shown in figure 2-18 (Zou, et al., 2006). They show that in the early life of the brick, the inner surface of the brick shrinks at a higher rate than the outer surface, causing brick bore cracking to occur.

The experiments confirm that later in the life of the graphite brick, after the stress reversal, where the brick begins to swell further than its original size, keyway root cracking can occur at a higher rate. This is as the outer region of the fuel brick undergoes tensile stresses, while the inner region undergoes compressive stresses. Stress concentration at the key ways can result in crack initiation at the keyway route and propagate though the brick bore. These cracks can join up with cracks created during the initial shrinking of the brick resulting in the fracture of the brick (Treifi, et al., 2015).

In some cases, these cracks can occur in opposites ends of the brick resulting in the brick splitting into two. Cracks that occur in the keyways are the most severe cracks that can occur to the fuel brick, as it can lead to the failure of the whole keying system and can result in multiple channels becoming compromised and compromise the structural integrity of the entire core (Zou, et al., 2006).

These types of cracks were shown to occur with a series of experiments aiming to examine the failure strength of an un-irradiated graphite moderator brick. In these experiments, the reactor conditions were simulated to replicate a real reactor (McLachlan, et al., 1996). During these experiments, slices of the graphite brick were removed from the brick, and a small wedge was removed, where one side on the brick was restrained. At the same time the other was rotated with a moment, to simulate the tensile stresses induced by irradiation of the brick.

These experiments showed that the crack would initiate from a keyway and propagate through the brick bore. These experiments have been modelled using finite element analysis to study the failure behaviour of the moderator brick. These simulations were completed using finite element code ABAQUS. The continuum damage failure model was employed to predict the failure process and resulted in a good agreement between the predicted failure strength and the available experimental data (Zou, et al., 2006).

2.4.3 Multi-brick core performance

During irradiation, the dimensional changes occur at different rates for each layer of bricks, with graphite bricks located at the centre of the core becoming irradiated faster and undergoing changes at faster rates. For the core to continue to operate safety, the moderator must maintain its structural integrity, where a cracked brick can weaken the lattice allowing for channels to become distorted. These effects can have severe consequences for reactor safety as different bricks along one channel could fall out of alignment. Hence, the risk of fuel channels jamming could be significant. Therefore, modelling the effects of irradiation for the whole core is of vital importance. However, accurate modelling of the whole core has not been possible.

2.4.3.1 Single layer modelling

While whole scale modelling of the core with deformable bricks has not been complete previously, finite element modelling of one specific layer has been. Modelling of Layer 6 of the core, which undergoes the largest dimensional changes, has been completed to predict the number of bricks that will see cracks during operation. Tan et al used finite element modelling along with ManUMAT subroutine with maximum in-plane principal stress as the primary output of interest. Once stresses in the brick surpassed the strength of the brick, a crack is assumed to have occurred (Tan, et al., 2016).

The study found that cracking was predicted to occur after 23 years of operation. Following this, further cracks occur at a higher rate, with 10% of the bricks cracking by year 28. Figure 2-19 (Tan, et al., 2016) shows the rate of bricks cracking over 40 years of operation. This data can be used as a method for the validation of the model, but as it only a conservative estimation that only considers changes in one layer, the results produced may differ.
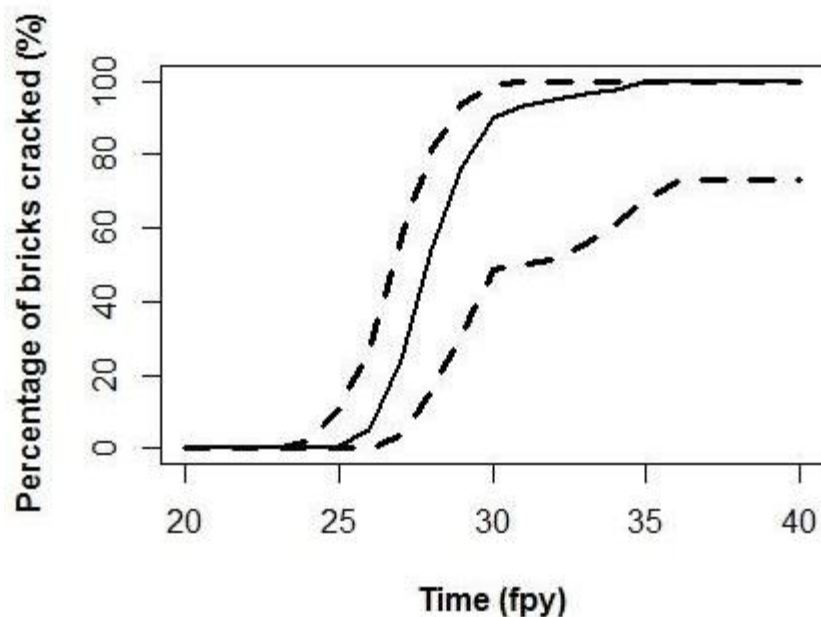
Figure 2-19: Percentage of bricks fractures on layer 6 over 40 years (Tan, et al., 2016)

2.4.3.2 Whole core modelling

Whole core modelling of the reactor has also been established by Ahmed et al. With the whole core containing several hundred thousand degrees of freedom, analysis took place using rigid masses for the bricks instead of deformable bricks. The model is built using a Fortran code that uses the geometry, keying arrangement and restraint of the core, as well as the ageing effects, to generate a finite element model input file that can be used to study static, nonlinear solutions using ABAQUS (Mummery, et al., 2020).

In their work, the rigid-body displacements of the centre of gravity of each brick were taken as coordinates variables, which resulted in the minimisation of the total number of coupled equations that were to be integrated. This meant that each brick was treated as a rigid mass having both translational and rotational inertia, which allows the impact of one brick on another to be analysed with a finite set of parallel springs/dampers.

The contact between the bricks (keys and keyway system) has been simulated using contact spring elements. These springs represent the impact stiffness, friction, damping, and clearances that occur between the contact of the bricks. This allows the load transmission or impacts between the bricks as well as the effects of dovetailing and the irradiation to be included in the model. (Ahmed, et al., 1985). The limitations of such a model are such (Mummery, et al., 2020):

- The model cannot predict the absolute maximum displacement of the bricks
- Due to use of rigid properties, the model will become invalid should analysis involving interactions that occur during operation be investigated.
- The stick and spring nature of the keys design does not recognise that key disengagement can occur, which can have a substantial effect on the interactions between the bricks.
- Spatial variations between the bricks cannot be modelled accurately
- Internal stresses in the bricks, as well the effects of material failure and cracks cannot be modelled.

While the studies on full scale modelling provided information on core response due to irradiation, they do so with strict limitations. The results gathered can be compared to experimental rigs built however the reliability and realism of the results gathered will be questionable. This has created a void for a more realistic way of modelling full core behaviour, that can model gradual changes to channel alignment as a result of changes in stiffness, dimensions and interactions between bricks.

2.5 Test Rigs and Validation of numerical modelling

Validation of numerical modelling of whole behaviour is difficult, with experimental rigs having been limited to quarter scale with static analysis taking place. The effect of lifetime core changes on the reactor have proved too difficult to analyse on experimental rigs, due the difficulty in modelling the driving forces causing dimensional change in the core. Analysis on these rigs have been limited to studies on the effects of tilting the core and the addition of cracked bricks (Mummery, et al., 2020).

Validation using inspection data is once again very limited, with the core only allowing for inspection to occur at limited times and with a limited number of channels. This means the exact date cracked and damage bricks begin to occur is uncertain.

2.5.1 Experimental rig analysis

Requirements for experimental rigs have been to reproduce reliably the conditions for core distortion by capturing the geometry of the brick and whole core, while applying the driving forces behind distortion in a controlled, quantifiable and representative manner. The rigs must be able to model changes in core stiffness and accurately measure the resulting displacement through the rigs. Once achieved the core should be able to (ONR, 2011):

- Compare channel distortions as a result of neutron irradiation with those measured on active reactors

- Compare the effects of future levels of primary and secondary cracking and their associated core distortions, measured on active reactors.

Figure 2-20 (Taylor & Crewe, 2018) displays the static quarter scale rig developed by wood group consists of twelve layers, each with 476 fuel, 429 interstitial bricks and 1904 loose keys. These bricks are made from aluminium to enable easy and accurate machining of the parts. The bricks have keyways similar to those in the reactor machined into the fuel bricks and the interstitial bricks have keyways built into the brick. The bricks are generic and loosely based on Hunterson B, Hinkley point, Heysham and Torness reactors.

Figure 2-20: Experimental Quarter-Scale rig (Taylor & Crewe, 2018)

The rig is built on a fixed grid base whose pitch can be varied to represent the age of the reactor. The bottom layer of bricks is fixed into position on the grid, while a steel box restrains surrounds the remaining array of bricks. Acetate targets are positioned at the top of the bricks which become illuminated from below by diffused light formed by LEDs. A camera is used to scan the rig and enables the position of the bricks to be determined.

Channel distortions and loads in the rig are generated using a combination of (Mummery, et al., 2020):

- Gravity induced instability of individual components
- Simulated single crack opening with the application of pressure at crack location.

Validation of whole core modelling is difficult due to unique properties of graphite and the difficulty in creating a full-scale experimental rig. While large scale rigs have previously been developed, they have been limited to a quarter of core (Flaig, 2019). Research on these rigs has been able to study the effects of seismic loads on a reactor with varying levels of cracked bricks, however the long-term effects of irradiation have been out of scope. Data from these test rigs have shown the cores can withstand severe seismic activity, and state there is no impact on the safe operations of the reactor.

2.5.1.1 Comparison of Rig and Numerical analysis

Experimental rigs and Numerical analysis of the core have evolved over time. While experimental rigs have seen improvements, finite element analysis is still limited to rigid body brick analysis. Experiments have been performed to test the mechanisms assumed in the rigid body numerical modelling, in order to better understand the effects of key variables on core distortion. The studies on the experimental rigs have considered the following effects (Mummery, et al., 2020):

- Removal of keys
- Column bowing
- Removal of rocking features
- Distribution of single and double cracked bricks.

These studies have improved understand of core behaviour; however, these data cannot be used to validate numerical analysis as some uncertainties exist with the data produced such as:

- Similar analysis shows significant differences in the final array position, even when using the same loads. These variations have been attributed to the effects of friction and keys not returning to their original positions, effecting core stiffness.

- It is impossible to decouple column tilting from interlayer shear due to the acetate placed on top of the bricks, which creates uncertainties in displacement data. This is observed in the minimum diameter circle calculations. Such calculations are essential in determining if a channel can allow free movement of the fuel assembly or control rod.

- Limited arrangements of single and double cracked bricks have been used in each study. Channel displacements are sensitive to the distribution of cracked bricks and the lack of study in the range of possible distortions for the same damage state limits confidence in the results.

- Uncertainties exists with variables that can greatly affect the result, such as brick mass, friction, array build quality etc. Experiments are not repeatable; hence the reliability of the quantitative results is contentious.

When comparing the experimental rig with a rigid body model, it was found the model does not represent the experiment well. Attempts to add keys to the array further decreased the agreements between the two approaches, with the finite element analysis predicting significantly smaller magnitudes of displacements often by a factor of 5 or 6, with no correlation with direction of displacement (Mummery, et al., 2020).

Improved comparisons were observed with larger models, where the distribution of loading is stratified, however the reason behind this improvement were uncertain with it being assumed to be due to the additional constraints on column displacement. While larger models appear to perform better than smaller models, the difference is still significant, and the therefore cannot be viewed as reliable (Mummery, et al., 2020).

2.5.2 Inspection Data

EDF carries out inspections frequently at their two longest operating reactors, Hunterson B and Hinkley point B. These inspections take place during statutory outages which take place every three years. The frequency of inspections is expected to increase as the AGRs age (EDF, n.d.).

Inspections take place by removing the fuel and lowering specialist measuring equipment (Bradford, 2005). The inspections include:

- Analysis using cameras to provide an indication as to how many new cracks have formed since the last inspection, and how cracks have evolved over the 3 years.
- Measurements of shrinkage of bricks and distortion of channels with a Channel Bore Measurement Unit.
- Sampling of the irradiated graphite are removed and analysed to confirm the level of weight loss that has occurred since the last inspection and in comparison, to virgin graphite.

These inspections are limited to a number of channels which EDF states will be enough to give a good understanding of the state of the core. The outcomes gathered from these inspections allow EDF to add an understanding of graphite behaviour allowing for comparisons with numerical models, confirming if the reactor is aging as expected. From these inspections EDF has found the reactors to be safe to remain operational and that they pose no threat from a seismic event (EDF, n.d.).

A report by the office for nuclear regulations (ONR, 2011) reports the results of inspections that took place in 2011, detailing the number of cracked bricks on both Hunterson B and Hinkley point B reactors. Both reactors began operation in 1976, meaning the age of the reactors would be 35 at time of inspection.

Of the 29 channels inspected in Hunterson B, 16 were inspected for the first time and 13 were previously inspected. Of a possible 348 bricks in the 29 channels, 21 bricks were

found to be cracked in 15 different channels, with 8 of cracks found in layer 9. Of the 21 cracked bricks 5 were old previously observed cracks and 16 were newly observed cracks.

Of the 31 channels inspected at Hinkley point B, 18 were inspected for the first time, while 13 were previously inspected. A total of 21 cracked bricks were discovered in 17 channels, 9 of which were newly formed and 12 were previously observed during previous inspections. Layer 9 saw the most cracked brick with 9 found to have taken place, of which 5 were new.

While this data can be used to confirm if damage has occurred at 35 years of service, it cannot be used to compare how the number of cracked bricks evolves over time. This is as it is unclear how many cracked bricks were only observed in channels that had previously been inspected. It can be assumed based on the limited sample size that at least 6% of bricks were cracked in both reactors after 35 years of service (Mummery, et al., 2020).

2.5.3 Validation of model

Validation of the model being generated for this report will be difficult. Past numerical models consider only rigid body model, with very limited results modelling the reactors integrity during operation. However, results do exist that consider the amount of damage that should be observed over time, and validation against these results can create confidence in the model being created (Mummery, et al., 2020).

While experimental rigs exist on a quarter scale, they cannot model the effects of lifetime dimensional changes, however can model static core condition with varying percentages of cracked bricks. Such analysis is outside the scope of this project, therefore experimental models cannot be used to validate the model in this report.

Inspection data gathered from the reactor in general show very little cracked bricks when compared to numerical data. Inspection of the core requires the reactor to be shutdown, which has limited the number of inspections that can take place; therefore, the gradual

build-up of cracked bricks is unknown. Inspection data can be used to confirm if cracked

bricks should be observed at specific operation date in the reactor.

3 Model Formulation

To investigate the integrity of the core during operation, finite element analysis was used and a hypothetical reactor was created. The structure and geometry used to make this model are loosely based on that of Hinkley Point B. The model will attempt to remain as realistic to the original design as possible, however simplifications are made to improve computational efficiency. The created model consists of four types of graphite bricks: the fuel brick (where the fuel assembly would be placed), the interstitial and filler interstitial bricks (which hold the controls rods), and the keys (which limit the displacement of the bricks). These bricks are stacked on top of each other and are connected via a system of keys and keyways with gaps between the bricks allowing for each brick to expand and contract before any contact occurs.

The model was generated in ABAQUS, which allows for modelling of a continuum damage and simulation of contact between bricks. ABAQUS splits the analysis into three separate stages. Figure 3-1 shows the process that took place from pre-processing to post-processing. During pre-processing model formulation takes place, and an input file is created. Processing or finite element analysis occurs next using the data provided in the input file to create an output file. Finally, post-processing is conducted where the information in the output file is used to produce an indication of when the model failure will take place. To generate the input file, Python scripting has been used.
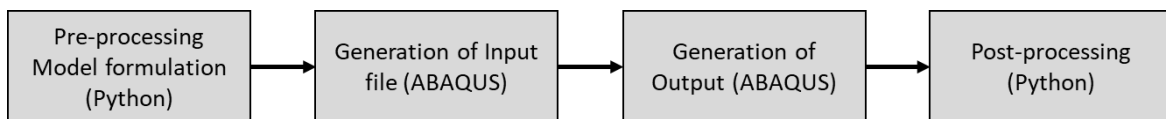
Figure 3-1: Process of model development

Multiple Python scripts were used alongside ABAQUS to formulate a model. These scripts define the part definition, assembly, material definition, interactions, and boundary conditions. Flow chart are shown in each section to explain the process that took place when Python scripting was utilised to generate the model, with more detailed

pseudocodes included in the appendix D. Once the input file has been written, additional changes are made directly to the input file, where predefined fields are listed.

Model formulation can be split into multiple phases resulting with an input file which Abaqus will use to run analysis. While in theory each step is thought to independent from the next, as seen is figure 3-2 (a), with such a complex model every new step can cause alterations in the model requiring the previous steps to be revisited. For example, the addition of boundary conditions required the addition of new parts, altered the assembly and mesh, while also introducing new interactions into the model. Consequently, model formulation is a more complex process as shown in figure 3-2 (b).
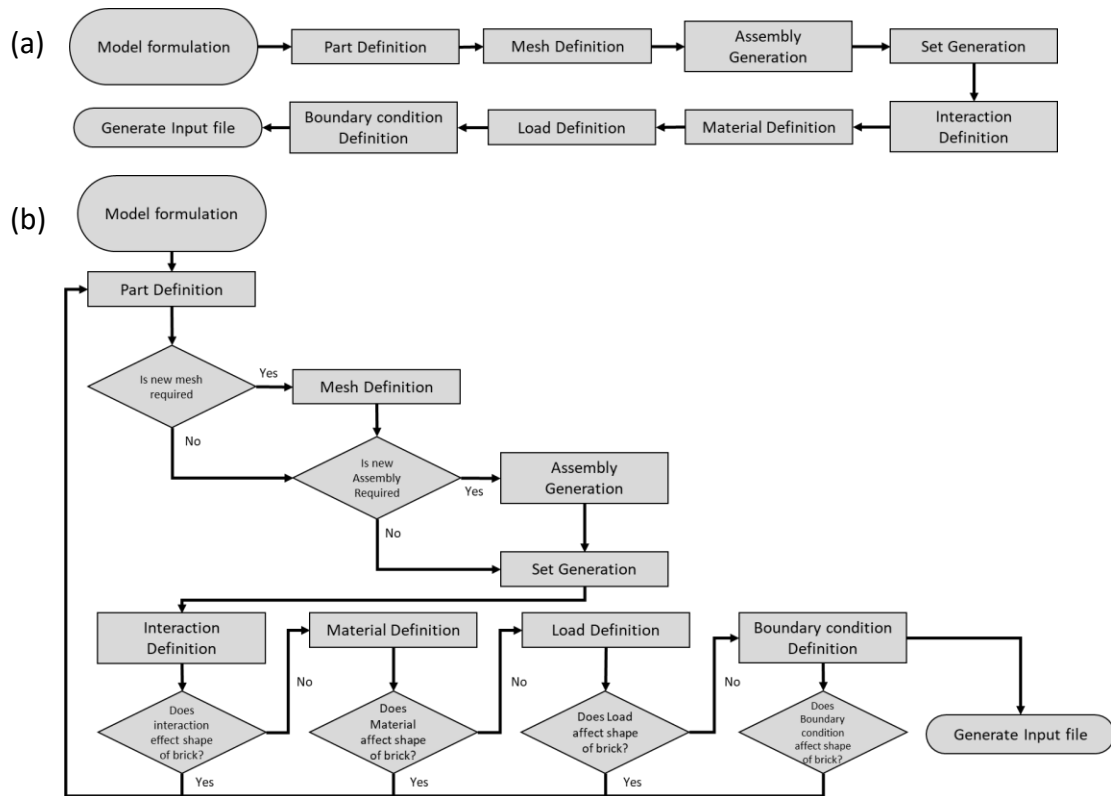
Figure 3-2: Flow chart showing Input file creation

With several hundred thousand degrees of freedom in a full-scale model, alterations and assessments on the full-scale model would be inefficient and time consuming, therefore, to ensure the full-scale model being generated is computationally efficient and accurate,

a smaller model was created and tested. The results generated from this model would not be realistic but would give confidence to the full-scale model being generated.

3.1 Geometry of model

The theoretical reactor designed consists of a row of 20 fuel bricks in each layer, with 12 total layers. This structure was replicated for the model being investigated. The model will attempt to be as realistic as possible, even with the limitations due to computational power. The entire assembly contains 3984 fuel bricks, 3516 interstitial Bricks, 3516 Filler interstitial bricks, and 7488 Keys.

Figure 3-3 shows the smaller model, consisting of a model with six rows and columns of fuel bricks within each of its five layers of bricks. This model consists of 120 fuel bricks, 65 filler and interstitial bricks, and 180 keys.

When designing the models, each brick has been numbered and coded to ensure it is simple to identify a specific brick when analysing the model. The coding of the bricks is completed by first identifying the type of brick via a code (FB for fuel brick, IB for interstitial brick, FIB for filler interstitial brick, or K for keys), followed by the number of
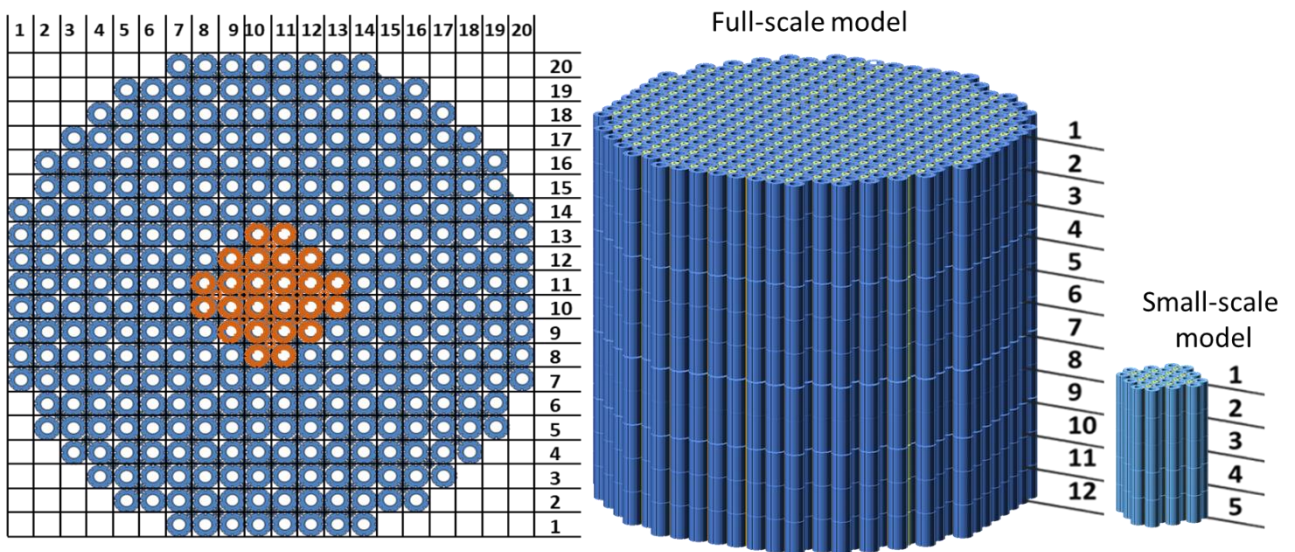
Figure 3-3: Numbering system applied in model

the column, row, and layer the brick belongs to respectfully. The numbering system is shown in figure 3-3. The model of the core was generated using python, which generates the model and writes an input file ready for analysis.

When generating the models in ABAQUS, the scripting was split into multiple categories, part creation, and assembly. During the part creation script, the dimensions of the bricks were defined, followed by the definition of any partitioning of the bricks. This allowed for a better mesh to be defined. After partitioning, the meshing of the bricks is completed. A second script was used to generate the model's assembly. This included the placement of every brick into the correct position and the deletion of any additional bricks generated in the creation of the models.

3.2 Designing individual bricks

The dimensions of the bricks were collected from a CAD diagram of the fuel bricks included in the appendix A.1. The remaining bricks dimensions were approximated using the dimensions of the fuel brick. The dimensions of all the bricks are detailed in the appendix A.1.

The mesh chosen for analysis is an 8 node-linear brick, with reduced integration and an hour glass control (C3D8R). This mesh creates hexahedral elements. The C3D8R elements created are general-purpose linear brick element, with 1 integration point. With full
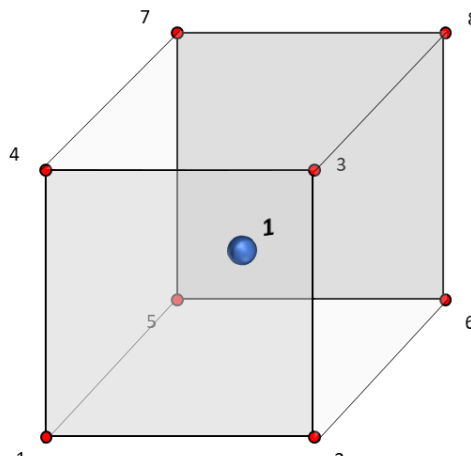
Figure 3-4: C3D8R element showing integration point on a hexahedral element. (Dhondt, 2002)

integration, the element behaves badly for isochoric material behaviour as being defined here, hence, a reduced integration has been utilised. There do exist some shortcomings with this method of meshing the elements. As shown in figure 3-4. the stresses and strains are most accurate in the integration points which is located in the middle of the element when reduced integration is used. Thus, smaller elements are required to capture a stress concentration at the boundary of a structure (Dhondt, 2002).

In addition, under bending loads the results gathered can be very inaccurate in a coarse mesh is used. This reason behind this is shown in figure 3-5. As bending loads are applied to the element, neither of the dotted visualisation lines change in length, while the angle between them also remains unchanged. This means all components of stress at the elements single integration point are zero. To overcome this error in results, the mesh will need to be refined. In addition, the possibility that the correct solution is superposed by arbitrarily large displacements can lead to massive hourglassing, which results in the displacement values becoming unreliable. Therefore, hourglassing controls are activated to alleviate this issue (Dhondt, 2002).
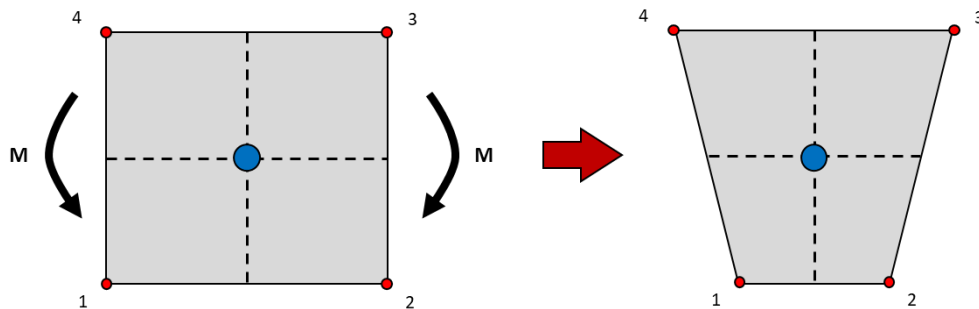
Figure 3-5: Effects of bending loads on a C3D8R element (Dhondt, 2002)

When choosing the mesh for the model, generally a finer mesh will improve result confidence, however this will also result in more degrees of freedom in the model, and the higher requirements for computational power to run an analysis. A full detailed look at how mesh refinement affected the damage observed in analysis and what mesh density was eventually chosen is included in section 4.2.

The full-scale model contains 18504 bricks, which all need to be positioned in the correct location in the assembly. This was completed using scripting, first by defining the position of a single fuel brick, an interstitial brick, filler interstitial brick, and two keys. Following this, a linear pattern was made, where the bricks were replicated along the x-axis and y-axis to create a pattern with 20 fuel bricks by 20 bricks.

To identify an individual brick in the matrix of the bricks, a key was used to identify each brick. Each brick was renamed at this point. This allowed for redundant bricks to be deleted, creating a full layer of bricks, as shown in figure 3-3. The layer was once again repeated along the Z-axis, creating 12 layers of bricks. Finally, renaming of all the bricks in each layer took place, allowing for the identification of any single brick in the entire model. The full process of assembly creation is shown in figure 3-6. A pseudocode of how this chart was converted to python script is shown in Appendix D. When creating a smaller model, the same method was also used.
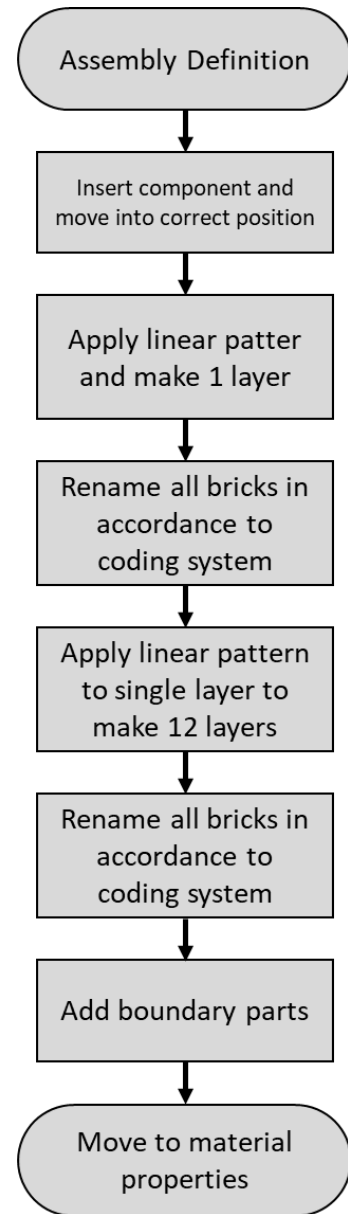
Figure 3-6: Flow chart explaining how model assembly was defined

3.3 Material Properties

While Graphite is quasi-brittle material, modelling it as such will require significant computational power. Therefore, a simplification of material properties is required, with various approaches of modelling the material properties with varying degrees of complexity being considered. First, a purely elastic model will be assumed. This is followed by an elastic model with variable elastic properties between the bricks. The final model created will include material softening behaviour.

All models will assume the density of the graphite does not change during analysis, and virgin graphite properties are used as a constant density throughout. While it is known that through oxidation density will change significantly, as discussed in chapter 2.2.5, the effects are how changes in density affect the model are out of the scope of this analysis taking place here, with only the effects of dimensional changes on the bricks being investigated.

3.3.1 Elastic properties

The first two models created will assume a purely elastic model. The Graphite is considered to be an isotropic material; hence, the elastic material properties are defined using the Young's modulus *E and the* Poisson's ratio. The modulus of elasticity will be dependent on temperature and dose, while the Poisson's ratio remains constant throughout the reactor's lifetime (Arai, 1993).

Computationally, the effects of temperature and irradiation dose are imposed by the local changes of Young's modulus. Young's modulus varies with the dose rate γ, and has been previously approximated by a 5th degree polynomial given by Eq. (4-4) (Li, et al., 2007) (Savija, et al., 2018), where B_0, B_1, B_2 etc. are coefficients derived from the respective polynomial fits given in table 4-3. While data from these sources provide reliable values based on experimental data for how the dose will affect the stiffness of the Gilsocarbon over time, this data is limited to 30 years of service. This creates a distrust in results

gathered that look at reactor integrity beyond 30 years of service. The full-scale modelling performed will therefore be limited to 30-years whereas small-scale modelling will model an additional 10 years, assuming the stiffness continues to follow equation 3.1 beyond 30 years. For future modelling it would be advised to perform additional elasticity testing on Gilsocarbon which has undergone irradiation to the extent expected beyond 30 years of service.

$$E^{ir} = B_0\gamma^5 + B_1\gamma^4 + B_2\gamma^3 + B_3\gamma^2 + B_4\gamma + B_5 \qquad\qquad (3.1)$$

Similarly, the Young's modulus dependence on temperature T can be approximated by a 5th degree polynomial given by Eq. (4-5) (Maruyama, et al., 1987) where C_0, C_1, C_2 etc. are coefficients derived from the respective polynomial fits given in table 4-3. Once again, this data is limited to 30-years of service, and there will be uncertainty in data looking beyond this timeframe.

$$E^T = C_0T^5 + C_1T^4 + C_2T^3 + C_3T^2 + C_4T + C_5 \qquad\qquad (3.2)$$

3.3.2 Plastic properties

Non-linear material behaviour is defined using a Concrete Damage Plasticity model. To define the non-linear properties for Graphite the yield surface, flow rule, load response, and material degradation need to be defined. Previous data from Becker who performed finite element analysis of Gilsocarbon was used to derive the uniaxial compressive yield stress to biaxial yield compressive stress ratio (f_{b0}/f_{c0}), eccentricity (ϵ_{cc}), and the dilation angle (ψ). This data included softening behaviour under compression and tension. Becker's showed good agreement to experimental data from Brocklehurst who collected data from Sato et al, Jortner, Bradshaw and Greenstreet.

The continuum model created will assume two primary failure mechanisms. These are tensile cracking and compressive crushing. Under uniaxial tension, the stress-strain response follows a linear elastic relationship until the value of the failure stress is reached. At this point, the onset of micro-cracking in the graphite material is observed. Beyond the failure stress, the formation of micro-cracks is represented macroscopically with a

softening stress-strain response, which induces strain localisation in the graphite structure.

The Tensile softening behaviour is defined using the fracture energy. Modelling stiffness degradation is not yet possible due to lack of available data. Therefore, linear evolution of the damage variable with effective plastic displacement is assumed.

Under uniaxial compression, the response is linear until the value of initial yield. Following this, plasticity will occur, first with a response categorised as stress hardening up to the ultimate stress. This is followed by strain softening. The compressive load response was collected using data from Brocklehurst model, which used data from Becker and Oku. All values used to model damage are displayed in table 3-1.

Elastic properties		
Young's Modulus	E is dependent on temperature T and dose γ	
Poisson's ratio	v	0.21
Damage Plasticity model		
Dilation angle	30°	
Eccentricity	ϵ_{cc}	4.8
Biaxiality ratio	f_{b0}/f_{c0}	0.81
Fracture energy	G	250 J/m²
Tensile strength	σ_{Tmax}	20 MPa
Compressive hardening	20 MPa	
	65 MPa	
	1 MPa	
Compressive displacement	0 mm	
	0.015 mm	
	0.045 mm	
Density	1.805 g/cm3	

Table 3-1: Material properties for Graphite (Data from (Becker & Marrow, 2013) (McNally, et al., 2017))

To apply these properties to the model, python scripting was once again utilised. This took place in two steps; first the material properties were created, followed by the application of these properties to the bricks. Due to the way interactions were modelled (explained in chapter 3.4), a second material was created, which represented the gaps between the bricks. The gap is discussed further in section 3.2.4.

The value of the modulus was placed in a tabular format, which required equations 4-4 and 4-5 to be converted into a table. The table has been included as part of the appendix A.4.

3.3.3 Varying modulus of elasticity

In reality, bricks will fail at different rates, despite the same loads being applied. This is caused by the variation in deformations in the crystalline structure, resulting in a variation in material properties from brick to brick. To create a more realistic model, a second model is created where the value of Young's modulus E ranges from ±10% based on each brick. The value for variation in material properties has been selected as an arbitrary value to act as a starting point for a future investigation into how variations in material properties affect the core. For future analysis, this value can be increased or decreased based on the investigation.

A table was created where every brick was listed, followed by a random number generator being deployed to define each brick a number between -10 and 10. The distribution of how the bricks are defined is shown in figure 3-7 3.2. The aim was to ensure
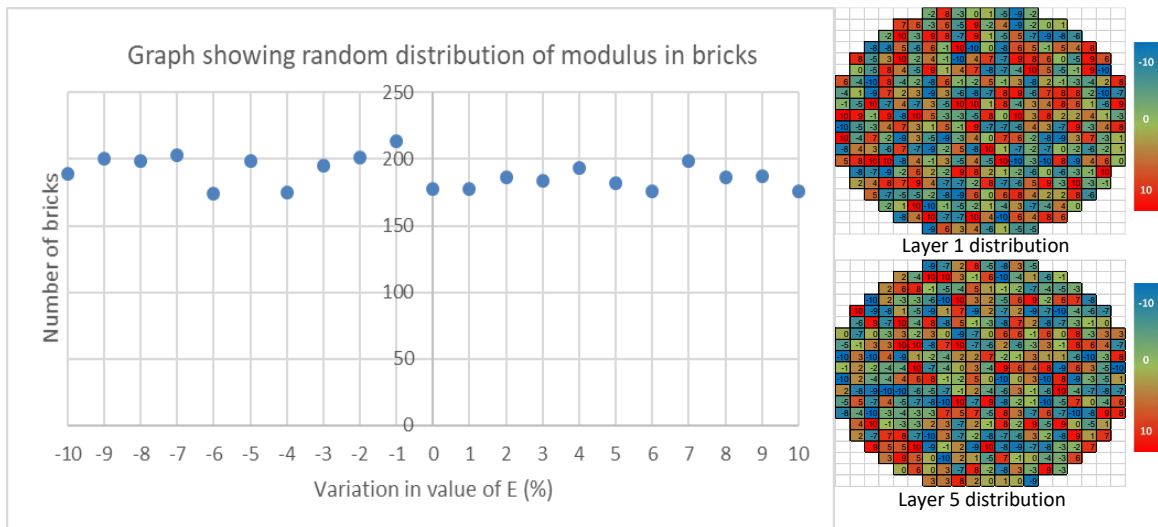
Figure 3-7: Random distribution of bricks, layer 1 and 5 shows varying in stiffness in each layer

a similar number of bricks in each category, and this was achieved to a reasonable degree, creating a model with truly random properties from brick to bricks. Once a brick was

assigned a number, a new Python script was written, placing all the bricks into sets, with each set being given different properties. Work here will use uniform distribution of values, whereas future work could investigate how different distributions of the material properties provide different results. For example, would normal distribution provide differing results to uniform distribution?

3.3.4 Applying thermal and irradiation strain.

The study will consider stress/displacement analysis where the temperature difference between a predefined temperature field and any initial temperatures will create thermal strains causing expansion and contraction of the bricks. To ensure the model undergoes dimensional changes, a thermal coefficient of expansion and an irradiation coefficient of expansion are applied.

The total strain in the model can be defined using equation 3.3, where ε^{th} represents the thermal strain, and ε^{ir} represents the irradiation strain.

$$\varepsilon = \varepsilon^{th} + \varepsilon^{ir} \tag{3.3}$$

The model assumes the thermal coefficient of expansion to be constant throughout the analysis. This means the thermal strain can be given by:

$$\varepsilon^{th} = \alpha \, \Delta T \tag{3.4}$$

Where α represents the thermal coefficient of expansion and ΔT represents the change in temperature from initial conditions to a defined load temperature (Li, et al., 2007).

The irradiation strain ε^{ir} can be expressed as a function of fast neutron dose γ using a 4th degree polynomial, as shown in equation 3.5, where A_0, A_1, A_2 etc. are coefficients derived from the respective polynomial fits given in table 3-2 (Savija, et al., 2017) (Marsden, et al., 2016). These polynomials are collected from figure 2-13 displayed in chapter 2 of this paper.

$$\varepsilon^{ir} = A_0\gamma^4 + A_1\gamma^3 + A_2\gamma^2 + A_3\gamma + A_4 \tag{3.5}$$

This polynomial value was chosen as it closely matched the values of experimental data, however, it must be noted that the data is limited to 30 years of service. Therefore, any full-scale analysis performed in this paper will be limited to 30 years of service, while the small-scale mode will continue to 40 years. This model will assume the value increases at the rate given by the polynomial in equation 3.5. More experimental data is required to investigate the effect of dose on strain beyond 30 years.

Equations (3.4) and (3.5) can be combined to provide a value for the total strain induced by particular temperature and irradiation dose in any finite element of any brick:

$$\varepsilon = (\alpha \, \Delta T \, + A_0 \gamma^4 + A_1 \gamma^3 + A_2 \gamma^2 + A_3 \gamma + A_4) \qquad (3.6)$$

The coefficients of thermal expansion are input as material properties in a tabular format. If a load value falls between two given points, then Abaqus will interpolate between the two given material points to produce a coefficient of expansion at that load value.

Coefficient	A_0	A_1	A_2	A_3	A_4	
Value	0.15	- 4.1228	41.792	- 135.79	0.6446	
Coefficient	B_0	B_1	B_2	B_3	B_4	B_5
Value	9.397E-7	4.610E-4	6.923E-2	-2.6907	2.793E1	1.399E4
Coefficient	C_0	C_1	C_2	C_3	C_4	C_5
Value	8E-07	0.0038	6.0112	2253.5	241532	1E10

Table 3-2:Polynomial coefficients for calculating irradiation-induced strains (Ai) and Young's modulus variation with irradiation dose (Bi) and temperature (Ci) (Haiyan, et al., 2008) (Marsden, et al., 2016)

Three different studies took place each looking at different material properties. First a study considering only elastic material properties, then a second study considering the addition of variations in material properties and finally a study considering the addition of material softening behaviour. Python scripting was used to specify which study was being investigated, with the flow chart in figure 3-8 showing the process behind the material definition script. A pseudocode of the python script is shown in Appendix E.
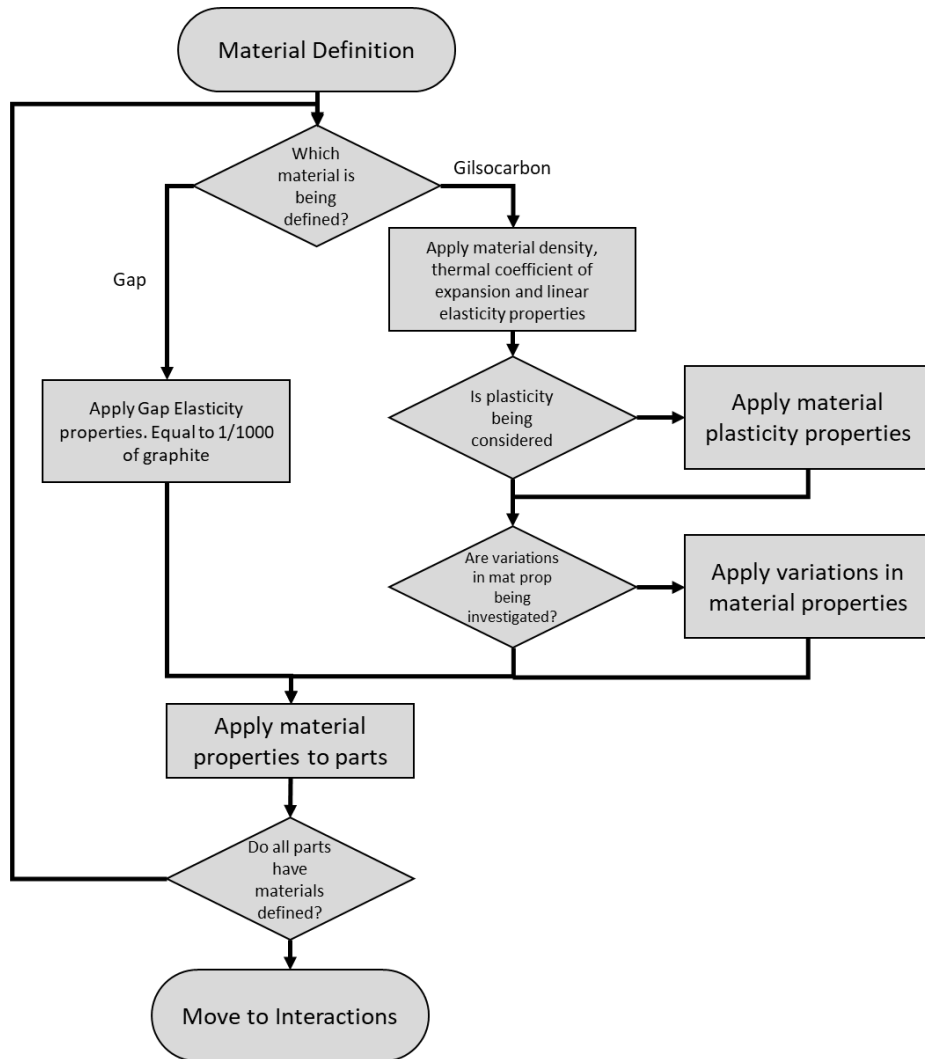
Figure 3-8: Flow chart showing process behind creation of material properties scripts

3.4 Interactions

Due to the large number of interacting surfaces in the model, the type of interaction used can influences the reliability of the model, and computational efficiency. Any simplifications to how the interactions are modelled can result in a reduction in the computation power required to generate a solution. While oversimplification of the interactions can result in a reduction in the reliability of results gathered. The various interactions that would need to be modelled are shown in figure 3-9 and table 3-3. These interactions would need to be replicated as closely as possible to create a model that will reliably replicate the contact between the bricks, and the stresses and strains this contact creates. (Duncan & Kralj, 2007) (Voyagaki, et al., n.d.).
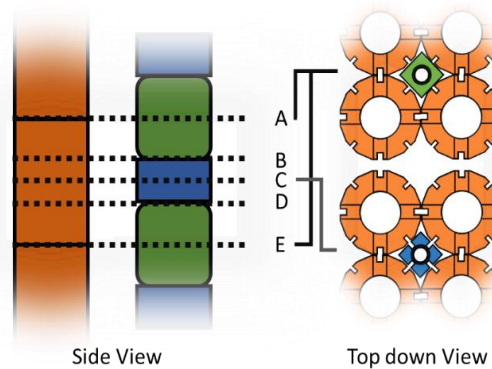
Figure 3-9:Different connections at different points. Details are in table 3-3

Position	Vertical Position in Fuel Brick Column	Vertical Position in Interstitial Brick Column	Interaction In lateral Direction	Interactions in Vertical Direction
A	FB Top surface	FIB Centre of mass	FB-FB Direct Contact	FB-FB Connection
	FB Bottom Surface		FB-FIB Direct Contact	
B	Top of FB-FB Keys	FIB Bottom Surface	FB-FIB Direct Contact	FIB-IB Connection
			FB-IB Key Contact	
		IB Top surface	FB-IB Direct Contact	
			FB-FB Direct Contact	
C	FB centre of mass	IB Centre of mass	FB-IB Direct Contact	N/A
	Centre of key contact	Centre of key contact	FB-FB Direct Contact	
			FB-IB Key contact	
D	Bottom of FB-FB Keys	IB Bottom Surface	FB-IB Direct Contact	FIB-IB Connection
			FB-IB Key Contact	
		FIB Top Surface	FB-FIB Direct Contact	
			FB-FB Direct Contact	
E	FB Bottom Surface	FIB Centre of mass	FB-FB Direct Contact	FB-FB Connection
	FB Top surface		FB-FIB Direct Contact	

Table 3-3:Contact at different points. figure 3-8 displays these positions in detail

3.4.1 Interactions investigated

To create a reliable model, the interactions in the lateral and vertical directions were considered separately. Three different approaches were considered for modelling interactions between bricks within each layer; these were:

- Connector Elements
- Cohesive Elements
- Surface to Surface Interaction

To model interactions between bricks in the various layers, two different methods were considered, these were:

- Surface to Surface Interactions
- Cohesive Elements

Each of these methods was analysed and compared with the preferred method being used for the final model. Each method required the dimensions of the bricks to change, which altered the number of degrees of freedom, number of nodes, and number of elements being defined with each method. This would all result in varying degrees of reliability in the results gathered, while also effecting the computational power required to provide a solution.

3.4.1.1 Connector Elements

Connector elements in ABAQUS allow an easy and versatile way of modelling contact between two different nodes. In the model, the keys and keyways system were replaced by connector elements (shown in figure 3-10). Connector elements allow complex connections which include:

- Stopping mechanisms, which restrict the range of motion of an otherwise unconstrained relative motion;

- Internal friction, such as the lateral force or moments on a bolt generating friction in the translation of the bolt along a slot.

- Failure conditions, where excess force or displacement inside the connection causes the entire connection or a single component of relative motion to break free.

- Locking mechanisms that engage after some force or displacement criteria is met, such as a snap-fit connector or a falling-pin locking mechanism on a satellite deployment arm.

Creating a connector element between two nodes requires first choosing an appropriate connector element type, then defining the elements behaviour. In this case the connector element type used was a bushing element, which provides a connection between two nodes that allow independent behaviour in three local Cartesian directions as well as allowing different behaviour in two flexural rotations and one torsional rotation.
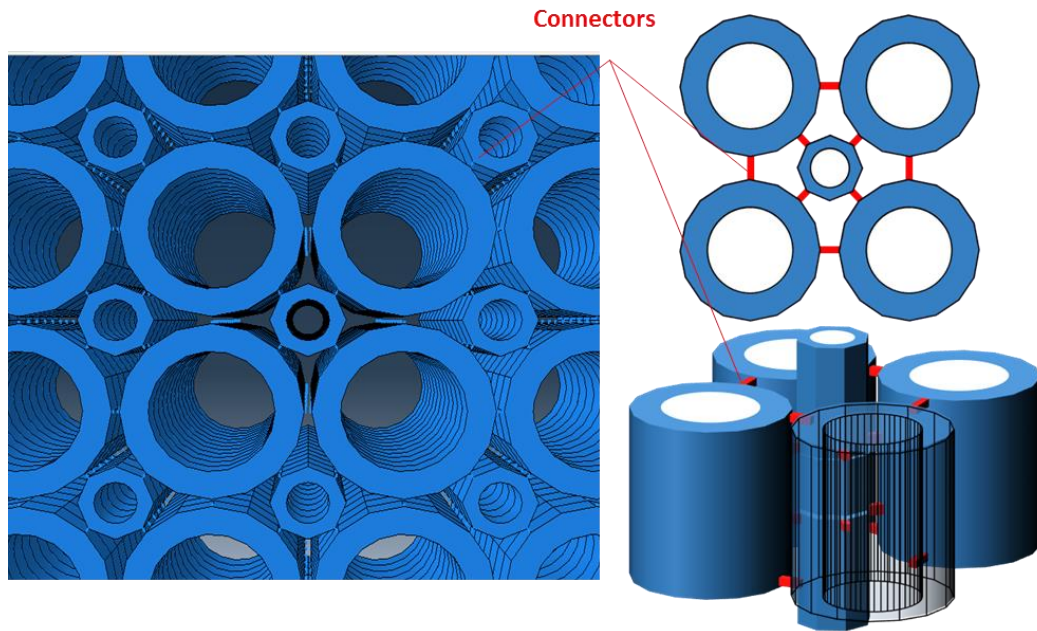
Figure 3-10:Location of connector elements in the model

For the model designed on ABAQUS the fuel and interstitial bricks were simplified by removing the keyway and keys from the model. The connections between the bricks were replaced with connector elements, with a connector placed at all nodes in contact. This

resulted in a simplified model which can be very computationally efficient. When fully assembled the whole core contains a total 10,723 bricks. This number is reduced from the real model due to the removal of the keys. A full-scale model will contain 21840 connector elements. The removal of keys already limits the ability to investigate the stresses and damage of the keys.

3.4.1.2 Cohesive elements

Cohesive elements provide an alternative analysis method as shown in figure 3-10. ABAQUS offers a library of cohesive elements to model the behaviour of adhesive joint and other situations where the integrity and strength of interfaces may be of interest. Cohesive elements are useful in modelling adhesives, bonded interfaces, gaskets and fractures. The response of a cohesive element is based on certain assumptions about the deformation and stress states that are appropriate for each application area. The nature of the mechanical constitutive response may broadly be classified to be based on:

- Continuum based modelling, where the modelling of adhesive joints involves situations where two bodies are connected together by a glue-like material which would have a finite thickness.

- Traction-separation description of the interface, where the modelling of bonded interfaces in composite materials often involve situations where the intermediate glue material is very thin and for all practical purposes may be considered to be of zero thickness.

- Uniaxial stress state appropriate for modelling gaskets and/or laterally unconstrained adhesive patches. These can be defined using only meso-scale properties such as stiffness and strength.
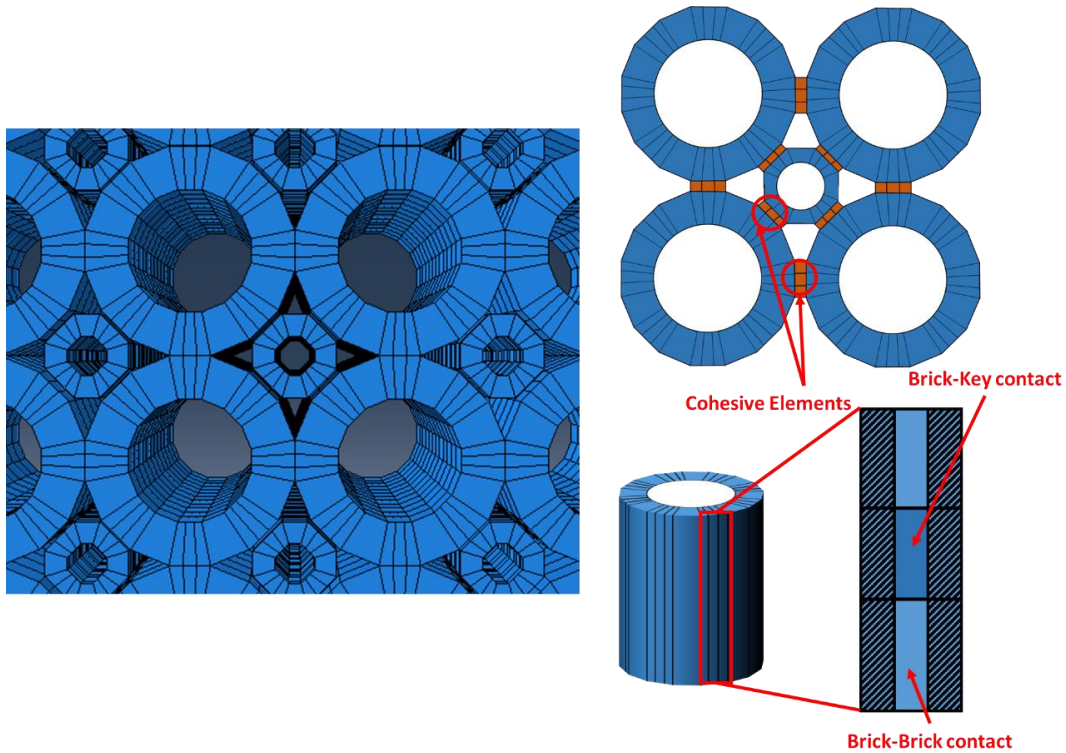
Figure 33-11: Cohesive element placement in the model for lateral interactions

Lateral Interactions

Similar to when using connector elements, the keys are replaced by connector elements as shown in figure 3-11. The allows for a simpler model to be investigated, resulting in less computational power being required. A model with cohesive elements has a total of 5388 cohesive element parts within each layer instead of keys. This increases the degrees of freedom in the model, producing a much more complicated model in comparison to connector elements, which results in a larger computational time. The upside to the use of cohesive elements is that stresses in keys can be seen through the cohesive elements.

Vertical Interactions

Using cohesive elements for vertical interactions will mean realistic properties can be applied to the model. However, this comes at a major cost to computation power required. Using cohesive elements means extra elements will need to be added as shown in figure 3-12, and which will increase the degrees of freedom in the model, greatly

affecting the computational run time. For every fuel brick to fuel brick interaction, an additional part containing 56 elements are required. The entire model will require an additional 326,064 elements at a minimum, with any future refinements resulting in further increases.

This additional computational power does provide reliable result as specific tangential and normal properties can be applied. This means that bricks lifting off each other can be models. Something which could be seen with an earthquake load; however, the load being applied for this project are a dimensional change based on irradiation and thermal load, which at no point will require the bricks to lift off each other. Therefore, the additional computational power will not produce sufficiently improved results.
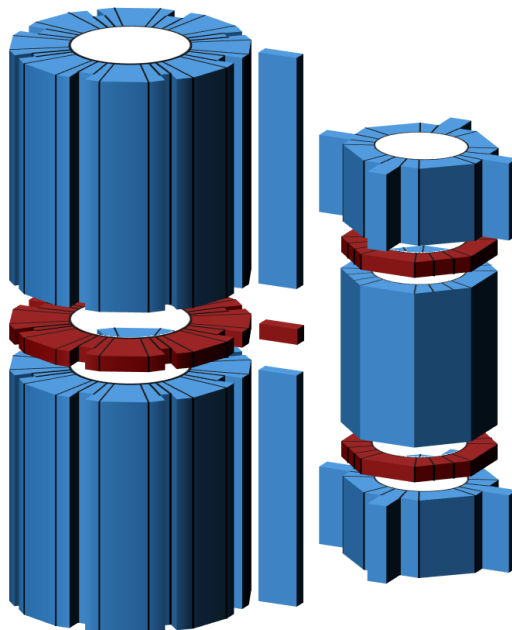
Figure 33-12: Cohesive element placement between brick as vertical interactions along z-axis

3.4.1.3 Surface-to-surface contact

Finally, surface-to-surface interaction were considered which describe the contact between two deformable surfaces, or between a deformable surface and non-deformable or rigid surface. This method also allows self-contact interaction between different areas on a single surface.

With surface-to-surface contact, defining the behaviour of contact is very simple. Any surface that is contact with another would count as one interaction. The interaction between 2 fuel bricks via keys and keyway would have a total of 8 surfaces interacting. This is shown in figure 3-13. The specific analysis methods used to describe interactions between surfaces when using surface-to-surface interactions are:

- Normal behaviour, which assigns a constitutive model for the contact pressure-overclosure relationship that governs the motion of the surfaces in a mechanical contact analysis
- Tangential behaviour which assigns a friction model that defines the force resisting the relative tangential motion of the surfaces in a mechanical contact analysis.
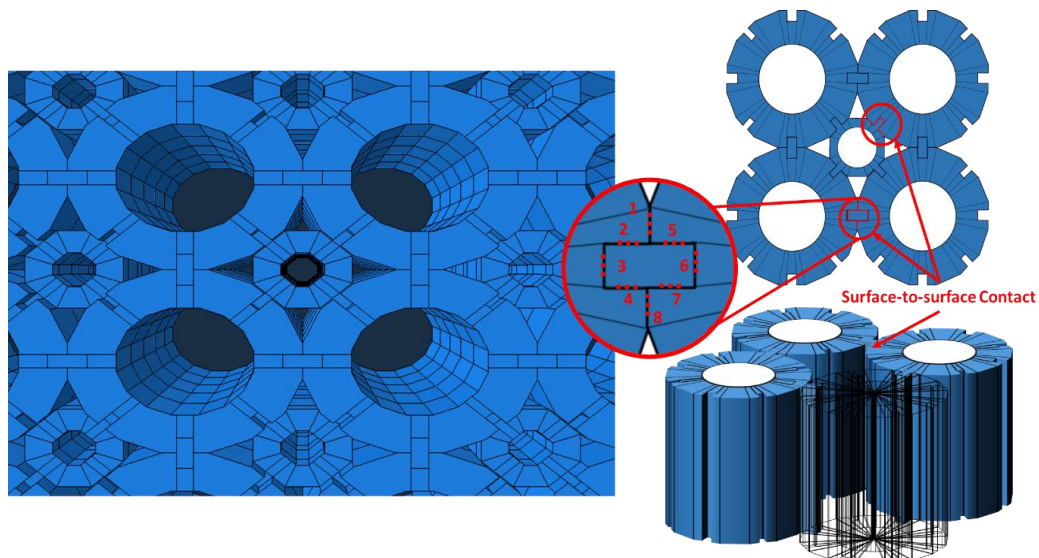
Figure 33-13: Figure showing where surface to surface lateral interaction are placed

Lateral Interactions

When using surface-to-surface interaction, the bricks can be simplified to the same extent as seen with cohesive elements, however produce more a realistic model, the bricks can be made more complex with addition of keyways and keys. Doing this results in a very computationally demanding model, but should also result in the most realistic model. The complexity with this method comes from the definition of the surfaces, with each key and brick surface contain eight interacting surfaces. This will result in hundreds of thousands of individually interacting surfaces, creating a very computationally demanding model.

Vertical Interactions

While surface to surface interactions in the lateral direction require many individual interactions to be defined, this is less so a problem when defining interactions in the vertical direction. Figure 3-14 shows how surface to surface interactions would be arranged in the vertical direction. As this technique defines one interaction between two surfaces, only 1755 additional interactions would be added to the whole model.
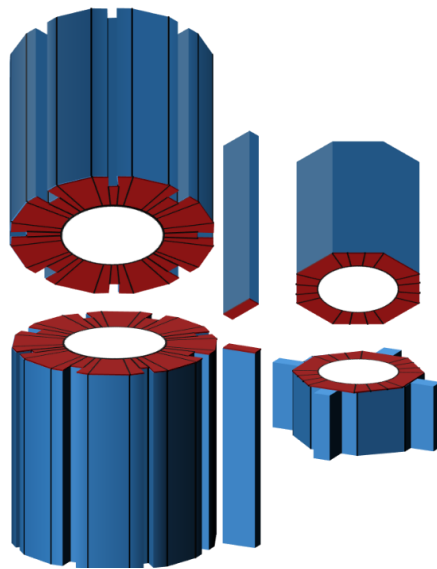
Figure 33-14: Surface-to-surface Vertical interaction placement between bricks along the z-axis

Using surface to surface interactions will not require an increase in the number of elements or degrees of freedom. This means that surface-to-surface interactions will not

significantly increase the computational power required to develop an accurate model, especially in comparison to using cohesive elements.

It is worth nothing that a keying system is also present in the brick when stacked on top of each other. As the model being developed is looking static bricks with lifetime deformations being investigated, this system was ignored. However, if an investigation is needed when looking at the effects of seismic activity, it would be possible for the bricks to move vertically and hence these keyways should be included. This would result in a more computationally demanding investigation.

3.4.1.4 Selecting the modelling technique

Two factors play a key role in deciding which contact technique is suitable for modelling a whole core model. The chosen method must produce a realistic model, while also producing a computationally efficient model. Figure 3-15 shows the expected pattern of stresses when shearing a key held between two bricks. Here regions shown in red show locations of high stress, whereas regions shown in blue indicate location of low stress. Figure 3-14 clearly shows that high stresses are seen in areas of the keyway in contact with the key, and clearly show a region of high stress within the key itself. Each method
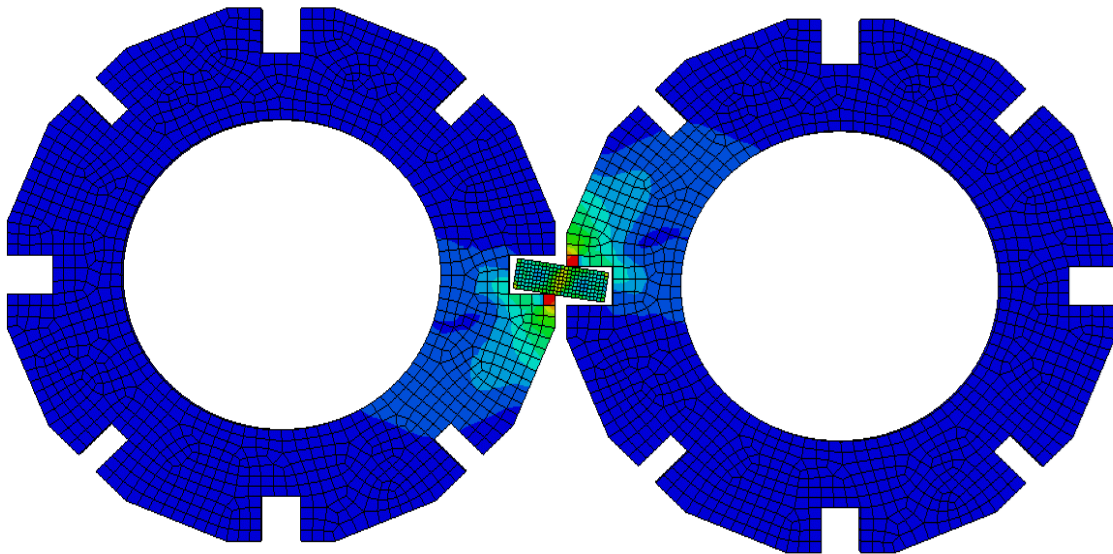
Figure 3-15:Distribution of stresses between 2 fuel bricks and a key

of modelling interactions was subjected to the same test to investigate which replicates the stresses in the bricks most accurately.

All three methods of interaction were investigated, by creating a 2-brick model and using the interaction method to show the distribution of stresses in the brick. The results for this are shown in figure 3-16. When connector elements were chosen, no key was present, furthermore, without the use of keyway the stresses are distributed evenly across both sides of the brick when a shear force is applied. The same is observed when a connector element is chosen. The distribution of stresses being even on both sides of the brick, but this time there is the benefit of a connector element acting as a key.

Connector elements   Cohesive elements   Surface-to-surface contact
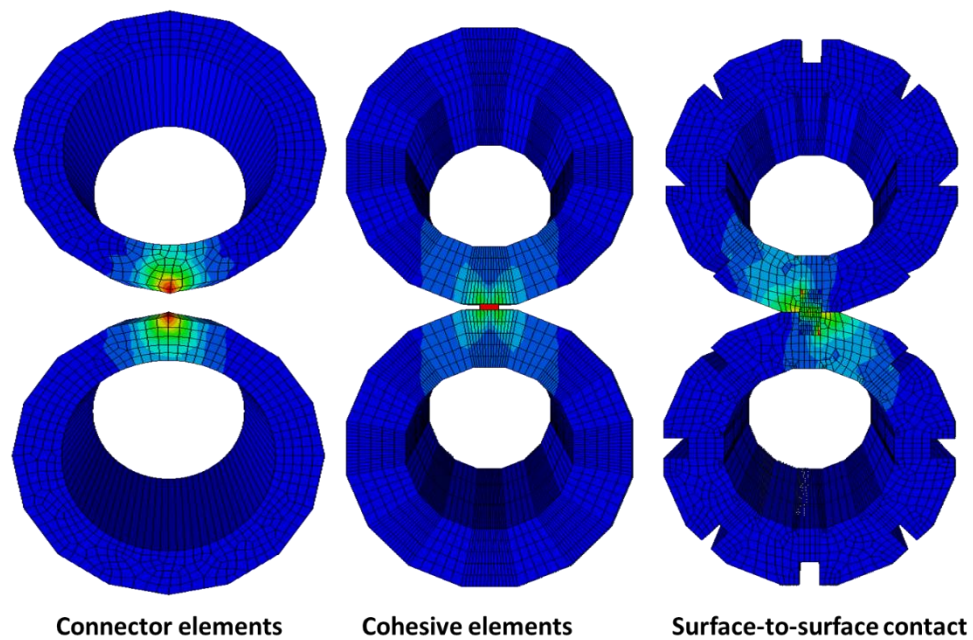
Figure 3-16: Stress distribution when a shear force is applied

The surface-to-surface interactions provided the most accurate method for modelling the contact. The method clearly shows a distribution of stresses in one direction of the brick while a high stress is also visible passing through the middle of the key. The downside to the modelling approach however lied in the fact that surfaces need to be in contact meaning peak stresses are seen in the corners and not in the bricks themselves.

Depending on the technique being utilised to model the interaction between various surfaces, the fuel and interstitial bricks were simplified in different ways. This resulted in significantly different models being created, each impacting the overall accuracy in the model, whilst also impacting the computational power required to investigate the model.

Another test that was carried out involved the development of a small 4 x 4 model to investigate how forces are distrusted across keyway and multiple bricks. While a full-scale model with no boundaries was also created to investigate how much the interaction method chosen affected the number of nodes and elements in a full model. Table 3-4 shows the difference between the three methods analysed.

Effect on model	Interaction type		
	Connector Element	Cohesive Element	Surface to Surface
Number of Instances	7,500	75,379	18,504
Number of interactions	21,840	106,404	182,221
Number of Nodes	367,488	1,865,312	2,407,296
Number of elements	91,872	529,160	979,632
Run time for 4x4 model	34.1 Seconds	N/A	149 seconds

Table 3-4: Comparing data from the three contact methods analysed.

Connector elements where the least computationally demanding approach containing both the least nodes and elements, while also taking the shortest amount of time to run analysis. Cohesive elements saw a large increase in run time and model complexity, however an error stopped run time being analysed. This error was due to the complex nature of the interaction properties needed. Surface-to-surface interactions required the most computational power, while the inclusion of keyways resulted in a large increase of nodes and elements in the model.

3.4.2 Lateral interactions

Within each layer, interactions take place between two fuels bricks and an interstitial brick and a fuel brick. This includes a total of 624 Fuel-Fuel brick connections and 1172 Fuel-Interstitial Brick connections within each layer. The behaviour of these interactions is shown in figure 3-17, which shows the normal and tangential interaction behaviour of the bricks, when a key is present.

When considering direct contact between bricks, under tension, the connection should fail as no resistance is present as bricks are separated. Under compression, the bricks will undergo no resistance until the gap between the bricks is closed, following which compressive contact occurs. Defining such properties using connector elements was possible; however, it would require very complicated interaction properties while breaking the connection was not possible. This means that the connector elements could not be considered due to the unrealistic nature of the results.
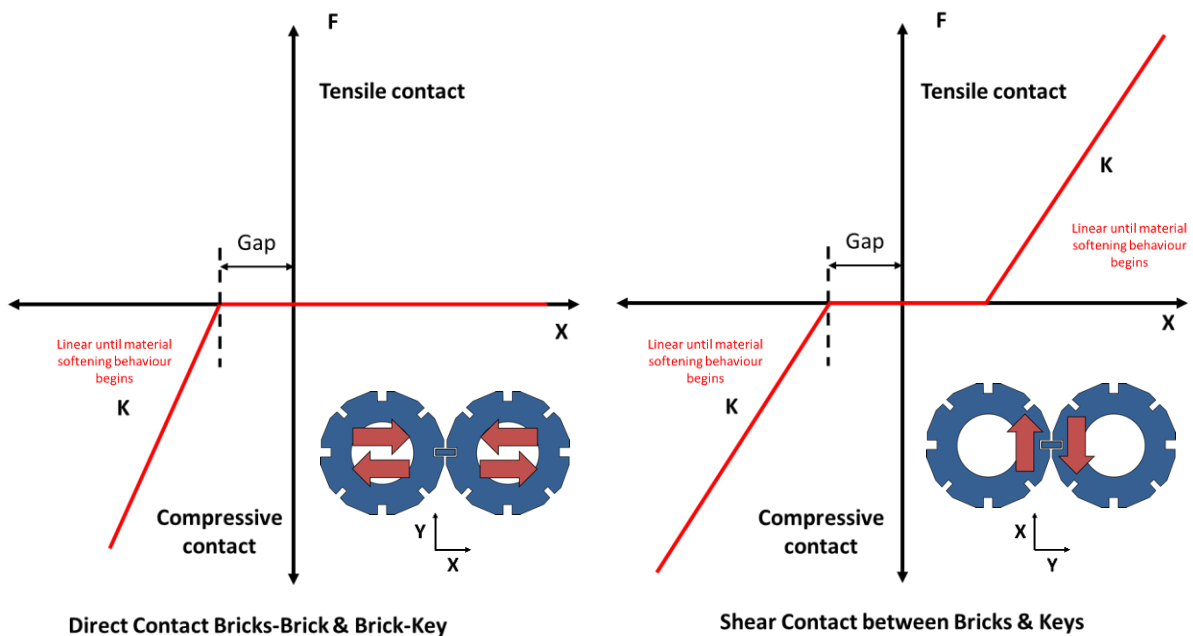
Figure 3-17:Graphs displaying Force against Displacement for contact between brick and keys. F = Force, X=Displacement

K=ΔF/ΔX =Stiffness coefficient

The shear contact, which is effectively the shearing of the keys, also contains a gap between contacts occurs. This gap here will account for the gap between the keys and brick, as initially they are loosely connected. The gap will open over time as initially, the bricks shrink due to irradiation, before shrinking and closing as the bricks swell.

Following an investigation of the various forms of modelling contact, it was clear that the best method of modelling contact was to used surface-to-surface contact. Interactions modelled this was created a very realistic model, where stress distribution is the bricks followed a similar pattern to that of the actual model. Surface-to-surface interactions were the most computationally demanding. The solution to the computational limitation created when using surface-to-surface interaction is addressed in chapter 3.4.5.

3.4.3 Vertical Interactions.

Each of the different bricks now need to be connected along the vertical direction. A connection between the various layers of bricks needs to defined. Figure 2-5 in chapter 2.1.4 shows these interactions. These connections include:

- Fuel Brick to Fuel Brick interactions. There is a total of 332 Fuel bricks in each layer, with a total of 12 layers. This results in a total of 3652 fuel brick to fuel brick interactions. With the fuel bricks, all rotations are blocked via a series of keys and keyways that are built into the top and bottom of the bricks. However, the bricks can still lift off each other with no resistance.

- Interstitial Brick to Filler Interstitial Brick Interactions. In the whole assembly, there are a total of 12 layers of Interstitial bricks, each consisting of 293 bricks. Between these bricks lays a layer Filler interstitial bricks. This creates a total of 6739 Interstitial Brick to Filler Interstitial Brick interactions. The interactions here differ due to the keying system used. The bricks can rotate, however not move along the basal plane. This rotation is only stopped via the keyway contact between the fuel bricks and interstitial bricks along the basal plane.

- Key to Key Interactions. Each layer consists of 624 keys. These keys will sit on top of keys directly below them, with contact between fuel bricks and keys in the basal plane, ensuring the keys stay in position. There will be a total of 6864 key to key interactions.
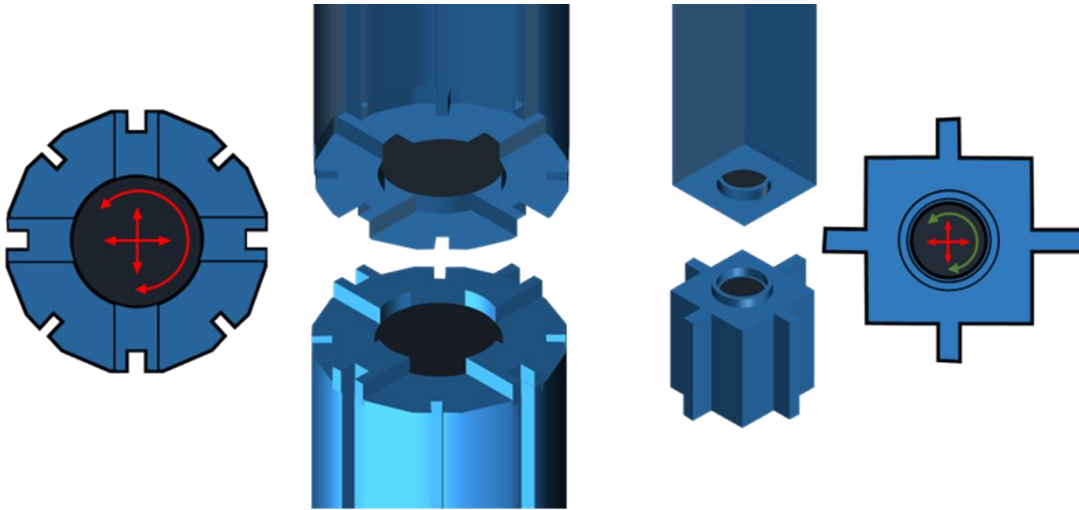
Figure 3-18: Structure of bricks at the base on the surface

When considering the interactions between the different layers of bricks, two approaches were investigated. These were Cohesive elements and surface-to-surface interactions. Analysis of both approaches showed the most computationally efficient and realistic method for modelling perpendicular interactions was to use surface-to-surface contact.

However, while surface-to-surface contact was deemed the most realistic method of modelling contact, there still remains an error in the results due to the lack of gap between the bricks. How this error was addressed is subsequently discussed.

3.4.4 Modelling the Gap

To create a realistic full-scale life-time model of the core, a gap must be modelled between the bricks. A detailed explanation of how the removal of a gap affects the results is included in appendix B. A limitation of using surface-to-surface interactions is that the bricks must always be in contact with each other. The addition of a gap between the bricks will result in the model having unconnected regions. This would result in convergence not being possible.

To overcome this, a similar approach was used to that of cohesive elements. The gaps between the bricks were included as part of the model not as separate parts but as an extension of the bricks themselves. Figure 3-19 shows the approach used to model the gaps between the keys and the bricks.

Abaqus contains a feature that allows objects to be split into multiple parts, referred to as partitioning. The partition toolset can be utilised to divide a part or assembly into regions. By utilising cell partitioning, regions of the bricks were extended to account for the addition of a gap. With this method, the key, Interstitial brick, and Filler interstitial brick will all include an extension to parts to accommodate for a gap. Following this, cell
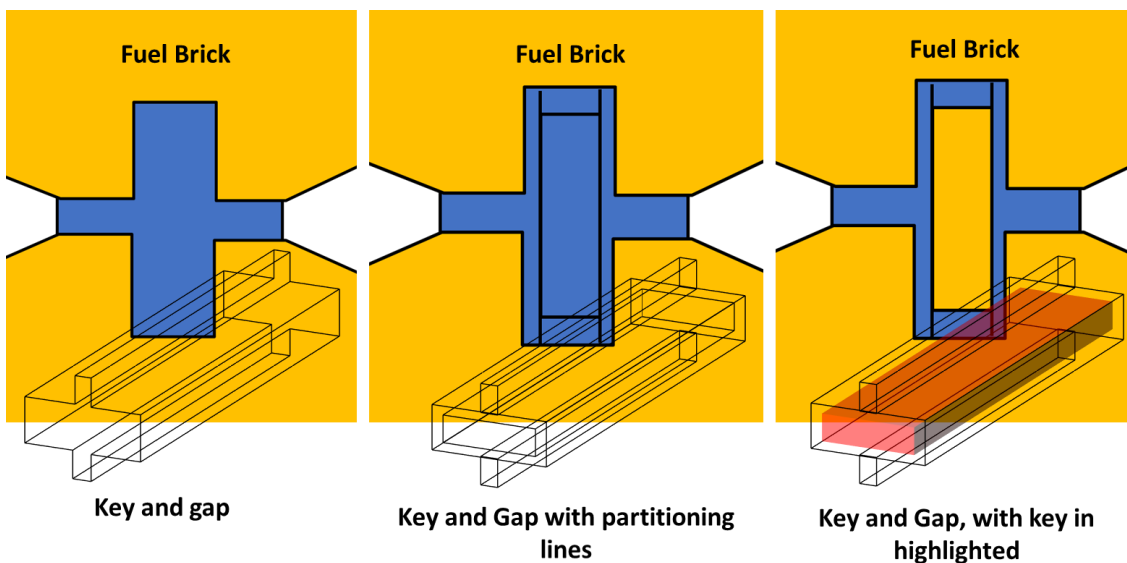
Figure 3-19: How Gap between bricks is modelled

partitioning takes place with the region of the gap being partitioned from the rest of the brick, allowing for unique material properties to be defined for the gap and the bricks. In the model it is assumed the gap size to be up to 5mm thick.

Elastic material properties will be assigned to regions where a gap exists. The modulus of elasticity will be significantly lower than that of the graphite bricks. This means as the graphite bricks undergo dimensional changes, very little resistance will be provided by the regions of the gaps. As the bricks expand, the gap will disappear and the graphite bricks will come into contact with each other. At this point, a different surface-to-surface interaction will activate between the graphite bricks. The behaviour when modelling the gap, is shown in figure 3-20. The value of $K(Graphite) \approx 10^3 K(Gap)$. The difference is so large that the resistance provided by the existence of the gap can be ignored.
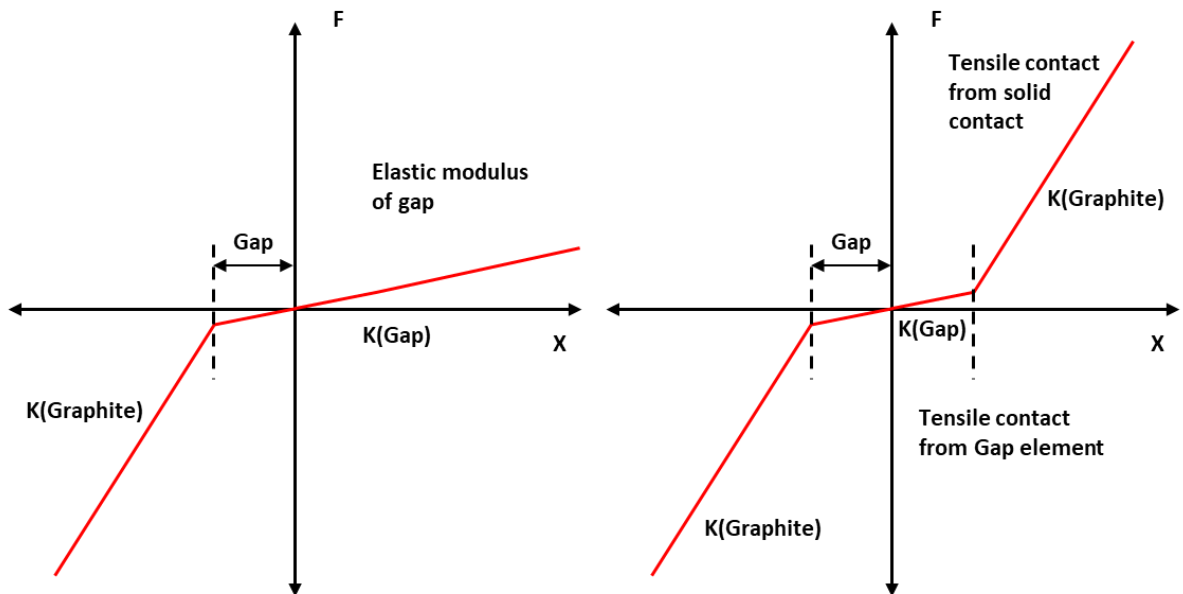
Figure 3-20:Graphs displaying Force against Displacement for contact between brick and keys with surface-to-surface contact being used

The final value of K(Gap) was chosen to be 1/1000 of the value of K(Graphite), multiple other values were tested and it was found that the value for K(Gap) must not be higher than 100th of the value of K(Graphite). A value larger than this would provide too great a resistance to the displacement of the bricks before they come into contact. Values lower

than this had no effect on the results but did slightly increase computation time for analysis when the value of K(Gap)=10^6K(Graphite). These tests were carried out on a small model. As any small increase in computation power on the small model results in significant increases on a full-scale model a final value for K(Gap) was chosen to be 1/1000 of K(Graphite)

An example from Abaqus of how the interaction with a gap will function is shown in figure 3-21. The figure shows a distribution of stresses similar to what would be expected from when two bricks are sheared.
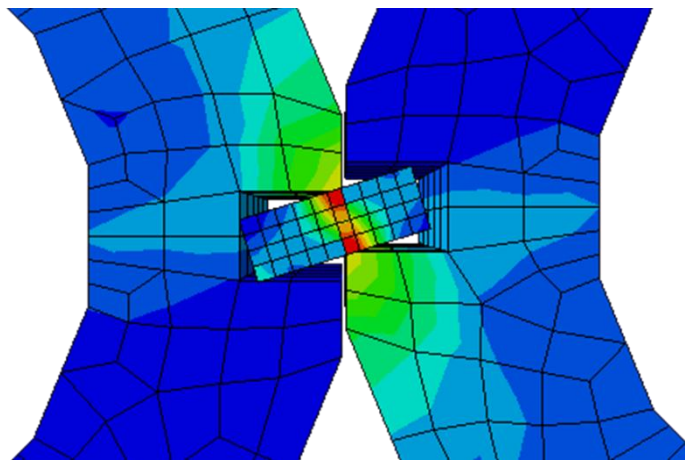
Figure 3-21: Example of modelling of Gap showing model without Gap elements

3.4.5 Improving efficiency

The entire core consists of over 91000 interacting surfaces, and defining each of these surfaces individually will produce a significantly large input file, which cannot be analysed due to the lack of computational power available. To overcome this problem, the different interacting surfaces were placed into sets.

In total 10 different types of surface interactions are occurring in the model as shown in table 3-5. To reduce the computational power, instead of defining single brick to single bricks as one interaction, the surfaces on a collection bricks are selected to interact with a collection of surfaces on another brick. These collections of surfaces are then compiled into a single set.

This means brick-to-brick interactions are replaced with set-to-set interactions reducing the total number of interactions being defined in the model from 91000 to just ten. This vastly reduces the computational time required for analysis, as well as a 63% reduction to the size of the input file, allowing for full-scale analysis to take place. Up to now the large size of the input file blocked such analysis taking place.

The viability of reducing the definition of contact surfaces in this way were verified on a small model. While the same outcomes were produced, a significantly shorter CPU time was observed. This investigation experienced analysis time drop from over 1200 seconds when defining each surface individually to less than 300 seconds when grouping surfaces together.

3.4.6 Defining Interactions

When defining the sets for the contact between the surfaces, Python scripting was used. The process of set definition is displayed in figure 3-21. Building sets was completed by construction a script defining all contact surfaces in 1 layer, and repeating this script for every layer in the core. Following this every interacting surface in each layer will have been assigned a set, so the final step would be to combine all the same contact surfaces in every layer into one new set. A pseudocode explaining the creations of the sets is shows how in the Appendices E.

Once all the surfaces are placed in sets, a simple python script was written to defined the interactions between surfaces in contact. The process which this took place is shown in figure 3-22. This was completed by first specifying the interaction properties for both gap contact and brick to brick contact. This contact property would then be applied as a surface-to-surface interaction between two surface sets.

The surface-to-surface interaction properties were defined by specifying the tangential and normal properties of the bricks. For brick to gap contact the tangential interaction was specified as rough, which specifies an infinite coefficient of friction and prevents slipping regardless of contact pressure, while normal behaviour was specified as hard
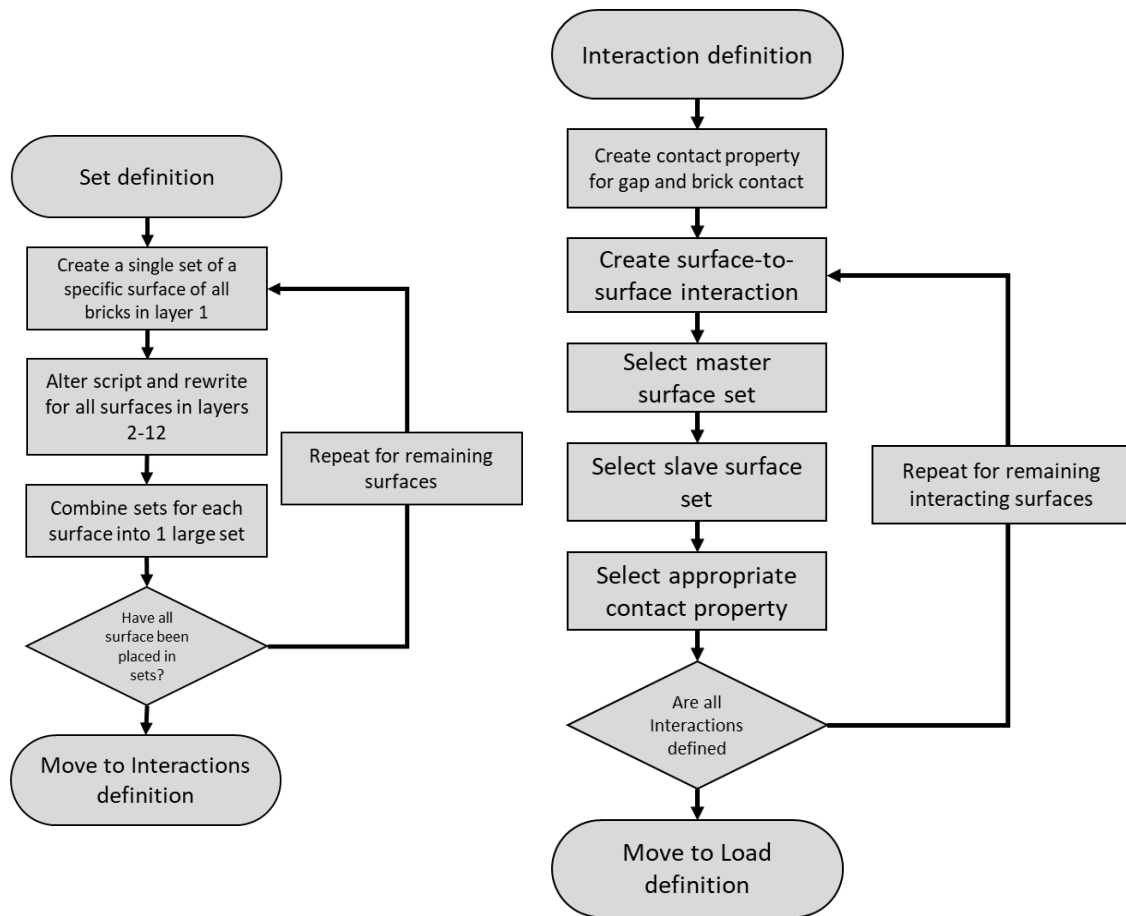
Figure 3-22: Flow chart showing the process behind creation of python scripts for sets and interactions definitions
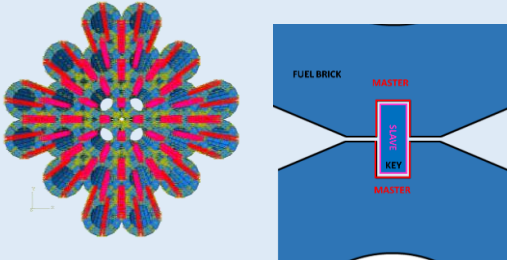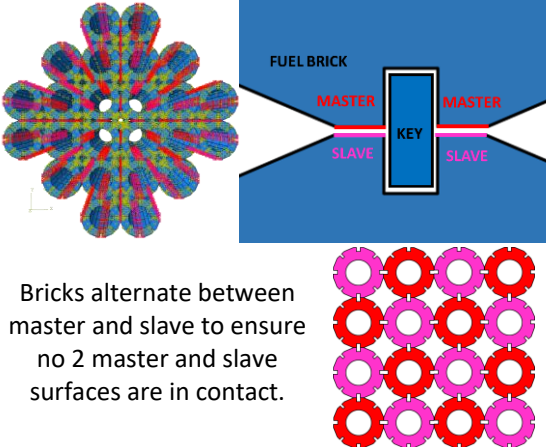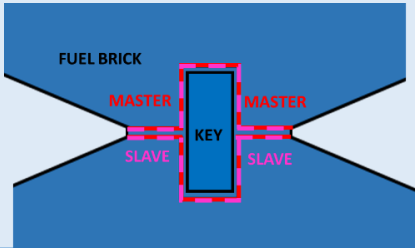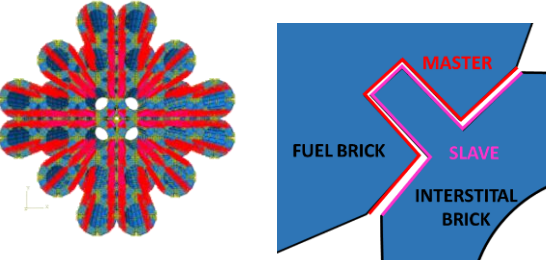
effectively blocking the surfaces from separating. Within the interaction menu it was also specified that the surfaces would be tied together ensuring the surfaces are in contact at the start and remain in contact throughout the analysis.

When the gap is closed and the bricks come into contact a new interaction takes place which is the brick-to-brick contact. Here the tangential contact was specified as frictionless where it would be assumed that surfaces in contact slide freely without friction. A penalty option was tested and it was found to not affect the results gathered in any way and but did slightly increasing the analysis time. In future full-scale analysis, the friction can be a point of examination to discern its effects on the bricks. The normal behaviour of the brick-to-brick contact was specified a linear penalty, where Abaqus calculated the penalty stiffness to 10 times a representative underlying element stiffness.

In tangential brick-to-brick contact, where contact between different layers of bricks is defined, a different contact property was created. Here the tangential properties were given as rough in order to prevent slipping of any kind. In reality a keying system exists in vertical direction which would block the lateral movement of the bricks, and modelling this system would greatly increase analysis time. Therefore, this was replicated by blocking all slipping of the bricks altogether. The normal contact of the bricks was specified as rough and the surfaces were tied together blocking the movement of the bricks.

As the analysis is considering only lifetime deformations, modelling the brick contact in this way is both accurate and computationally efficient, however these properties would need to be altered if seismic load is being applied where bricks may separate in the vertical direction.

Table 3-5 shows all the different contact surfaces being modelled, including which surfaces are the master surface and which would be the slave surfaces. In most cases where possible, the master surface was chosen as it was the surface with the coarser mesh. In incidents where the mesh density was identical on both surfaces, the fuel brick was made the master surface. For vertical interactions, the top surface of the brick was chosen as the master, whereas the base was chosen as the slave surface. The images included are from the smaller 6 by 6 by 5 model.

Master Set	Slave Set	Contact Property	Image of interaction
Fuel Brick	Key	Tangential: Frictionless Normal: Pentaly (linear) Tie: No	
Fuel Brick	Fuel Brick	Tangential: Frictionless Normal: Pentaly (linear) Tie: No	Bricks alternate between master and slave to ensure no 2 master and slave surfaces are in contact.
Fuel Brick	Gap of Key	Tangential: Rough Normal: Hard Tie: Yes	
Fuel Brick	Interstitial Brick	Tangential: Frictionless Normal: Pentaly (linear) Tie: No	
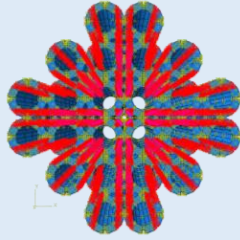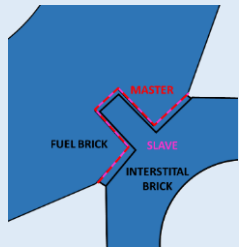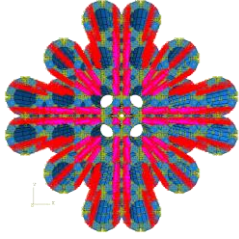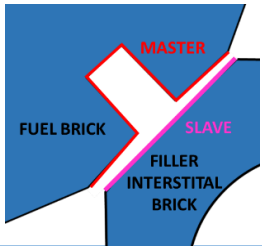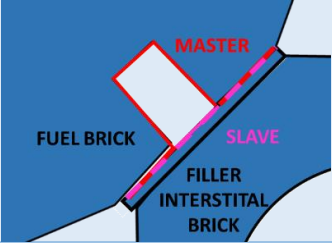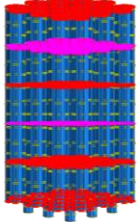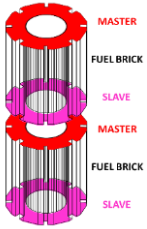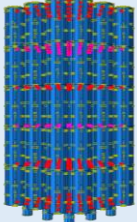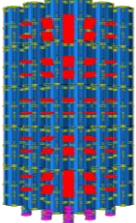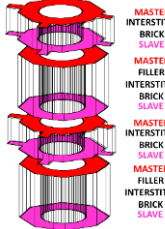
Master Set	Slave Set	Contact Property	Image of interaction
Fuel Brick	Gap Interstitial Brick	Tangential: Rough Normal: Hard Tie: Yes	
Fuel Brick	Filler Interstitial Brick	Tangential: Frictionless Normal: Pentaly (linear) Tie: No	
Fuel Brick	Gap of Filler interstitial	Tangential: Rough Normal: Hard Tie: Yes	
Fuel Brick	Fuel Brick	Tangential: Rough Normal: Hard Tie: Yes	
Key	Key	Tangential: Rough Normal: Hard Tie: Yes	
Interstitial Brick	Filler Interstitial Brick	Tangential: Rough Normal: Hard Tie: Yes	

Table 3-5: Table showing the sets and interactions taking place in a small-scale model

3.5 Loads

Two operational loads causing dimensional changes are considered: temperature and irradiation. These are applied separately to the model. Each load induces non-mechanical strains, a thermally-induced strain, ε^{th}, and an irradiation-induced strain, ε^{ir}, which modify the gaps between the bricks. When bricks get in contact due to gap closure, further expansive strains cause deformation of these bricks with associated stresses.

3.5.1 Thermal Load

The temperature distribution within the core is assumed constant from start to end of the reactor's lifecycle (outages not considered). The temperature varies between the different layers, with the central bricks having a higher temperature than the bricks at the top and bottom of the reactor. Within each fuel brick in a particular layer, the temperature decreases by around 50°C from the inner edge to the outer edge. These variations are illustrated in figure 3-23 (Marsden, et al., 2016).
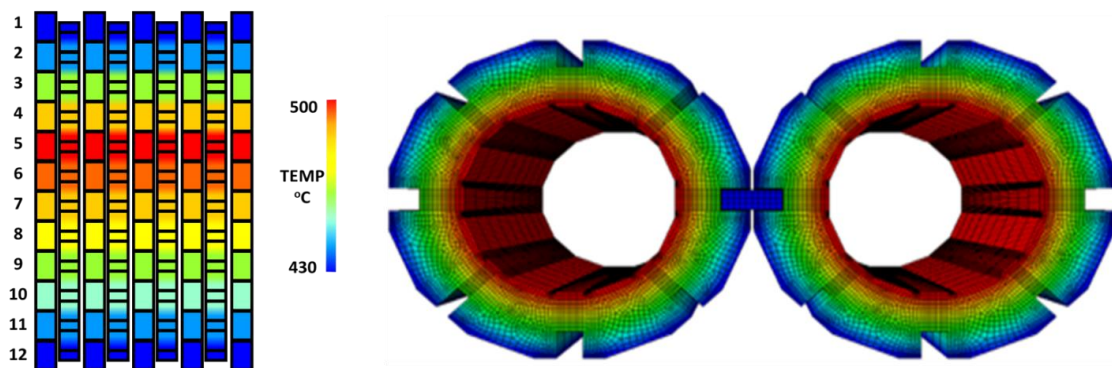
Figure 3-23:. Illustration of temperature fields in the core and inside bricks (Marsden, et al., 2016)

The temperature variation between layers and between brick surfaces used in the present work is shown in a graph in figure 3-24 (Marsden, et al., 2016) (Haiyan, et al., 2008). Notably, the highest temperature is not at the central layer, but at layer 5 of the core. This bias is due to the airflow passing through the reactor, passing vertically from layer 12 to layer 1. This causes a distortion in the distribution of the temperatures. The

temperature field is assigned by a Python script to the elements of individual bricks, assuming linear variation across the brick thickness. Thermal strains result from temperature gradients, as described by equation 3.8 (Kyaw, et al., 2014), where the coefficient of thermal expansion, α, used in the present work was 4.39×10^{-9} (Li, et al., 2007). This value remained constant throughout the reactor's life cycle.

$$\varepsilon^{th} = \alpha \, \Delta T \tag{3.8}$$
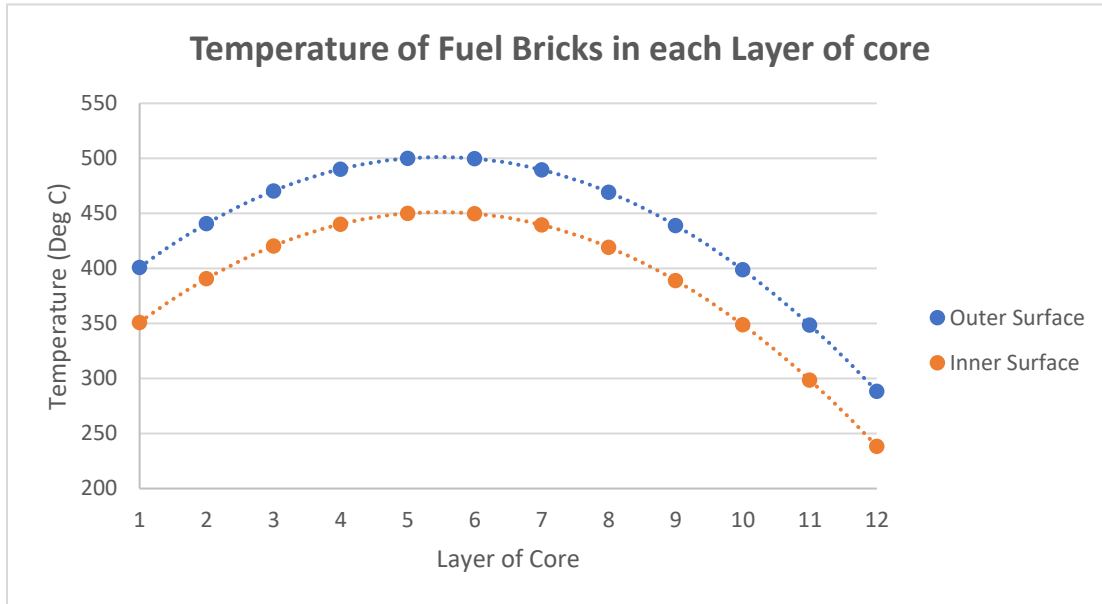
Figure 3-24:Temperature variation between layers and bricks surface (Li, et al., 2007)

To apply the thermal loads, an analytical field was developed to better replicate the load application of the real brick. This would ensure the highest temperature is at the centre of the brick, followed by a drop of 50 degrees to the outer surface (Haiyan, et al., 2008). The analytical field for each fuel brick was calculated separately using equation 3.9, where A_L, B_L and C_L are coefficients derived from polynomials of best fits, which vary with each layer. The values for A_L, B_L and C_L are included in the appendix in chapter A.5. The equation makes sure the temperature varies across the X and Y-axes, but it keeps it constant across the bricks Z-axis, and would replicate the loads.

$$T_{FB} = A_L x^2 + B_L x + A_L y^2 + B_L y + C_L \tag{3.9}$$

The Thermal load for the remaining bricks was assumed to be the same as the outer thermal load of each fuel brick in the layer. The thermal load for the remaining bricks was calculated using equation 3.10, where D, E, and F are coefficients derived from polynomials of best fit. This equation is based on the outer surface line shown in figure 3-17. The equation specifies a varying thermal load along the Z-axis of the bricks, with a constant load applied along the X and Y-axes.

$$T_{ALL-FB} = Dz^2 + Ez + F_L \qquad\qquad (3.10)$$

With the exact load known for each brick, python scripting was utilised to apply the loads to the bricks. These scripts specify the thermal load on all fuel bricks. The scripts are split into two parts: first, the equation above is input as analytical field, then this field is applied as a load to the bricks. Applying the load to fuel bricks requires the extra step of specifying the centre of the brick from which the load is applied. A pseudocode is included in the appendix E, with flowchart figure 3-25 showing the process behind the code definition.

The loads being initially applied by the analytical field will be for a 30-year analysis. If analysis beyond this is to take place, the magnitude of the load can be increased (e.g., when magnitude=1, time=30 year and when magnitude=2, time=60 years etc).
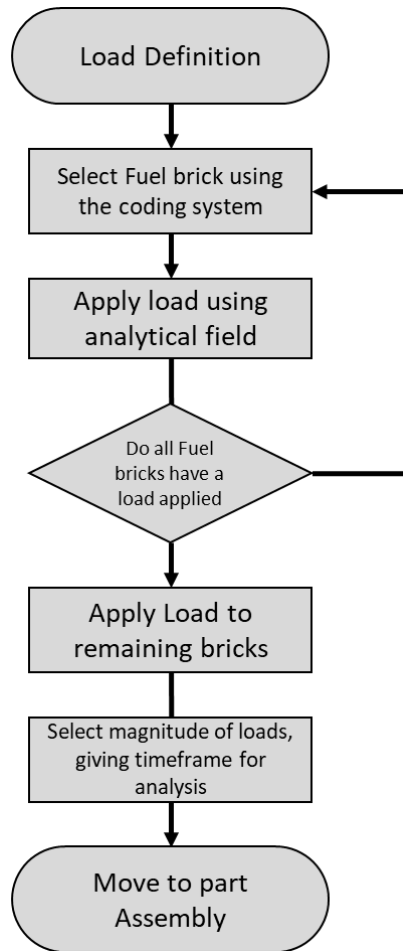
Figure 3-25: Flow chart showing process behind creation of python scripts for load definition

3.5.2 Irradiation Load

The effects of irradiation on a single brick have been modelled and discussed in previous works, e.g. (McLachlan, et al., 1996). It has been found that as graphite bricks irradiate, they firstly shrink, then expand beyond their original dimensions, a process which has been discussed in depth in chapter 2.2.4. As fuel bricks' interiors receive higher dosages, the inner surfaces shrink at a faster rate than the outer surfaces. After 30 years of service, the dose on the inner surface of the brick is approximately 200×10^{20} n/cm^2 while the dose on the outer surface is 112×10^{20} n/cm^2 (Haiyan, et al., 2008).

The dosage received by each layer varies based on the layer of the brick, with the first and last layers receiving no doses. The irradiation loads are modelled with a constant dose throughout each layer, but a variable dose between inner and outer brick surfaces. The dose distribution in the core is shown in figure 3-26.
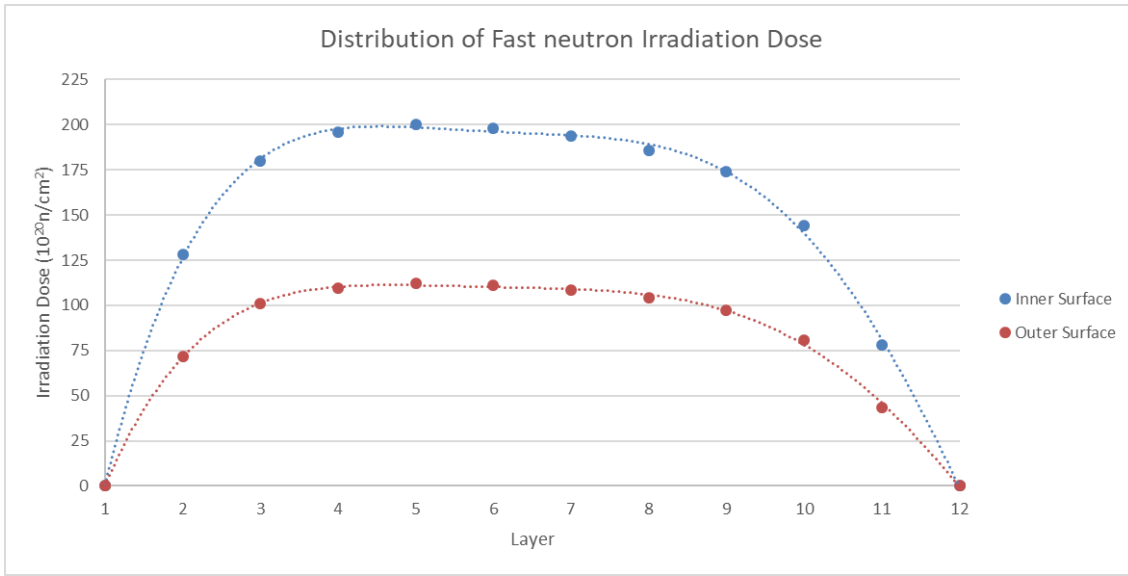
Figure 3-26:Distribution of fast neutron irradiation dose within reactor core.

Applying these loads to the model is completed in a very similar way to the thermal loads, by creating an analytical field from which the equation specifying load distribution can be applied. The analytical field for each fuel brick was calculated separately using equation 3.11, where A_L, B_L and C_L are coefficients derived from polynomials of best fits. The values for A_L, B_L, and C_L are included in the appendix in chapter A.5. The equation makes sure the dose varies across the X and Y-axes, but it keeps it constant across the bricks Z-axis.

$$\gamma_{FB} = A_L x^2 + B_L x + A_L y^2 + B_L y + C_L \tag{3.11}$$

The model assumed that only the fuel bricks are affected by the dosage, with no dose being applied to the remaining bricks. The pseudocodes used when applying thermal loads were adapted and used to apply the irradiation loads to the model. With only one load applied to a brick at a time.

3.5.3 Loads of smaller model

Three smaller models were created, each considering the loads in a different layer of the full-scale core. The smaller model consists shown in figure 3-3, consist of only five layers, compared to the full models twelve. To be able to thoroughly investigate every single layer, three smaller models were created. Table 3-6 shows which loads were applied when modelling each of the smaller models. Small model 1 (SM1) has both thermal and irradiation loads from layers 1-5 of the full-scale model applied to it. SM2 has the loads between layer 5-9 of the full-scale model applied to it. SM3 has the loads of layers 8-12 applied to it. The most considerable difference will be lack of additional stresses as a result of no gravitational forces applied on the bricks. This means models SM2 and SM3 will not any additional pressure on the bricks.

Loads in Full-Scale Model	Small Model 1 (SM1)	Small Model 2 (SM2)	Small Model 3 (SM3)
1	1		
2	2		
3	3		
4	4		
5	5	1	
6		2	
7		3	
8		4	1
9		5	2
10			3
11			4
12			5

Table 3-6: What loads are applied with each model

3.6 Boundary Conditions

At the core-periphery, a system is used for load transfer to ensure the core can breathe as bricks expand and contract. This system contains Warwick locks and steel restraint beams. Modelling a system that acts exactly as this would be complex and computationally demanding; therefore, the boundaries have been simplified.

3.6.1 Full-Scale Model Boundary conditions

As shown in figure 3-27, the boundary has an outer border with a rigid body, non-deformable boundary. This boundary contains contact properties with the outer surfaces of the fuel bricks. This ensures these bricks do not pass the boundary of the core. To guarantee the Bricks stay in position laterally, a second part is added to the boundary, which acts as a key locking into the outer keyways of the fuel bricks. This section of the boundary is defined with weak linear elastic material properties, which allows for expansion and contraction of the entire graphite core. This system is straightforward, and will be both computationally efficient, while still abiding by the specifications required for an accurate model. The boundary ensures the core can expand and contract with little resistance, until contact is made with the outer boundary.

Based on the loads being applied, it can be assumed the bricks in layer 12 of the model will not be displaced in the vertical direction, where the floor of the reactor lies. Knowing this, the base surface of every brick on layer 12 of the model have a zero vertical displacement boundary condition applied. This will block vertical displacement while allowing for lateral movement of the bricks. An alternative method could have been applied where similar to the rigid boundary walls a rigid floor was placed at the base of the core, however by just locking the floor of the model, a more computationally efficient approach was selected. This method will not affect the results as the loads are only considering lifetime damage, where during the life cycle, vertical displacement of the bottom layer of bricks is limited. If other loads (e.g., seismic load) were applied, alternative boundary conditions would be more suitable.
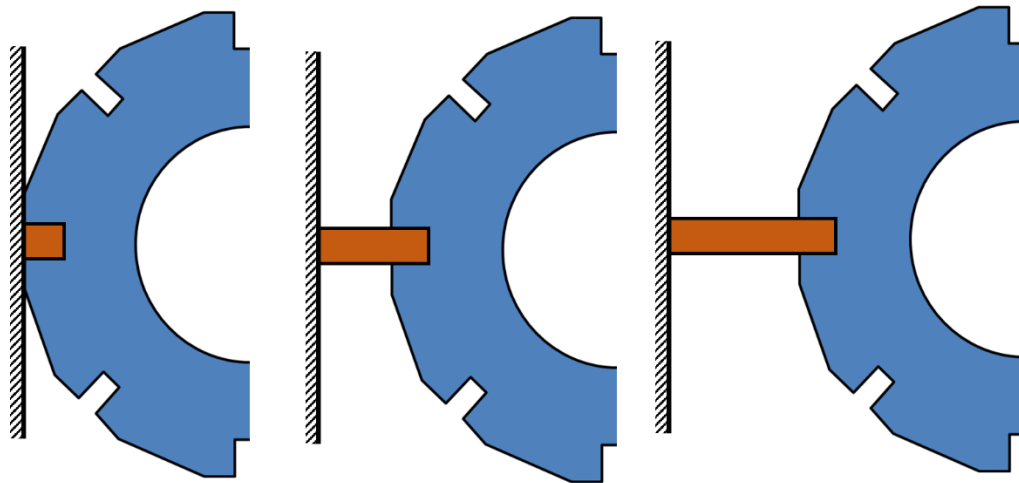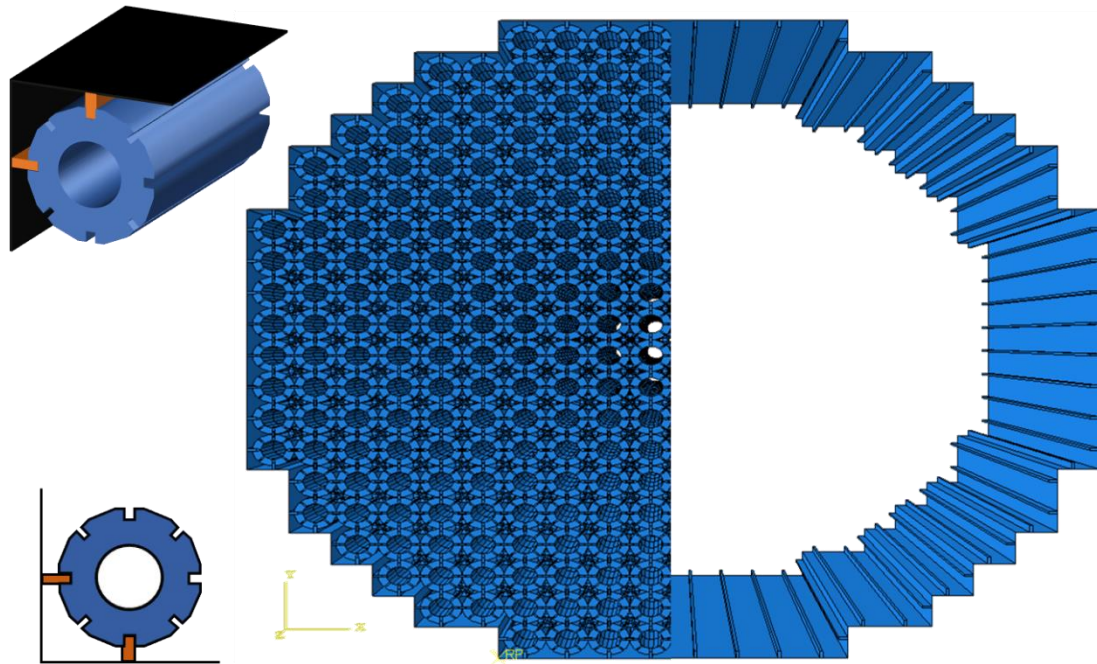
Outer brick can expand up to a limit

Outer brick can expand and contract with small resistance

Outer brick can contract freely, only limited by contact with other bricks

Figure 3-27:How the boundary system functions in the model

3.6.2 Small-Scale model Boundary conditions

Up to now, the same loads, dimensions, and interactions were used on the smaller model compared to the full-scale model. The boundary conditions are where there will be a significant difference between the models. The same method is used with a rigid wall build around the model; however, if it is to be assumed the smaller model is a series of bricks plucked from anywhere on the full-scale model, then it is essential to model the stresses caused by the contact of bricks in the same layer. In the small model, these additional stresses were ignored. In addition, the displacement of a brick is dependent on the movement of the bricks above and below it, with a small model not including all 122 layers, displacement data would be unreliable. For this reason, it will not be possible to trust the results gathered from the small model. The rigid boundary used for modelling the small model is shown in figure 3-27.
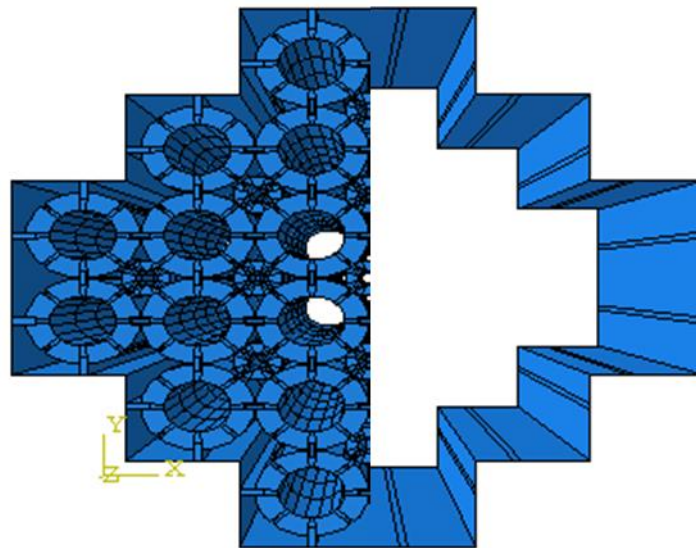
Figure 3-28: Boundary condition for small model

The biggest error with modelling a small core comes from the lack of stresses caused from other bricks in the core. These stresses appear as various bricks lean on each other laterally, or due to the gravitational loads of more bricks being on top of each other. These

loads do not exist when modelling a small core, so the results gathered using the small model cannot be viewed as realistic due to the boundary conditions applied to the model.

However, they can provide information on if the modelling approach used is feasible when modelling the entire core. Through modelling on a smaller model, the most computationally efficient approach was chosen. Changes to modelling approach would take minutes to test on the small model as appose to changes on the full-scale model which can take weeks to complete analysis. The analysis on the smaller model gives confidence that approach used on a full-scale model will be possible to complete.

4 Analysis Approaches

Post processing of the result takes place using a process described in figure 4-1. Depending on the investigation being conducted a different approach is necessary. Python scripting is utilised to create 3 text files containing all the data that will be analysed. Maximum stresses in each brick are collected, which can be used to observe the rate of damage in the core graphically show the percentage of bricks to have undergone failure in each layer.

Following this a larger file is created which contains the stress values of the brick at each element. This file is used to judge how many elements in the brick have undergone damage, and how this damage evolves over time, both on a whole core and by each layer. In addition, using the numbering of the elements, it can be also clear how much damage is seen in each region on the brick.

The final data collected will look at node displacement for each brick. From this data, the change in internal diameter of the bricks can be shown. In addition, the change in alignment of the channels can also be found and displayed. This can be used to understand if the core is still fit for purpose. The entire post-processing procedure is displayed in figure 4-1.

By analysing the output file produced, both visual and mathematical indications can be gathered when the core safety will become compromised. To analyse the results, initially python scripting is used to generate multiple text files containing both the maximum principal stresses at each element in the model, followed by a separate file listing the displacements of every node in the model. These text files are then analysed to accumulate a timeframe for the failure of core.

As discussed previously, it is assumed that the bricks with the highest dosage received a dose 200×10^{20} n/cm^2 over 30-years (Haiyan, et al., 2008). The analyses performed on the smaller models take place over 40-years, while due to computational limitations, the full-scale model only takes place over 30 years. This means the maximum dose applied on the
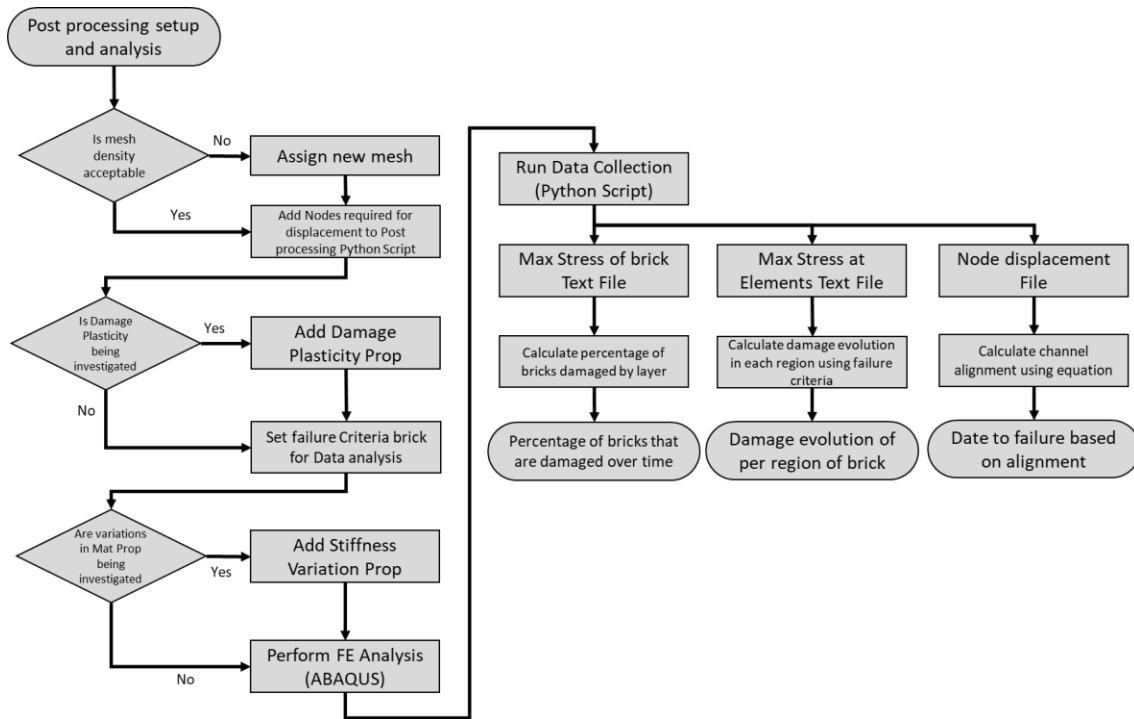
Figure 4-1: Flow chart showing process defined in python scripts that leads to establishment of core failure date

smaller models is 266×10^{20} n/cm^2, while the full-scale model only received a maximum dose of 200×10^{20} n/cm^2 (Haiyan, et al., 2008).

The smaller model will collect the stresses and displacements at 1-year intervals creating 40 data points. The full-scale model, due to computational limitations, will only collect data at 2-year intervals creating 15 data points. Through these data points, graphs and plots can be created, indicating how damage evolves. This can then be compared to previous models created to investigate the accuracy of the results.

4.1 Defining Core failure

The office for nuclear regulations defines that modelling of the core should be able to measure channel distortions as a result of neutron irradiation with those measured on active reactors while also comparing the effects of future levels of primary and secondary cracking and their associated core distortions, measured on active reactors. This report

considers channel distortion without considering cracked bricks. This is done by considering the stresses in the bricks and also the displacement of nodes over time.

4.1.1 Stress Analysis

Using Python script, the maximum principal stresses at the element centroids are collected. These stresses are computed through extrapolation of element tensor quantities. This is performed on the individual tensor components in the local material coordinate system. Abaqus uses the extrapolated data from all contributing elements to compute the invariants and displays them in table format.

Considering the reactor, an elastic model will consider 2 modes of damage initiation (Yang, 2004). Under tension, the maximum tensile limit of graphite, which is given as $\sigma_{T_{max}} = 20\ MPa$ (Savija, et al., 2018), can be utilised to deduce that damage will initiate under tension when the maximum principal stress increases beyond 20 MPa.

While under compression, if we consider the maximum compressive stress or the minimum principal stress of graphite, given as $\sigma_{C_{max}} = 20\ MPa$, we can deduce that damage will initiate under compression when maximum principal stress falls below negative 20MPa (Becker & Marrow, 2013).

While it can still be assumed that damage initiation will occur after the limits are passed, as displayed in figure 4-2 (a), the elastic models will not contain any softening behaviours following damage initiation.

While the maximum principal stress can be used to determine the time of damage initiation of an elastic model, a plasticity model is analysed differently. The plasticity model is a continuum, damage model. It assumes that the main two failure mechanisms are tensile cracking and compressive crushing of the graphite. The evolution of the yield or material softening behaviour is defined by equivalent plastic strains $\tilde{\varepsilon}_T^{pl}$ and $\tilde{\varepsilon}_C^{pl}$. These variables specify failure mechanisms under tension and compression loading, as shown in figure 4-2 (b).
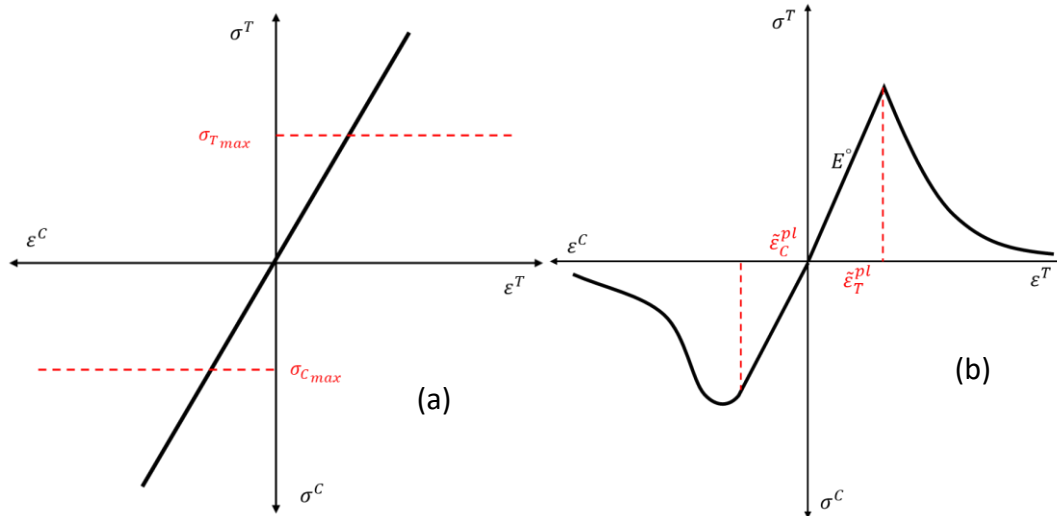
Figure 4-2: Damage initiation limits in both tension and compression

Abaqus uses the equivalent plastic strain to identify when a material is actively yielding. The software provides an identifier, where a value of either 1 or 0 is given as an output for each element to indicate if the material is currently yielding or not.

Python script is used to create 2 text files for each model analysed. The first will look at the maximum stress in each brick. This data will provide a clear indication of the percentage of bricks that are damaged at any time in the core as a whole and in each individual layer. This data can be used to compare the different analysis approaches being considered.

The second text file will consider damage evolution in the core as a whole and by region. by collecting the stress of the by element, and calculating how many of the elements have passed the point of damage initiation. This is then also broken down as to investigate damage imitation by region of the brick.

Abaqus also provides a label for each element, which can be utilised to calculate where the bricks have undergone damage initiation and evolution. The fuel bricks can be split into three regions, fuel brick to fuel brick keyways, fuel brick to interstitial brick keyways, and the remainder of the fuel brick. Each of these regions is shown in figure 4-3. Appendix

C.1 shows the element number and the region of the brick each of the values corresponds to.
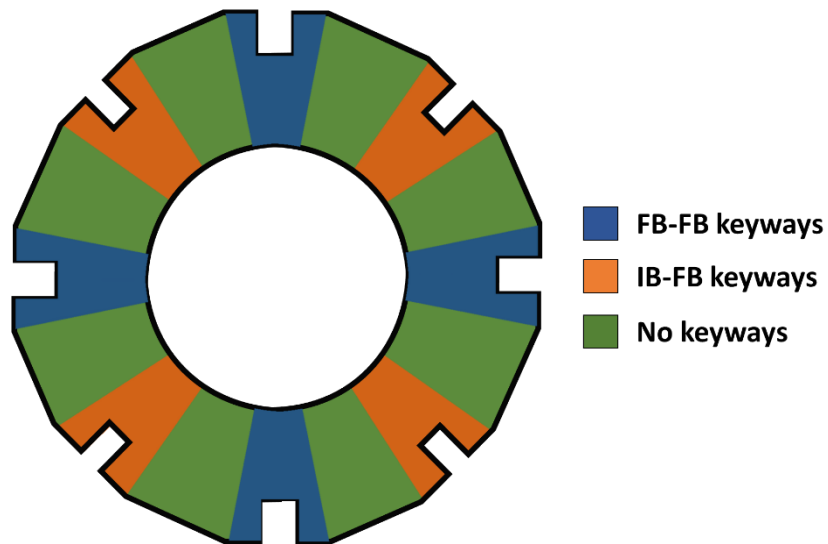
Figure 4-3: Different regions of the Fuel brick:

Understanding where a brick fails can be very important, as it will indicate where the weakest regions of the bricks are and where cracks are is most likely to appear. Another vital statistic is the investigation of whether using a plasticity model where a material begins to yield will move stresses away from the keyways or concentrate them more. Analysis of the damage evolution should also show how contact between bricks affects damage in each region of the brick.

4.1.2   Channel alignments

As Fuel bricks shrink and expand the core profile will shift into different phases, altering the alignment of the channels and increasing the possibility for fuel assemblies to become blocked from either entering or being removed from the core. The potential for a blockage to occur is dependent on two variables; the diameter of the inner channel and the change in angle of bricks between layers of bricks.
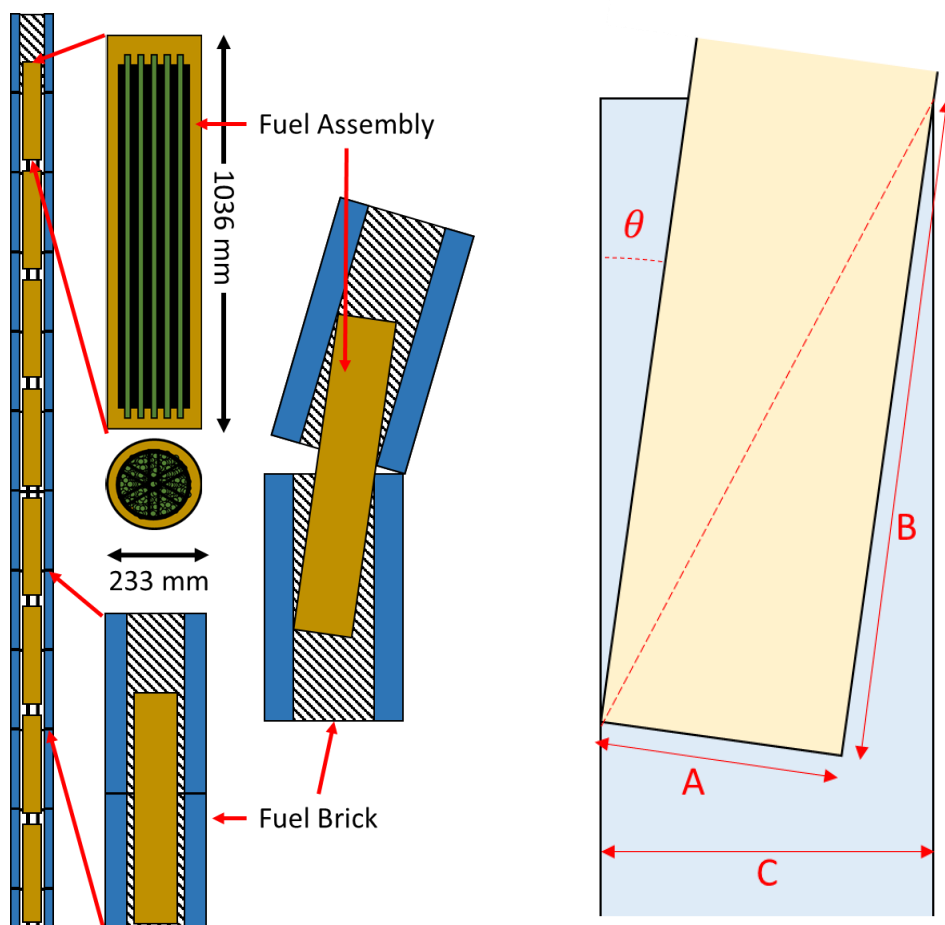
Figure 4-4: How fuel assembly can become jammed

As 4-4 shows, the fuel assemblies can become jammed in channels if the fuel bricks rotate too far. As the bricks are exposed to irradiation, the diameter of the fuel channels changes over time, which causes this angle to change over time as well.

How the angle limit is calculated is based on the diameter of the fuel assembly A, half the length of the fuel assembly B, and the diameter of the channels C. The maximum angle of rotation θ is calculated using the equation:

$$\theta = \tan^{-1}\left[\frac{C}{\sqrt{A^2 + B^2 - C^2}}\right] - \tan^{-1}\left[\frac{A}{B}\right] \tag{4.1}$$

It is assumed the fuel assemblies do not change in size; however, the diameter of the channels can change due to irradiation. This diameter is calculated using the data given by Abaqus field output, which provides the magnitude of the brick's displacement along the basal plane. This magnitude is given at eight pre-selected nodes. These nodes are all based on the inner fuel channels, as shown in figure 4-5.
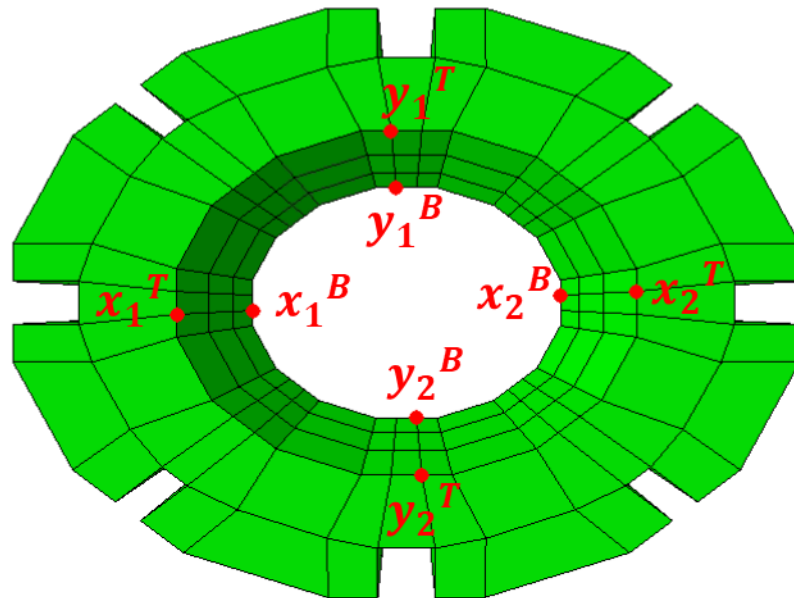
Figure 4-5: Nodes on brick that are investigated

The values for U1 are used on nodes x_1^T, x_2^T, x_1^B and x_2^B while the values for U2 are considered for nodes y_1^T, y_2^T, y_1^B and y_2^B. The diameter is calculated by taking the initial value of the diameter and subtracting the magnitude of the displacements at the nodes

at four different points. The minimum value for the diameter C is found by subtracting the maximum displacement values at the nodes as shown in equation 4.2.

$$C = C_0 - \max[(x_1^T - x_2^T), (x_1^B - x_2^B), (y_1^T - y_2^T), (y_1^B - y_2^B),] \qquad (4.2)$$

From this, the limit of rotation θ can be found by combining equations 4.1 and 4.2.

The angle in which each brick rotates is found by using equation 4.3, where L represents the length of the fuel brick. This equation is used to find the rotational angle for every brick at four points. This is then subtracted from the values at the same points from the brick in the layer below (as shown in equation 4.4), providing the angle difference between two bricks.

$$\theta_L$$
$$= \max\left\{\left[tan^{-1}\left(\frac{x_1^T - x_1^B}{x_1^B}\right)\right], \left[tan^{-1}\left(\frac{x_2^T - x_2^B}{x_2^B}\right)\right], \left[tan^{-1}\left(\frac{y_1^T - y_1^B}{y_1^B}\right)\right], \left[tan^{-1}\left(\frac{y_2^T - y_2^B}{y_2^B}\right)\right]\right\} \quad (4.3)$$

$$\theta_A = \theta_L - \theta_{L+1} \qquad (4.4)$$

From these results, the following can be assumed:

$$\theta_A \geq \theta \quad or \quad C < A \qquad \text{Blockage will occur}$$

$$\theta_A < \theta \quad or \quad C > A \qquad \text{No blockage will occur}$$

The same system was used for calculating if the channels where the control rods lay are aligned and safe. The control rods are significantly narrower than the fuel assemblies (ALDAMA & GUAL , n.d.), it can be assumed that the channels will remain safe significantly longer than those containing the fuel assemblies. This will be investigated with a smaller model first.

4.2 Mesh density analysis.

The mesh density is of great importance when developing a model. Previous studies have showed a more refined model will improve confidence in the results, however at an increase computational cost (Liu & Glass, 2013). In this section a sensitivity study is studies to observe the difference a refined mesh will have on a small model, looking at damage taking place using loads being applied to layers 5-8 of the core. While validating which mesh generates the most accurate reflection of damage in the core is not possible (Mummery, et al., 2020), the study here will concentrate on how the mesh changes damage seen in the core and CPU time required to complete analysis.
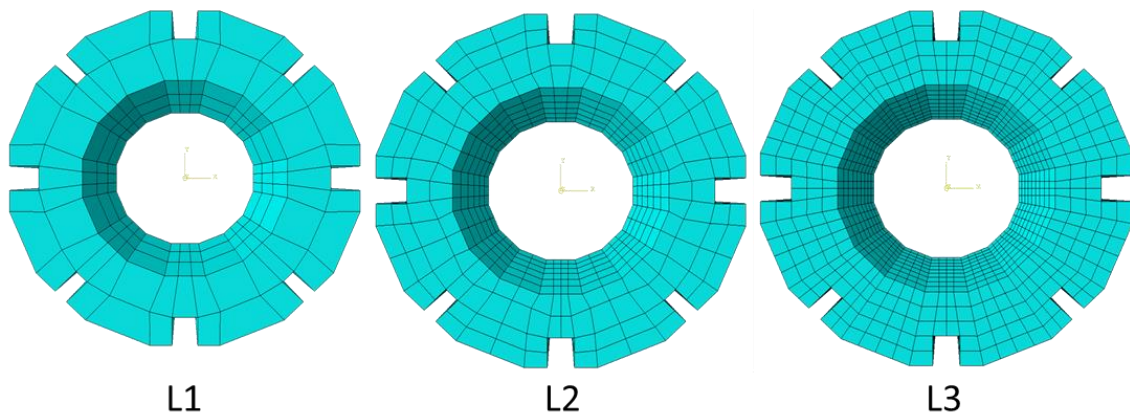
Figure 4-6: Different meshes investigated

Three levels of refinement were analysed as part of this study, with each level increasing the number of elements in the model. As displayed in figure XX, L1 is the coarsest mesh, L2 is more refined and L3 used the most refined mesh analysed. The number of elements in L1 were 168 per fuel brick, with L2 having approximately 6 times more elements at 876 per fuel brick. This translates to almost 6 times longer analysis time. The most refined mesh, L3 has 2844 elements per fuel brick, almost 17 times the number of elements in the coarsest mesh L1. The additional computational time however increased at much larger rate as shown in table 4-1, resulting in a computational time 50 larger in the finer mesh L3 over the coarsest mesh L1.

Mesh		L1	L2	L3
Fuel	Nodes	384	1421	4000
Brick	Elements	168	876	2544
Whole	Nodes	77692	202132	511612
core	Elements	30965	115925	352085
Total CPU Time (Sec)		217	1131	11482

Table 4-1: Table showing difference between 3 mesh analysis

How this mesh density affects the percentage damage observed in the bricks is displayed in figure 4-7. Damage in the bricks was predicted to begin sooner with a more refined mesh, with damaged beginning at 24 years of service with meshes L2 and L3, and 27 years with L1. Through analysis it was also found that the amount of damage observed in the core as a whole would remain very similar between all mesh. A refined mesh going from L1 to L2 saw an increase in damage, however, this was not observed when the most refined mesh L3 was used. From these results it can be assumed that approximately 40-50% of the brick would see damage within 40 years of service. However, it is important to also analyse where this damage is occurring and if both methods predict similar damage distributions and failure dates for each layer.

Figure 4-8, shows the damage percentage damage that takes place in each layers of the core, both at and away from the keyways, with all three variations of meshes. Initial comparison of the three approaches to meshing shows layers becoming damaged in the same order, with layers 5 and 6 undergoing damage first followed by layer 7 and 8.

When considering data collected at the elements located away from the keyways (figure 4-8 (a) (c) and (e)), it is clear very little difference exists in the overall damage that will take place, with meshes L1, L2 and L3 all reaching approximately 50% damaged elements over a 30-year period. A difference is observed when considering the gradual increase of damage. A finer mesh results in a steady increase in damage, whereas the coarser meshes reach the 50% damage threshold very suddenly. Consequently, the mesh at the regions away from the keyways can remain coarse saving on computational power.

VARIATION OF DAMAGE WITH MESH REFINEMENT
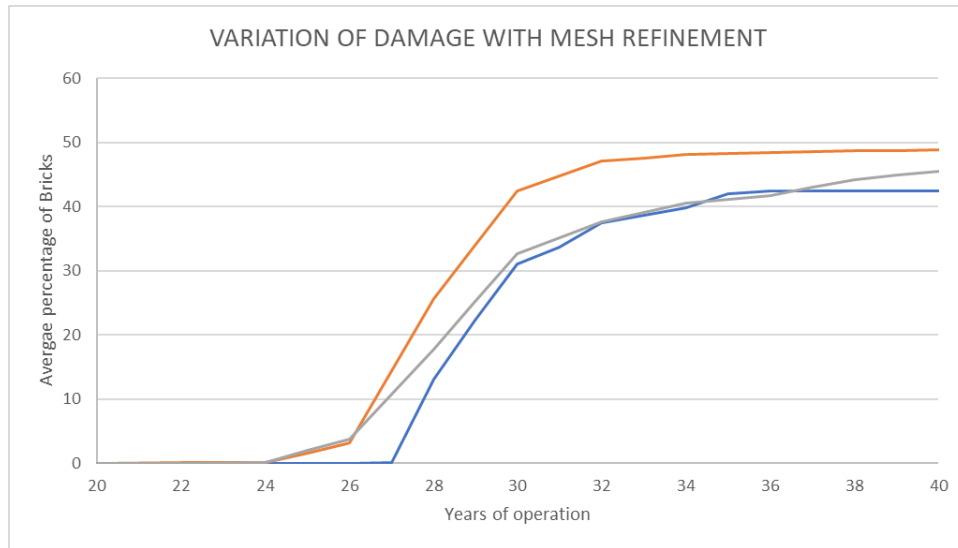
Figure 4-7: Evolution of damage with three different mesh refinements (L1-Blue, L2- Orange, L3-Grey)

A different outcome is observed again when considering damage at the keyways. The threshold of damage at the keyways is significantly different with the different mesh densities considered. Mesh L1 shows a peak damage of 40% (figure 4-8 (b)), this increases to 70% with mesh L2 (figure 4-8 (d)) and is around 50% with mesh L3 (figure 4-8 (f)). It remains unclear which mesh displays the most realistic percentage damage. Due to the large differences between the 3 approaches, further refinement would be recommended until a peak damage is replicated along multiple mesh densities being investigated. Based on the results gathered, a finer mesh is recommended to be used around the keyways.

Overall, the results from this study show the most computationally method of showing analysing the core would be to use a coarse mesh, with a finer mesh taking 53 times longer to complete analysis. They also suggest a coarse mesh is acceptable in regions away from the keyways, with a finer mesh showing a gradual build-up of damage, but reaching the same threshold as a coarser mesh. In regions around the keyways, it is suggested that a finer mesh be used, as results gathered showed an increase in the percentage of elements that passed the tensile limits of the graphite, therefore to better observe these regions of damage, a finer mesh would be recommended. Due to the limited computational power available, mesh L1 has been used for all analysis in this report.
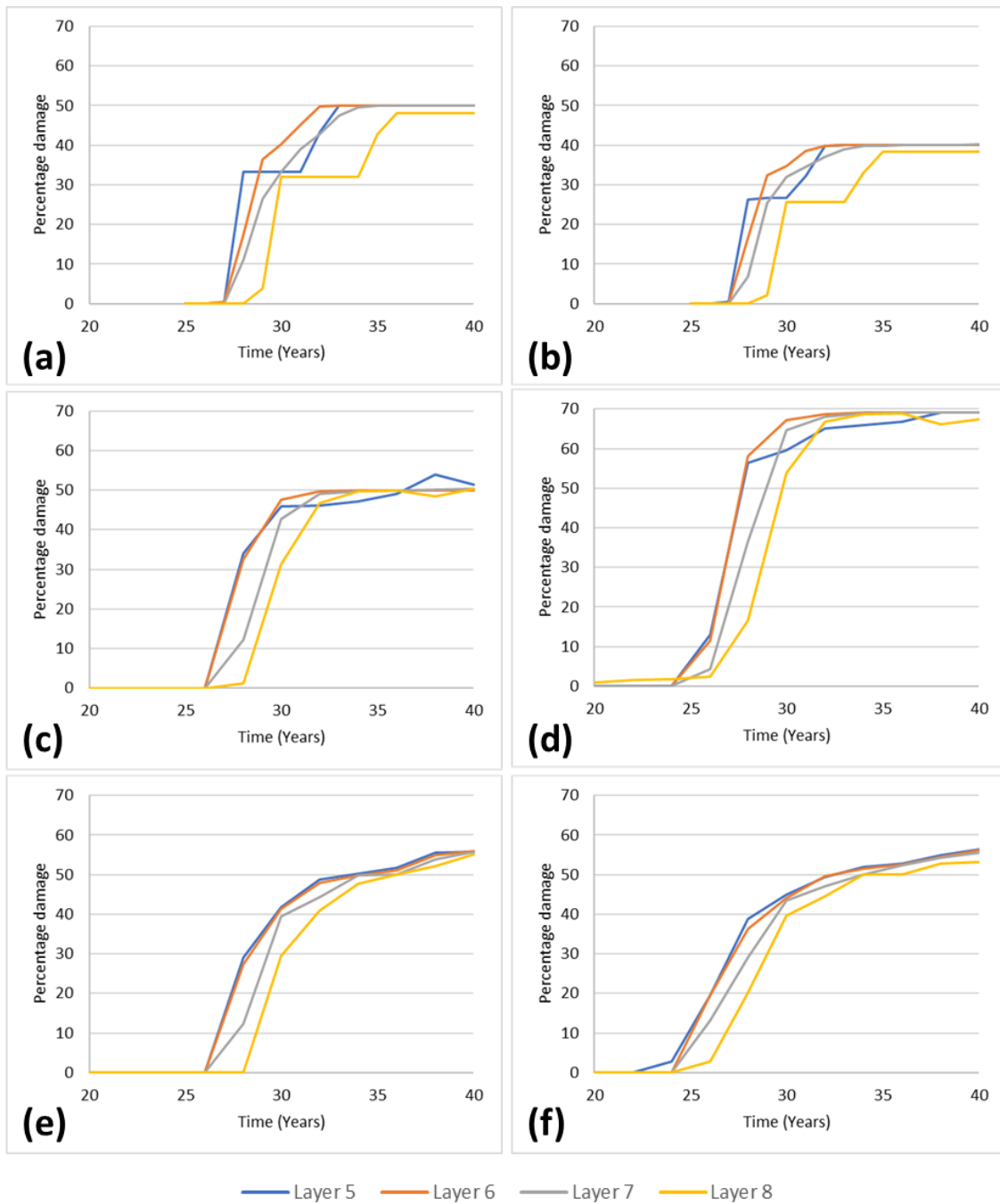
Figure 4-8: Evolution of damage of different regions of bricks in each layer of the core considering different meshes (

(a) Mesh L1 away from keyways) ((b) Mesh L1 at keyways) ((c) Mesh L2 away from keyways) ((d) mesh L2 at keyways)

((e) Mesh L3 away from keyways) ((f) Mesh L3 at keyways)

5 Results and Discussions

When producing results, two models were generated, a small model and a full-scale model. The small model, containing an array of 120 fuel bricks, was used to perform various sensitivity studies on the modelling approach being considered and to test the feasibility of the modelling method being employed before moving onto a full scale. To ensure the loads applied are correct for all layers, three small models were produced. Small model 1 considered the loads in layers 1-5, small model 2 considered loads between layers 5-9 and small model 3 considered loads between layers 8-12. This will allow analysis of all layers of the core occur at one time.

The studies have been conducted as part of the small model analysis; these were:

- Effects of introducing variations in material properties
- Effects of introducing material softening behaviour

The graphs gathered in section 5.1 show the results gathered from the small model, while section 5.2 shows results gathered from a full-scale model. Each section is split into three again, with the first set of graphs showing the damage initiation graphs, followed by the section showing the locations of failure and evolution of damage in each region. The final graphs show the channel alignments for the fuel assemblies against time.

Note: all small-scale analysis has been performed on a desktop PC with 16GB Ram. Full scale analysis has been performed on a server with limited 20GB RAM.

5.1 Small model

5.1.1 Percentage of bricks damaged
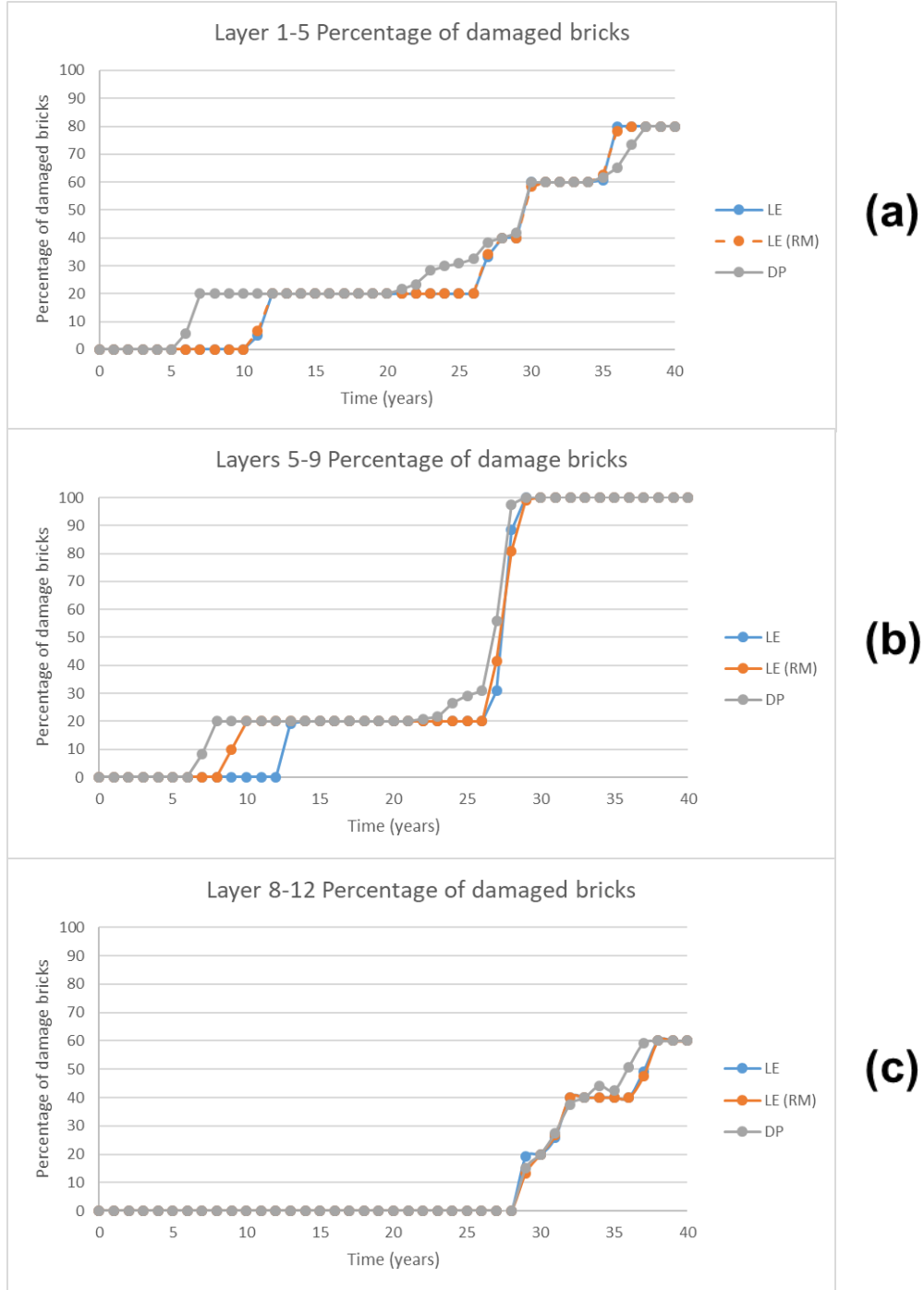
Figure 5-1:Percentage of bricks damaged in each model. (a) Model representing layers 1-5, (b) Model represents results from layers 5-9, (c) Model represents results from layers 8-12.

Figure 5-1 shows three graphs displaying the percentage of bricks that experienced damage (y-axis) over 40 years (x-axis). Graph (a) shows the data from layers 1-5 of the full model, graph (b) shows the data from layers 5-9, and (c) shows data from layers 8-12. These graphs provide an indication of when damage initiation occurs in the bricks when three different approaches are used. The blue line in the graphs shows results where only Linear elastic material properties were defined. The orange line shows linear elastic results with the addition of randomly distributed material properties. Finally, the grey line shows the data from a model where damage plasticity was included. This allows for an easy comparison of the three approaches to modelling the core.

When analysing graphs in figure 5-1, it is clear that the elastic models and plastic model shows very little difference as to when the bricks will initially fracture, with the result when adding random material properties being almost identical. Figure 5-1 (a) shows the fracture of 80% of bricks within 40 years of operation. Figure 5-1 (b) shows that for bricks between layers 5-9, it can be assumed all the bricks will fracture within 30 years of operation.

When considering figure 5-1 (a) and (b), it can be assumed that 20% of bricks fail within 15 years. With further analysis of these results, it is clear that this is due to an incompatibility between the boundary conditions and the loads on the bricks. The bricks are expanding due to irradiation loads; however, the boundary conditions restrict the base of the bricks from expanding. This conflict causes the final layer of bricks in each model to fracture significantly early than the rest of the layers. This becomes clearer when graph (c) is observed, where only results in layers 8-12 are considered, where boundary conditions placed on layer 12 do not conflict with the loads applied. With no irradiation loads being applied to the final layer of bricks, no bricks ended up fracturing early in figure 5-1 (c). Due to this, data for layer 5 of model 1, and layer 9 of model 2 are ignored from this step onwards.
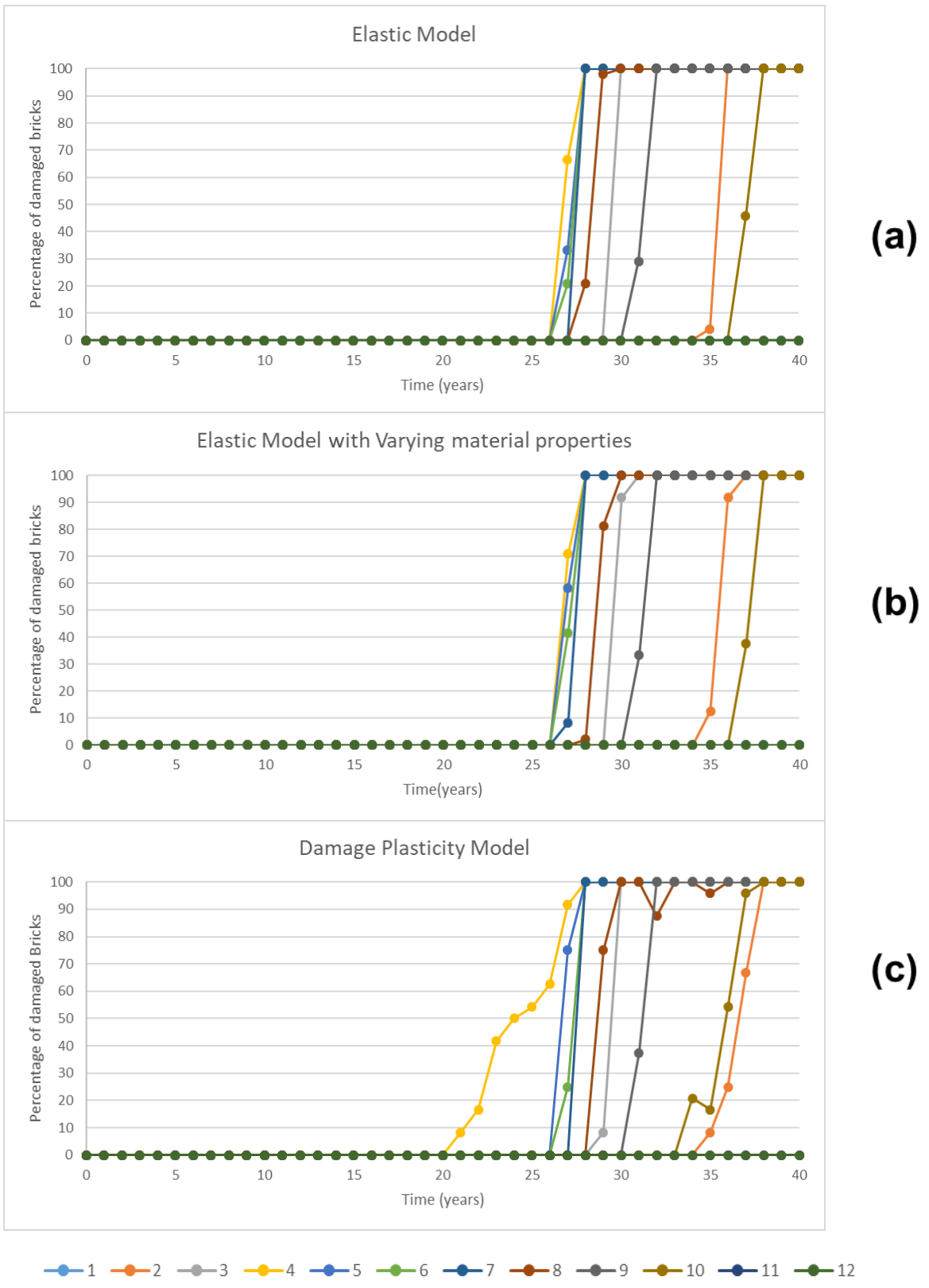
Figure 5-2:Percentage of brick damaged within each layer of bricks in the model. (a) shows purely elastic model, (b) shows elastic model with the addition of random material properties in the bricks, (c) shows a damage plasticity model

Figure 5-2 shows graphs showing the percentage of damage to each layer of bricks (y-axis) over 40 years (x-axis). Graph (a) displays data when only elastic material properties were defined. Graph (b) shows data when random material properties were applied to an elastic model. Graph (c) shows data from the model where damage was included. A colour coded key is also included, which shows which layers each line on the graphs refers.

Layer	Elastic Model		Elastic Model (RnD Mat)		Damage Plasticity Model	
	Time to damage initiation	Time to 100% damage	Time to damage initiation	Time to 100% damage	Time to damage initiation	Time to 100% damage
1	No damage					
2	35	36	35	36	35	38
3	30	30	30	31	29	30
4	27	28	27	28	21	28
5	27	28	27	28	27	28
6	27	28	27	28	27	28
7	28	28	27	28	28	28
8	28	30	28	30	29	30
9	32	33	31	32	31	32
10	37	38	37	38	34	38
11	No damage					
12	No damage					

Table 5-1: Time to damage initiation and 100% damage in each of the core

Table 5-1 shows the date by which the bricks in each layer experienced damage initiation, followed by the date where 100% of the bricks in each layer were damaged. Both the table and the graph show no damage to the bricks in layers 1, 11, and 12 of the core. The earliest damage is seen to occur in layers 4, 5, and 6. This is expected as they are the layers where the highest levels of irradiation are also seen.

When comparing the results from graphs (a) and (b), once again, the results show that the addition of random material properties to the model do not significantly affect the results. However, the addition of plasticity does show changes with layers 4 and 10 predicting damage to begin much sooner with a plasticity model. However, while damage initiates sooner, the time at which 100% of the bricks are damaged occurs at an almost identical time.

Figure 5-2 (c) also shows some bricks fracturing followed by a reversal of fracture, specifically in layers 8 and 10. This initial fracture due to the shrinking of the brick resulting

in 100% of bricks fracturing. This is followed by 15% of the bricks damage reversing as the brick expands again only to fracture again once either contact with other bricks occurs or when stresses exceed the maximum tensile loads.

The failure of the bricks will be of great importance. Table 5-2 shows the dosage at each layer at the time when 100% damage in every brick was observed. The table shows that 8 of the 9 layers of bricks that experienced 100% damage within 40 years, only predicted this damage to occur when the inner surface of the bricks received at a dose of over 180×10^{20} n/cm^2 and the outer surfaces received a dose of over 100×10^{20} n/cm^2. This suggests that initial damage of the bricks is dependent on the dosage the bricks receive rather than due to the bricks coming into contact.

When comparing these dosages to that of figure 2-13, which shows the dimensional change in graphite based on the dosage it receives, the cause of the fractures becomes clear. At the point where 100% damage is observed, the inner surfaces of the bricks are expanding beyond their original dimensions, while the outer surfaces are still shrinking and are at the smallest value they will reach and beginning to expand again. This suggests the cause of fracture is the reversal of stresses on the outer surface or the expansion on the inner surface at a higher rate than the outer surface. It is clear the bricks fracture due to internal stresses rather than due to interactions between the bricks.

| Layer | Dosage at 100% damage | | | | | |
| | Elastic Model | | Elastic Model (RnD Mat) | | Damage Plasticity Model | |
	Inner surface	Outer Surface	Inner surface	Outer Surface	Inner surface	Outer Surface
1	No Damage					
2	153.6	86.0	153.6	86.0	162.1	90.8
3	180.0	100.8	186.0	104.2	180.0	100.8
4	182.9	102.4	182.9	102.4	182.9	102.4
5	186.7	104.5	186.7	104.5	186.7	104.5
6	184.8	103.5	184.8	103.5	184.8	103.5
7	181.1	101.4	181.1	101.4	181.1	101.4
8	186.0	104.2	186.0	104.2	186.0	104.2
9	191.4	107.2	185.6	103.9	185.6	103.9
10	182.4	102.1	182.4	102.1	182.4	102.1
11	No Damage					
12	No Damage					

Table 5-2: Dosage of bricks in each layer when 100% damage took place.

5.1.2 Evolution of damage and stress
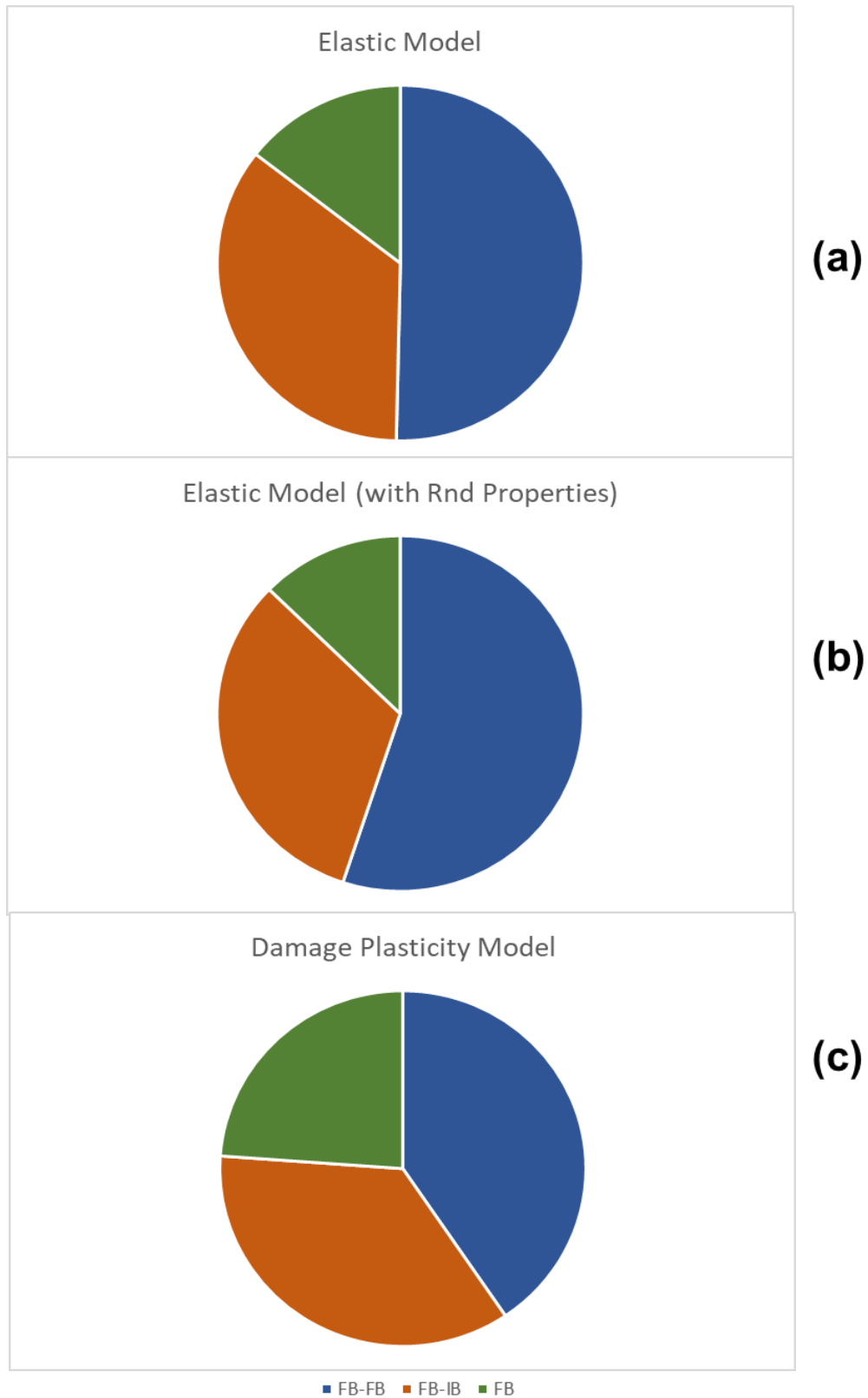
Figure 5-3:Location of damage initiation in the fuel bricks. (a) elastic model, (b) elastic model with random material properties, (c) damage plasticity model.

As discussed in chapter 4.1, the brick can be split into different regions when considering where the brick is damaged. Figure 5-3 shows the location of damage initiation based on which region is shown in figure 4.3. Based on the data gathered, the location where initial damage occurs can be deduced by considering the element with the highest stress value at the time of failure. The pie charts show damage initiation in three colour-coded locations, the blue regions are fuel brick to fuel brick keyways, the orange regions are the fuel brick to interstitial brick keyways, and the green regions represent the rest of the brick. Figure 5-3 also shows the difference between the modelling approach used, with (a) showing the data from the elastic model. (b) shows results from the elastic model where random material properties are added. (c) shows results with damage plasticity included.

Figure 5-3 (a) shows that in an elastic model, half of the initial damage took place in the fuel brick to fuel brick connecting keyways. Approximate a third of the damage initiated in the interstitial brick to fuel brick keyways and the remainder of the damage initiated elsewhere in the brick. When considering the addition of random material properties as seen in figure 5-3 (b), the damage initiation became more concentrated at the FB-FB keyways, with almost 60% of damage initiated here.

The most significant change observed was the addition of plasticity, which reduced damage initiation at the FB-FB keyways. This can be put down to the way the data is collected for elastic and plastic models. Whereas for the elastic model, the point of initial failure was chosen based on the elements that passed the stress limit causing failure to occurs. Multiple bricks pass the tensile limit simultaneously; therefore, the element where the maximum stress was observed was chosen. The plasticity model does not consider the elements that pass the highest stress, as upon failure this data is no longer viable, as most elements will undergo material softening and see a fall in stress. The method for element selection was randomly chosen and therefore sees a greater error.

The mesh sensitivity studies carried out in section 4.2, explain how damage by region can vary by refinement of mesh. The results here also show that the location of damage

initiation can also be greatly affected by material properties being applied. How this damage evolves is also significant. Here all analysis takes place using a coarse mesh due to limitations in computational capabilities. It is anticipated that the data at the keyways would differ with a finer mesh, while away from keyways the data should remain unchanged.
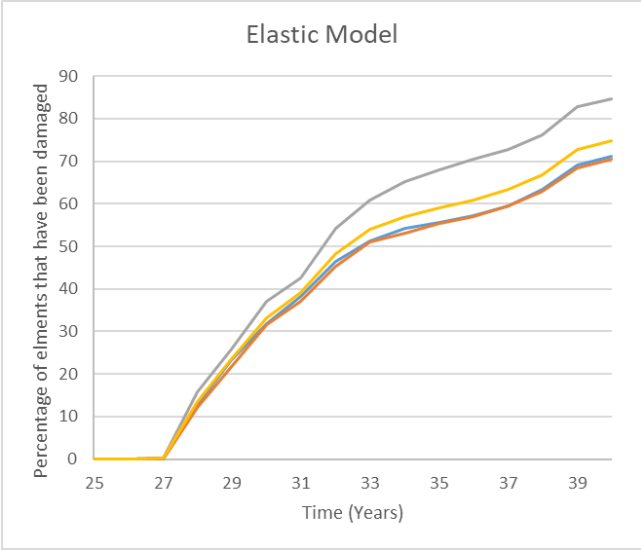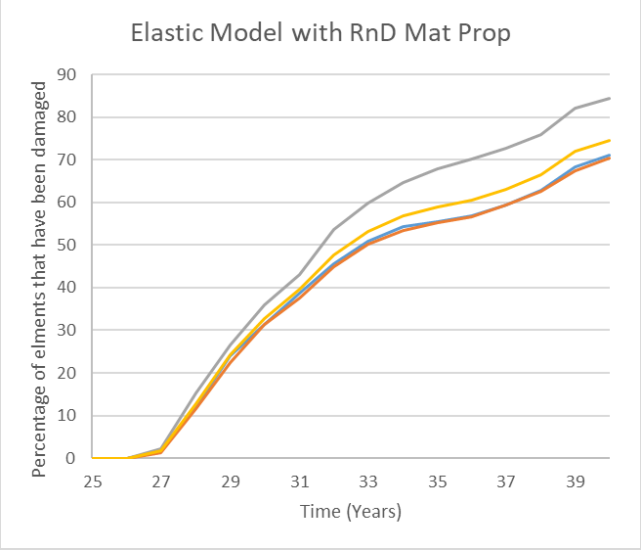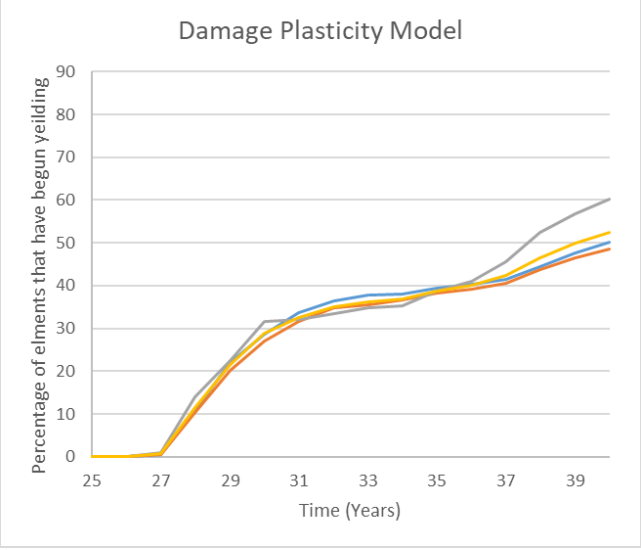
Figure 5-4:Percentage of damaged elements in an entire mode (a) elastic model, (b) elastic model with random material properties, (c) damage plasticity model.

Figure 5-4 shows the percentage of damage observed over time in elements in specific regions of the brick, mentioned in chapter 4.2. Table 5-1 showed damage initiating at 27 years, and therefore, the time line in the graphs begins after 25 years of service. Each graph shows three colour-coded lines, a blue line indicating a change in damage in the fuel brick to fuel brick keyways, an orange line indicating damage in interstitial to fuel brick keyways, a grey line indicating damage in parts of the brick away from the keyways and finally a yellow line showing the average for the brick as a whole.

The three graphs in figure 5-4 each represent data from a different model, with (a) showing data from the model with elastic material properties, (b) showing an elastic model with random material properties, and (c) showing a model with material softening occurring as well.

Figure 5-4 (a) shows after 40 years of service that 75% of the bricks will have passes the tensile limit of the material in an elastic model. The damage in the brick is mainly observed in the areas away from the keyways. This could be due to the coarse mesh, with a finer mesh expected to show a concentration of damage at the keyways. There is very little difference seen between figure 5-4 (a) and (b) where random material properties are added, with the graphs being almost identical.

The most significant difference was observed when comparing the elastic models in figure 5.4 (a) and (b) with the plasticity model in figure 5.4 (c). The results suggest switching to a plasticity model significantly reduces the damage of the bricks over time. This suggests the Plasticity model releases stresses in other regions of the brick, causing fewer failures over time. This can be further analysed by considering damage in specific layers, as seen with figures 5.5, 5.6, and 5.7.
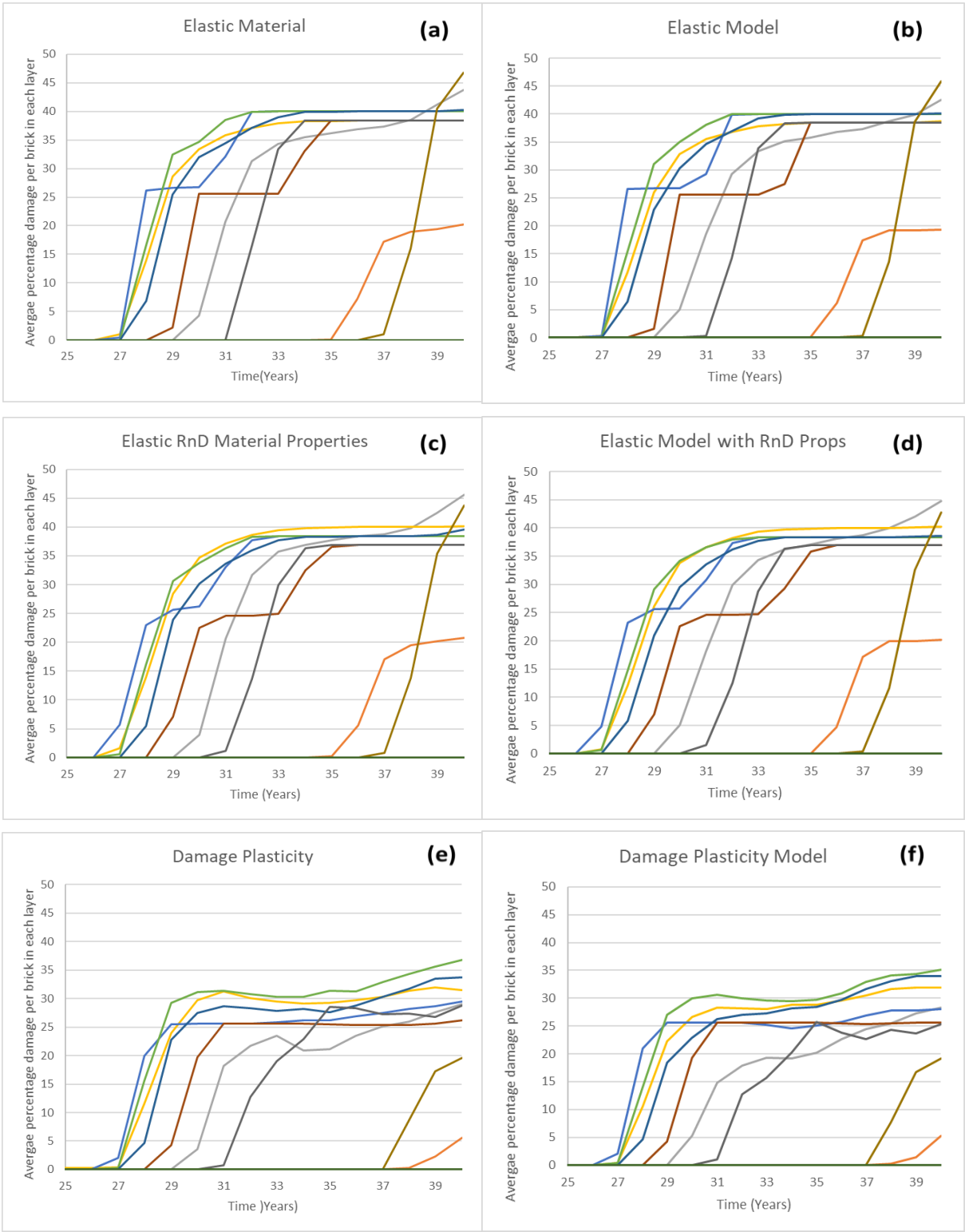
Figure 5-5:Average percentage damage at fuel brick keyways between 25 and 40 years.

Figure 5-5 shows the percentage of damage in the keyway elements (y-axis) between 25 years and up to 40 of service (x-axis). Each layer of the core is shown by a colour-coded line with a key included in the figure showing which layer each colour represents. Graphs (a), (c), and (e) all show data for the fuel brick to fuel brick (FB-FB) keyways, while graphs (b), (d), and (f) show data for the interstitial brick to fuel brick (FB-IB) keyways. Also, the top row of graphs (a) and (b) show results based on an elastic model, while the second row (c) and (d) show results with the addition of random material properties. The bottom row of graphs (e) and (f) show results based on the damage plasticity model.

The data shows almost identical graphs for damage at the FB-FB keyways and FB-IB keyways. Additionally, very similar results are also seen when comparing the results gathered from the elastic model and the elastic model with random material properties. Therefore, graphs (a), (b), (c), and (d) are all very similar and show almost no difference, while graphs (e) and (f) show very little difference as well.

The elastic models show damage stops in the bricks when approximately 40% of the brick is damaged. In contrast this value drops to 30% when a plasticity model is considered. The cause of the reduction in the rate of the damage can be found when contact between bricks is considered.

Table 5-3 predicts when all the brick in a given layer will be in contact with each other. The year in which this occurs is calculated based on the expansion of the bricks due to irradiation and the size of the gaps between the bricks. Upon comparing the data in table 5-4 and the graphs in Figure 5-4, a clear correlation is visible between the bricks' damage and when they interact with each other. The stresses in the bricks decreases away from keyways as more bricks come into contact with each other. Once all bricks are in contact damage reaches a maximum threshold in an elastic model. The damage plasticity model at this point shows a gradual increase in damaged elements.

Layer	1	2	3	4	5	6	7	8	9	10	11	12
Year which bricks will all interact	N/A	47	34	31	30	31	31	32	35	42	77	N/A

Table 5-3: Prediction of when bricks will be in contact
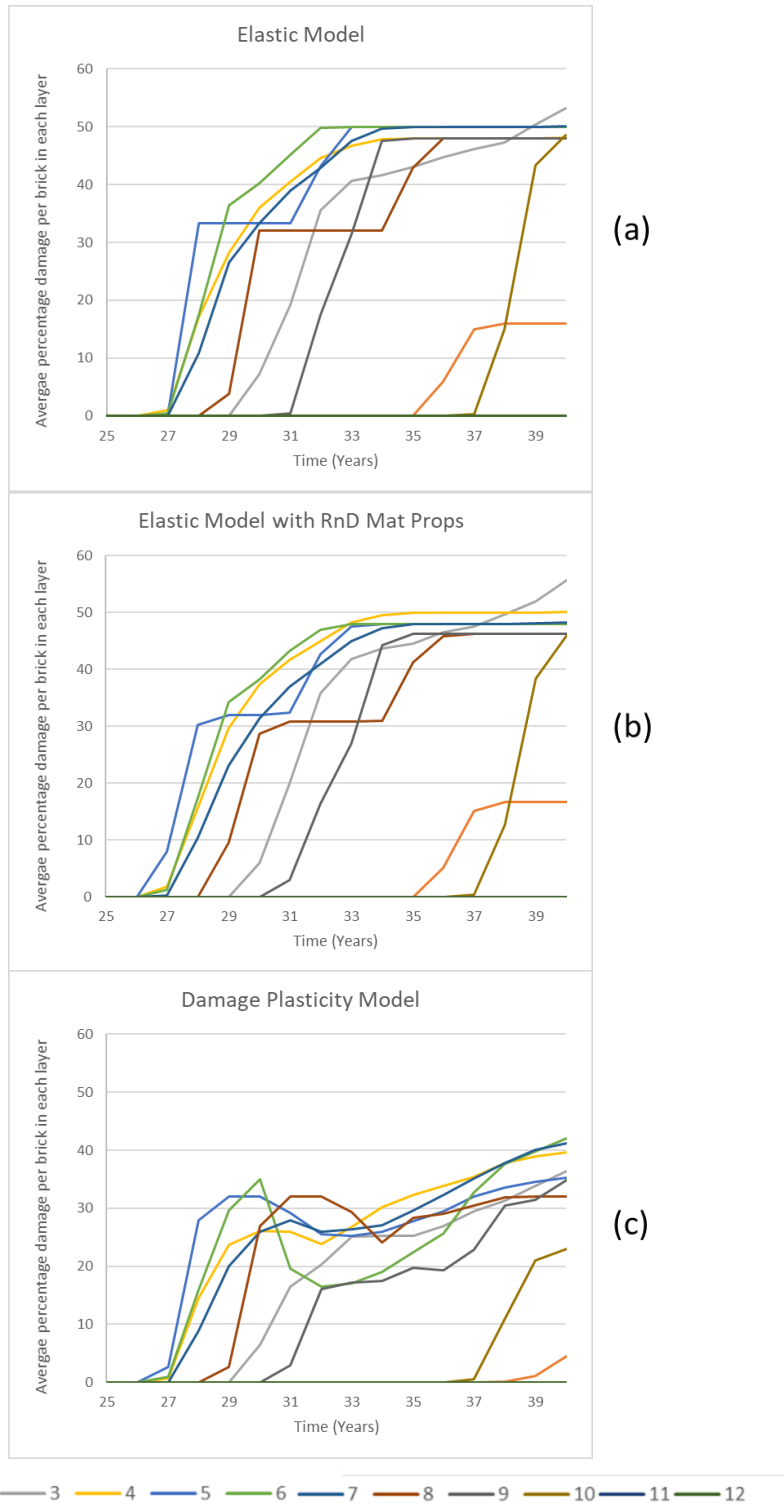
Figure 5-6:Average percentage damage outside of keyways 25 and 40 years. (a) Elastic model, (b) elastic with random modulus model, (c) damage plasticity model

Figure 5-6 shows the damage in the regions of the fuel bricks away from the keyways (y-axis) between 25 and 40 years of operation (x-axis). Once again, each layer is colour-coded and is represented individually in each graph. Graph (a) shows data from an elastic model, graph (b) includes the addition of random material properties, and (c) is based on the damage plasticity model.

Graphs (a) and (b) produce very similar results to each other, once again suggesting the addition of random material properties doesn't affect the results in a significant way. Additionally, the elastic models (a) and (b) predict a significantly larger amount of damage in comparison to the plasticity model (c). An elastic model predicts approximately 50% of elements will be damaged, while with the damage plasticity model this falls to 30%.

The significance of the data in figure 5-6 however, is that graph (c) indicates a large reduction in damage, and even damage reversal, at the point in which the bricks all contact each other. This suggests that once contact between the bricks occurs the stresses in the bricks move away from the regions with no keyways and a concertation of stresses occurs at the keyways. Following this, as the stress begins to build up again at the keyways, these stresses begin to be distributed again into regions away from the keyways until a point at which damage away from keyways reaches the same value seen before contact occurred. At this point, the rate of damage in the whole brick increases simultaneously.

How much further the rate of damage increases is unclear and would require analysis beyond 40 years. However, there is a significant difference in the results when moving from elastic material properties to the addition of plasticity and damage. The different phases a brick goes through in a plasticity model is displayed in table 5-5.

Phase	What happens	Description
1	Elastic period	Stresses in brick decrease and increase based on irradiation dose. This occurs throughout the brick but no damage occurs.
2	Plastic softening	As a dosage of 180×1020 n/cm2 on the outer surfacesand 100×1020 n/cm2 on the inner surfaces is reached, damage begins at keyways and other regions
3	Brick contact occurs	Rate of damage decreases as more bricks come into conatc and no more damage occurs after full contact between all bricks in the layer occurs.
4	Stress redistribution	Damage remains uniform at keyways but disipates and builds up again in regions away from keyways until initial maximum damage value is reached
5	Damage Phase	Damage builds at high rate throughout brick as stresses build up due to irradiation and contact between the bricks.

Table 5-4: Different phases Fuel bricks go through in a damage plasticity model
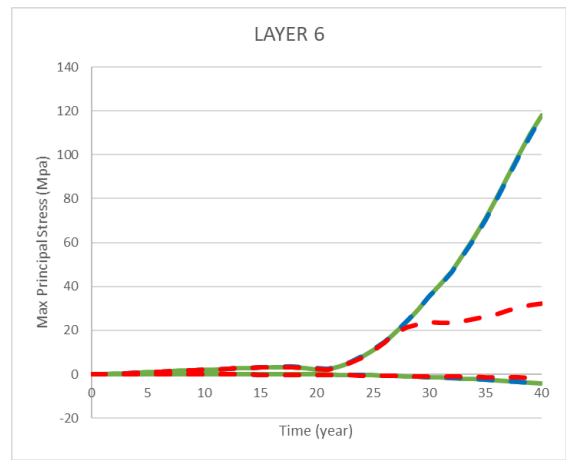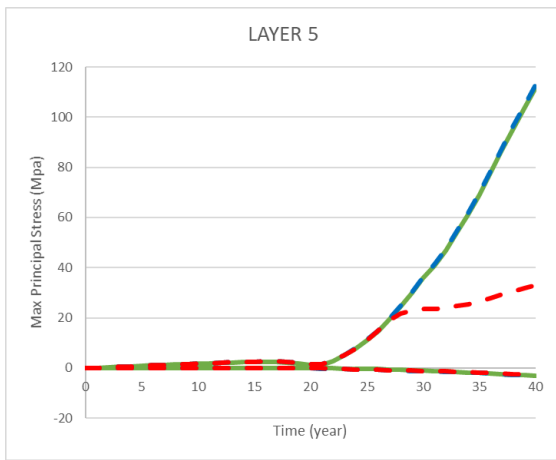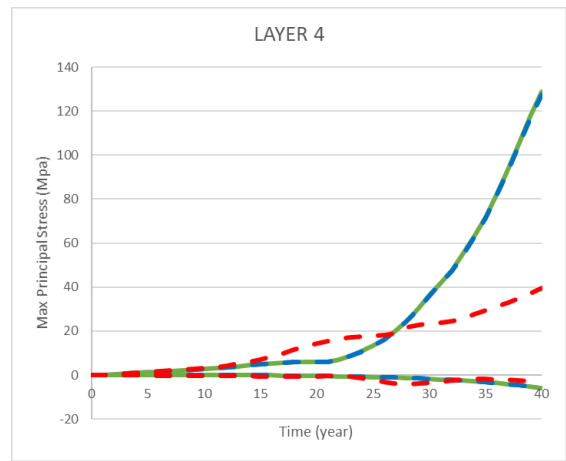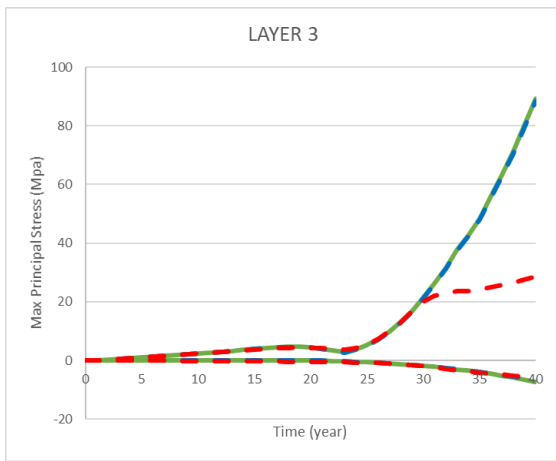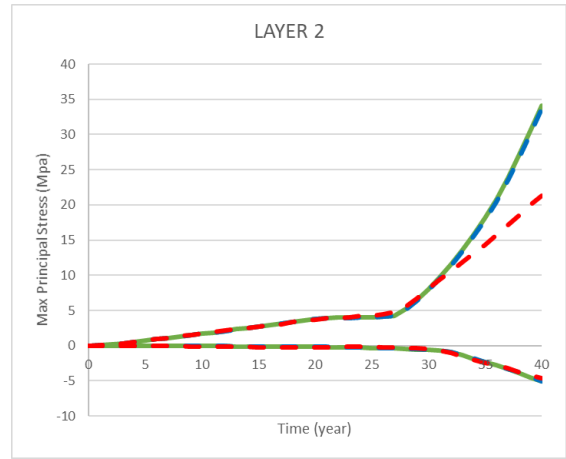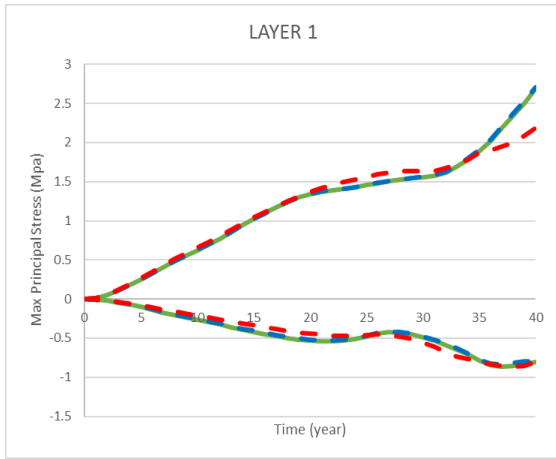
Figure 5-7: Evolution of maximum and minimum stress observed in each brick with each form of modelling. Layers 1-6
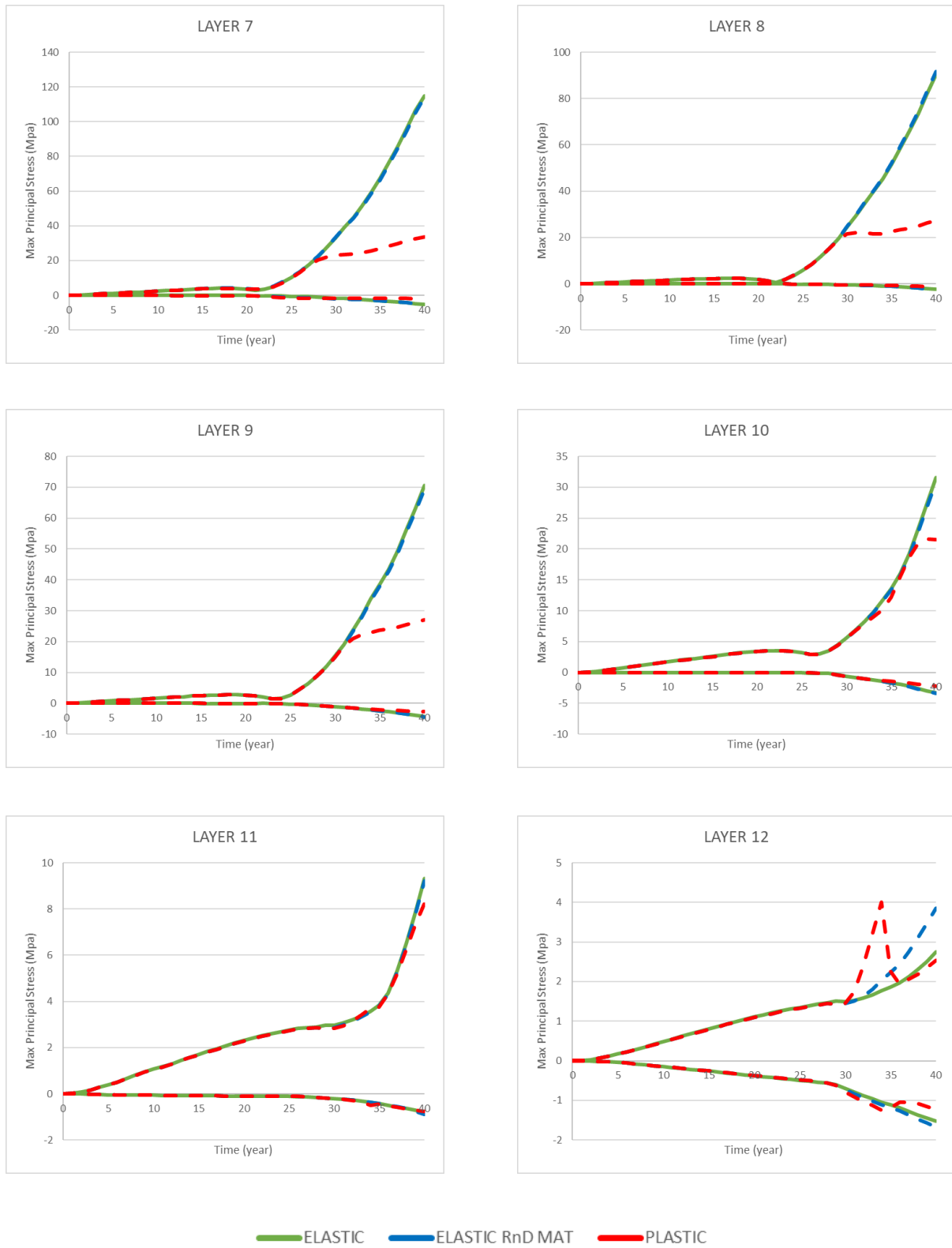
Figure 5-8:Evolution of maximum and minimum stress observed in each brick with each form of modelling. Layers 7-12

Figure 5-7 and 5-8 shows ranges of stresses in each layer of the core over time with each method of modelling investigated. Each graph shows results gathered from each layer, displaying the range of the maximum principal stress from the highest and lowest value in the fuel bricks. In the graphs, the colour green displays range of values from the elastic model, blue displays data when a variation in elasticity is added and red adds softening behaviour to the graphite bricks.

The results here display that the bricks all fail due to reaching the tensile limits of the material. The compressive limit of 20MPa was not reached in any brick throughout 40 years of service. It can be therefore assumed the bricks fracture through tensile cracking and not compressive crushing. Once again very little difference is observed when variations in material properties are applied. This is not the case when plasticity is applied. Here, the values for the stresses are identical until stress limits are reached, at this point the maximum stresses decrease as material softening takes place. However, the stresses do continue to rise gradually, and this is due to the viscous parameter used. The parameter here was set to a value of 1, however lowering this value will increase computational time, but should result in more accurate results.

The maximum stress observed in each layer corresponds to the doses the layer is receiving. The largest value of stress is observed in layers 4,5,6 and 7. These are layers which receive the highest dosage from the fuel. Once again, this strongly indicates the damage in the bricks is due to irradiation more so than anything else in the bricks. However, the stresses in layers 2 and 11 show sharp increases earlier than expected failure due to irradiation. Previous prediction suggest failure should occur at 45years, however here stresses increase towards the limit much earlier. This indicates stresses are transferring between layers of bricks, suggesting full-scale models with multiple layers is vital to creating realistic life-time models of the core.

The rate of increase of the stresses in each layer rises once contact between bricks occurs. This correlates with results in figure 5-5 and 5-6, indicating an increase in the damage following contact between bricks, leading to an overall reduction in the age of the core.

Previous modelling of the core has not accounted for contact between bricks, deformations of the bricks, and the evolution of stresses in the bricks, therefore this method of modelling is a much-needed step forwards in full-scale modelling of the core.

5.1.3 Alignment of the channels
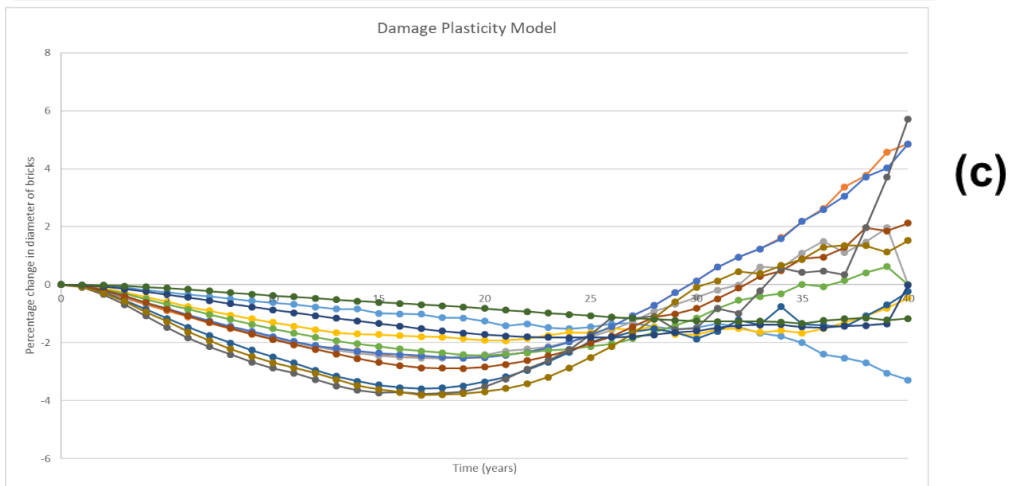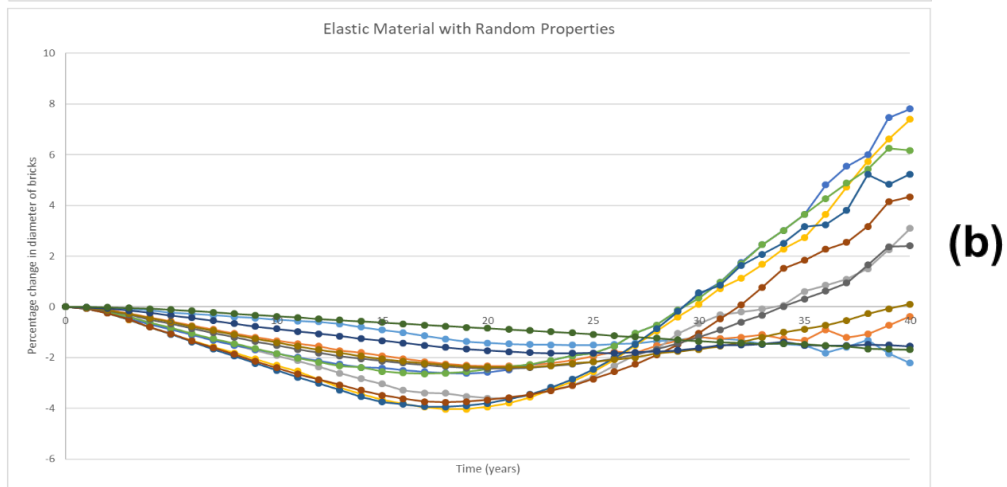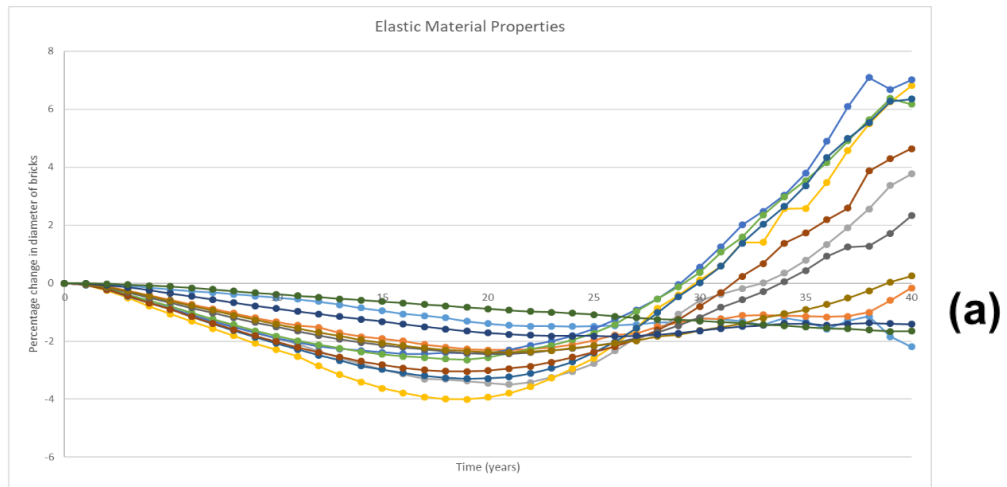
Figure 5-9:Change in the diameter of the bricks in each layer. (a) shows an Elastic model, (b) shows an elastic model with randomisation of material properties, and (c) shows a damage plasticity model.

Figure 5-9 displays three graphs showing how the internal diameter of the bricks change as a percentage (y-axis) over 40 years (x-axis) due to irradiation. Graph (a) shows results gathered from a model with elastic material properties, graph (b) includes the addition of random material properties, and graph (c) shows data gathered from a model with damage plasticity included. Each graph shows the diameter of the bricks in each layer, with each layer being colour-coded. A key is included to show which layer corresponds to which line in the graph.

All three graphs show how the diameters decrease due to irradiation and increase again as the dosage increases, eventually passing the initial diameter of the brick. This indicates that the diameter of the bricks has a direct correlation to the irradiation dose that each layer of bricks receives. However, each layer's diameter does not seem to be only influenced by the dose but also by contact with other bricks. Table 5-4 predicts the year in which different layers of brick are entirely in contact with each other.

As the bricks come into contact, an elastic model predicts the internal diameters of the bricks will continue to increase at the same rate they were already increasing due to irradiation. However, the plasticity model suggests that when bricks come into contact, the internal diameters of the bricks do not increase at the same rate. This suggests the elastic model predicts contact between bricks to not affect the internal diameter of the bricks. In contrast, damage due to material softening reduces the rate by which the bricks were expanding, and reduces the maximum diameter of the channels.

This is significant as the diameter of the brick has a direct influence on whether the channels are aligned enough to allow for fuel assemblies to pass through, as seen with equations 4.1 and 4.3. A reduced diameter increases the possibility of a blockage occurring in the channels.
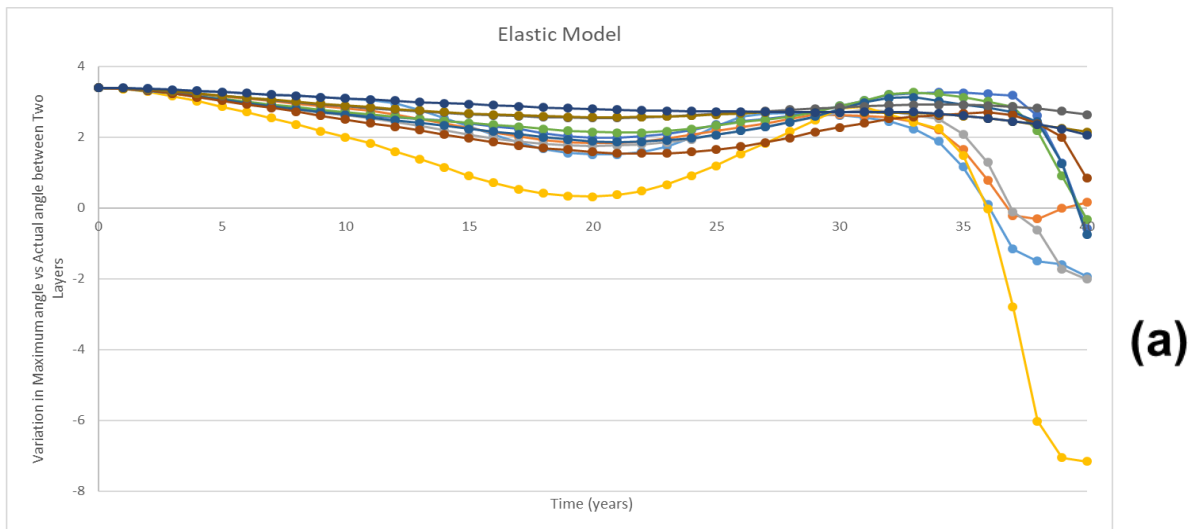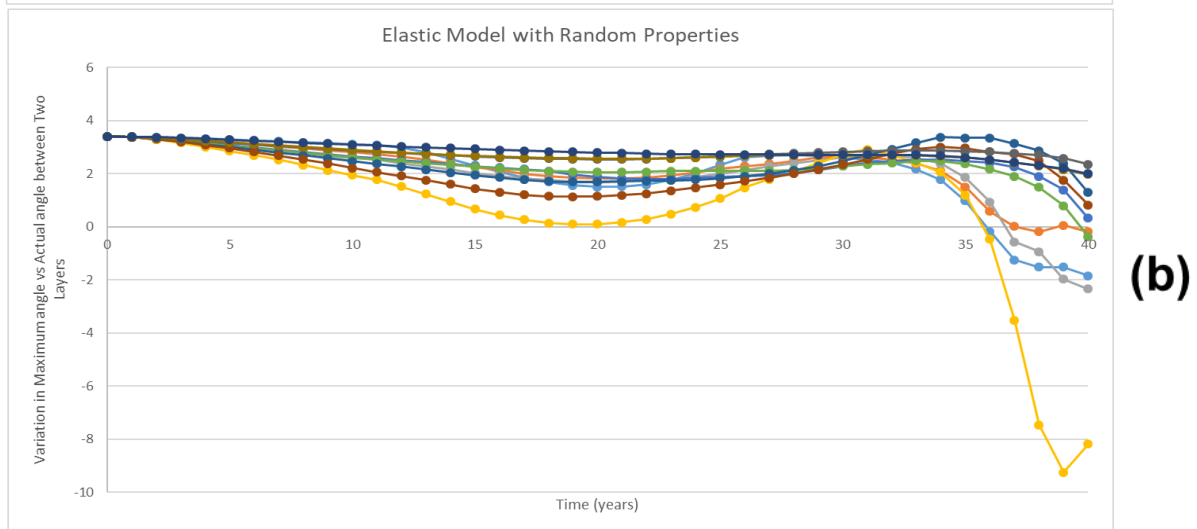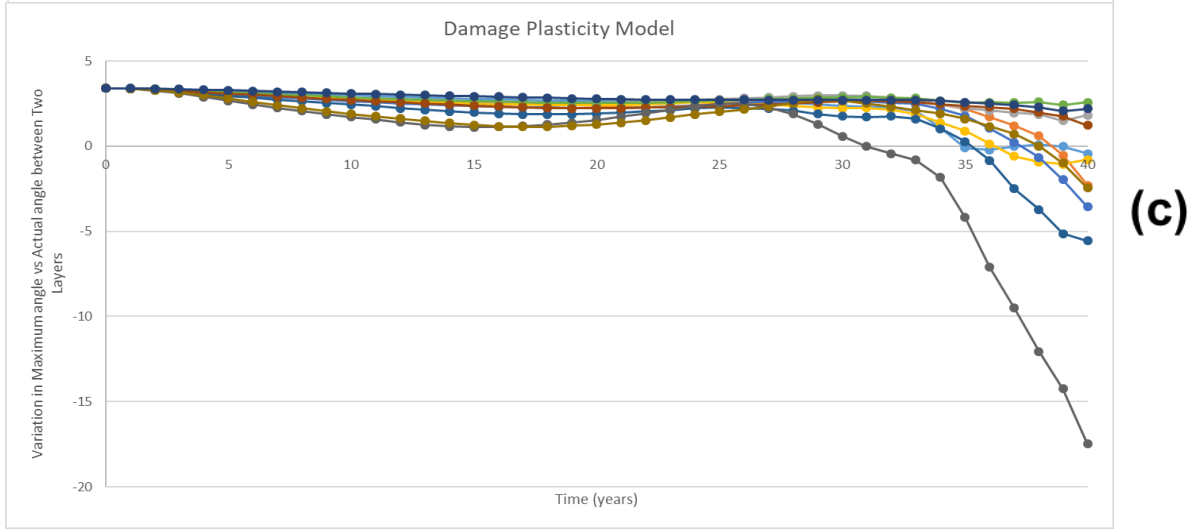
Figure 5-10:Safe alignment of each layer of bricks. a negative value indicates that the channel is not safe for the insertion or removal of the fuel assemblies. (a) elastic model, (b) elastic model with random material properties, (c) damage plasticity model.

Figure 5-10 displays a series of graphs showing how the alignment of channels changes over time. This value is calculated by subtracting the calculated values for equation 4.4 from equation 4.1. Each line in the graphs shows if it's possible for a brick to pass through 2 bricks on two separate layers, as displayed in the colour-coded key. If the line drops below zero, then a fuel assembly cannot pass through the bricks of that layer. Graph (a) shows results based on a model with elastic properties, with graph (b) adding random material properties. Graph (c) adds damage plasticity properties to the graphite bricks in the model.

As the maximum angle possible between bricks is greatly dependant on the diameter of the bricks, the graph follows a similar trend to that shown in graphs in figure 5-7. The possibility of a blockage occurring increases as the diameter decreases, and then the reverse is true as the bricks expand again due to the irradiation of the brick. After 30 years of service, a sudden drop is shown, even though the diameters of the brick continue to expand. This sudden drop will as a result of bricks rotating too far on top of each other.

This sudden possibility of blockage coincides with the point where the bricks come into contact within each layer, as the bricks move into phase 3, as shown in figure 4-5. At this phase, the middle layer bricks are expanding at a faster rate than the upper and lower layers of bricks, causing large differences in the angles between bricks in two separate layers. It could have been assumed that contact between the bricks and the outer wall would have stopped the bricks rotating further, but this is not the case, and the possibility of blockage occurring becomes very high.

The model with elastic material properties suggests the safety of the core becomes compromised after 35 years of service, with multiple layers falling below zero. By 40 years of service, 6 layers are below the line, signifying the damage and deformation of the bricks results in the core no longer being fit for purpose.

The addition of random material properties indicates a possible early failure. Due to how close the line trends towards zero, there is a large possibility of blockage at 20 years of service. Although the line doesn't go below zero at this point, it trends very close,

suggesting more extreme variations in material properties could conclude in a blockage occurring at 20 years of service.

The addition of plasticity sees a specific layer of the brick, layer 9-10, fall below the zero at 30 years. This is 5 years earlier than other layers. When these two layers are analysed, it is clear that at 30 years of service, layer 9 is beginning to expand, while layer 10 is still shrinking due to irradiation. This difference could be creating large variations in the angles of the bricks, increasing the possibility of a blockage occurring much earlier than other layers.

It is important to note that the results in Figure 5-8 are collected by considering the minimum diameter observed in any brick within each later, while the maximum angle was chosen based on the highest value seen between any 2 bricks in the layer. Consequently, the results cannot be used to guarantee blockage, but only indicate that there is a possibility of failure. This is seen as acceptable as the variation in the diameter in each layer is very small.

5.1.4 Modelling approaches used

Throughout all the findings from the small models, it has been clear that there is not a significant difference in the results gathered using a model with elastic material properties and one where random material properties are included. However, a significant difference was observed in the run times, with the addition of random material properties resulting in a 30% increase in computational run time. These results show that the additional computing power required for the creation of random material properties was unnecessary. If uniform material properties were used between all the graphite bricks, it can be assumed the results gathered have a ±10% variation. This will provide similar results without the additional computational power.

A more considerable increase of 103% run time was seen when running a model with damage plasticity included. While this is a significant increase, the change in results is also

significant. The addition of damage plasticity is seen as worth the additional computational power, due to the increase in the reliability of the results generated.

Complete run times for all three approaches are shown in table 5-5. The table shows the wall-clock time, which shows the elapsed time between the start of the process the end. Included in the table is User-CPU times and System-CPU times which show the amount of time spent in user code and the amount of time spent in operating systems code. All Units are in seconds.

Model Material Properties	Wall clock time			CPU time			User time		
	L 1-5	L 5-9	L 8-12	L 1-5	L 5-9	L 8-12	L 1-5	L 5-9	L 8-12
Linear Elastic	2888	2224	1572	2886	2222	1546	2823	2173.8	1547
Linear Elastic (Rnd Mat)	4176	2878	2310	3762	2876.6	2034	3690	2835.5	1993
Damaeg Plasticity	5533	5065	2936	5532	5062	2935	5434	4979	2878

Table 5-5: Run times (seconds) for the small model

The extra computational power required to apply random materials is better used refining the mesh. The addition of random materials does not improve results as much as a refined mesh would. While plasticity requires significantly more computational power, the differences observed going from linear to plasticity model are significant, and the additional computational power is deemed necessary.

It is also worth noting that similar tests of max stress and the possibility of blockage in channels holding the control rods were conducted on the interstitial and filler interstitial bricks. The results indicated no damage in the bricks throughout a 40-year life cycle, and also indicated the channels are unlikely to become jammed. This is as contact between fuel bricks and other bricks do not occur within the 40 years of operation tested here.

Therefore, to improve computational time, removing all bricks other than fuel bricks from the field output would significantly improve run time and reduce the size of the output file. These results cannot be viewed as fully reliable as no irradiation load was applied to these bricks, and from results gathered when considering the fuel bricks, it is clear that

the major contributor to a bricks damage is the irradiation load applied to the bricks and not contact between bricks.

Analysis on the small model, has produced the following findings:

- All models show damage initiation to occur after 25 years and is caused due to stress reversal in the bricks due to irradiation.
- Contact between bricks pauses damage in the bricks, and results in reversal of damage in areas away from keyways. More damage occurs as stresses increase again due to additional irradiation.
- Bricks will fail due to reaching tensile limit of graphite and not the compressive limits.
- Channel alignment is compromised after 35 years of service; however, this can occur sooner in a plasticity model.
- The most realistic form of modelling damage would be to include some form material softening behaviour. While computationally demanding, the improvement in data gathered is significant.
- The addition of variation in elastic properties will result in increased computational power, but not essentially result in improved predictions. A more computationally effect way of modelling would be to assume a ±10% error instead.

5.2 Full-Scale model

A full-scale elastic model with elastic material properties was tested and is displayed and discussed here. Further models were prepared but were unable to run due to time constraints and the lack of computational power available at the time of writing. Also, due to computational limitations, the time scale for analysis was reduced from 40 years, as seen with the small model, to 30 years, while the number of data points was reduced from one every year to one ever 2 years.

5.2.1 Percentage of bricks damaged
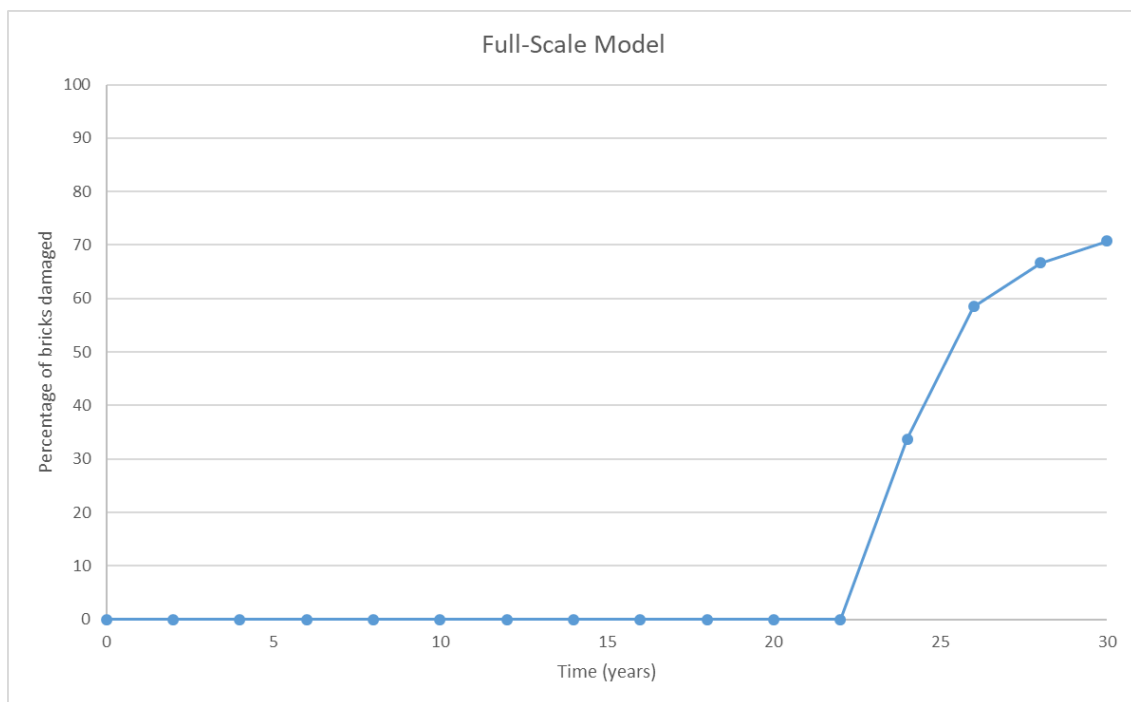
Figure 5-11: Percentage of damaged brick in a full-scale model

Figure 5-11 shows how many bricks have fractured in a full-scale model over 30 years. This includes bricks were the maximum stress in any element in the brick surpasses the tensile limit of the brick. Assuming the brick to be brittle, at this value, we can predict a fracture will occur.

As previously discussed, the cause of failure in the bricks is due mainly to the radiation of the bricks, and contact between the bricks has little to no effect on bricks initially becoming damaged. Consequently, the full-scale elastic model produced very similar results to that of the small model elastic model when predicting how many bricks would be damaged. The full-scale model predicts initial failure to occur at year 24 with over 70% of bricks seeing some form of damage after 30 years of service.

While a plasticity-based model could not be investigated, it is clear from the small model that initial failure of bricks would not be greatly affected by the material softening properties.
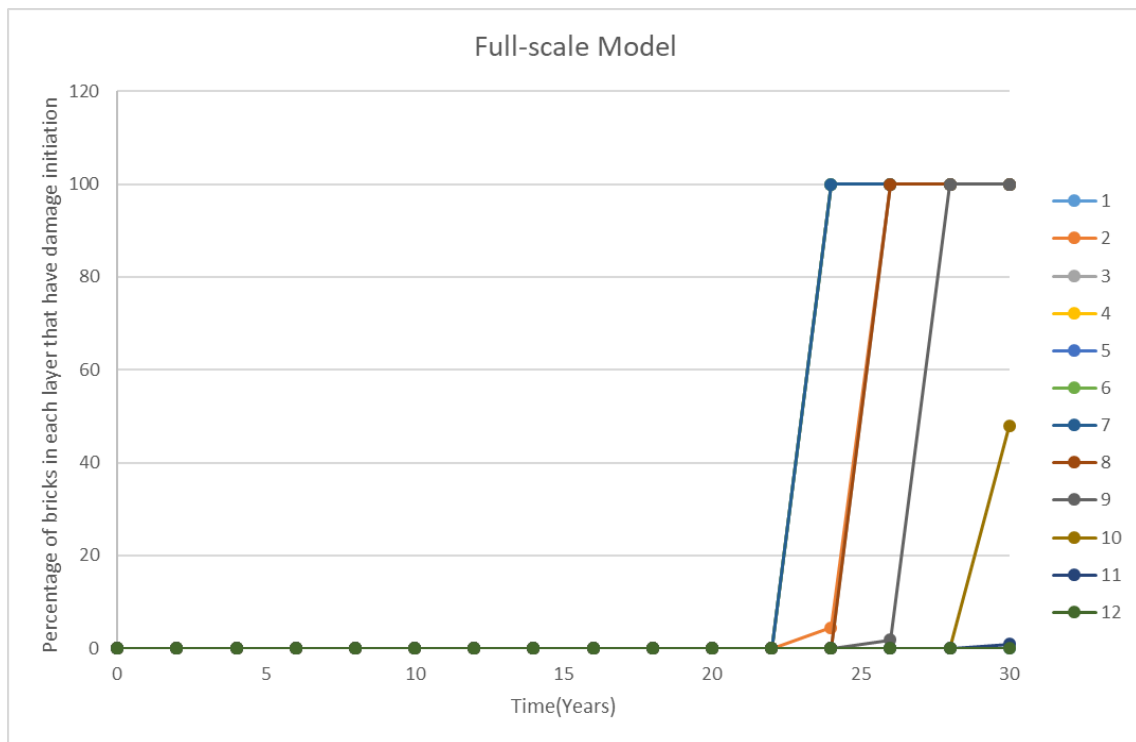
Figure 5-12: Percentage of bricks damaged full scale considering each layer individually

Figure 5-12 shows the percentage of bricks that would be damaged (y-axis) in each layer of brick in a full model over 30 years (x-axis). Each layer is colour coded with a key included.

When considering individual layers, layers 4, 5, 6 and 7 are predicted to fail first at 24 years, with layers 2, 3 and 8 at 26 years and layers 9 and 10 follows at 28 and 30 years

respectively. Previous research suggested layer 6 would fail anywhere between 24 and 35 years as seen in figure 2-17 graph and these results are within that range giving confidence to the reliability of the results collected.

These results are similar to the smaller models tested previously, but do see some layer failing sooner. This is most likely due to the increased gravitational forces on the bricks causing earlier failure.

5.2.2 Evolution of damage
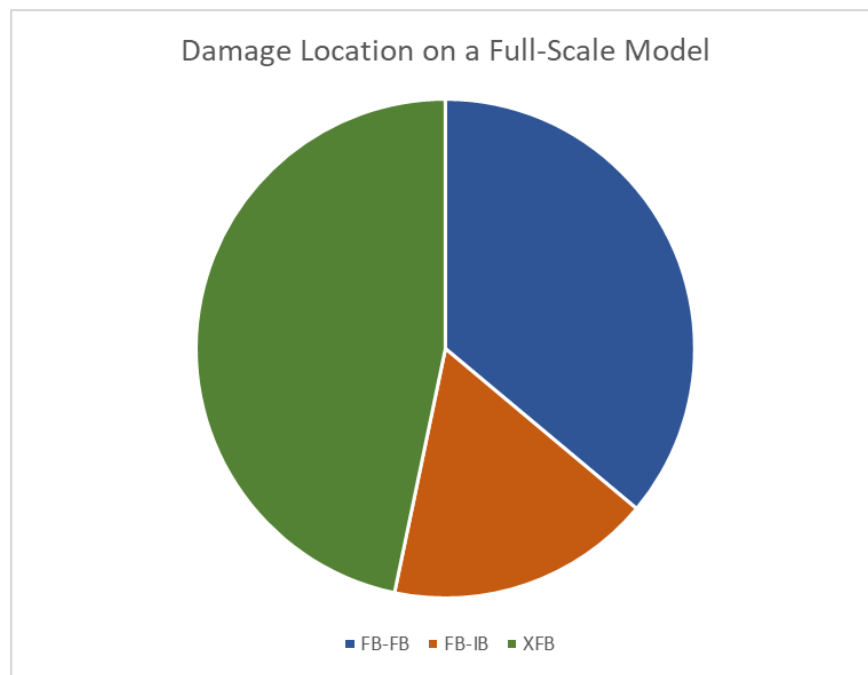
Figure 5-13: Location of damage initiation when considering a full-scale model

The pie chart in figure 5-13 shows which region failure is likely to initiate. Each region is colour coded, with blue and orange indicating the fuel brick and interstitial brick keyways, while the green region indicates at regions away from the keyways. The region is selected based on the location of the element where the maximum stress was observed at the point of failure.

The figure displays some large differences to that seen in the elastic model in figure 5.3. The pie chart suggests a larger percentage of damage initiates at the regions with no

keyway. This could be down to the additional gravitational forces having a larger effect on these regions of the bricks. However, as previously discussed, this result is highly dependent on the mesh, and a more refined mesh should see damage initiating at the keyways.
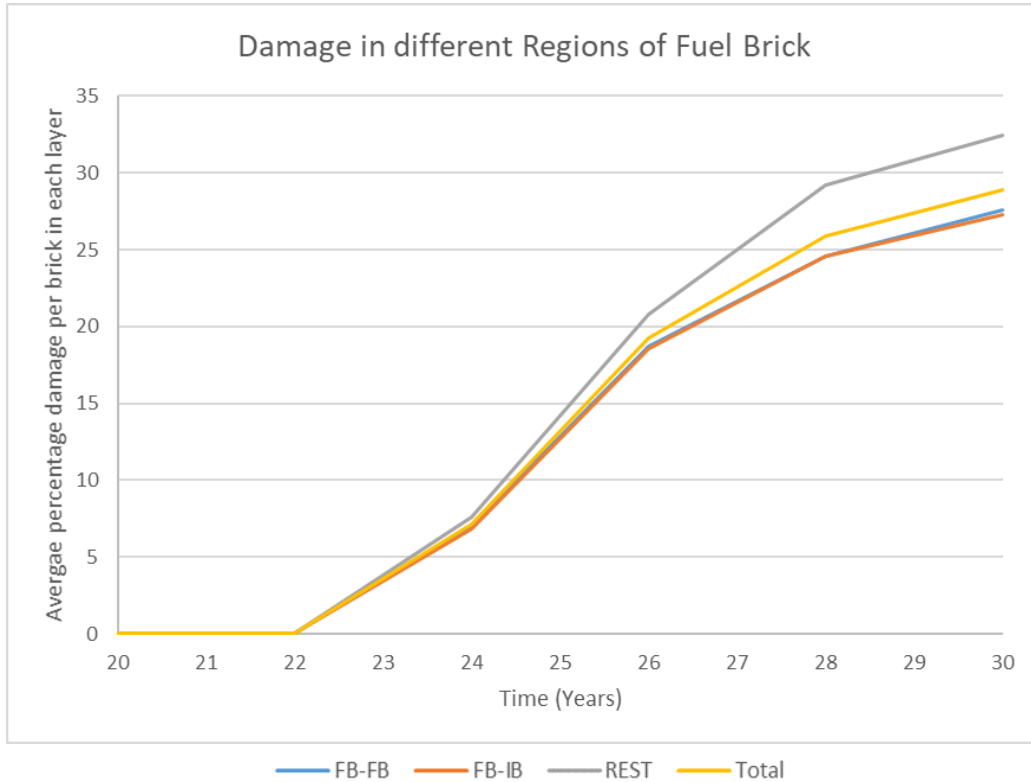
Figure 5-14:Percentage of damaged elements in an entire model

Figure 5-14 shows the percentage damage seen in different regions of the bricks (y-axis) over a 30-year time period (x-axis). The different regions are shown via a colour coded line, with blue shown damage in fuel brick to fuel brick keyways, orange showing damage in fuel brick to interstitial brick regions and grey showing the regions away from the keyways. In addition, a yellow line shows data based on the whole brick together.

While figure 5-13 showed large variation with the same results gathered from the small model, results shown in figure-12 are almost identical to those created using the smaller model shown in figure 5-4(a). The smaller model predicted approximately 35% damage in all the bricks by 30 years. This is slightly lower in a full-scale mode with only 28% observed here.

This indicates that while bricks are damaging earlier as shown in figure 5-11, the amount of damage is lower than that observed in the smaller model. For improved analysis the model would need to be investigated beyond 30-years.
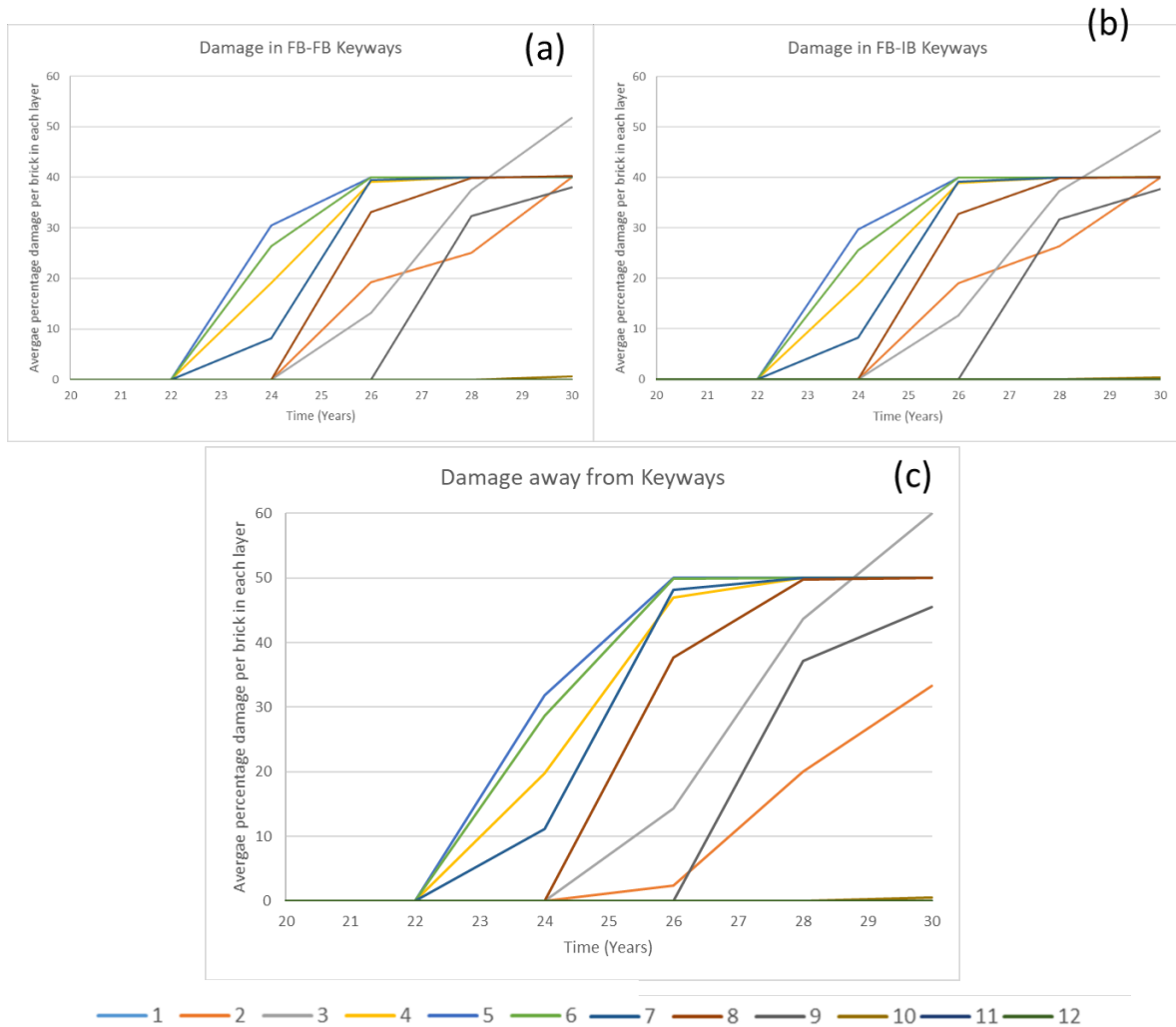
Figure 5-15:Average percentage damage in fuel brick (a) FB-FB keyways (b) FB-IB Keyways, (c) Away from keyways

Figure 5-15 percentage damage in the bricks specific to each region of the brick over a 30-year period. Graph (a) shows damage in the fuel brick keyways, (b) shows damage at the interstitial brick keyways while (c) shows damage away from keyways. Each graph shows the damage based on each layer of the core, with each layer colour coded based on a key shown in the figure.

The data once again is very similar to figure 5-5 (a), (b) and 5-6(a) which all display the damage on a model with elastic material properties similar to the full-scale model. The damage in the FB-FB and FB-IB keyways is once again very similar and seemed to max out at 40% whereas the damage for the rest of the brick increased to 50%. The results indicate there is no difference between damage at the fuel brick- keyways and the interstitial brick keyways and all keyways can be modelled together.

Comparing individual layers gives a very different result to the small model. In the small model, layers 2 and 9 at 30 years experienced no damage in any region, however the full-scale model indicated up to 40% of the Fuel brick would be damaged on average in the bricks in layer 2. A similar case was seen with every layer indicating that the full-scale model will predict failure to occur significantly earlier than the smaller model, however the level of damage in the bricks remains the same once the maximum level is reached. This is most likely due to the boundary conditions and the additional gravitational forces present in the full-scale model.

In all models, layer 3 experienced a sudden increase in damage compared to the other layers of bricks. This sudden increased occurred earlier in the full-scale model. As the same phenomena is seen in both the small and large model, it can be predicted that cause is not related to boundary or gravitational loads.

This sudden increase in damage of bricks in layer 3 is occurring at the same time the bricks in layer 3 begin to expand beyond their original size. At the same time stress reversal has just begun in the inner surface of layer 2 while layer 4 is expanding at a faster rate. This difference of stresses between 3 layers seems to cause more damage in the bricks in layer 3. This is clearer when the damage in layer 2 is compared, as the rate of damage in layer 2 decreases, at the same time damage in layer 3 begins to increase. This suggest the stresses in layer 2 are redistributed down the channel into layer 3 causing it to fail earlier, and to undergo more damage than any other brick. This was not observed in a smaller model.

This predicts that stresses can be redistributed down the channels if large differences exist between different layers of bricks.

5.2.3 Alignment of the channels
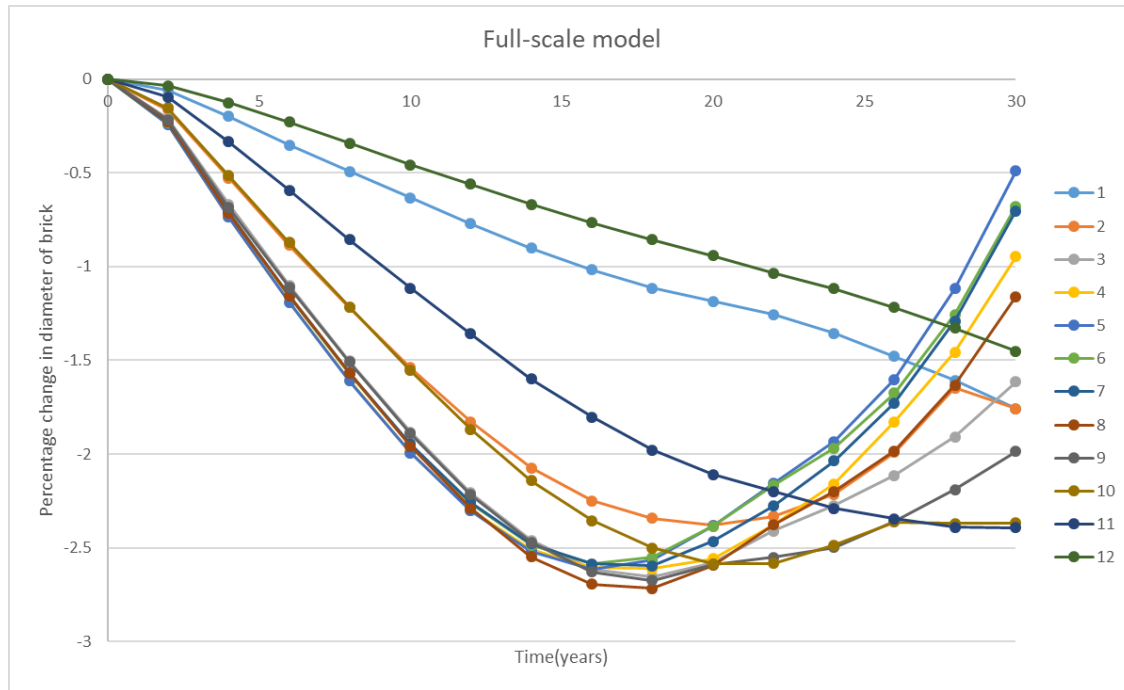
Figure 5-16: Alignment of channel graphs (a) how diameter of bricks changes and (b) Maximum angle based on diameter - actual angle

Figure 5-16 shows how the diameters of each layer changes over the course of 30 years. Each layer is colour coded using key present in the figure.

The pattern here follows the dosage each brick receives. This follows a very similar pattern to the smaller elastic models. Comparing figure 5-9 (a) with figure 5-16 (b) shows the alignment is also following a similar pattern up to 30 years. The smaller model shows a sudden drop after contacts occurs between brick starting at year 31, this was not possible to analyse on a full-scale model due to computational limitations at the time of writing.

What is different in the full-scale models that bricks in the lower channels underwent further deformations which resulted in a smaller diameter of 30 years. This again implies

that gravitational forces have a profound effect on the bricks and how much they deform over time, and will greatly affect the life of the reactor.
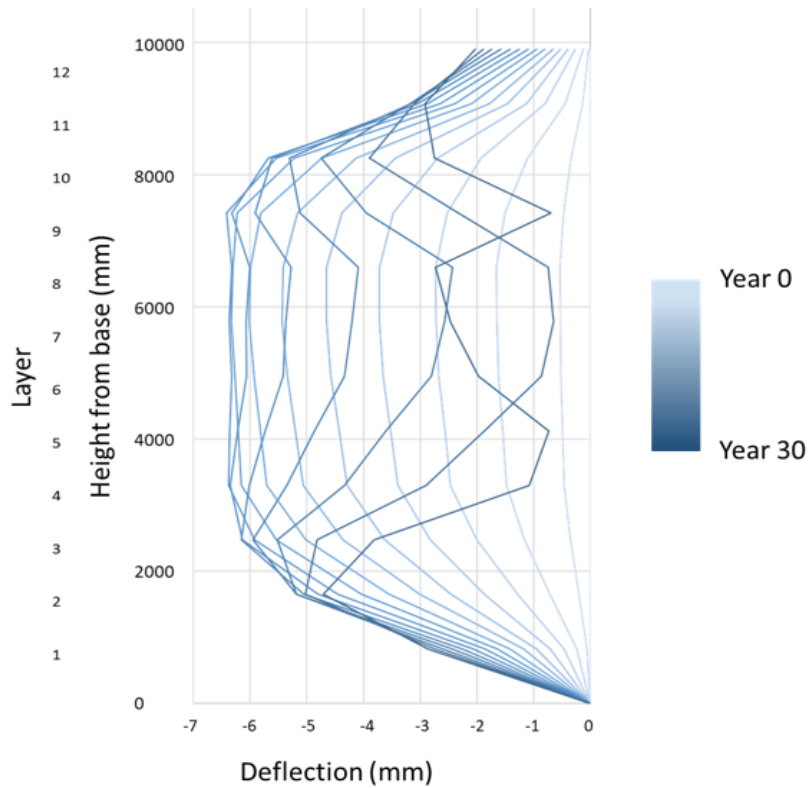
Figure 5-17: Profile of core over time

Figure 5-17 shows the profile of the core, and how it evolves over time. As the bricks shrink it is clear the core as a whole shrinks a total of 7 mm, before the middle channels begin expanding again due to the expansion on the bricks. As the channels begin expanding, the angles between different layers also changes significantly, increasing the potential for a blockage to occur in channels.

Figure 5-18 displays the potential for blockage to occur based on the diameters of the bricks and the angles of the bricks between 2 layers. This value is calculated using equations 4.1 and 4.4, where a value of less than zero indicates a blockage can occur.

The full-scale model is only considering a 30-year time period, and as seen with the smaller model blockages are not expected to occur until 35 years of service, therefore, no blockages occur according to data shown in figure 5-18. However, the small model in figure 5-10(a) displayed a downward trend towards blockage after 33 years of service. The full-scale model sees a downward trend much sooner at 28 years, indicating failure could occur much sooner than expected with the smaller model. This is most likely due to the additional gravitational forces affecting the diameters of the bricks seeing the lower layers of bricks shrink more so than upper layers of bricks.
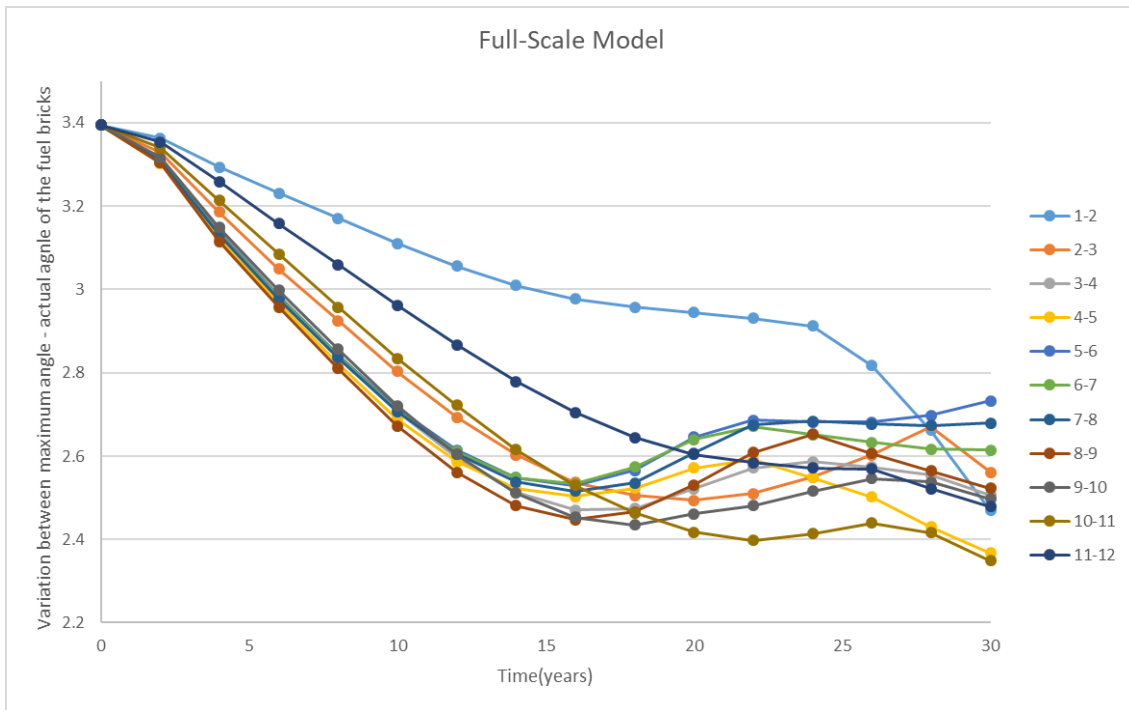
Figure 5-18: Alignment of the channels over 30-years

6 Conclusions

There are currently 14 AGRs in operation in the UK, with closure planned for most over the next decade. Delays to the operation time of new reactors mean that plant life extension may be required going forward. One of the life-limiting components of the reactor is its graphite moderator, which acts both as a moderator to ensure the nuclear reaction remains stable, and as a significant structural component.

Up to now, studies performed on the reactor have not been able to realistically model the whole reactor. Smaller scale modelling been performed by considering only one layer of bricks or single bricks. Due to a large number of bricks present in the core, past research into large-scale modelling has taken place on models with rigid-body bricks connected by spring elements representing the keys. In such cases, all mechanical effects are assigned to the springs: stiffness, friction, damping, and damage/failure. While the approach allows for calculating load transmission or impacts between the bricks, it has a major limitation deformation, damage and fracture of the bricks has not been analysed.

This project aimed to develop a method for modelling a full-scale model of the core and apply lifetime dimensional changes on the brick, discovering at what time the integrity of the core becomes compromised.

The creation of a realistic whole-scale model of an AGRs moderator is of significant industrial importance. The complexity of developing such a model lies with a large number of graphite bricks in the model and the interactions between them. In order to overcome this issue, Python scripting was employed alongside ABAQUS to develop a realistic model. To overcome computational limitations, multiple simplifications were made. The dimensions, material properties, interactions, and boundaries conditions were simplified where possible without significantly affecting either the reliability of the results or increasing the computational power required.

Initially, a small model was created, where two primary investigations were performed. First, how variations of elastic material properties in the bricks affected the overall results

gathered. Subsequently, how plasticity affected the results. The following conclusions were made from the small model analysis:

- The primary cause of fracture of fuel bricks is due to irradiation damage, with Fuel bricks fracturing once a dose of 180×10^{20} n/cm^2 is absorbed in the inner surface of a brick, and a dose of over 100×10^{20} n/cm^2 is absorbed in the outer surface of a brick. At this outer dosage, stress reversal is occurring in the bricks.
- The brick is most likely to fail at the keyways first, with this more prominently visible when a finer mesh is employed.
- The addition of damage plasticity will result in 20% less damage in the fuel bricks than purely elastic material properties.
- Tensile cracking the method by which the bricks will fail and not compressive crushing.
- Contact between bricks causes stresses to move into keyways and away from regions with no keyways.
- After contact between bricks, stresses slowly build up again at the regions away from the keyways resulting in a second wave of damage to occur as seen in the plasticity model.
- Contact between bricks causes rotations between the bricks that results in the alignment of the channels becoming compromised. Modelling suggests a blockage could occur at 35 years.
- The addition of random material properties does not yield improved data, and is not deemed beneficial due the addition computation power required.
- The addition of damage plasticity material properties provides profound changes in the amount of damage seen and will impact the life expectancy of the reactor.

A full-scale elastic model was then developed, which provided more insight into the age and damage in the reactor. The full-scale model provided the following:

- Full-scale analysis predicts initial damage in the bricks at 24 years, 4 years sooner than predicted by the small model.

- Stress distribution is seen between layers which results in more damage being observed in layer 3 of the core.
- Increased damage is seen in lower layers due to gravitational forces, with diameters of lower layers of bricks shrinking further than the upper layers of bricks
- Earlier alignment problems could exist but require further analysis beyond the 30 years carried out here.

Validation of such a model is not possible due to difficulties in creating an experimental rig showing the long-term gradual effects of irradiation on the core. Past numerical modelling and analysis of the core has shown similarities with crack initiation in the core, but damage evolution and channel alignment cannot be validated. Comparison to real core observations again show similarities with modelling indicating cracked bricks would exist at the time they were observed in the core. Beyond this, validation of the results is not possible.

While a full-scale model of the core was tested and investigated here, due to the lack of computational facilities available, only 30 years were analysed, with only elastic material properties being applied. While a full-scale model was developed, it is clear from the smaller model that material softening behaviour must be included as findings indicate damage properties will have a significant impact on the predictions made based on the model. The full-scale model currently predicts the reactors are safe to continue to operate after 30 years of operation. With the addition of damage properties, it will be possible to investigate how damaged bricks influence the surrounding bricks and the integrity of the entire matrix of bricks. Ultimately, assessments of the whole core fitness-for-service will be made with higher confidence.

7 Future work

The methodology presented here for modelling a full-scale representation of a graphite moderated core is a major improvement on what has been previously modelled in the past. While it is clear through the work that improvements in the computational power allows for more accurate representation of results, the validity of these result will always remain a concern. To overcome this problem further funding and research would be required, with the creation of a scale experimental rig with life time changes being applied

In addition, to further validate the models here, more detailed observations of the core would be necessary. Up to now limited channels have been observed, however observation of all channels would provide vital information on how the gradual effects of irradiation effect the core, and will bring confidence to any model can replicate the damage observed.

ONR assessment considers many factors, not all of which were considered with the analysis that was detailed in this report. The addition of single and double crack bricks will provide more information regarding the safety of the reactor to remain operational beyond current closure dates. In addition, the effects of oxidation and weight loss would also be of vital importance. The graphite will undergo weight loss due to oxidation, as discussed in chapter 2.2.5, which results in density changes in the graphite as well. The analysis in this report assumed the density of the graphite remains constant throughout analysis.

By performing experiments on nuclear graphite, a clearer understanding of how irradiation affects the weight loss and dimensional changed beyond 30-years can be achieved. The findings of such experiments can then be applied to the model, which would result in significant changes to the estimated life expectancy of the core.

With every step taken more confidence can be found with the results achieved.

8   References

Ahmed, K. M., Parker, J. V. & Proffitt, D. E., 1985. *SEISMIC RESPONSE OF THE ADVANCED GAS COOLED REACTOR CORE ,* Amsterdam: Elsevier Science.

ALDAMA, D. L. & GUAL , M. R., n.d. *DETERMINATION OF THE CONTROL ROD WORTH FOR RESEARCH REACTORS,* La Habana: Nuclear Technology Center, Nuclear Energy Agency.

Arai, T., 1993. *An analytical study of porosity changes of nuclear graphites under high temperature irradiations,* Ibaraki: Department of high temperature engineering.

Becker, T. & Marrow, J., 2013. *Modelling Damage in Nuclear Graphite.* Beijing, 2013.

Blackman, L. C. F., 1970. *Modern Aspects of Graphite Technology,* London and New York: Academic Press.

Bodel, W., 2012. *THE RELATIONSHIP BETWEEN MICROSTRUCTURE AND YOUNG'S MODULUS OF NUCLEAR GRAPHITE,* Manchester: University Of Manchester .

Bradford, M. R., 2005. *An Overview of British Energy's Graphite Core Assessment Methodology,* Cambridge: The Royal Society of Chemistry.

British Energy, 2006. *How an AGR power station works ,* s.l.: British Energy Group plc .

Brocklehurst, J. E. & Kelly, B. T., 1993. The dimensional changes of highly-oriented pyrolytic graphite irradiated with fast neutrons at 430C to 600C. *Carbon,* 31(1), pp. 179-183.

Demir, A. et al., 2018. EFFECT OF VISCOSITY PARAMETER ON THE NUMERICAL SIMULATION OF REINFORCED CONCRETE DEEP BEAM BEHAVIOR. *The Online Journal of Science and Technology,* 8(3), pp. 50-56.

Devenport, W., Kapania, R., Rojiani, , K. & Li, J., n.d. *Mohr's Circle for 2-D Stress Analysis.*
[Online]
Available at: http://www.engapplets.vt.edu/Mohr/java/nsfapplets/MohrCircles2-3D/Theory/theory.htm
[Accessed 1 March 2020].

Dhondt, G., 2002. *Eight-node brick element with reduced integration (C3D8R and F3D8R).*
[Online]
Available at: http://web.mit.edu/calculix_v2.7/CalculiX/ccx_2.7/doc/ccx/node27.html
[Accessed 4 Dec 2019].

Duncan, B. & Kralj, B., 2007. *Seismic Modelling of an AGR Nuclear Reactor Core.* Bristol, Atkins.

EDF, n.d. *Graphite blocks in nuclear power stations.* [Online]
Available at: https://www.edfenergy.com/about/nuclear/graphite-core
[Accessed 29 December 2020].

Elcoate, C. D. & Payne, J. F. B., 2001. *Pile Grade A Graphite- Constitutive Modelling,* Bristol: Frazer-Nash Consultancy Limited.

Flaig, J., 2019. *'Shaking table' research protects UK from earthquake-triggered nuclear disaster.* [Online]
Available at: https://www.imeche.org/news/news-article/%27shaking-table%27-research-protects-uk-from-earthquake-triggered-nuclear-disaster
[Accessed 12 2 2021].

Gramoll, K., n.d. *Maximum and Minimum Normal Stress.* [Online]
Available at: https://www.ecourses.ou.edu/cgi-bin/eBook.cgi?doc=&topic=me&chap_sec=07.2&page=theory
[Accessed 1 March 2020].

Haiyan, L., Fox, A. S. L. & Marsden, B. J., 2008. An analytical study on the irradiation-induced stresses in nuclear graphite moderator bricks. *Nuclear Materials,* 372(2-3), pp. 164-170.

Hillerborg, Modeer, A. M. & Petersson, P. E., 1976. Analysis of Crack Formation and Crack Growth in Concrete by Means of Fracture Mechanics and Finite Elements. *Cement and Concrete Research,* Volume 6, pp. 773-782.

IAEA, 2000. *Irradiation damage in graphite due to fast neutrons in fission and fusion systems,* Vienna: Nuclear Power Technology Development Section.

IAEA, 2012. *General Design and Principles of the Advanced Gas-Cooled Reactor (AGR).* [Online]
Available at:
https://nucleus.iaea.org/sites/graphiteknowledgebase/wiki/Guide_to_Graphite/General%20Design%20and%20Principles%20of%20the%20Advanced%20Gas-Cooled%20Reactor%20(AGR).aspx
[Accessed 12 1 2021].

IAEA, 2017. *Other Designs of Nuclear Power Stations.* [Online]
Available at:
https://nucleus.iaea.org/sites/graphiteknowledgebase/wiki/Guide_to_Graphite/Other%

20Designs%20of%20Nuclear%20Power%20Stations.aspx
[Accessed 23 May 2017].

IAEA, 2019. *Skip Navigation LinksGeneral Design and Principles of the Advanced Gas-Cooled Reactor (AGR).* [Online]
Available at:
https://nucleus.iaea.org/sites/graphiteknowledgebase/wiki/Guide_to_Graphite/General%20Design%20and%20Principles%20of%20the%20Advanced%20Gas-Cooled%20Reactor%20(AGR).aspx
[Accessed 4 September 2019].

International Atomic Energy Agency, 2000. *Irradiation Damage in graphite due to fast neutrons in fission and fusion systems,* Vienna: IAEA.

International Atomic Energy Agency, n.d. *Graphite Behaviour under Irradiation.* [Online]
Available at:
https://nucleus.iaea.org/sites/graphiteknowledgebase/wiki/Guide_to_Graphite/Graphite%20Behaviour%20under%20Irradiation.aspx
[Accessed 1 March 2016].

Ishihara, M. et al., 1991. An Explication of Design Data of the Graphite Structural Design Code for Core Components of High Temperature Engineering Test Reactor. *JAERI-M,* pp. 91-153.

Jimenez Pique, E., Dortmans, L. & De With, G., 2003. A model material approach to the study offracture process zone of quasi-brittle materials. *Journal of Material Science,* Volume 38, pp. 4003-4011.

Johnson, K., Hewett, S., Holt, S. & Miller, J., 2000. *Advanced Physics for You.* Cheltenham: Nelson Thornes.

Jortner, J., 1971. *Multiaxial Behavior of ATJ-S Graphite,* Santa Monica: MDDONNELL DOUGLAS ASTRONAUTICS CO-WEST .

Kane, J. et al., 2011. Microstructural characterization and pore structure analysis of nuclear graphite. *Journal of Nuclear Materials,* 415(2), pp. 189-197.

Kumar, S. & Barai, S. V., 2011. *Concrete Fractur Models and Applications.* Berlin: Springer Berlin Heidelberg.

Kyaw, S. T. et al., 2014. Modelling Crack Growth within Graphite Bricks due to Irradiation and Radiolytic Oxidation. *Procedia Materials Science,* Volume 3, pp. 39-44.

Lee, J. & Fenves, G. L., 1998. Plastic-Damage Model for Cyclic Loading of Concrete Structures. *Journal of Engineering Mechanics,* 124(8), pp. 892-900.

Liang, T., 2012. *Something about nuclear graphite.* Beijing, Nuclear Graphite Research Group.

Li, H., Fok, A. S. & Marsden, B. J., 2007. An analytical study on the irradiation-induced stresses in nuclear graphite moderator bricks. *Journal of nuclear materials,* 372(2-3), pp. 164-170.

Liu, Y. & Glass, G., 2013. Effects of Mesh Density on Finite Element Analysis. *SAE Technical Papers,* Volume 2.

Lubliner, Oliver, J., Oller, S. & Oñate, E., 1989. A Plastic-Damage Model for Concrete. *International Journal of Solids and Structures,* Volume 25, p. 299–329.

McNally, K. et al., 2017. A core-monitoring based methodology for predictions of graphite weight. *Nuclear Engineering and Design,* Volume 314, pp. 56-66.

Mantell, C. L., 1968. *Carbon and Graphite Handbook.* s.l.:Interscience Publishers.

Marrow, T. J., Joyce, M. R., Mummery, P. & Marsden, B. J., 2008. Observations of microstructure deformation and damage in nuclear graphite. *Engineering Fracture Mechanics,* 12(75), pp. 3633-3645.

Marrow, T. J. & Mostafavi, M., 2011. Quantitative in situ study of short crack propagation in polygranular graphite by digital image correlation. *Fatigue and fracture of Engineering Materials & Structures,* Volume 35, pp. 695-707.

Marsden, B. J. et al., 2008. Dimensional and material property changes to irradiated Gilsocarbon graphite irradiation between 650 and 750C. *Journal of Nuclear Materials,* Volume 381, pp. 62-67.

Marsden, B. J. et al., 2016. Dimensional change, irradiation creep and thermal/mechanical property changes in nuclear graphite. *International Materials Reviews,* 61(3), pp. 155-182.

Maruyama, T., Eto, M. & Oku, T., 1987. Elastic modulus and bend strength of a nuclear graphite at high temperature. *Carbon,* 25(6), pp. 723-726.

McLachlan, N. et al., 1996. A Probabilistic approach to assessing AGR core life. *Nuclear Energy,* 35(1), pp. 15-23.

Morrison, C. N., 2015. *Lattice-Modelling of Nuclear Graphite for Improved Understanding of Fracture Processes,* Manchester: University of Manchester.

Mummery, P., Novovic, M. & Hall, G., 2020. *Validation of Whole Core Modelling,* Manchester: ONR GRAPHITE TECHNICAL ADVISORY COMMITTEE FOR NUCLEAR PLANT.

Muncaster, R., 1993. *PHYSICS.* 4th ed. Cheltenham: Stanley Thornes Ltd.

Nonbel, E., 1996. *Description of the Advanced Gas Cooled Type of Reactor (AGR),* Roskilde: Riso National Laboratory.

Office for Nuclear Regulations, 2018. *Nuclear Safety Technical Assessment Guide,* s.l.: ONR.

Oku, T. & Eto, M., 1993. Relation between static and dynamic Young's modulus of nuclear graphites and carbon. *Nuclear engineering and design,* 143(2), pp. 239-243.

Oku, T. & Ishihara, M., 2004. Lifetime evaluation of graphite components for HTGRs. *Nuclear Engineering and Design,* Volume 227, pp. 209-217.

ONR, 2011. *Conditions on the graphite cores in nuclear reactors,* s.l.: ONR.

Poh, H. L., Simek, P., Sofer, Z. & Pumera, M., 2013. *Halogenation of graphene with chlorine, bromine, or iodine by exfoliation in a halogen atmosphere..* [Online] Available at: https://www.ncbi.nlm.nih.gov/pubmed/23296548 [Accessed 29 November 2016].

Qidwai, S., 2020. *Mechanics of Materials: Stress Transformation.* [Online] Available at: https://www.bu.edu/moss/mechanics-of-materials-stress-transformation/ [Accessed 1 March 2020].

Ren, W., Sneed, L. H., Yang, Y. & He, R., 2014. Numerical Simulation of Prestressed Precast Concrete Bridge Deck Panels Using Damage Plasticity Model. *International Journal of Concrete Structures and Materials,* 9(1), pp. 45-54.

Sato, S. et al., 1987. Fracture criteria of reactor graphite under multiaxial stesses. *Nuclear Engineering and Design,* 103(3), pp. 291-300.

Savija, B. et al., 2017. Modelling deformation and fracture of Gilsocarbon graphite subject to service environments. *Journal of Nuclear Materials,* Volume 499, pp. 18-28.

Savija, B. et al., 2018. Modelling deformation and fracture of Gilsocarbon graphite subject to service environments. *Jornal of nuclear materials,* Volume 499, pp. 18-28.

Tan, E., Fahad, M., Hall, G. & Warren, N., 2016. *Prediction of keyway root cracking in graphite core of AGRs.* Southampton, s.n.

Taylor, C. & Crewe, A., 2018. *Physical Model of an AGR Nuclear Reactor Graphite Core for Shaking Table Explorations of Seismic Behaviour.* [Online]
Available at: https://southwestnuclearhub.ac.uk/plex-agr-nuclear-graphite-core/
[Accessed 10 February 2021].

Treifi, M., Marsden, B. J., Hall, G. N. & Mummery, P. M., 2015. *KEYWAY ROOT CRACK ARREST IN AN AGR GRAPHITE BRICK.* Manchester, 23rd Conference on Structural Mechanics in Reactor Technology, p. 190.

Voyagaki, E. et al., n.d. *Earthquake Response of a mult-block nuclear reactor graphite core: experimental mode vs simulations,* Bristol: EDF Energy.

World Nuclear Association, 2017. *Nuclear Power in the United Kingdom.* [Online]
Available at: http://www.world-nuclear.org/information-library/country-profiles/countries-t-z/united-kingdom.aspx
[Accessed 15 May 2017].

Yahr, G. T., Valachovic, R. S. & Greenstreet, W. L., 1973. Deformation and fracture of thin-walled graphite tubes under biaxial states of stress. *Carbon,* 11(6), p. 679.

Yang, B., 2004. *Stress, Strain, and Structural Dynamics.* California: Elsevier Science.

Zou, Z., Fok, S. L., Marsdem, B. J. & Oyadiji, S. O., 2006. Numerical simulation of strength test on graphite moderator bricks using a continuum damage mechanics model. *Engineering Fracture Mechanics,* Volume 73, pp. 318-330.

Appendices

The appendices are split into three section each adding additional information into how a different aspect of the was developed. Section A will provide additional dimensional, mesh, and assembly information, while providing great detail into the different approaches considered for modelling the interactions between the bricks. Section B will provide greater detail into how the gap was introduced into the model. This will include great detail into the various approaches considered for applying the gap. Section C will provide additional information on the analysis approach and results gathered. Section D provides pseudocodes used to develop all python scripts used for model formulation and analysis of results. Section E provides 2 papers written as part of the work, one submitted to the journal of pressure vessel technology and a conference paper submitted for the SMiRT 25 conference.

A. Model Formulation

A.1   Part Dimensions

The various brick dimensions used for modelling the fuel bricks is shown in figure A-1. All measurements are in millimetres. The model consists of 5 different parts they are:

- Fuel Brick
- Key
- Interstitial Brick
- Filler Interstitial Brick
- Boundary Brick
- Rigid Boundary

Some bricks include partitioned lines to improve meshing and to separate regions of the brick allowing for application of different material properties.

A.1.1   Fuel Bricks
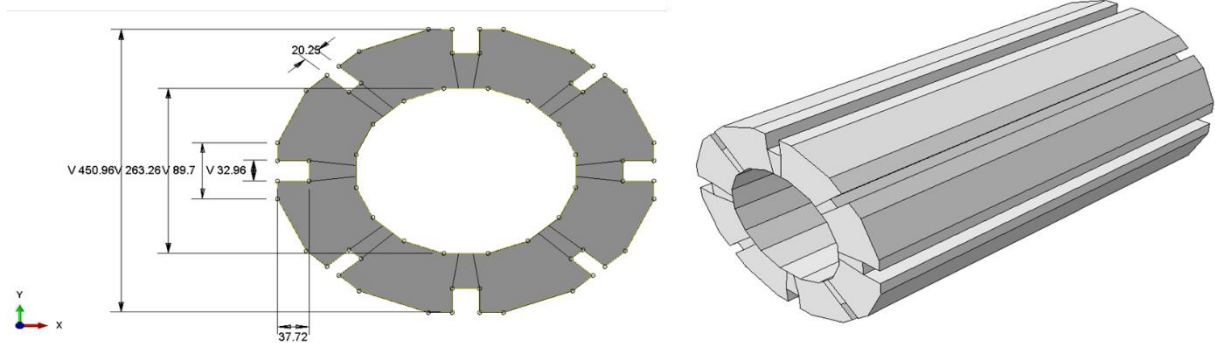
Figure A-1: Fuel brick dimensions

Figure A-1 shows the fuel brick and the its dimensions. The brick is 825 millimetres long. The image also includes black lines where partitioning took place to improve the quality of the meshing. The dimensions used are based on real bricks in an attempt to create the most realistic model possible.

A.1.2 Key
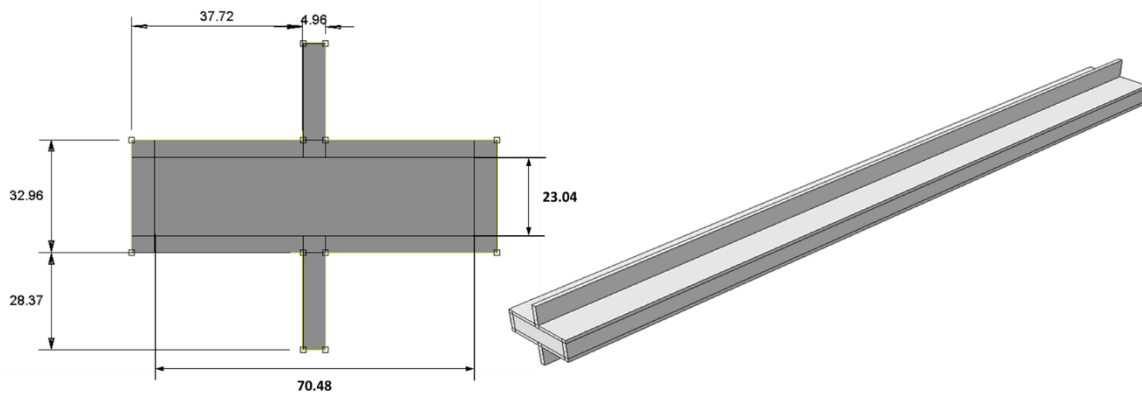
Figure 0A-2: Key dimensions

Figure A-2 shows the dimensions of the key, including the gap around the key. The has a length similar to the fuel brick of 825mm. The black lines within the key are places where cell partitioning takes place, splitting the material into multiple regions. The central region is provided with the properties of a graphite brick, while the remaining regions are given material properties that represent the gap between the bricks.

A.1.3 Interstitial brick
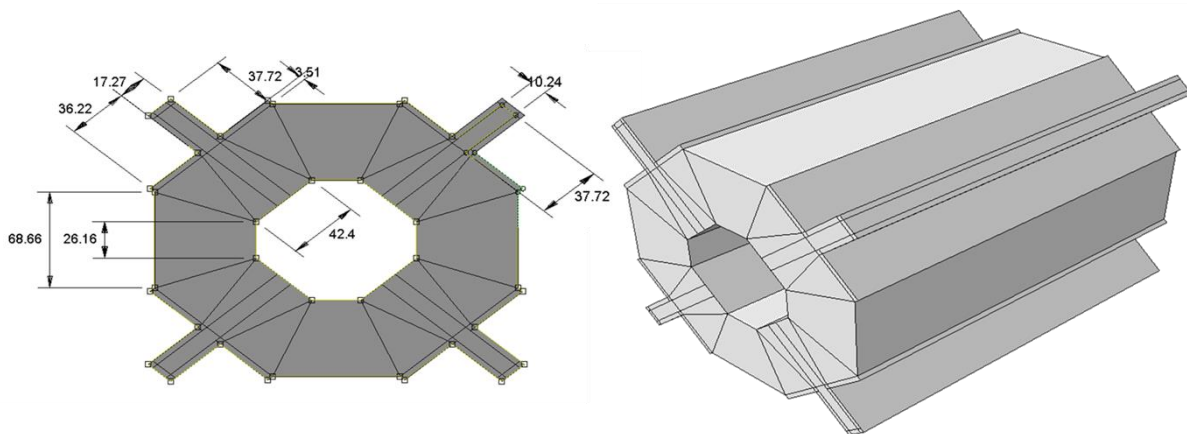
Figure 0A-3: Interstitial Brick dimensions

Figure A-3 Shows the dimensions of the interstitial brick. These dimensions were calculated from the dimensions of the fuel brick in order to create a brick that replicates interstitial bricks used in AGRs. The brick includes partitioned lines, some used for improving mesh and other used to create multiple regions where both graphite and gap

materials can be defined. The length of the brick is ⅓ the length of the fuel brick at 275mm.

A.1.4   Filler interstitial brick
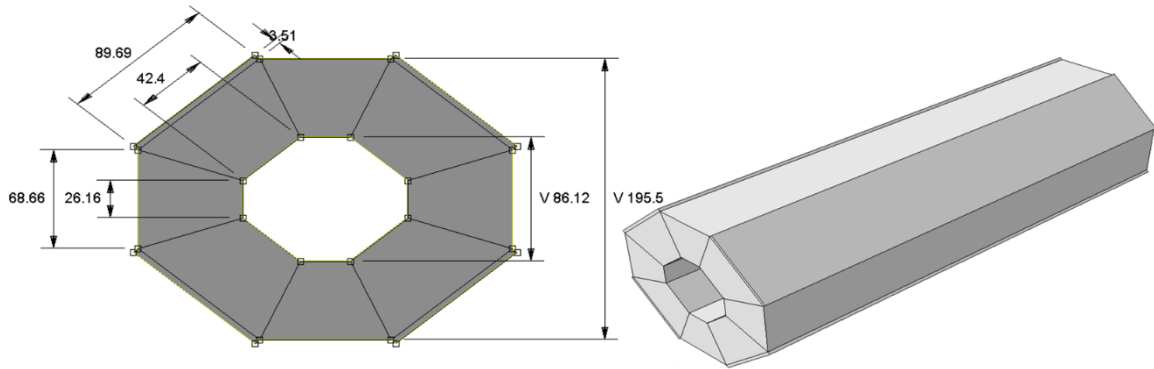
Figure 0A-4:Filler interstitial brick dimensions

Figure A-4 shows the filler interstitial bricks dimensions. The dimensions are similar to the interstitial brick however the keys were removed. There exist partition lines on the surface of the brick to allow for division of the brick into multiple regions do define different material properties, while also allow for better mesh quality. The length of the brick is ⅔ the size of the fuel brick at 550mm.

A.1.5 Boundary
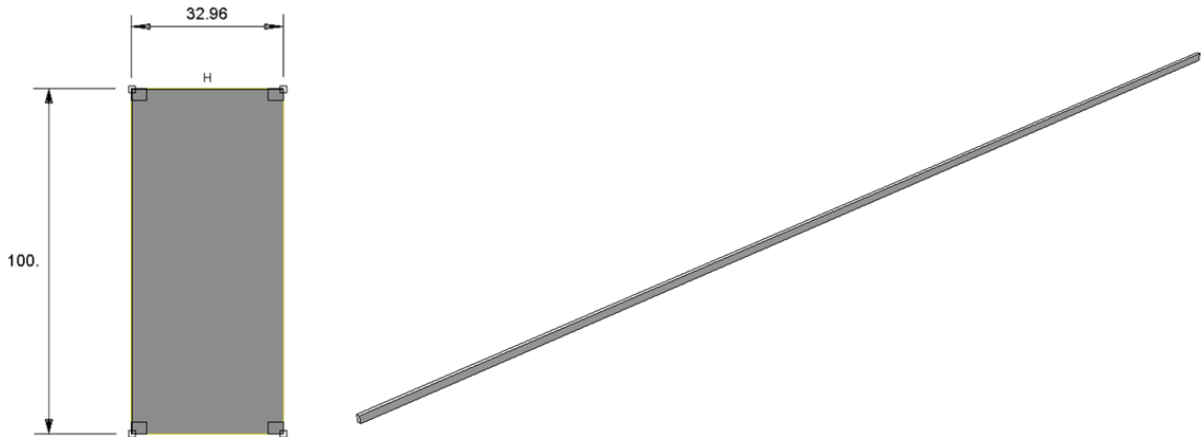
Figure 0A0-5: Boundary dimensions

The boundary elements displayed in figure A-5 functions only as a connector connecting the outer fuel bricks to the rigid wall surrounding the model. the length of the boundary part is equal to the length of 12 layers of fuel brick at 9900mm. This part is given material properties similar to the gaps on the keys, interstitial and filler interstitial bricks.

A.1.6 Rigid Boundary
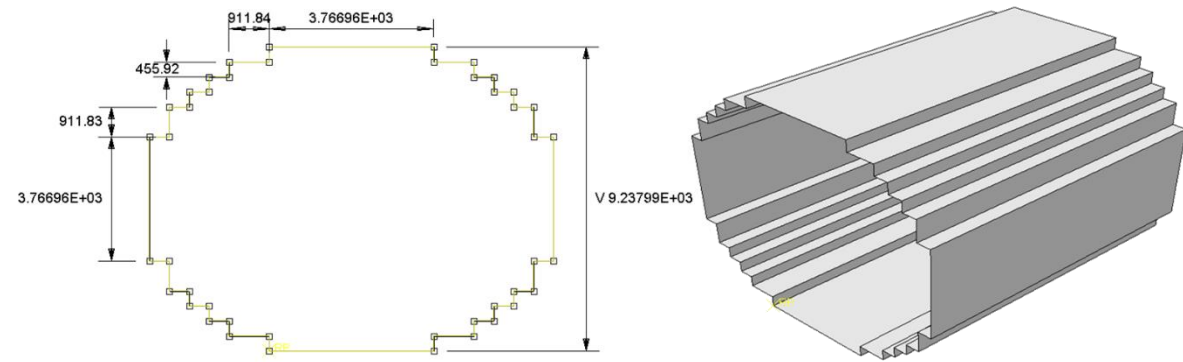
Figure A-6: Rigid boundary dimensions
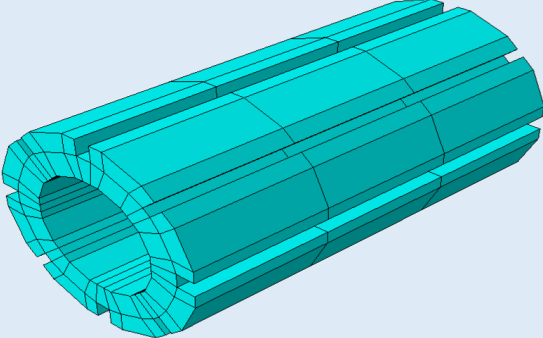
The rigid boundary part shown in figure A-6 acts as a wall surrounding the entire core blocking bricks expanding beyond the limits provided. The length of the Rigid boundary element is equal to the length of 12 bricks at 9900mm. As this is rigid part, no material
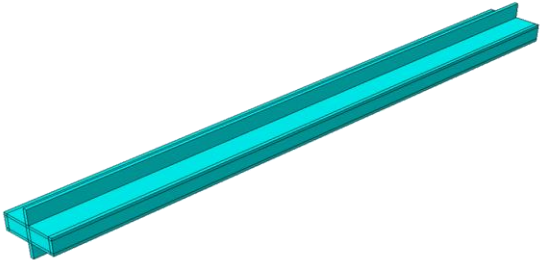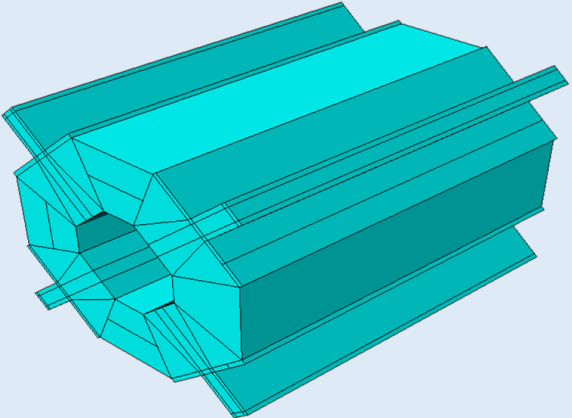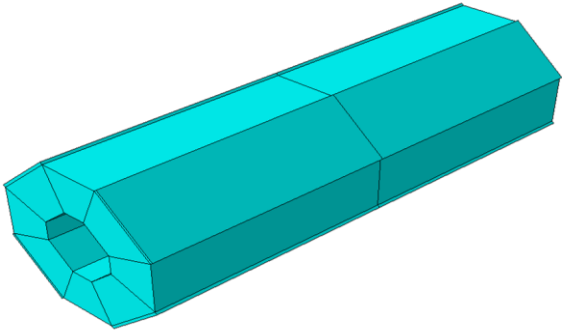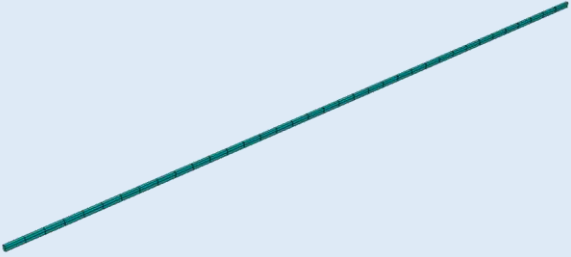
properties were needed however a reference point was set in the bottom corner of the part as shown in figure 9-6. A smaller rigid boundary was created when building a small model.

A.2   Mesh definition

The mesh used greatly influences the accuracy of the results generated. A finer mesh would not only create more realistic results but as shown in table 5-3, a finer mesh can also predict damage initiation to occur elsewhere in the brick. However, a finer would require more computational power to perform analysis.

For the models generated and analysed, the coarsest mesh possible was created as a starting position, allowing for refinement when necessary, further in the future. Table A-1 shows the mesh used for each part and the number of elements this created.

Brick	Number of elements	Mesh image
Fuel brick	168	

Key	17	
Interstitial brick	72	
Filler interstitial brick	24	
Boundary	72	
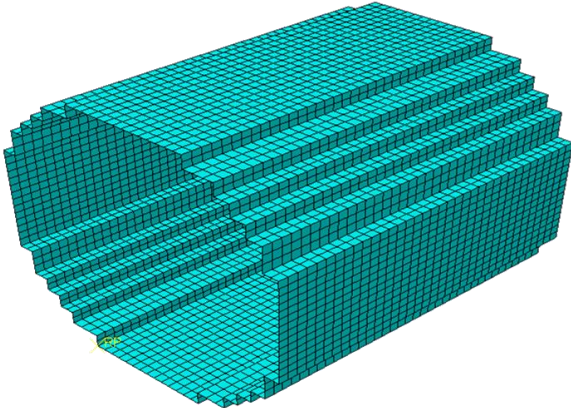
Rigid Boundary	5184	

Table 0A-01: Mesh used for each part in the model

A.3   Model assembly

Figure A-7 shows the assembly of the core, with and without the outer boundary and with and without the gaps in the bricks. The model consists of:

- 12 layers of fuel brick, each containing 332 bricks, with a total of 3984 fuel bricks.
- 12 layers of keys, each layer containing 624 keys creating a total of 7488 keys.
- 12 layers of interstitial brick, each layer containing 293 bricks with a total of 3516 interstitial bricks.
- 12 layers of filler interstitial bricks, each layer containing 293 bricks with a total of 3516 filler interstitial bricks.
- 80 Boundary part
- 1 rigid boundary.

A total of 18585 parts exists in the model and when combined with the mesh specified in table A-1, the model contains a total of 1,145,088 elements.
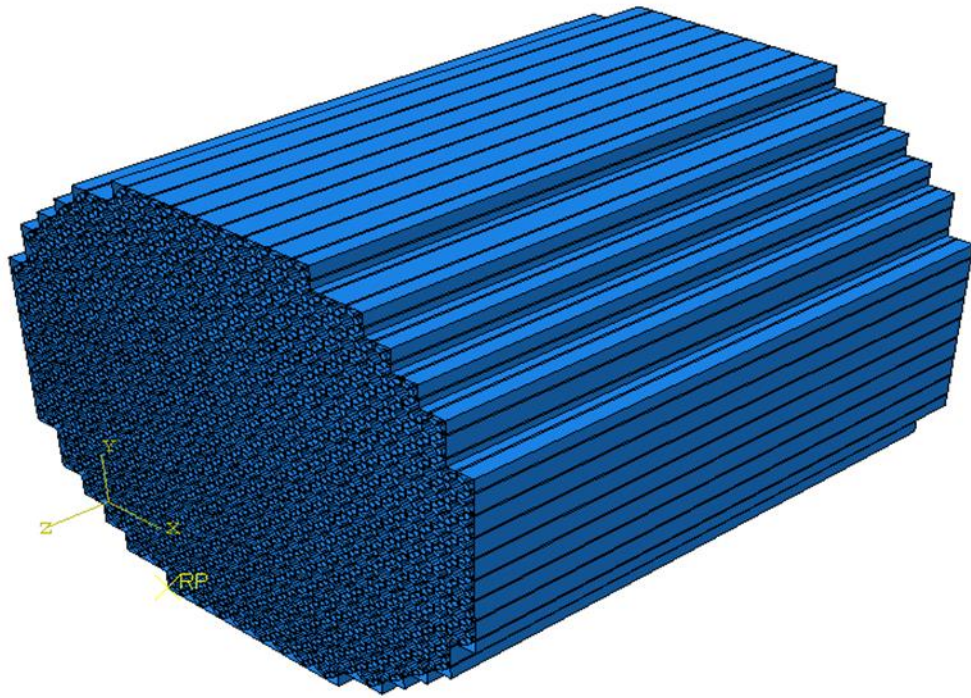
Figure A-7: Full-scale model fully assembled.

A.4 Material definitions

While the material properties in the model were based on polynomial equations, when applying these values to the core, they were applied in a tabular format to improve the computational efficiency of the model. Table A-2 displays the variation in the modulus when thermal loads are applied. Table A-3 displays the variation when irradiation loads are applied. Predefined fields were later added where a ±10% variation to the modulus was added.

Modulus of elasticity	Poison ratio	Thermal load
10000	0.2	100
10000	0.2	200
10050	0.2	300
10050	0.2	400
10125	0.2	500
10250	0.2	600
10370	0.2	700
10550	0.2	800
10750	0.2	900
11100	0.2	1000
11370	0.2	1100
11700	0.2	1200
12100	0.2	1300

Table 0A-02: Variation of modulus based on thermal loads in tabular format

Modulus of elasticity	Poison ratio	Irradiation dose
5450	0.2	10
5450	0.2	20
5995	0.2	30
5995	0.2	40
6540	0.2	50
7085	0.2	65
10900	0.2	85
15805	0.2	105
21800	0.2	135
25070	0.2	147.5
28340	0.2	165
27250	0.2	175
25070	0.2	180
22890	0.2	185

20710	0.2	200
16350	0.2	250
16350	0.2	300

Table 0A-03: Variation in dose based on Irradiation in tabular format

While the expansion coefficient was constant through thermal analysis, this expansion varied with dosage with irradiation load. This variation was applied in tabular format and is displayed in table A-4.

Expansion coefficient	Dose
0	0
-0.00014	10
-0.00023	20
-0.00026	30
-0.00028	40
-0.00028	50
-0.00028	60
-0.00028	70
-0.00027	80
-0.00025	90
-0.00024	100
-0.00021	110
-0.00019	120
-0.00016	130
-0.00013	140
-8.91E-05	150
-4.90E-05	160
-5.22E-06	170
4.21E-05	180
9.29E-05	190
1.47E-04	200
2.05E-04	210
2.67E-04	220
3.31E-04	230
4.00E-04	240
4.72E-04	250
5.47E-04	260
6.26E-04	270
7.09E-04	280
7.95E-04	290
8.84E-04	300
9.77E-04	310
1.07E-03	320
1.17E-03	330

1.28E-03	340
1.38E-03	350
1.49E-03	360
1.61E-03	370
1.73E-03	380
1.85E-03	390
1.97E-03	400

Table 0A-04: Coefficient of irradiation expansion by dose

A.5 Loads

The loads applied in the model were applied by an analytical field for each layer of bricks. The formulas used for these loads is shown in table A-5 for thermal loads and A-6 for irradiation loads. There was no irradiation load applied to layer 1 and 12 so these were ignored.

THERMAL LOAD	
LAYER 1	-0.00149*pow(X,2)+2.997E-15*X-0.00149*pow(Y,2)+2.997E-15*Y+426.84
LAYER 2	-0.00149*pow(X,2)+0.00000000000000921*X-0.00149*pow(Y,2)+0.00000000000000921*Y+466.598
LAYER 3	-0.00149187939461981*pow(X,2)-0.0000000000000003219646771412950*X-0.00149187939461981*pow(Y,2)-0.0000000000000003219646771412950*Y+496.348984030878
LAYER 4	-0.00149187939461978*pow(X,2)+0.0000000000000002109423746787800*X-0.00149187939461978*pow(Y,2)+0.0000000000000002109423746787800*Y+516.098984030878
LAYER 5	-0.00149187939461978*pow(X,2)+0.0000000000000002109423746787800*X-0.00149187939461978*pow(Y,2)+0.0000000000000002109423746787800*Y+525.848984030878
LAYER 6	-0.00149187939461978*pow(X,2)-0.0000000000000012101430968414200*X-0.00149187939461978*pow(Y,2)-0.0000000000000012101430968414200*Y+525.598984030875
LAYER 7	-0.00149187939461981*pow(X,2)-0.0000000000000010325074129014000*X-0.00149187939461981*pow(Y,2)-0.0000000000000010325074129014000*Y+515.348984030876
LAYER 8	-0.00149187939461981*pow(X,2)-0.0000000000000010325074129014000*X-0.00149187939461981*pow(Y,2)-0.0000000000000010325074129014000*Y+495.098984030876
LAYER 9	-0.00149187939461981*pow(X,2)-0.0000000000000003219646771412950*X-0.00149187939461981*pow(Y,2)-0.0000000000000003219646771412950*Y+464.848984030878
LAYER 10	-0.0014918793946198*pow(X,2)-0.0000000000000004107825191113080*X-0.0014918793946198*pow(Y,2)-0.0000000000000004107825191113080*Y+424.598984030877
LAYER 11	-0.00149187939461978*pow(X,2)+0.0000000000000002109423746787800*X-0.00149187939461978*pow(Y,2)+0.0000000000000002109423746787800*Y+374.348984030878
LAYER 12	-0.00149187939461978*pow(X,2)-0.0000000000000004996003610813200*X-0.00149187939461978*pow(Y,2)-0.0000000000000004996003610813200*Y+314.098984030877

Table 0A0-5: Thermal Loads

IRRADIATION LOAD	
LAYER 2	-0.00168045295009973*pow(X,2)-2.22044604925031E-16*X+157.116295612381-0.00168045295009973*pow(Y,2)-2.22044604925031E-16*Y
LAYER 3	-0.00236313696107775*pow(X,2)-4.44089209850063E-16*X+220.94479070491-0.00236313696107775*pow(Y,2)-4.44089209850063E-16*Y

LAYER 4	-0.00257319357984021*pow(X,2)-6.66133814775094E-16*X+240.584327656458-0.00257319357984021*pow(Y,2)-6.66133814775094E-16*Y
LAYER 5	-0.00262570773453083*pow(X,2)-2.22044604925031E-15*X+245.494211894344-0.00262570773453083*pow(Y,2)-2.22044604925031E-15*Y
LAYER 6	-0.00259945065718553*pow(X,2)+1.11022302462516E-15*X+243.039269775402-0.00259945065718553*pow(Y,2)+1.11022302462516E-15*Y
LAYER 7	-0.00254693650249491*pow(X,2)-4.44089209850063E-15*X+238.129385537513-0.00254693650249491*pow(Y,2)-4.44089209850063E-15*Y
LAYER 8	-0.00244190819311368*pow(X,2)-1.33226762955019E-15*X+228.30961706174-0.00244190819311368*pow(Y,2)-1.33226762955019E-15*Y
LAYER 9	-0.00228436572904183*pow(X,2)-3.10862446895044E-15*X+213.579964348079-0.00228436572904183*pow(Y,2)-3.10862446895044E-15*Y
LAYER 10	-0.00189050956886219*pow(X,2)+1.4432899320127E-15*X+176.755832563928-0.00189050956886219*pow(Y,2)+1.4432899320127E-15*Y
LAYER 11	-0.00102402601646703*pow(X,2)-1.4432899320127E-15*X+95.7427426387941-0.00102402601646703*pow(Y,2)-1.4432899320127E-15*Y

Table 0A-06: Irradiation Loads

B. The gap problem

One key factor in improving the realistic nature of the results was the inclusion of a gap. As bricks in a core expand, this expansion is taken up by the gaps in the model, allowing the entire core to expand significantly until any contact occurs. Adding a gap in the model will require a lot of computational power, and is a complex problem. This chapter will explain the different methods considered for adding a gap, and how the addition of a gap changed the results and ultimately changed the life expectancy time of the core.

B.1   How a gap was implemented

The major limitation of the model at one point revolved around the lack of a gap between the bricks. Multiple methods were considered for how to include a gap and these are discussed below:

B.1.1   Adding a space between bricks

The first method considered was to have none of the bricks in contact and to include the gap as initial conditions as shown in figure B-1. This resulted in there being many unconnected regions and convergence was not possible with a small 2 brick model.

Abaqus requires all parts of the model to be in contact, and by simply adding a gap between bricks results in many errors occurring and ultimately results in analytical failure.
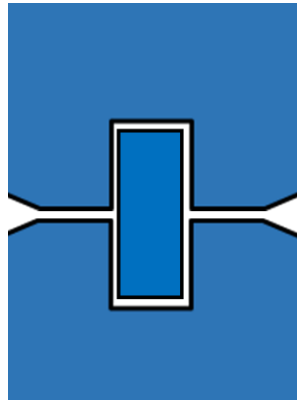
Figure 0B-1: Adding a space between the bricks

B.1.2   Displacement change

The second method considered was to add a step where a displacement is given to all parts as shown in figure B-2. The displacement would ensure the bricks are in contact, hence no unconnected regions would exist. While this method did converge when used on a small 3 brick model, convergence was not possible on a 6x6x5 model. In-addition the run time was significantly increased when this method was attempted as multiple steps are added to include brick displacement. This method also increased the complexity of the scripting, where developing a script for the full model would prove very difficult and complicated.
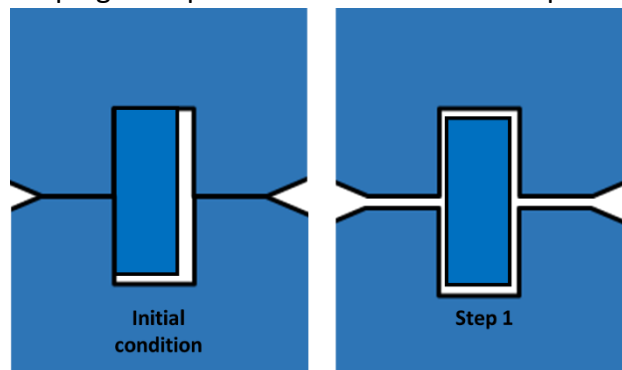
Figure 0B-2: Adding a displacement step

B.1.3 Temperature change

Similar to the previous method this method started with all parts in contact at initial conditions, however it also assumed a high initial temperature, and during the first step this temperature would decrease. This is shown in figure B-3. Using the coefficient of thermal expansion as way of shrinking the bricks to fit into the smaller gap between the bricks. Once again analysis worked 3 brick model, however was unsuccessful on a 6x6x5 model. In addition, the inclusion of an extra step significantly increased the run time. Ensure the bricks did not all stay in contact after shrinking occurred also required extra steps and extra boundary conditions to be applied, which resulted in a significantly more complex model.
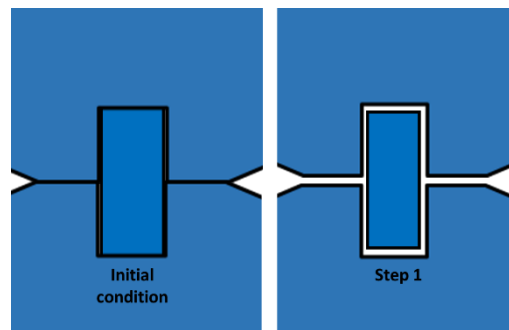
Figure B-3: Using the thermal coefficient of expansion to shrink the brick

B.1.4 Modifying the interaction/material properties

With this method, all the bricks would be in contact however the interaction/material properties of the bricks would differ in such a way as to make up for a gap existing between the bricks. After many attempts no successful method was found by altering the material properties as any changed made affected the whole material and not the boundary. Changes to the interaction properties yielded more possibilities, an example being the addition of over closer between the surfaces or adding a penalty, however non were suitable for the model being created.

B.1.5 Cohesive elements

The final method tested would require the addition of extra parts to the model. This method was considered when deciding how to model interaction between bricks, and at the time it was found to be too complex, not reliable and required a lot of computation power to run. These cohesive elements would have their own properties which would
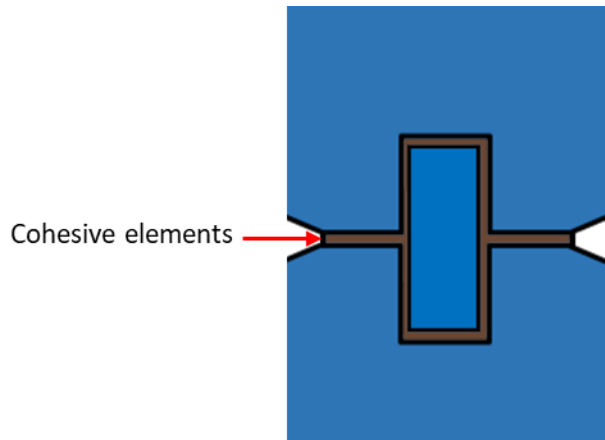
Figure B-4: Cohesive elements filling for the gaps

account for the gap between the bricks. Once again with a 3 brick model this method worked. Furthermore, when creating a more complex 6x6x5 model convergence was possible, but with a greatly increased run time. The cause of this increase was found to be due to the additional parts being added.

A method was eventually found for reducing the number of parts in the model. This required the cohesive parts to be built into the bricks and then partitioned. This creates multiple regions in the bricks, where different material properties can be applied to each region. Ore detail on this is provided in chapter 3.4.2.

B.2   Significance of a gap being added

To better understand why the addition of a gap is significant, it is important to consider a small model of the core where gaps are included and removed. Finite element analysis of the model was used to access the evolution of the maximum principal stress at brick keyways. The results for all brick types were analysed and the evolutions of the most stressed bricks of each type are given in figure B-5. The figure shows the evolution of the maximum principal stress over 30 years of service in the bricks. With this model it was tensile limit was 0.6MPa, and therefore any brick that passes this limit was assumed to have fractured.
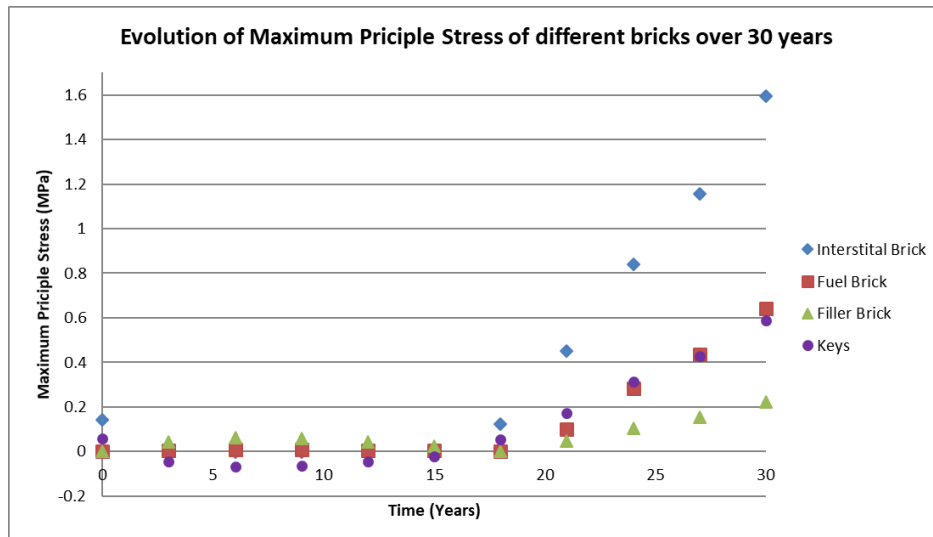
Figure B-5: Evolution of stresses when gap is removed

This model assumed that the maximum dose a brick will receive after 30 years of service is 200×1020n/m2. By comparing to the tensile limit value required for a crack to occur to the maximum principal stresses found through finite element analysis, it is found that an interstitial brick will crack first after 19 years of operation, followed by a key after 22 years, and a fuel brick after 23 years. The filler interstitial bricks will be the last bricks to show signs of cracking at 30 years.

Furthermore, figure B-6 shows the percentage of bricks that are damaged over 30 years. This was calculated by counting the number of bricks in the entire model to have passed

the tensile limit of graphite. This value is then converted to a percentage and plotted on the graph. The figure indicates that 15% of the interstitial brick will become damaged after 30 years of service.
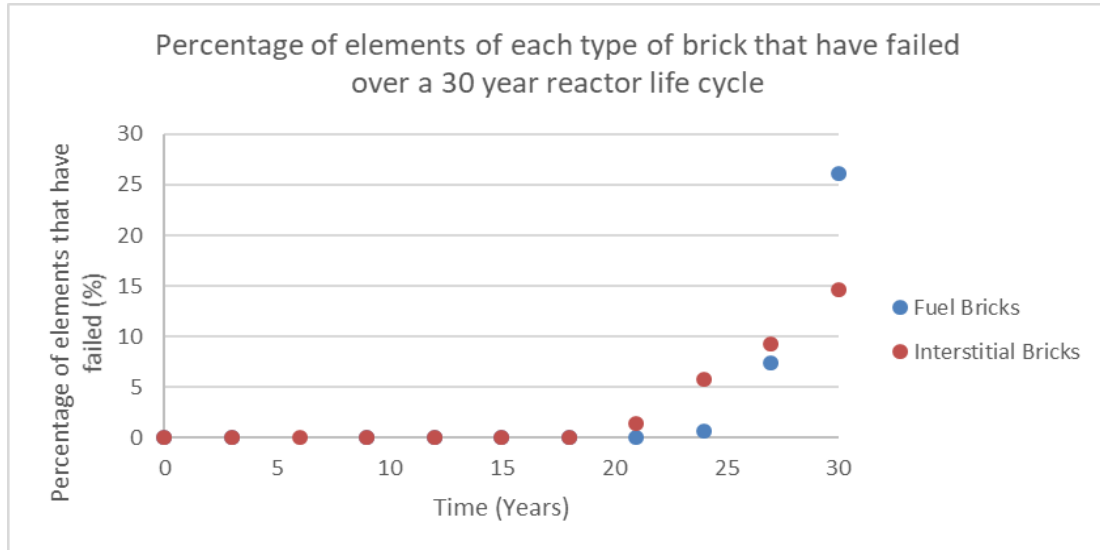
Figure 0-6: Percentage of bricks damaged over 30 years

The significance of these results is that when no gap exists in the core, the life of the reactor significantly decreases. This is due to the expansion of the graphite bricks, specifically as they expand, they expand into each other rather than the space between the bricks. This causes early failure of the bricks. When this is compared to the results gathered in section 5.1 and in figure 5.1, it becomes clear that without gaps the reactors life expectancy is reduced significantly.

Furthermore, the addition of the gap resulted in zero damage being observed in the keys, interstitial and filler interstitial bricks. Without gaps almost damage was expected within 30 years of service, but the addition of gaps increases this by at least 10 years, with no damage observed in the 40-year analysis completed when gaps were included. It can therefore be stated that the inclusion of the gaps in the model is of paramount importance and will result in a significant increase in the life expectance of the reactor.

C. Additional results data

C.1 Elements in each region of fuel brick

When calculating the percentage damage in each brick, each region of the brick needed to be analysed separately. This was done by selecting the elements which belong to a specific region of the brick. Table C-1 shows the element numbers and which region they belong to. The values at each region were used to calculate the overall damage in the bricks.

The regions shown in the table are as follows

- FB-FB: Fuel brick to fuel brick keyways.
- FB-IB: Fuel brick to interstitial brick keyways.
- Rest of FB: All regions in the furl brick away from the keyways.

Table C-1 Elements and their location on the fuel brick:

FB-FB	FB-IB	Rest of FB
1	2	6
3	4	7
5	8	10
9	11	14
13	12	20
15	16	21
17	18	24
19	22	28
23	25	34
27	26	35
29	30	38
31	32	42
33	36	48
37	39	49
41	40	52
43	44	56
45	46	62
47	50	63
51	53	66
55	54	76
57	58	77
59	60	79
61	64	80
65	67	84
69	68	90
71	70	91
73	72	94
75	74	98
78	81	104
83	82	105
85	86	108
87	88	112
89	92	118
93	95	119
97	96	122
99	100	126
101	102	132
103	106	133
107	109	136
111	110	140
113	114	146
115	116	147
117	120	150
121	123	154
125	124	160
127	128	161
129	130	164
131	134	168
135	137	
139	138	
141	142	
143	144	
149	148	
155	151	
157	152	
159	156	
163	158	
167	162	
153	165	
145	166	

C.2   Model images and codes

Python codes and images of model are available on request

D. Pseudocodes for Python coding

Here pseudocodes that were used to create each python scripts have been displayed.

Script: Defining Parts

Brick Generation
    Draw 2D shape of brick face
        Print Co-ordinate of line in X-Y axis
            Repeat for every edge of brick
    Print depth of brick along Z-axis
E**nd** brick generation

Partitioning brick surface
    Select surface that will be partitioned
        Print co-ordinates of line that will partitioned
            Repeat for all lines on partition surface
        Repeat for all surfaces that need to partitioned
End Partitioning brick surface

Partitioning Brick Cell
    Repeat "partition brick surface" to draw cell that will be partitioned
        Select surface from mask
            Print node number on partitioned surface
            Print edge number where node lies
        Select Cell partition along line
        Repeat for remaining cells on surface
    Repeat until all surfaces on brick are partitioned
End Cell Partitioning

Mesh generation
    Select edge using edge mask
        Print number of seeds along edge
            Repeat for remaining edges
    Generate mesh
End mesh generation

End part definition

Script: Defining Model assembly

Generate one layer of bricks
    Add part to assembly by selecting them by their name (FB, IB, FIB, K (2))
        Translate position of each brick

Print position of brick
    Repeat for all bricks
Rotate position of second key
    Print angle of rotation and axis of rotation (Z)
Create linear pattern
    Print name of all 5 bricks
    Print number of replicas and axis of replication
Rename all bricks
    Select brick by selecting current name
    Print new name of brick based on keying system
    Repeat for all bricks
Delete all unwanted bricks by using the keying system to identify bricks
End Generation of one layer

Generate multiple layers
Create linear pattern
    Print name of all bricks in one layer
    Print number of replicas and axis of replication
Rename all bricks
    Select brick by selecting current name
    Print new name of brick based on keying system
    Repeat for all bricks
End generation of multiple bricks

Generate Boundary Part
Add part to assembly by printing name of part
    Translate to correct position
    Print position of boundary part
    Repeat for all parts
Rename the Boundary parts
    Select brick by selecting current name
    Print new name of brick based on position of boundary
    Repeat for all additional parts
End generation of boundary
End model assembly

Script: Material Properties

Material generation
Define material properties for graphite
    Print elastic properties in tabular format
    Print damage plasticity data
    Print density value

        Print expansion data

            Print material name

    Repeat for all materials

End material generation

Applying material properties to bricks

    Select brick using name

        Select region of brick using mask

            Print name of material to assign property to cell

        Repeat for all regions of brick

    Repeat for all bricks

End Material application

End Material Properties

Script: Defining Sets

Sets creation for random material properties

    Print f (#) =

        Select every brick in model using naming system

            Print the mask for cell

        Repeat for every brick in model

   Print fx+fy+fz… selecting every brick based on value assigned in excel randomiser

        Print name for set indicating which group it belongs to e.g. MAT-10

    Repeat for all material types

End set generated for a material randomiser

End Set definition

Script: Defining Sets

Sets creation for one layer

    Print f (#) =

        Select brick using naming system

            Print the mask for contact surface

        Repeat for every brick in one layer

   Print f1+f2+f3……fn-1+fn selecting every surface given with the masks

        Print name for set indicating the layer

    End set generated for a specific surface

Combining multiple sets

    Print name of each sets being combined

        Repeat name of set for each layer

    Print name for set

End Set generation for a specific surface across every brick

End Set definition

Script: Defining interactions

Defining interaction properties
    Print name of interaction property
        Print properties of interaction (e.g. HARD for hard contact)
    Repeat for all 3 interaction types
End interaction properties
Defining interactions between sets
    Print name of interaction
        Print Master set
            Print Slave set
                Print Interaction property
    Repeat for all 10 interactions
End Interactions between sets

End interaction definition

Script: Defining Thermal Load

Defining Field output
    Print name of Load,
        Print equation for brick/s
            Print origin on load (datum)
        Repeat for every Fuel brick and once for all other bricks
    Repeat giving each equation a unique name from which loads can be identified
End creation of analytical field

Defining load on each brick
    Specify brick/set load is being applied to
        Print mask to specify area load is applied to on brick
            Print the equation name for specific load
            Print magnitude of load
    Repeat for every load on every brick/set
End application of loads

End Thermal load definition

E. Publications

In this Chapter each published work will be outlined with a brief overview including context and discussion. Please note that although the content of published works remains unchanged from the published form, the paper itself may be presented in its unpublished format or with changes made to formatting to provide continuity with the rest of this thesis.

The first paper here was submitted for the conference for the 25th International Assassination for Structural Mechanics ain Reactor Technology (SMiRT-25). The work presented took place during the second year of the project, where gaps between bricks were not included. This was later included and provided later failure dates for each layer of the core.

The second paper has been submitted to the Journal of Pressure vessel technology and currently being peer reviewed. This paper was submitted towards the end of the project and displays results based on work conducted the smaller model, discussing the effects of including material softening behaviour.

LARGE SCALE MODELLING OF DAMAGE AND FAILURE OF NUCLEAR GRAPHITE MODERATED REACTOR

Ahmadreza Farrokhnia[1], Andrey P Jivkov[2]

[1]   PhD   student,   University   of   Manchester,   Manchester,   M13   9PL, ahmadreza.farrokhnia@manchester.ac.uk

[2] Professor, University of Manchester, Manchester M13 9PL, andrey.jivkov@manchester.ac.uk

ABSTRACT

The UK Advanced Gas-Cooled reactors (AGRs) have cores made of graphite bricks with dual functions: as structural elements of the core, providing space for and separating fuel and control rods; and as moderator of the nuclear reaction. Nuclear graphite is a quasi-brittle material, where the dominant mechanism for failure is cracking. While cracking of isolated bricks is expected due to operation-induced changes in graphite microstructure and stress fields, these could be tolerated as far as the overall structural function of the core is maintained. Assessment of the whole core behaviour has been previously done with whole scale models where bricks have been considered as rigid body elements connected by elastic-brittle springs. This approach does not allow for the realistic assessment of the stresses in the bricks and associated brick cracking. Reported here are results from an ongoing project, which addresses this shortcoming. The proposed model uses deformable bricks with appropriate interactions, allowing for physically realistic whole core analysis. The results are focused on the damage that a graphite moderated reactor develops during a life cycle, how this affects the behaviour of the whole core, and how changes in bricks' behaviour impacts the core integrity. The proposed methodology is a major step towards high-fidelity assessment of AGRs' fitness for service, required for supporting continuous safe operation and life-extension decisions.

INTRODUCTION

The Advanced Gas-Cooled reactors (AGR) in the UK use graphite as a moderator and also as a structural component. The reactor core contains three different types of interlocking graphite moderator bricks: fuel bricks, interstitial bricks and filler interstitial bricks as shown in Fig. 1. The bricks are stacked vertically on top of each other, with the entire core consisting of 12 layers of bricks. Each layer contains 323 fuel bricks and 293 interstitial and filler interstitial bricks. The gaps in the bricks create vertical channels for fuel assemblies, control rods and coolant flow. The entire structure is connected via a system of loose keys and keyways, which allow the core to expand and contract during service. A layer of Upper Neutron Shield of graphite bricks covers the assembly. The whole system is kept laterally stable using a system of restrain rods and beams, centralising brackets and Warwick links tied to restrain rings (Ahmed, et al., 1985).

During the reactors life cycle, different fuel bricks undergo dimensional changes at different rates due to temperature and irradiation gradients, e.g. bricks located in central layers are irradiated at a faster rate. The structural integrity of bricks is critical to the safe reactor operation, because cracked bricks can lead to core distortion and potentially to channels misalignment. This could cause blockages that prevent insertion or extraction of fuel and control rods. The whole core behaviour due to dimensional changes has been a subject of a number of past works. Due to the large number of bricks, these works have been mostly based on models with rigid-body bricks connected by spring elements representing the keys. In such case, all mechanical effects are
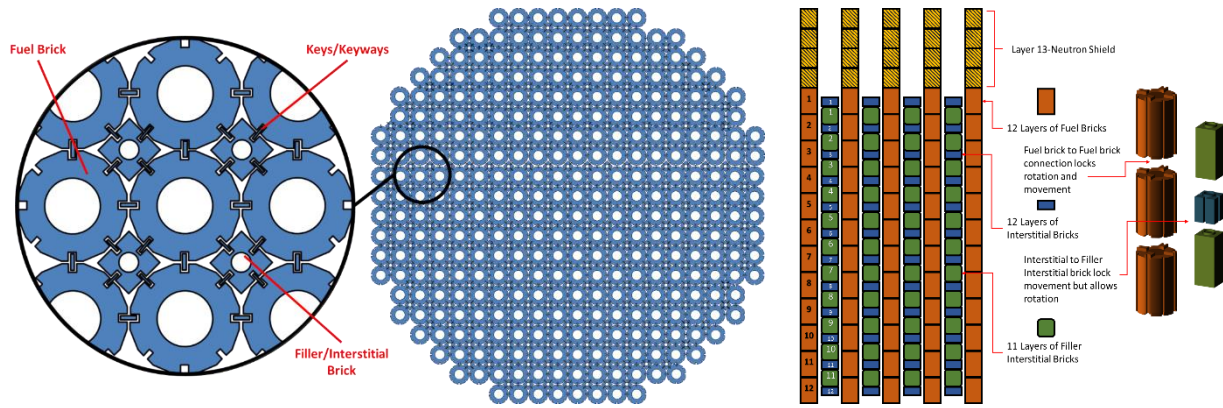
Figure 1. Layout of one layer of graphite moderated reactor.

assigned to the springs: stiffness, friction, damping and damage/failure. While the approach allows for calculating load transmission or impacts between the bricks (Duncan & Kralj, 2007), it has a major limitation – deformation, damage and fracture of the bricks cannot be analysed. As a consequence, the effect of bricks' damage and failure on the core behaviour cannot be investigated.

The aim of the project reported in this work is to gain better understanding of temperature and irradiation effects on a graphite reactor core by developing a more realistic model with deformable bricks and bespoke interactions. The model presented allows for investigations of how the changes of graphite properties throughout the course of a reactor's lifespan affect the whole core geometry and integrity. In particular, this development will allow for improved assessment of the core fitness-for-purpose towards its projected end of life and inform life-extension decisions

REACTOR CORE MODEL

A finite element model of the whole core has been developed using deformable brick elements and surface interactions. Thus far computational power has been a major limiting factor for constructing such a large model. One of the difficulties lies in the definition of individual contact surfaces. With a whole model containing 18504 individual bricks, each tessellated into continuum finite elements, over 90000 different interacting surfaces exist in the model. Via a purpose-built Python script for ABAQUS, only surfaces in direct contact were defined, reducing substantially the computational power required. These surfaces were grouped together allowing for a whole-scale model to be created. The model contains initial gaps of 10 mm between the individual bricks, as per design specification.

While graphite is quasi-brittle material, it is assumed to be linear elastic for the purposes of this work. However, the Young's modulus E is made dependent on temperature and dose, while the Poisson's ratio is kept constant. Two operational loads causing dimensional changes are considered: temperature and irradiation. These are applied separately to the model. Each load induces non-mechanical strains, a thermally-induced strain, ε^{th}, and an irradiation-induced strain, ε^{ir}, which modify the gaps between the bricks. When bricks get in contact due to gap closure, further expansive strains cause deformation of these bricks with associated stresses.

The temperature distribution within the core is assumed constant from start to end of the reactor's lifecycle (outages not considered). The temperature varies between the different layers, with the central bricks having a higher temperature than the bricks at the top and bottom of the reactor. Within each fuel brick in a particular layer the temperature decreases by around 50°C from the inner edge to the outer edge. These variations are illustrated in Fig. 2.

Figure 2. Illustration of temperature fields in the core and inside bricks

The temperature variation between layers and between brick surfaces used in the present work are shown in Fig.3. Notably, the highest temperature is not at the central layer, but at layer 5 of the core. This bias is due to the air flow through the reactor passing from layer 12 to layer 1, causing a distortion in the distribution of the temperatures. The temperature field is assigned by a Python script to the elements of individual bricks, assuming linear variation across brick thickness. Thermal strains result from temperature gradients, as described by Eq. (1)**Invalid source specified.**, where the coefficient of thermal expansion, α, used in the present work was 4.39×10^{-9} (Li, et al., 2007). This value remained constant throughout the reactor's life cycle.

$$\varepsilon^{th} = \alpha \, \Delta T$$
(1)
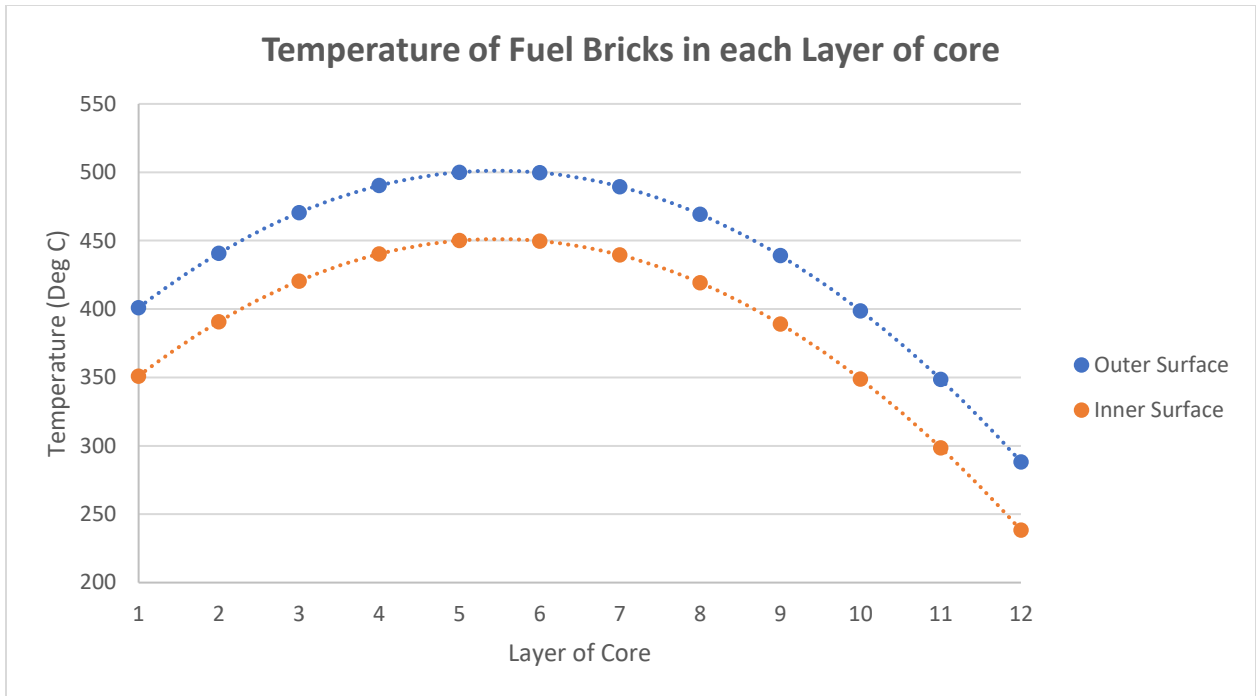
Figure 3. Temperature variation between layers and bricks surface

The effects of irradiation on a single brick have been modelled and discussed in previous works, e.g. (McLachlan, et al., 1996). It has been found that as graphite bricks irradiate, they firstly shrink, then expand beyond their original dimensions, a process illustrated in Fig. 4. As fuel bricks' interiors receive higher dosages, the inner surfaces shrink at a faster rate than the outer surfaces. After 30 years of service the dose on the inner surface of the brick is approximately 200×10^{20} n/cm^2 while the dose on the outer surface is 112×10^{20} n/cm^2. This creates a potential for bore cracking, where tensile stresses exist close to the centre of the brick and compressive stresses exist on the outside. The effect is reversed later in the bricks life with generation of compressive stresses at the inner surface and tensile stresses at the outer surface. These changes cause stress concentration at key ways and could lead to crack initiation. The cracks created due to bricks expansion can join up with cracks created during the initial shrinking resulting in brick failure.

Figure 4. Effects of irradiation-induced dimensional changes on brick stresses.

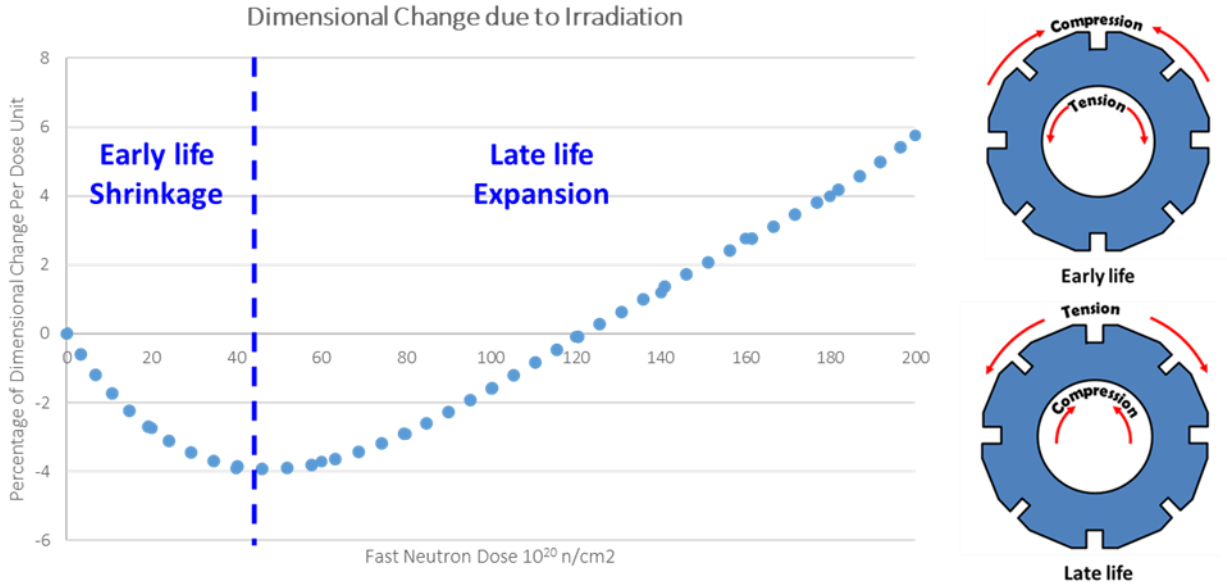Keyway cracking is of greatest concern to operators, as multiple brick failures can lead to compromising the whole keying system or multiple channels (Zou, et al., 2006). Such scenarios have been examined by a series of experiments with single un-irradiated graphite moderator bricks and corresponding finite element analyses replicating the conditions in a real reactor (McLachlan, et al., 1996). The results showed good agreement between the predicted failure strength and available experimental data. Furthermore, fast cracking at one keyway is anticipated to trigger a secondary crack at another, potentially opposite keyway, leading to brick disintegration. This phenomenon, known as prompt secondary cracking has been investigated in detail by dynamic fracture analysis, with results clearly confirming the anticipation (Crump et al., 2017; Crump et al., 2019).

Considering the data in Fig. 4, the irradiation strain ε^{ir} can be expressed as a function of fast neutron dose γ using a 4th degree polynomial, Eq. (2), where A_0, A_1, A_2 etc. are coefficients derived from the respective polynomial fits given in Table 1.

$$\varepsilon^{ir} = A_0\gamma^4 + A_1\gamma^3 + A_2\gamma^2 + A_3\gamma + A_4$$
(2)

Similarly, to the thermal loads, the irradiation loads are modelled with a constant dose for each layer, variable dose between the layers, and variable dose between inner and outer brick surfaces. The dose distribution in the core is shown in Fig 5. Equations (1) and (2) can be combined to provide a value for the total strain induced by particular temperature and irradiation dose in any finite element of any brick:

$$\varepsilon = (\alpha\,\Delta T + A_0\gamma^4 + A_1\gamma^3 + A_2\gamma^2 + A_3\gamma + A_4)$$
(3)

Table 1: Polynomial coefficients for calculating irradiation-induced strains (A_i) and Young's modulus variation with irradiation dose (B_i) and temperature (C_i)

Coefficient	A_0	A_1	A_2	A_3	A_4	
Value	0.15	- 4.1228	41.792	- 135.79	0.6446	
Coefficient	B_0	B_1	B_2	B_3	B_4	B_5
Value	9.397E-7	4.610E-4	6.923E-2	-2.6907	2.793E1	1.399E4
Coefficient	C_0	C_1	C_2	C_3	C_4	C_5
Value	8E-07	0.0038	6.0112	2253.5	241532	1E10

Figure 5. Distribution of fast neutron irradiation dose within reactor core.

Computationally, the effects of temperature and irradiation dose are imposed by the local changes of Young's modulus they incur. Young's modulus varies with the dose rate γ, can be approximated by a 5th degree polynomial given by Eq. (4) (Li, et al., 2007), where B_0, B_1, B_2 etc. are coefficients derived from the respective polynomial fits given in Table 1.

$$E^{ir} = B_0\gamma^5 + B_1\gamma^4 + B_2\gamma^3 + B_3\gamma^2 + B_4\gamma + B_5$$
(4)

Similarly, the Young's modulus dependence on temperature T can be approximated by a 5th degree polynomial given by Eq. (5) (Maruyama, et al., 1987) where C_0, C_1, C_2 etc. are coefficients derived from the respective polynomial fits given in Table 1.

$$E^T = C_0T^5 + C_1T^4 + C_2T^3 + C_3T^2 + C_4T + C_5$$
(5)

The effects of irradiation and temperature on Young's modulus are illustrated in Fig.6.

Figure 6. Shows how the value for young's modulus varies with dose rate (left) and temperature (right).

RESULTS AND DISCUSSION

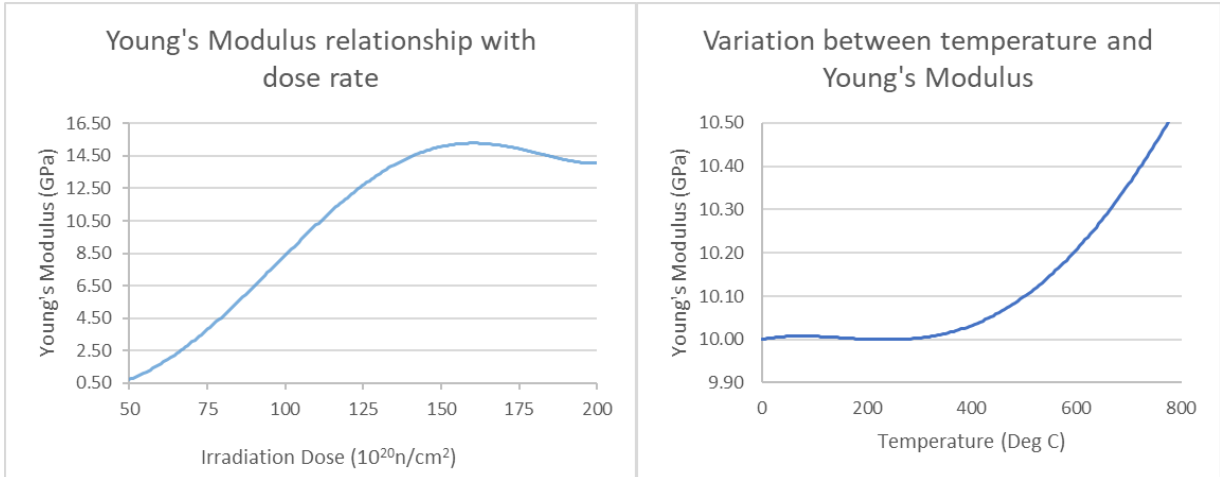A whole scale model containing all the bricks and keys is displayed in Fig.7, where a solution due to gravitational forces is used for illustration. The inclusion of all gaps in this model makes the analysis due to thermal and irradiation loads computationally expensive at this stage. Therefore, a smaller model is used to develop confidence in the modelling approach used to represent the gaps between the bricks, before moving analysis back onto a full-scale model. The smaller model contains 120 fuel bricks, and a total of 430 bricks and is shown in Fig.8. The gaps between the various bricks have been modelled by deformable continuum finite thickness cohesive elements. The stiffness of these elements is significantly lower than that of the graphite bricks.
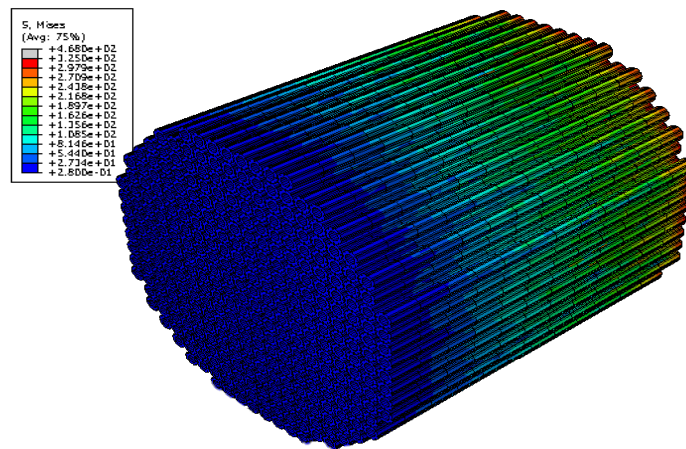

Figure 7. Stresses due to gravity on whole scale model

Due to the reduced number of bricks the loads shown in the previous section could not be applied to this model in principle. However, for the purposes of illustration, the same distribution of thermal loads and irradiation loads is applied here as shown in Fig. 9. It is noted that the load

gradients in this case are larger than in the full-scale model, which may lead to larger stress gradients between layers.
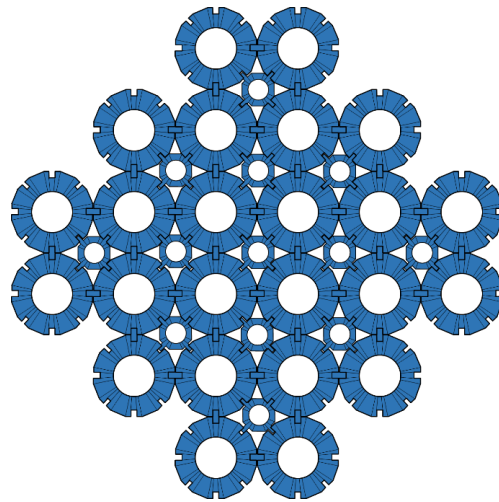
Figure 8. A 6 by 6 by 5 model generated to test approach used.
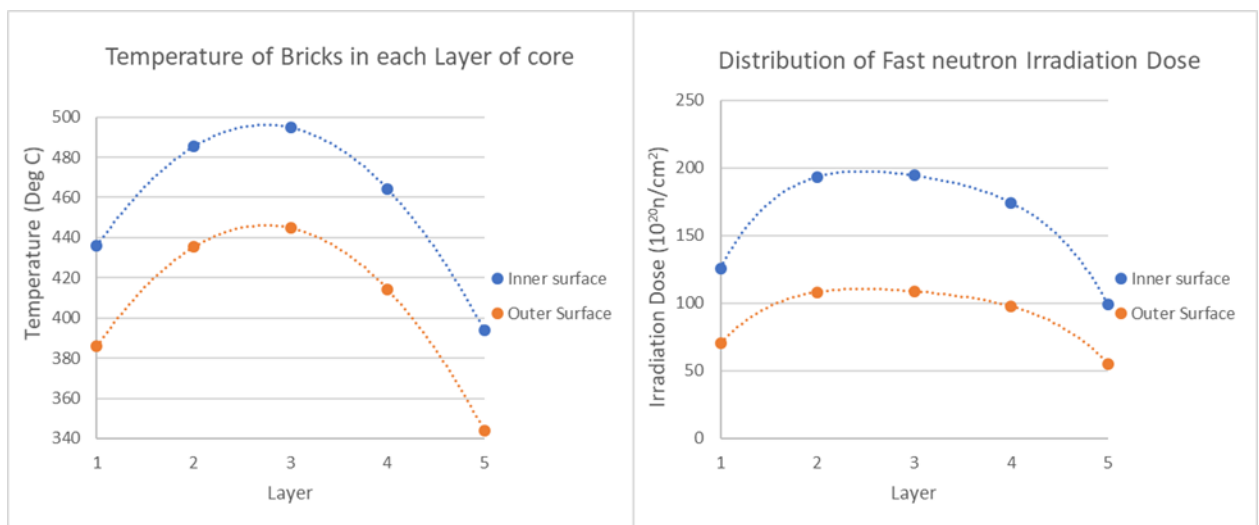
Figure 9: Thermal (left) and irradiation dose (right) loads applied to a 6 by 6 by 5 model

The initiation of cracking in graphite is controlled by the maximum principle stress. An estimate for the energy release rate, G, upon cracking can be made by assuming that the maximum principal stress, σ_I, acts over a material-dependent distance or length scale, d (a crack-jump). It is assumed here that the material length scale equals the mean particle size in Gilsocarbon, which is estimated to be 914 µm**Invalid source specified.**. Cracking occurs when the energy release rate reaches a critical value – the fracture energy, G_c. From the fracture toughness and elastic modulus of Gilsocarbon, the fracture energy is estimated to be 200 J/m^2 **Invalid source specified.**. This provides an estimate for the critical value of the maximum principal stress of 0.22MPa.

Finite element analysis of the model is used to access the evolution of the maximum principal stress at brick keyways. The results for all brick types are analysed and the evolutions of the most stressed bricks of each type are given in Fig. 10. Specifically, the fuel brick with the largest maximum principal stress displays a final value of 0.64MPa. This brick is located in column 2, row 3 and on layer 3 of the system. The largest maximum principle stress was found to occur in one interstitial brick, 1.6 MPa, as shown in the figure. Assuming that the maximum dose a brick will receive after 30 years of service is $200 \times 10^{20} n/m^2$, comparing to the maximum stress value required for a crack to occur to the maximum principle stresses found through finite element analysis, it is found that an interstitial brick will crack first after 19 years of operation, followed by a key after 22 years, and a fuel brick after 23 years. The filler interstitial bricks will be the last bricks to show signs of cracking at 30 years. Comparing Fig.10 with Fig.4, it is clear that the maximum principal stress increases when the bricks begin to expand beyond their original size, indicating correlation between the expansion of the brick and stress value seen in the keyways of the bricks. The reason for the sudden increase in stress is the initiation of contact between bricks, which according to the analysis here is after 19 years of service.
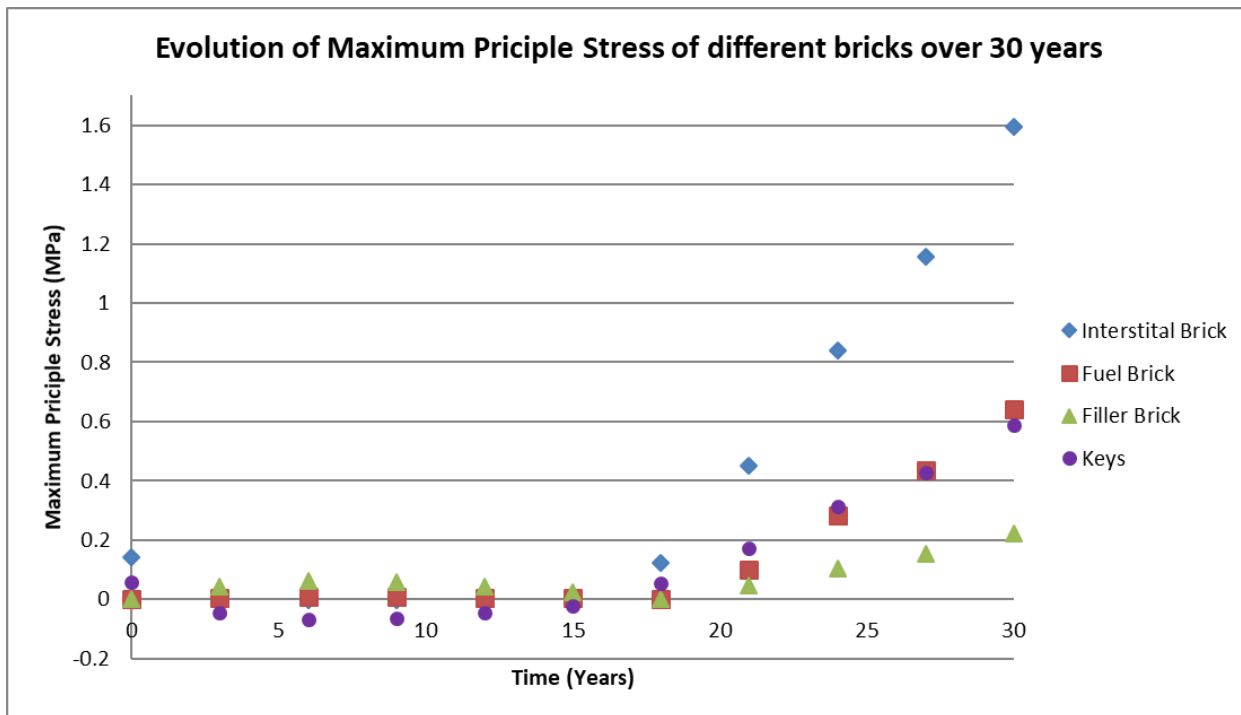
Figure 10: Maximum stress in bricks over a 30-year time period

Fig.11 shows the percentage of elements where the calculated maximum principle stress surpasses the 0.22MPa calculated as the requirement for a crack to occur. Fig.10 shows that the interstitial bricks fracture first and will reach a higher peak maximum principle stress, however Fig.11 indicates a larger number of fuel bricks will fail over the 30-year operational time. In addition, Fig.11 shows that the interstitial bricks begin to fail at a linear rate beyond the 19th year where the first crack occurs, however the fuel bricks will fail exponentially following the 23rd year where the first crack occurs. This can be explained with the lack of irradiation load on the interstitial bricks in comparison to the fuel bricks, where stresses are caused by both the dimensional changes due to irradiation and the bricks coming into contact with each other.

Figure 11: Percentage of elements for each brick that have failed in the model

In order to ensure the plant can remain operational, the channels must remain sufficiently aligned for fuel assemblies and controls rods to both enter and exit the rector as shown in Fig.12. By measuring the displacement of each channel (shown with a red line in Fig.12) and comparing this to the original length the tortuosity of each channel can be found. Within the 6 by 6 by 5 model, it was discovered that the channel with the h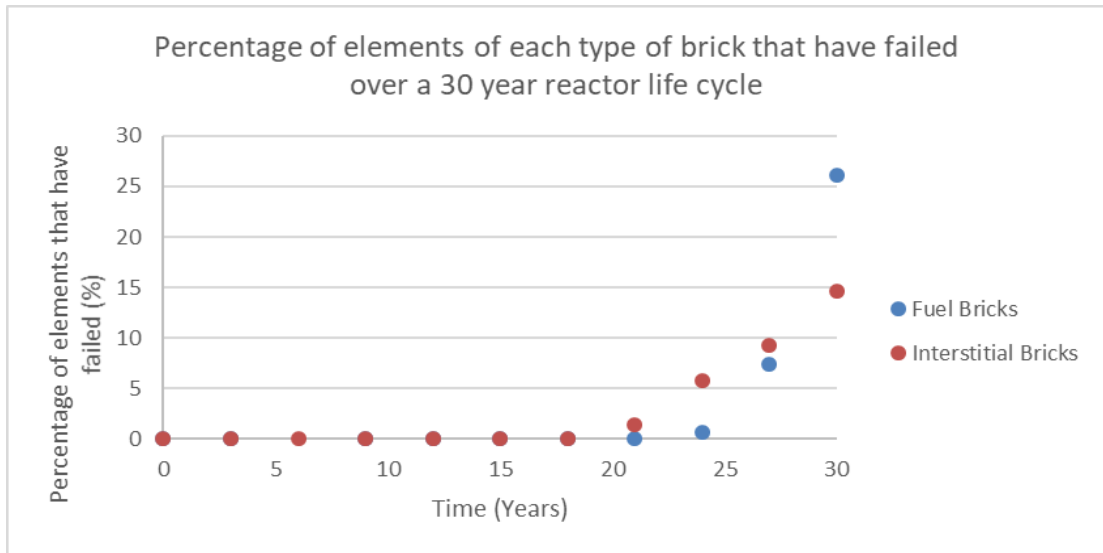ighest tortuosity was 2-2 which had a value of 1.0016. This indicates that all the channels alignment was not compromised after 30 years of service. However, due to only having 5 layers the assessment of tortuosity is only indicative; analysis of full-scale model is expected to provide a closer estimate.
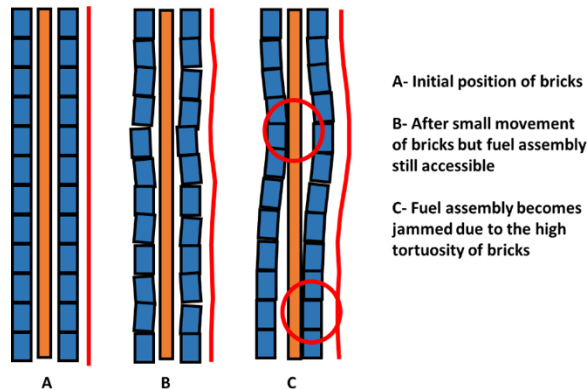
Figure 12: How tortuosity of each channel is measured

ONGOING WORK

While so far it has been shown that the method used will be able to produce result of practical importance, a full-scale model remains to be developed where the gaps between the bricks are included. The inclusion of these gaps is vital in the understanding of when bricks will fracture and how they will affect each other. It was shown with Fig.10 that only when expansion occurs, the stresses in the bricks begin to rise, and without such gaps the stresses would be significantly higher, significantly sooner, creating unreliable results. Once a full-scale model is developed, life cycles load condition will be placed on the bricks. This will be completed by dimensional changes caused by irradiation and thermal loads. From investigation of the data gathered, it will become clear how irradiation induced changes to individual bricks affects the integrity of the whole core.

CONCLUSION

The creation of a realistic whole scale model of AGRs moderator is of significant industrial importance. The complexity of developing such a model lies with the large number of graphite bricks in the model, and the interactions between them. In order to overcome this issue Python scripting has been employed alongside ABAQUS to develop a realistic model. Up to now a full-scale model has been developed which does not include gaps between the bricks. A smaller model, which does include gaps between the bricks, is used instead to demonstrate the capability of the approach. This will be extended to the full-scale in the near future.

While the results displayed in this work indicate that the onset of cracking is after 19 years of operation in interstitial bricks, followed by faster cracking in fuel bricks, these outcomes cannot be claimed to be relevant to a real reactor, because of the size of the model analysed. The approach proposed however creates confidence that it is possible to develop a full-scale model and analyse the development of cracking in the core throughout the duration of the rector's life cycle. With the addition of damage properties, it will be possible to also investigate how

REFERENCES

Abrahamson, J., 1973. The surface energies of graphite. Carbon, 11(4), pp. 337-362.

Ahmed, K. M., Parker, J. V. & Proffitt, D. E., 1986. Seismic response of the advanced gas cooled reactor core. Nuclear Engineering and Design, 94(1), pp. 67-92.

Duncan, B. & Kralj, B., 2007. Seismic Modelling of an AGR Nuclear Reactor Core. Bristol, Atkins.

Kyaw, S. T. et al., 2014. Modelling Crack Growth within Graphite Bricks due to Irradiation and Radiolytic Oxidation. Procedia Materials Science, Volume 3, pp. 39-44.

Crump, T., Jivkov, A.P., Mummery, P., Ferte, G., Tran, V-X., 2019. Analysis of dynamic fracture and fragmentation of graphite bricks by combined XFEM and cohesive zone approach. International Journal of Pressure Vessels and Piping, 171, pp. 117-124.

Crump, T., Ferté, G., Mummery, P., Jivkov, A.P., Martinuzzi, P., Tran, V-X, 2017. Dynamic fracture effects on remote stress amplification in AGR graphite bricks. Nuclear Engineering and Design, 323, pp. 280-289.

Li, H., Fok, A. S. & Marsden, B. J., 2007. An analytical study on the irradiation-induced stresses in nuclear graphite moderator bricks. Journal of nuclear materials, 372(2-3), pp. 164-170.

Maruyama, T., Eto, M. & Oku, T., 1987. Elastic modulus and bend strength of a nuclear graphite at high temperature. Carbon, 25(6), pp. 723-726.

McLachlan, N. et al., 1996. A Probabilistic approach to assessing AGR core life. Nuclear Energy, 35(1), pp. 15-23.

Morrison, C. N., Jivkov, A. P., Vertyagina, Y. & Marrow, T. J., 2016. Multi-scale modelling of nuclear graphite tensile strength using the site-bond lattice model. Carbon, Volume 100, pp. 273-282.

Mostafavi, M., McDonald, S. A., Mummery, P. M. & Marrow, T. J., 2013. Observation and quantification of three-dimensional crack propagation in poly-granular graphite. Engineeing Fracture Mechanics, Volume 110, pp. 410-420.

Zou, Z., Fok, S. L., Marsdem, B. J. & Oyadiji, S. O., 2006. Numerical simulation of strength test on graphite moderator bricks using a continuum damage mechanics model. Engineering Fracture Mechanics, 73(3), pp. 318-330.

LARGE SCALE MODELLING OF DAMAGE AND FAILURE OF NUCLEAR GRAPHITE MODERATED REACTOR

ABSTRACT

The UK Advanced Gas-Cooled reactors (AGRs) have cores made of graphite bricks with dual functions: as structural elements of the core, providing space for and separating fuel and control rods; and as moderator of the nuclear reaction. Nuclear graphite is a quasi-brittle material, where the dominant mechanism for failure is cracking. While cracking of isolated bricks is expected due to operation-induced changes in graphite microstructure and stress fields, these could be tolerated as far as the overall structural function of the core is maintained. Assessment of the whole core behaviour has been previously done with whole scale models where bricks have been considered as rigid body elements connected by elastic-brittle springs. This approach does not allow for the realistic assessment of the stresses in the bricks and associated brick cracking. Reported here are results from an ongoing project, which addresses this shortcoming. The proposed model uses deformable bricks with appropriate interactions, allowing for physically realistic whole core analysis. The results are focused on the damage that a graphite moderated reactor develops during a life cycle, how this affects the behaviour of the whole core, and how changes in bricks' behaviour impacts the core integrity. The proposed methodology is a major step towards high-fidelity assessment of AGRs' fitness for service, required for supporting continuous safe operation and life-extension decisions.

INTRODUCTION

The Advanced Gas-Cooled reactors (AGR) in the UK use graphite as a moderator and also as a structural component. The reactor core contains three different types of interlocking graphite moderator bricks: fuel bricks, interstitial bricks and filler interstitial bricks as shown in Fig. 1. The bricks are stacked vertically on top of each other, with the entire core consisting of 12 layers of bricks. Each layer contains 323 fuel bricks and 293 interstitial and filler interstitial bricks. The gaps in the bricks create vertical channels for fuel assemblies, control rods and coolant flow. The entire structure is connected via a system of loose keys and keyways, which allow the core to expand and contract during service. A layer of Upper Neutron Shield of graphite bricks covers the assembly. The whole system is kept laterally stable using a system of restrain rods and beams, centralising brackets and Warwick links tied to restrain rings [2].

During the reactors life cycle, different fuel bricks undergo dimensional changes at different rates due to temperature and irradiation gradients, e.g. bricks located in central layers are irradiated at a faster rate. The structural integrity of bricks is critical to the safe reactor operation, because cracked bricks can lead to core distortion and potentially to channels misalignment. This could cause blockages that prevent insertion or extraction of fuel and control rods. The whole core behaviour due to dimensional changes has been a subject of a number of past works. Due to the large number of bricks, these works have been mostly based on models with rigid-body bricks connected by spring elements representing the keys. In such case, all mechanical effects are assigned to the springs: stiffness, friction, damping and damage/failure. While the approach allows for calculating load transmission or impacts between the bricks [3], it has a major limitation – deformation, damage and fracture of the bricks cannot be. As a consequence, the effect of bricks' damage and failure on the core behaviour cannot be investigated.

The aim of this work is to gain better understanding of temperature and irradiation effects on a graphite reactor core by developing a more realistic model with deformable bricks and bespoke interactions. The model presented allows for investigations of how the changes of graphite properties throughout the course of a reactor's lifespan affect the whole core geometry and integrity. In particular, this development allows for improved assessment of the core fitness-for-purpose towards its projected end of life, and can inform life-extension decisions with higher fidelity.

REACTOR CORE MODEL GEOMETRY

Fig. 1 shows a finite element model of the whole core, which has been developed using deformable brick elements and surface interactions. This contains 3984 fuel bricks, 3516 interstitial and filler interstitial bricks, and 7488 keys, each tessellated into 1,145,000 continuum finite elements, leading to over 90,000 different interacting surfaces. The presence of contact surfaces puts a very high computational demand, and for this reason, the calculations and the results presented here are obtained with a smaller model containing only 120 fuel bricks, 65 interstitial and filler interstitial bricks, and 180 keys. This allows for an investigation into the most computationally efficient method of modelling a full-scale reactor while remaining as realistic as possible. Via a purpose-built Python script for ABAQUS, only surfaces in direct contact were defined,

reducing substantially the computational power required. These surfaces were grouped, allowing for a whole-scale model to be created. The model contains initial gaps of 10 mm between the individual bricks, as per design specification.

MATERIAL PROPERTIES

Two material models have been considered for the graphite bricks: an elastic-brittle model as a simplification of the graphite behaviour; and a damage-plasticity model as a potential representation of the graphite quasi-brittle behaviour. To define the non-linear properties for graphite, the yield surface, flow rule, load response, and material degradation are defined. These values are collected from various literature sources considering the biaxial behaviour of Gilsocarbon. References [1, 13-16] were used to find the uniaxial compressive yield stress to biaxial yield compressive stress ratio (f_{b0}/f_{c0}), eccentricity (ϵ_{cc}), and the dilation angle (ψ).

The continuum model created assumes two primary failure mechanism; these are tensile cracking and compressive crushing. Fig. 2 displays the full material behaviour applied to the Graphite bricks. Under uniaxial tension, the stress-strain response follows a linear elastic relationship until the value of the failure stress $(\sigma_{T\,MAX})$ is reached. At this point, the onset of micro-cracking in the graphite material is observed. Beyond the failure stress, the formation of micro-cracks is represented macroscopically with a softening stress-strain response, which induces strain localisation in the graphite structure.

The Tensile softening behaviour is defined using the fracture energy G. Modelling stiffness degradation is not yet possible due to lack of available data; therefore, linear evolution of the damage variable with effective plastic displacement is assumed.

Under uniaxial compression, the response is linear until the value of initial yield (σ_{C0}). Following this, plasticity will occur, first with a response categorised as stress hardening up to the ultimate stress (σ_{CU}). This is followed by strain softening. References [1, 13, 17] were used to collect the compressive load response data. All values used to model damage are displayed in Table 2. For both cases, the Young's modulus *E* is made dependent on temperature and dose, while the Poisson's ratio is kept constant [9].

LOAD AND BOUNDARY CONDITIONS

Two operational loads causing dimensional changes are considered: temperature and irradiation. These are applied separately to the model. Each load induces non-mechanical strains, a thermally-induced strain, ε^{th}, and an irradiation-induced strain, ε^{ir}, which modify the gaps between the bricks. When bricks get in contact due to gap closure, further expansive strains cause deformation of these bricks with associated stresses.

The temperature distribution within the core is assumed constant from start to end of the reactor's lifecycle (outages not considered). The temperature varies between the different layers, with the central bricks having a higher temperature than the bricks at the top and bottom of the reactor. Within each fuel brick in a particular layer, the temperature decreases by linearly by 50°C from the inner to the outer edge.

The temperature variation between layers and between brick surfaces used in the present work are shown in Fig.3. Notably, the highest temperature is not at the central layer, but at layer 5 of the core. This bias is due to the airflow through the reactor passing from layer 12 to layer 1, distorting in the distribution of the temperatures. The temperature field is assigned by a Python script to the elements of individual bricks, assuming linear variation across the brick thickness. Thermal strains result from temperature gradients, as described by Eq. (1) [4], where the coefficient of thermal expansion, α, used in the present work was 4.39×10^{-9} [7]. This value remained constant throughout the reactor's life cycle.

$$\varepsilon^{th} = \alpha \, \Delta T \tag{1}$$

The effects of irradiation on a single brick have been modelled and discussed in previous works, e.g., [12]. It has been found that as graphite bricks irradiate, they shrink first, then expand beyond their original dimensions. As fuel bricks' interiors receive higher dosages, the inner surfaces shrink at a faster rate than the outer surfaces. After 30 years of service, a brick in layer 4 of the model will receive a dose on the inner surface of the brick that is approximately 200×10^{20} n/cm^2 while the dose on the outer surface is 112×10^{20} n/cm^2. This is illustrated in Fig. 4. This creates a potential for bore cracking, where tensile stresses exist close to the centre of the brick, and compressive stresses exist outside. The effect is reversed later in the bricks' life with the generation of compressive stresses at the inner surface and tensile stresses at the outer surface. These changes cause stress concentration in keyways and could lead to crack initiation. The cracks created due to bricks expansion can join up with cracks created during the initial shrinking resulting in brick failure.

Keyway cracking is of most significant concern to operators, as multiple brick failures can lead to compromising the whole keying system or multiple channels (Zou, et al., 2006). Such scenarios have been examined by a series of experiments with single un-irradiated graphite moderator bricks and corresponding finite element analyses replicating the real reactor [12]. The results showed good agreement between the predicted failure strength and available experimental data. Furthermore, fast cracking at one keyway is anticipated to trigger a secondary crack at another, potentially opposite keyway, leading to brick disintegration. This phenomenon, known as prompt secondary cracking, has been investigated in detail by dynamic fracture analysis, with results confirming the anticipation [5,6].

By considering the data in Fig. 4, the irradiation strain ε^{ir} can be expressed as a function of fast neutron dose γ using a 4th degree polynomial, Eq. (2), where A_0, A_1, A_2 etc. are coefficients derived from the respective polynomial fits given in Table 1.

$$\varepsilon^{ir} = A_0\gamma^4 + A_1\gamma^3 + A_2\gamma^2 + A_3\gamma + A_4 \tag{2}$$

Like the thermal loads, the irradiation loads are modelled with a constant dose for each layer, variable dose between the layers, and variable dose between inner and outer brick surfaces. The dose distribution in the core is shown in Fig 5. Equations (1) and (2) can be combined to provide a value for the total strain induced by particular temperature and irradiation dose in any finite element of any brick:

$$\varepsilon = (\alpha \, \Delta T + A_0\gamma^4 + A_1\gamma^3 + A_2\gamma^2 + A_3\gamma + A_4) \tag{3}$$

Computationally, the effects of temperature and irradiation dose are imposed by the local changes of Young's modulus. Young's modulus varies with the dose rate γ,

can be approximated by a 5th degree polynomial given by Eq. (4) [7], where B_0, B_1, B_2, etc. are coefficients derived from the respective polynomial fits given in Table 1.

$$E^{ir} = B_0\gamma^5 + B_1\gamma^4 + B_2\gamma^3 + B_3\gamma^2 + B_4\gamma + B_5 \qquad (4)$$

Similarly, the Young's modulus dependence on temperature T can be approximated by a 5th degree polynomial given by Eq. (5) [8] where C_0, C_1, C_2 etc. are coefficients derived from the respective polynomial fits given in Table 1.

$$E^T = C_0T^5 + C_1T^4 + C_2T^3 + C_3T^2 + C_4T + C_5 \qquad (5)$$

FITNESS-FOR-SERVICE ASSESSMENT

To ensure the plant can remain operational, the channels must remain sufficiently aligned for fuel assemblies and control rods to both enter and exit the rector. As the bricks are irradiated, the diameter of the bricks changes while the angle of the bricks between the layers also changes, going through 3 phases, as shown in Fig. 6. Phase 1 sees the entire core shrink as middle layers shrink at a higher rate than the upper and lower layers of bricks. Phase 2 occurs when the middle layers begin to expand as upper and lower layers are still shrinking. Finally, phase three occurs as all bricks are expanding with the central layers of bricks expanding at a faster rate.

By noting the position of nodes at any given time, the angle of each brick can be calculated using Eq. (6), where $x_n{}^m$ and $y_n{}^m$ signified a node in the brick at position n on the surface of the brick, and m either at the top of the brick.

$$\theta_L = \max\left\{\left[tan^{-1}\left(\frac{x_1{}^T - x_1{}^B}{x_1{}^B}\right)\right], \left[tan^{-1}\left(\frac{x_2{}^T - x_2{}^B}{x_2{}^B}\right)\right], \left[tan^{-1}\left(\frac{y_1{}^T - y_1{}^B}{y_1{}^B}\right)\right], \left[tan^{-1}\left(\frac{y_2{}^T - y_2{}^B}{y_2{}^B}\right)\right]\right\} \qquad (6)$$

By comparing the angle of the brick from the upper brick with the angle of the brick in the layer below, the change in angle (θ_A) can be calculated as shown in Eq. (7).

$$\theta_A = \theta_L - \theta_{L+1} \qquad (7)$$

The maximum allowable angle of rotation can be calculated using the diameter of the brick C at any given time, along with the values of the fuel assembly's diameter A and length B. This gives a value given by Eq. (8).

$$\theta = \tan^{-1}\left[\frac{C}{\sqrt{A^2 + B^2 - C^2}}\right] - \tan^{-1}\left[\frac{A}{B}\right] \qquad (8)$$

By comparing the values of θ_A and θ it will become clear if the fuel assemblies are free to move along the channels or if a blockage will occur. Also, if the diameter of the brick becomes smaller than the diameter of the fuel assembly, a blockage can also occur. Therefore, a blockage will occur if $\theta_A \geq \theta$ or $C < A$. Fuel assemblies will be free to move if $\theta_A < \theta$ or $C > A$.

RESULTS AND DISCUSSION

The loads applied to this model were equal to the loads from layer 1 to 5 of the whole scale model only. A plasticity model takes 103% longer to complete analysis when compared to an elastic model. This increase in processing time becomes significant when moving to full-scale modelling. Analysis of the data from a small-scale model is provided in Fig. 7,8 and 9. Through examination of these figures, it will become clear this additional computation power will yield improved predictions of core behaviour.

The finite element analysis of the model is used to access the evolution of the maximum principal stress at brick keyways. The results for all brick types are analysed, and the evolutions of the bricks where the maximum stressed surpass the tensile limits

are given in Fig. 7. Very little difference was observed between an elastic model and a plastic model predicting similar fractures dates. Assuming that the maximum dose a brick will receive after 30 years of service is $200 \times 10^{20} n/m^2$, it is found that a crack will first occur after 6 years of operation in layer 5, followed by layer 4 at 28 years, with the remaining layer failing after 30 years. Comparing Fig. 7 with Fig. 4, it is clear that layers 2,3 and 4 and all fracturing during phase 2, where stress reversal has begun, and the bricks begin to expand beyond their original sizes, indicating a strong correlation between fracture of the bricks and stress reversal occurring. By considering the dosage of the bricks and the distance between the bricks, it is clear that the bricks are fracturing due to internal stresses and not due to contact between the bricks. Contact between bricks does not begin until 31 years of operation.

An outlier in the results is visible with the fracture date of Layer 5, with results suggesting the layer to fractures much sooner. Upon closer inspection of the data, it is clear this early fracture is down to the boundary conditions placed on the bottom layer of brick. The condition applied have an opposing effect to loads applied to the same layer of bricks, with one limiting expansion and the other causing it, resulting in high stresses in the brick. Therefore, results from layer 5 will be ignored from here.

Until the yield stress is reached, both elastic and plastic models predict similar core behaviour, following this behaviour changes due to the material properties being applied. Fig.7 shows how damage evolved over time in different regions of the brick. The brick can be split into three regions, the fuel brick keyways, the interstitial brick keyways, and the rest of the brick making up the final region. The models predict 65% of elements in the whole brick will be damaged in an elastic model; however, this value drops significantly with a damage plasticity model. Only 40% of the elements are fractured with a plasticity model.

Percentage damage observed in the bricks slows once contact between bricks initiates at 30 years. While an elastic model predicts the rate of damage in the whole brick slows at a similar rate before build up again, the plasticity model displays signs of stress distribution and a sudden increase and reversal of damage in the fuel brick keyways. Single brick models of the past predicted the keyways to fail first [10, 11], and a sudden build-up of stresses at the keyways after contact provides an indication of when the integrity of the can first become compromised.

While the core can still function with fractured bricks, it cannot function once channels fall out of alignment. Once this occurs, the free movement of fuel assemblies becomes compromised. Fig. 9 shows the results based on channel alignment. The blue line illustrates the maximum angle possible based on Eq. 8, while the orange line illustrates the maximum angle possible based on Eq.7. Once both lines cross the alignment of the channels becomes compromised. Once again, the method of modelling the core provides very different results, with an elastic model suggesting a blockage could happen as early as 18 years. After these channels move back into position before a second distortion after 35 years. The plasticity model experiences less displacements in the bricks during the early years of service, and displays a blockage won't occur until 31 years of operation. Following this date, the channels fall vastly out of alignment, to a greater extent than observed with an elastic model. This suggests the integrity of the core is compromised after contact between bricks initiates in a plasticity model.

While so far, it has been shown that the method used will be able to produce result, of practical importance, a full-scale model remains to be simulated. It was shown

with Fig.7 that only when expansion occurs, the stresses in the bricks begin to rise. Once a full-scale model is developed, life-cycle load conditions will be placed on the bricks. This will be completed by applying dimensional changes caused by irradiation and thermal loads. From the investigation of the data gathered, it will become clear how lifetime dimensional changes to individual bricks affects the integrity of the whole core.

CONCLUSION

The creation of a realistic whole scale model of AGRs moderator is of significant industrial importance. The complexity of developing such a model lies with the large number of graphite bricks in the model and the interactions between them. In order to overcome this issue, Python scripting has been employed alongside ABAQUS to develop a realistic model. This report displays a small model developed to demonstrate the capability of the approach used to model a full-scale model.

The results displayed in this work indicate that the onset of cracking is after 28 years of operation, following stress reversal in the fuel bricks. The results also show a substantial difference in the integrity of the core based on the material properties applied. The result reveal that realistic plastic material softening properties indicate core integrity will be compromised after 31 years of service, at the point that brick contact initiates. However, these outcomes cannot be claimed to be entirely relevant to a real reactor because of the size of the model analysed.

The approach proposed creates confidence that it is possible to develop a full-scale model and analyse the development of damage in the core throughout the rector's life cycle. With the addition of damage properties, a more realistic model can be developed, allowing us also to investigate how damaged bricks influence the surrounding bricks and the integrity of the entire matrix of bricks. Ultimately, assessments of the whole core fitness-for-service will be made with higher confidence through development of a full-sale model.

ACKNOWLEDGMENT

REFERENCES

[1] Brocklehurst, J. E. & Kelly, B. T., 1993. The dimensional changes of highly-oriented pyrolytic graphite irradiated with fast neutrons at 430C to 600C. *Carbon,* 31(1), pp. 179-183.

[2] Ahmed, K. M., Parker, J. V. & Proffitt, D. E., 1986. Seismic response of the advanced gas cooled reactor core. Nuclear Engineering and Design, 94(1), pp. 67-92.

[3] Duncan, B. & Kralj, B., 2007. Seismic Modelling of an AGR Nuclear Reactor Core. Bristol, Atkins.

[4] Kyaw, S. T. et al., 2014. Modelling Crack Growth within Graphite Bricks due to Irradiation and Radiolytic Oxidation. Procedia Materials Science, Volume 3, pp. 39-44.

[5] Crump, T., Jivkov, A.P., Mummery, P., Ferte, G., Tran, V-X., 2019. Analysis of dynamic fracture and fragmentation of graphite bricks by combined XFEM and cohesive zone approach. International Journal of Pressure Vessels and Piping, 171, pp. 117-124.

[6] Crump, T., Ferté, G., Mummery, P., Jivkov, A.P., Martinuzzi, P., Tran, V-X, 2017. Dynamic fracture effects on remote stress amplification in AGR graphite bricks. Nuclear Engineering and Design, 323, pp. 280-289.

[7] Li, H., Fok, A. S. & Marsden, B. J., 2007. An analytical study on the irradiation-induced stresses in nuclear graphite moderator bricks. Journal of nuclear materials, 372(2-3), pp. 164-170.

[8] Maruyama, T., Eto, M. & Oku, T., 1987. Elastic modulus and bend strength of a nuclear graphite at high temperature. Carbon, 25(6), pp. 723-726.
McLachlan, N. et al., 1996. A Probabilistic approach to assessing AGR core life. Nuclear Energy, 35(1), pp. 15-23.

[9] Morrison, C. N., Jivkov, A. P., Vertyagina, Y. & Marrow, T. J., 2016. Multi-scale modelling of nuclear graphite tensile strength using the site-bond lattice model. Carbon, Volume 100, pp. 273-282.

[10] Mostafavi, M., McDonald, S. A., Mummery, P. M. & Marrow, T. J., 2013. Observation and quantification of three-dimensional crack propagation in poly-granular graphite. Engineeing Fracture Mechanics, Volume 110, pp. 410-420.

[11] Zou, Z., Fok, S. L., Marsdem, B. J. & Oyadiji, S. O., 2006. Numerical simulation of strength test on graphite moderator bricks using a continuum damage mechanics model. Engineering Fracture Mechanics, 73(3), pp. 318-330.

[12] McLachlan, N. et al., 1996. A Probabilistic approach to assessing AGR core life. *Nuclear Energy,* 35(1), pp. 15-23.

[13] Becker, T. & Marrow, J., 2013. *Modelling Damage in Nuclear Graphite.* Beijing, s.n.

[14] S. Sata, Nuclear Engineering and Design 23 (1987) 62.

[15] J. Jortner, Technical Report AFML-TR-71 (1971) 253

[16] W. Greenstreet, G. Yahr, R. Valachovic, Carbon 11 (1973) -57

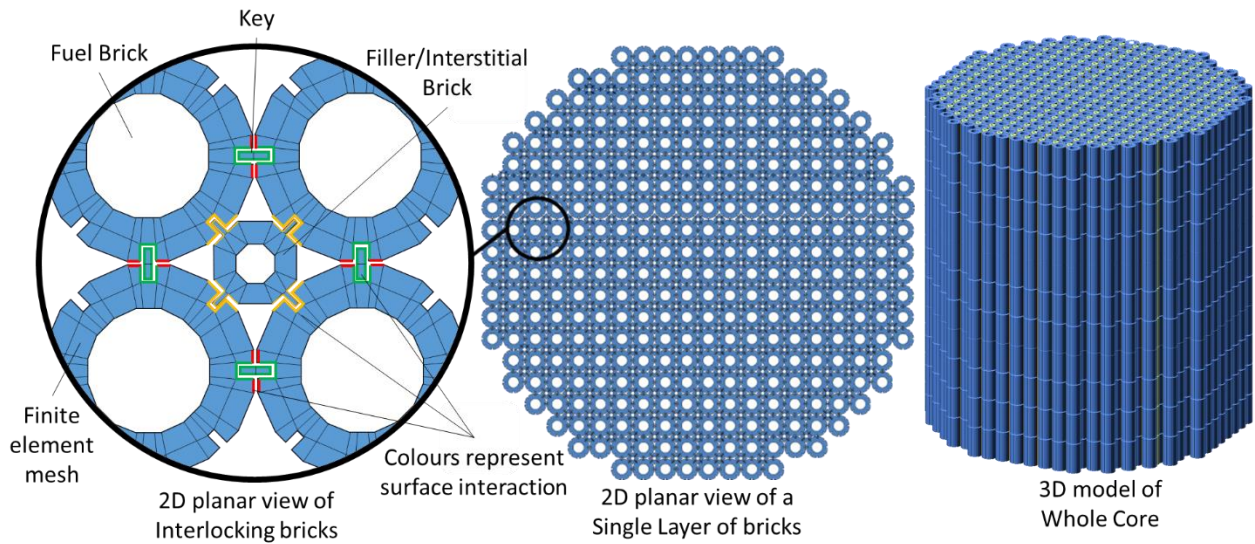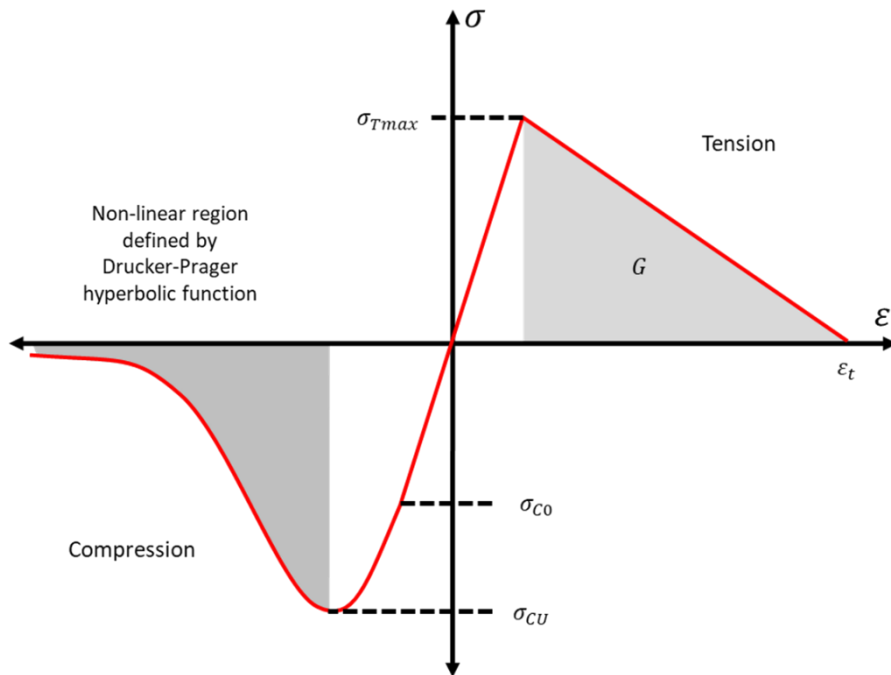[17] T. Oku, M. Eto, Nuclear Engineering and Design 143 (1993) 239–243

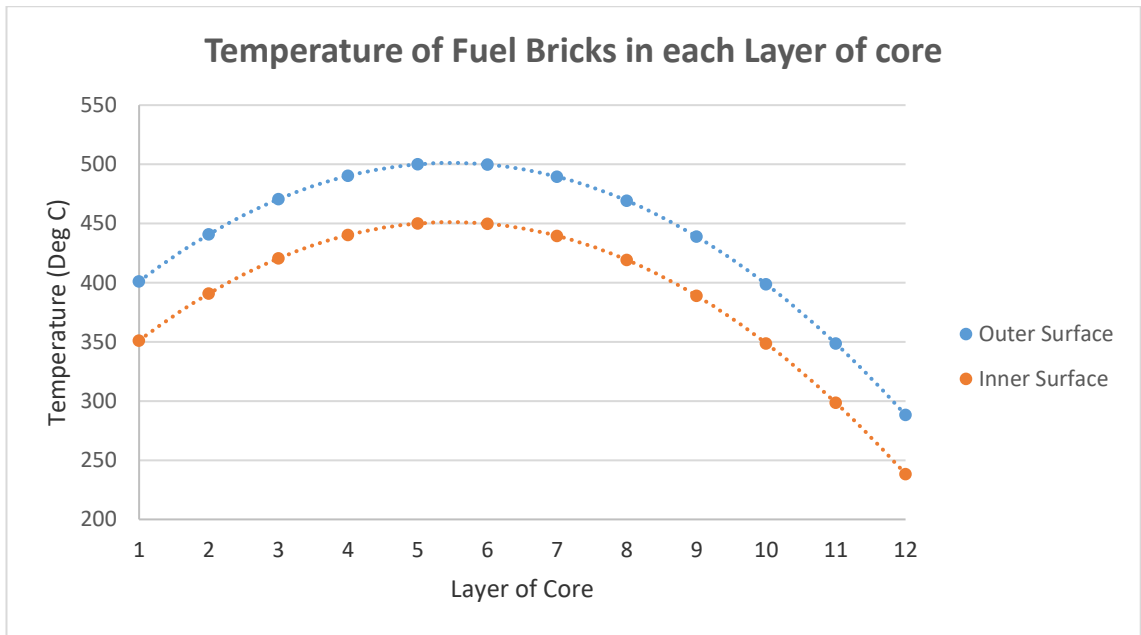Figure 1. Layout of graphite core and finite element model

Figure 3. Temperature variation between layers and bricks surface

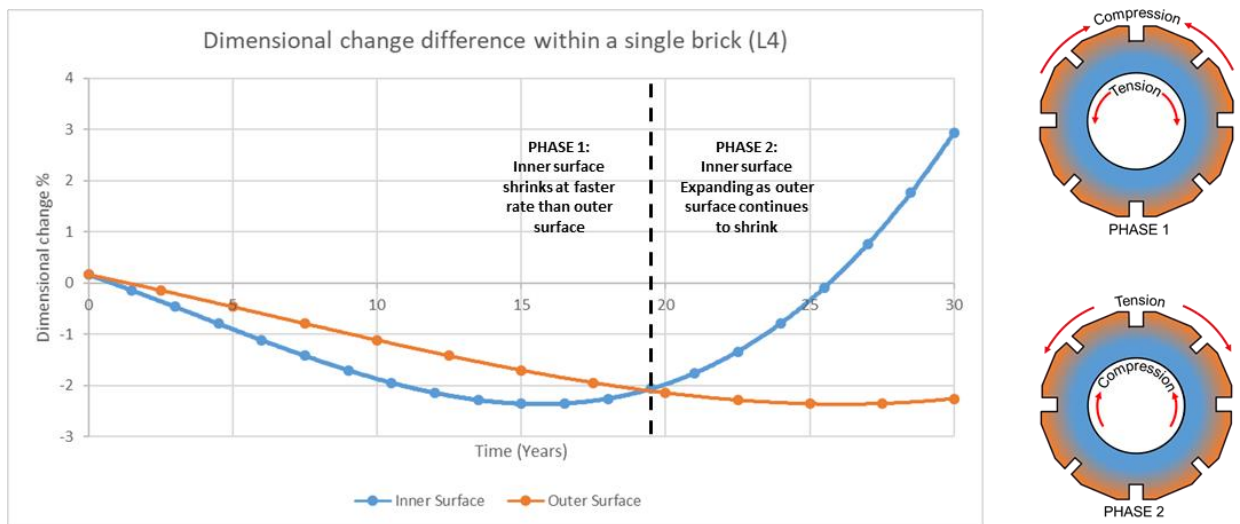Figure 4. Effects of irradiation-induced dimensional changes on brick

Table 1: Polynomial coefficients for calculating irradiation-induced strains (A_i) and Young's modulus variation with irradiation dose (B_i) and temperature (C_i)

Coefficient	A_0	A_1	A_2	A_3	A_4	
Value	0.15	- 4.1228	41.792	- 135.79	0.6446	
Coefficient	B_0	B_1	B_2	B_3	B_4	B_5
Value	9.397E-7	4.610E-4	6.923E-2	-2.6907	2.793E1	1.399E4
Coefficient	C_0	C_1	C_2	C_3	C_4	C_5
Value	8E-07	0.0038	6.0112	2253.5	241532	1E10

Table 2: Material properties used to model elastic behaviour and plastic damage.

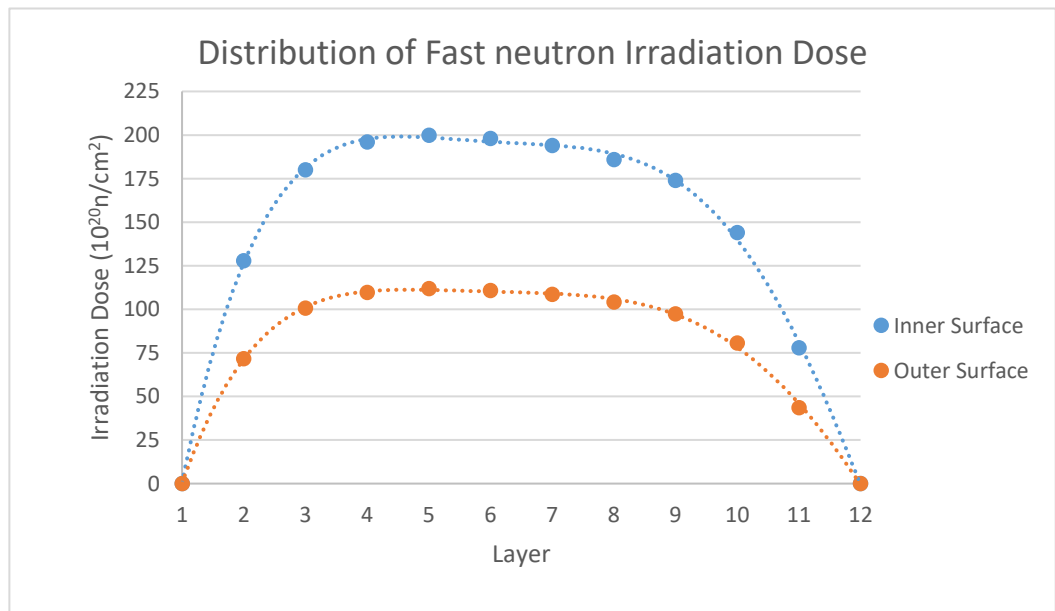|	Elastic properties	
Young's Modulus	E is dependent on temperature T and dose γ	
Poisson's ratio	v	0.21
Damage Plasticity model		
Dilation angle	30°	
Eccentricity	ϵ_{cc}	4.8
Biaxiality ratio	f_{b0}/f_{c0}	0.81
Fracture energy	G	250 J/m²
Tensile strength	σ_{Tmax}	20 MPa
Compressive hardening	20 MPa	
	65 MPa	
	1 MPa	
Compressive displacement	0 mm	
	0.015 mm	
	0.045 mm	

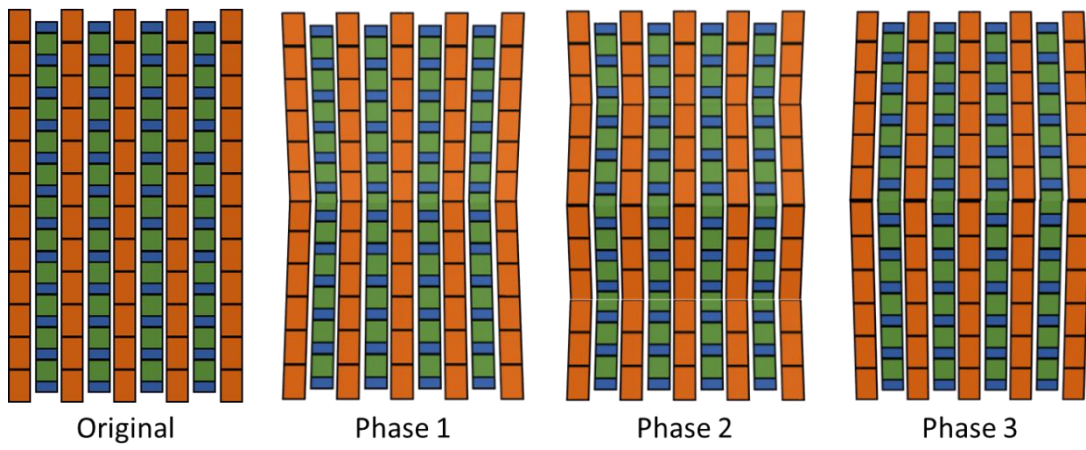Figure 5. Distribution of fast neutron irradiation dose within reactor core.

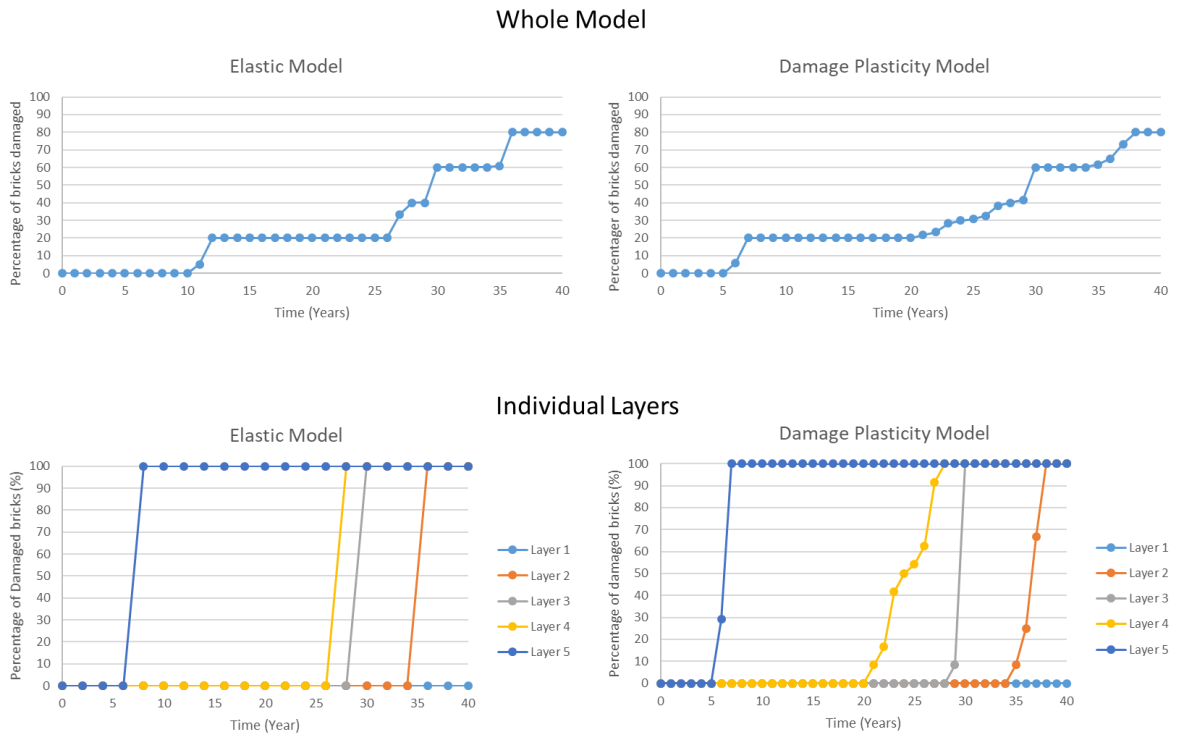Figure 6. Different rotational phases of the brick.

Figure 7. Percentage of bricks failed with an elastic and plastic model.
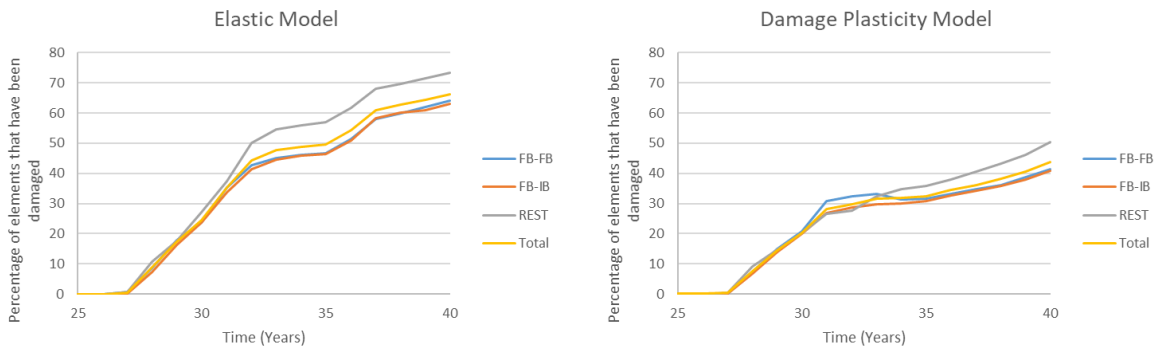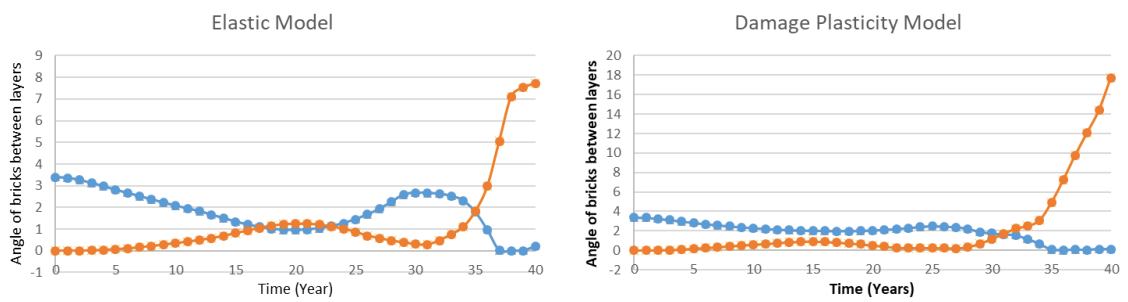
209

Figure 8. Percentage of elements damages in each region of the bricks

Figure 9. Channel alignment over 40 years